JOHANNES GUTENBERG UNIVERSITY MAINZ

Isotopic yield determination for thermal neutron induced fission of ^{235}U, ^{239}Pu and ^{241}Pu in the light, symmetry and heavy mass regions using calorimetric low temperature detectors

by

Santwana Dubey

A thesis submitted in partial fulfillment for the
degree of Doctor of Philosophy

in the
Institute of Physics, Mathematics and Computer Science
Johannes Gutenberg University Mainz

March 2019

Contents

"All truths are easy to understand once they are discovered; the point is to discover them"

Galileo Galilei

Abstract

Isotopic yield investigations for thermal neutron induced fission reactions are presented in this work, which were performed using calorimetric low temperature detectors (CLTDs) with the passive absorber method in a series of experiments at the LOHENGRIN spectrometer at the Institute Laue Langevin Grenoble. The present work expands the isotopic yield determination with the passive absorber method [1–3] from the light fragment mass region to the symmetry and heavy fragment mass region where the isotopic yield determinations were rather challenging or hardly accessible until now [2]. A new CLTD array of 25 detector pixels was constructed and a manipulator with several positions for SiN absorber foil stacks was installed in front of the detectors at only 5 mm distance. Although it was technically challenging to operate the manipulator at temperatures down to 1 K close to sensitive detectors with limited space inside the cryostat, it provided flexibility in the absorber foil thickness and improved the detection efficiency as compared to the previously used setup in the first tests of CLTDs with fission fragments [4] which was in the range of 10 - 70 % depending on the SiN absorber foil thickness to almost 100% for all absorber thicknesses in the present case. These improvements allowed to perform first systematic isotopic yield studies from thermal neutron induced fission reactions with CLTDs for fission fragments particularly produced in the symmetry region with extremely low intensities and in the heavy mass region by adapting optimum absorber thicknesses in the respective cases.

The operation of the new detector setup was tested at the accelerator at the Maier-Leibnitz Laboratory Munich with the heavy ion beams ^{130}Te and ^{127}I in the energy range of 45 MeV to 80 MeV where the CLTDs measured the ion beams with energy resolutions of less than 1 %. Energy loss measurements with the heavy ion beams ^{130}Te and ^{127}I were performed at the MLL at different SiN absorber thicknesses to estimate the expected quality of nuclear charge separation in the heavy mass region of fission fragments and to gain insights in the shape of energy loss distributions. This was in particular helpful for the analysis of overlapping peaks in order to determine the isotopic yields in the heavy fragment mass region.

In the experiments performed at the ILL reactor, isotopic yields were determined in the light, symmetry and heavy fragment mass regions for the thermal neutron

induced fission of ^{235}U, ^{239}Pu and ^{241}Pu targets. A first set of measurements was performed for the precise yield determination of ^{92}Rb for the three targets and of ^{96}Y for ^{235}U and ^{241}Pu targets due to its importance for the understanding of the reactor antineutrino anomaly studies [5]. The ^{92}Rb and ^{96}Y yield thus determined allowed to resolve the discrepancy between the recent independent measurement presented in [6] and the nuclear data libraries like [7] for the ^{92}Rb yield, as well as confirms the ^{96}Y yields from an independent measurement.

Yield measurements towards the symmetry region were performed for ^{239}Pu(n_{th}, f) and ^{241}Pu(n_{th}, f). Isotopic yields were determined for 24 masses in the range $89 \geq A \leq 112$ for ^{241}Pu(n_{th}, f) for the first time with LOHENGRIN. Towards the mass symmetry known Z-yield data were supplemented for masses A = 110 to 112 for ^{241}Pu(n_{th}, f), and for masses A = 110 to 113 for ^{239}Pu(n_{th}, f). The even-odd staggering in the isotopic yields thus determined towards the symmetry region for the first time for ^{241}Pu(n_{th}, f) and ^{239}Pu(n_{th}, f) provides insights in the even-odd effect conjectured in different theoretical fission models for symmetric fission and contrasting predictions based on the previously partially measured data at the LOHENGRIN.

Finally, isotopic yields were determined in the heavy fragment region for masses A = 128 to 137 for the first time with the passive absorber method for ^{239}Pu(n_{th}, f). Besides the possibility of cross-checking available experimental isotopic yield data with an alternative technique, it allowed to complete the experimental data sets with masses A = 130 - 132 and 135, which are either not easily or not at all accessible with gamma-ray spectroscopy.

Chapter 1

Introduction

There has been a continuous progress in the understanding of the nuclear fission phenomenon, ever since its discovery in 1939 [8]. This complex many body problem resulting from collective and intrinsic excitations within the nucleus of an atom is not completely understood despite several theoretical and experimental works (see for example [9]). The various theoretical models, namely- the statistical model [10], the microscopic-macroscopic model [11], the pure microscopic model with dynamical treatment of the fissioning nucleus [12] and others [13], calculate the fission fragment yields, but are unfortunately far from the required accuracy for nuclear applications.

The precise knowledge of fission fragment yield distributions from thermal neutron induced fission reactions, with respect to their mass, kinetic energy and nuclear charge is important, on one hand, for the understanding of the fission process itself, and on the other hand, for monitoring and securing nuclear reactor facilities by calculating the accumulation and inventory of fission products at various stages of the nuclear fuel cycle. Due to its importance, a big interest is observed in experimentally determining the fission fragments yields which are incorporated in the evaluated nuclear data libraries such as JEFF - 3.1.1 [7], ENDF/B-VII.0 [14] and JENDL-4.0 [15]. Efforts are continuously made to reduce fission yield uncertainties as well as to resolve the differences between these libraries. These

experimentally determined values are crucial, in addition, to extend reactor life times and for radiation protection security.

Measurements of fission yields, in particular isotopic yields, are rather challenging and several techniques have evolved over the years in order to provide reliable data. Techniques like radiochemical methods [16] and gamma-spectroscopy [17] have been corner stones for determining isotopic yields of fission fragments but also come with their limitations and cannot be applied for all elements produced in fission. The passive absorber method [2] with online mass separation, also used in the present work, is in principle, a rather universal technique that can be principally applied to determine isotopic yields for all elements and has proven to be successful for light fission fragments ($Z < 42$) [2, 3, 18]. The LOHENGRIN recoil mass spectrometer at the ILL nuclear reactor at Grenoble is one of the leading instruments for these investigations. The LOHENGRIN spectrometer [19, 20] has access to fission fragments produced at the high neutron flux reactor core ($\sim 5.3 \times 10^{14}$ neutrons cm^2 sec^{-1}) which allows measurements of yields as low as 10^{-7}%. It provides excellent mass (0.3%) and energy (1%) resolutions for a standard target size (70×10 mm). However, from the previous experiments [2] using the passive absorber method with ionization detectors, it was evident that a detector system with improved experimental set-up to provide better nuclear charge resolution is needed to study the symmetry region and the heavy mass region of the fission fragments.

In this work, a new detection system of calorimetric low-temperature detectors (CLTDs) is used to determine isotopic yields of fission fragments from thermal neutron induced fission reactions at LOHENGRIN by the passive absorber method. The CLTDs determine the particle energy by measuring the temperature rise due to thermalization of the particle's kinetic energy in the detector [21, 22]. Due to their principle of operation, which is independent of the ionization processes, CLTDs provide very good energy linearity and resolution for the spectroscopy of heavy ions at low energies [21, 23–26]. Owing to these advantages, CLTDs have already been applied in several Heavy Ion Research applications [24] like - atomic physics for the test of quantum electrodynamics [27], specific energy loss

measurements [28], accelerator mass spectroscopy [24], etc. When compared to conventional ionization detectors (solid-state Si or gaseous detectors), CLTDs have several advantages like− the more complete energy detection, the smaller energy gap of the detected quanta (phonons), and the absence of any entrance window or dead layer, which results in substantial improvements over conventional ionization detectors in basic detector properties, namely energy resolution, energy linearity, detection threshold, etc. The advantages of CLTDs allow to measure isotopic yields also for masses in the symmetry and the heavy mass region of the fission fragments which was otherwise inaccessible with the passive absorber method until now.

Silicon nitride (SiN) absorber foils are used for the passive absorber method, based on results of test experiments [29] performed to compare the performance of SiN foils with the old favourite Parylene C absorbers [2]. The resolution is found to be around 20% better with SiN foils compared to parylene C absorbers and hence SiN foils are chosen for the experiments in this work.

A recent prototype experiment [4, 29], which was mainly aiming to explore the experimental conditions at ILL, demonstrated the potential of this new experimental set-up using CLTDs and SiN absorbers for isotopic yield determination of fission fragments in the light mass region by the passive absorber method at the LOHENGRIN mass separator. Good Z-resolution was achieved for the light mass region (Z$<$ 42) of the fission fragments comparable to the historically best Z-resolutions obtained in previous investigations. However, this prototype experiment also indicated potential to improve the experimental set-up, particularly in terms of detection efficiency and flexibility in the choice of the absorber thicknesses, which determines among other parameters, the quality of the Z-resolution. The absorber foils in this first experiment were placed partly at a distance of $\sim$ 95 cm and were partly fixed at $\sim$ 10 cm from the CLTD array. This distance between the absorber foils and the detectors limited considerably the detection efficiency.

In the present work, the detector system was hence modified to achieve optimum Z-resolution and counter the transmission loss. This was realized by installing a

rotatable disk with several positions for different SiN absorber foil stacks in front of the detectors (at a distance of only $\sim$ 5 mm). This modified detector system allowed isotopic yield measurements for several masses in the light, and for the first time also in the symmetry and heavy mass region of the fission fragments for different targets giving us various insights on the fission process and reactor physics. The three main objectives of isotopic yield measurements in the present work are:

- **Precise yield determination of ^{92}Rb and ^{96}Y, important for insights in the reactor anti-neutrino anomaly studies** [30, 31]. A big interest is observed in the understanding of reactor anti-neutrino spectra as the results of reactor neutrino experiments are crucial to the establishment of a pattern in neutrino mixing and masses. Recently published results [32–36] on reactor anti-neutrino flux at reactor-detector distances $<$ 100 m lead to a ratio of observed event rate to predicted rate of 0.976$\pm$0.024. However, with new flux evaluation from $beta-$decay data of fission fragments [30], this ratio is shifted to 0.943$\pm$0.023. This deviation between experimental results and predictions is referred to as reactor anti-neutrino anomaly. Possible explanations to this anomaly could be a fourth non standard sterile neutrino, or wrong Z-yields of fission fragments. Calculations [5] show that the highest contribution to the very-high-energy portion of the reactor anti-neutrino spectra, which could explain the anomaly, comes from the decay of just two nuclides ^{92}Rb and ^{96}Y. Precise yield measurements for ^{92}Rb and ^{96}Y were hence performed for the three fissile targets - ^{235}U(n$_{th}$, f), ^{239}Pu(n$_{th}$, f) and ^{241}Pu(n$_{th}$, f) for a better understanding of the anti-neutrino anomaly and to resolve the inconsistency between recent yield measurement [6] and the data libraries like JEFF-3.1.1.

- **Isotopic yield determination towards the symmetry region for ^{239}Pu(n$_{th}$, f) and ^{241}Pu(n$_{th}$, f) for masses not measured before.** With the conventional ionization detectors, the nuclear charge resolution worsens for charges close to $Z = 45$ which, in addition to the low intensity of fragments

produced at symmetry, results in inaccessibility of isotopic yield measurements in the symmetry region for thermal neutron induced fission reactions. It is of great physics interest to push the measurements to study even-odd effects in the nuclear charge yields of fission fragments towards symmetry as it is evident from mass-energy correlations of fragments [37] that asymmetric and symmetric fission are two distinct modes. It is so far conjectured from structures in the mass yield curves that only a small even-odd effect should be present. On the way from asymmetry to symmetry, LOHENGRIN experiments point however to the onset of a sizable even-odd effect [9, 38]. Extending the nuclear charge yield measurements to a few more masses towards the symmetry would hence allow a noteworthy progress in confirming (or impairing) the onset of a pronounced even-odd effect. As even-odd effects in the transition from asymmetric to symmetric fission are a sensitive test of models claiming that even-odd effects always decrease from asymmetry to symmetry[9, 38], several measurements were performed towards the symmetry region for ^{239}Pu(n_{th}, f) and ^{241}Pu(n_{th}, f). Isotopic yields for 24 masses in the range $89 \geq A \leq 112$ were performed for the first time at the LOHENGRIN spectrometer for ^{241}Pu(n_{th}, f). For ^{239}Pu(n_{th}, f), isotopic yields were measured for the first time for the masses $110 \geq A \leq 113$.

- **Isotopic yield determination in the heavy fragment group (Z > 48, A > 128) for ^{239}Pu(n_{th}, f).** Due to the limitations of the conventional ionization detection techniques in terms of energy resolution and energy linearity (due to pulse height defect), isotopic yields were never determined in the heavy fragment region with the passive absorber method. Other methods like gamma spectroscopy not as universal, and which are specific to only certain nuclides, are also quite challenging and limited due to a limited knowledge of the decay schemes in many cases. It is therefore of high interest to perform direct yield measurements in order to verify results obtained with other methods and to add data on yields not reachable with other methods. With the advantages of CLTDs, it was possible to demonstrate for the first time the isotopic yield determination in the heavy mass region using the

passive absorber method to provide a wide scope for further improvements both from a methodical and technological point of view.

The experimental procedures and results of these measurements are discussed in the following chapters of this thesis. Chapter 2 presents a compilation of the experimental and theoretical background important for the understanding of these results. Chapter 3 presents the development and construction of the detection system, in particular the CLTD array and the installation for application of the passive absorber method. In Chapter 4 an experiment at the tandem accelerator of the Maier-Leibnitz-Laboratory at Munich performed with mono-energetic ion beams with the aim to test and optimize the new detection system is discussed. Results on the performance of the detection system and the characteristics of the absorber foils (SiN) is followed with the estimates on the quality of nuclear charge yield determination with this new detection system. Further tests to investigate the detector performance, are also discussed. Chapter 5 presents the experiment performed at the ILL nuclear reactor for the determination of the isotopic yields of fission fragments with the new experimental set-up. In particular, the detailed procedure of yield determination is discussed. Chapter 6 presents results from several measurements starting with the characterization of the new detection system under run conditions at the ILL. Results on the yields of ^{92}Rb and ^{96}Y for three different fissile targets and their significance in the understanding of the reactor anti-neutrino anomaly is discussed. The isotopic yields of a series of masses in the light mass region towards the symmetry region for ^{241}Pu(n$_{th}$, f) and ^{239}Pu(n$_{th}$, f) and the results on the isotopic yields of heavy mass fragments for ^{239}Pu(n$_{th}$, f) are presented. Finally chapter 7 discusses the conclusions of these results and an outlook concerning future experiments for Z-yield measurements, as well as potential improvements of the CLTD array.

Chapter 2

Theoretical and Experimental Background

This chapter contains a compilation of the theoretical and experimental background required for the understanding of this thesis. In the first Section 2.1, the phenomenon of nuclear fission is described, focusing in particular on thermal neutron induced fission reactions. An overview is provided on post fission events and their time-line influencing the fragment yields like neutron emission, gamma and beta emission for understanding the possibility and limitations of experimental measurements. Please note the standard definitions for fragment yields e.g. cumulative yields, independent yields, fractional yields as these are used extensively later in the thesis. The characteristics of isotopic yields are further discussed in Section 2.1.1 and Section 2.1.2 discusses the problem of anti-neutrino anomaly introduced in Chapter 1. Section 2.2 discusses briefly the operation principle and schematic of the ILL nuclear research reactor and the LOHENGRIN mass spectrometer. These provide us access to measure the fragment yields from thermal neutron induced fission reactions. Important technical details of these instruments and the fissile targets used in this work are provided. Section 2.3 gives an overview on the different methods of measuring isotopic-yield distributions of fission fragments with their advantages and limitations. The passive absorber method for Z-identification based on the specific energy loss, used in this work, is discussed

in detail. Further discussion on the topic of energy loss of heavy ions in matter is presented in Section 2.4. Section 2.5 discusses the quality of nuclear charge resolution with passive absorber method. In Section 2.6, the concept, design and advantages of CLTDs are discussed.

2.1 Nuclear Fission and Fragment Yields

Owing to its economic and military impact on the world, nuclear fission was without doubt one of the most important discoveries of the 20^{th} century. The phenomenon of a nucleus splitting into lighter nuclei was first established by Hahn and Strassmann [8] in 1939. Their identification of barium isotopes as products from the bombardment of uranium with neutrons was theoretically explained by Meitner and Frisch [39] who phrased the term "nuclear fission" as it is known today. On one hand, remarkable theoretical models, for instance the liquid-drop model [40] and the shell model [41] have been cornerstones for our understanding of the fission process, and on the other hand, the experimental discovery of spontaneous [42] and ternary fission [43] demonstrated the enormity of this field. This complex many body problem has ever since attracted physicists for completeness in the understanding of the fission process.

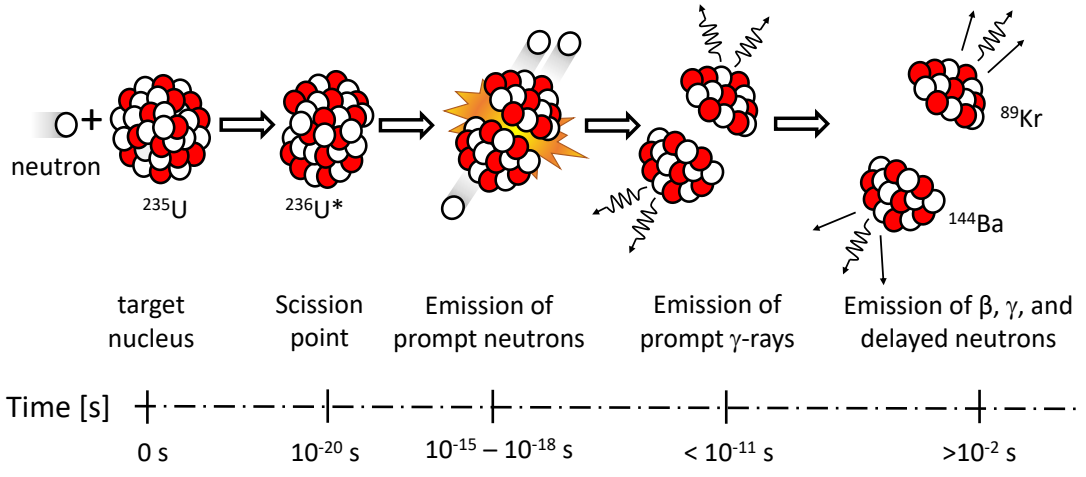

FIGURE 2.1: Schematics of a thermal neutron induced fission reaction including a time scale in the lower part.

The present work studies thermal neutron induced binary fission reactions (n_{th}, f) [Fig.2.1], which was defined as follows by Chadwick [44] in 1947: *"A neutron is captured by a nucleus, say uranium-235, forming a nucleus of uranium 236 in a highly excited state. This divides into two fragments of roughly equal mass, and one to three neutrons are emitted along with some $\gamma-$radiation. The fragments fly apart with high speed and are, in general, unstable and may undergo a series of transformations emitting $\beta-$particles and $\gamma-$radiations before they reach a stable configuration."*

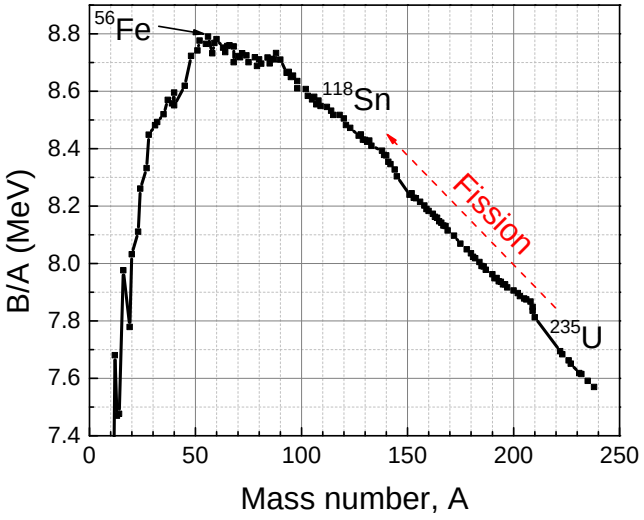

FIGURE 2.2: Binding energy per nucleon B/A versus mass number A curve demonstrating that fission is an energetically favourable process for nuclei heavier than Fe. Data taken from [45].

The binding energy per nucleon, B/A versus mass number, A, curve shown in Fig. 2.2 demonstrates that B/A is maximum for $_{56}$Fe with a value of about 8.8 MeV, and decreases with increasing mass number, A. This clearly supports that fission is an energetically favourable process for heavy nuclei and is illustrated in the following example: For $A = 235$ (uranium), the quantity $B/A \approx 7.6$ MeV, while it is ≈ 8.5 MeV for half this mass number. Using the definition of atomic mass: $M(Z, A) = Zm_p + (A-Z)m_n - B(Z, A)$, we find that the sum of the masses of two (more or less equal) fragments will be less than the mass of the fissioning nucleus $(A = 235)$ by $235 \times (8.5 - 7.6) = 211.5$ MeV.

A brief discussion on the turn of events with time in fission is presented below [46]

(see also Fig. 2.1):

At the scission point [1], the fragments are in highly deformed excited states. The excess energy mentioned above is stored dominantly in the form of coulomb energy and in the form of deformation and excitation energy. E.g, say for $Z_1 = 50$, $Z_2 = 44$, the Coulomb energy being $(Z_1 Z_2 e^2)/D \approx 210$ MeV; where $D = 15$ fm is the separation between the two fragments. The two fragments fly apart due to Coulomb repulsion picking up velocity and at the same time collapse to their equilibrium shape. With the increasing separation between the fragments, the Coulomb energy is converted to the fragment kinetic energies (at $D = 150$ fm, the Coulomb energy is already one tenth of its original value implying a fragment velocity of the order of 10^9cm/sec in roughly 10^{-20}s attaining 90% of the maximum kinetic energy).

As the primary fragments are neutron rich (since the neutron excess increases with atomic number), about 2 to 4 neutrons are emitted after the fragments have attained their maximum kinetic energy, within 10^{-15} to 10^{-18} s [47] post scission. It costs about 8 MeV/neutron for the fragments to evaporate these prompt neutrons and each neutron carries on in average around 2 MeV of energy in a Maxwell distribution.

When the fragment-excitation energy is below the neutron emission threshold, the fragments de-excite to ground state via $\gamma-$emission in less than 10^{-11}s after scission. These secondary fragments are far from the $\beta-$stability line and undergo the slow process of $\beta-$decay ($\sim 10^{-2}$s or more) releasing $\beta-$particles, anti-neutrinos and $\gamma-$ radiation to form stable end-products. At times, certain $\beta-$decay paths lead to a level that is neutron unstable, causing the emission of delayed neutrons. Although the contribution of delayed neutrons to the total neutron yield is only 1%, they play an important role for the control of a nuclear reactor.

[1] scission point: the instant at which division takes place

2.1.1 Characteristics of isotopic yields of fission fragments

Precise data on fragment yield distributions in terms of mass, nuclear charge, and kinetic energy from thermal neutron induced fission are of great interest, on the one hand, for a better understanding of the fission process and, on the other hand, for several nuclear applications, e.g. for calculating accumulation and inventory of fission products at various stages of the nuclear fuel cycle in a reactor, radioactive waste management, for determining the decay heat corresponding to the energy released by the β and γ radiation emitted during the decay of the fission products which is directly related to the independent yields of the fission products. For nuclear energy applications, the independent yields of fission fragments are useful to - a) determine the residual power of a fuel after shutdown of the reactor, b) manage the transportation and storage of fuels, c) for nuclear safety studies and d) nuclear waste management.

The elements produced by fission of the actinide series range from hydrogen(in case of ternary fission) to lanthanides. A remarkable variety of nuclides are formed by fission in terms of their atomic number, mass number, energy, half-lives, etc., which makes it very difficult to theoretically predict the fission fragment yield distributions with good precision. The readers are referred to book by C. Wageman [13] for a detailed discussion on different theories developed for nuclear fission. An overview can also be found in [9, 48, 49]. The evaluated nuclear data libraries such as JEFF-3.3, ENDF/B-VIII.0, etc., which are based on several independent measurements, have provided us insight on the fragment yield-distributions. For example Fig. 2.3 [50] shows the two-dimensional distribution of fission-fragment masses and kinetic energies after emission of prompt neutrons for $^{235}U(n_{th}, f)$. The fragments produced are distributed over the wide mass range of $A \approx 70$ to 165 with kinetic energies ranging from ≈ 40 to 115 MeV. The asymmetric mass distribution observed in Fig. 2.3 is attributed to the shell effects in the nuclear structure and deformations [9]. This results in a very low intensity of fragments produced from symmetric fission as they are less favourable in case of thermal neutron induced fission reactions. The mass distributions of such asymmetric fission processes are

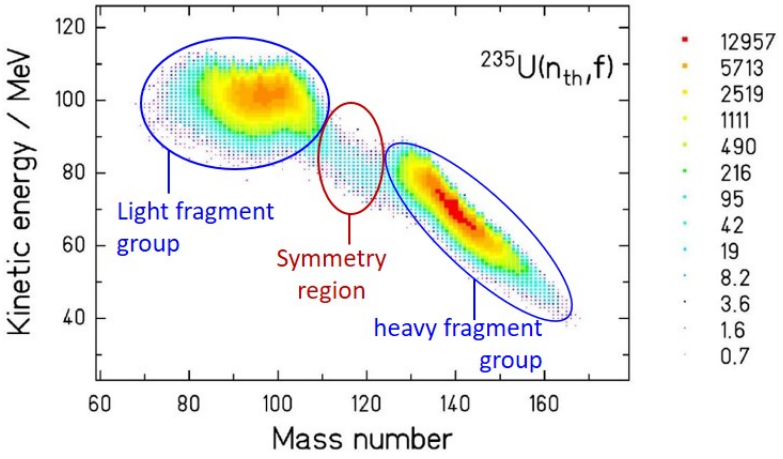

!htb

FIGURE 2.3: Energy versus mass distribution of fission fragments from ^{235}U(n_{th}, f). The color code represents the intensity of the mass produced at a particular energy. Figure from [50]

designated with the light mass region, the symmetry region and the heavy mass region as shown in the figure for further discussions.

Since more than four decades, the recoil mass spectrometer LOHENGRIN, at the ILL Grenoble (see Section 2.2), has been a leading instrument for fission fragment studies with prime interest in the determination of the mass, kinetic energy and nuclear charge distributions of fission fragments. For determining isotopic fragment yields, a fairly universal method is the passive absorber technique (discussed in detail in Section 2.3) exploiting the Z-dependent energy loss of fission fragments in an energy degrader (Section 2.4). Unfortunately this and other experimental methods (Section 2.3) based on the inspection of the ionization loss curve (employing ionization chambers, solid state and TOF detectors, photographic emulsions etc), in the past experiments [2, 18], are limited to measurements only in the light fragment group. Although the charge numbers in the heavy mass group can be approximated based on the conservation of charge, i.e., $Z_{comp} = Z_L + Z_H$, the accuracy of these predictions do not match requirements for understanding of the fission process and for nuclear energy applications (like, reactivity or decay heat in nuclear power, post-irradiation experiments, neutron flux determination, and so on). So far, reliable data isotopic yield data in the light fragment region of $^{235}U(n_{th}, f)$ for example are only available up to the masschain A = 109, corresponding to nuclear charges Z = 41 - 42. It is of great physics interest to push

the measurements to study even-odd staggering effects in the isotopic yields of fission fragments towards symmetry as it is evident from mass-energy correlations of fragments that asymmetric and symmetric fission are two distinct modes [9]. It is so far conjectured from structures in the mass yield curves that only a small even-odd effect should be present. On the way from asymmetry to symmetry, LOHENGRIN experiments upto mass chain A = 109 point however to the onset of a sizable even-odd effect. Extending the nuclear charge yield measurements to a few more masses towards the symmetry region would hence allow a noteworthy progress in confirming (or impairing) the onset of a pronounced even-odd effect. In particular, the even-odd effects in the transition from asymmetric to symmetric fission will be a sensitive test of models claiming that even-odd effects always decrease from asymmetry to symmetry [38].

The standard definitions used for the fission product yields are noted below:

The independent yield is the number of atoms of a specific nuclide (with mass A and nuclear charge Z) produced directly (after emission of prompt neutrons but excluding radioactive decay) per fission. This definition does not distinguish isomeric and the ground states. The independent yield represents a sum over all long-lived excited states and ground state. It is customary for binary fission where two products are formed in one fission reaction to normalize the independent yield to 2 per one fission event.

$$\sum_{A,Z} Y(A,Z) = 2 \tag{2.1}$$

The cumulative fission yield, is the number of atoms of a specific nuclide (A,Z) produced directly and via radioactive-decay of precursors per fission reactions.

The fractional Z-yields, is the fraction of a particular mass yield produced with nuclear charge Z. In other words, ratio of the number of nuclides produced with mass A and nuclear charge Z to the total number of nuclides produced with mass A.

2.1.2 The reactor antineutrino anomaly

A big interest is observed in the understanding of reactor antineutrino spectra which was triggered by new and refined theoretical predictions of the antineutrino flux from nuclear reactors resulting in the reactor neutrino anomaly [30]. The new calculations [30] of flux evaluation from β-decay data yield a result that is about 3.5 % (3σ) larger than the fluxes measured by a large number of short detector to reactor distance (< 100 m) and long baseline experiments [32–36].

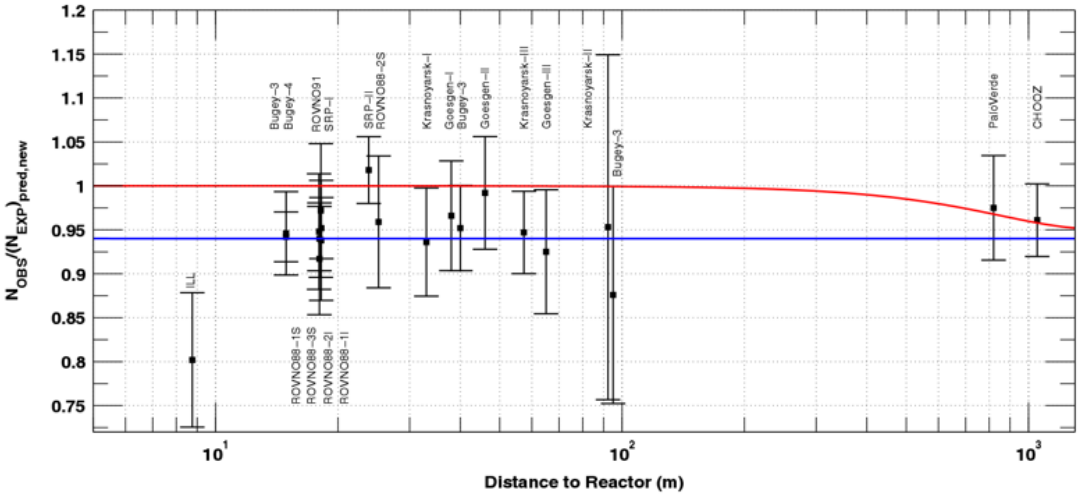

FIGURE 2.4: Illustration of the short baseline reactor antineutrino anomaly. The ratio of the predicted values to the experimental values is plotted versus the distance of the detectors to the reactor taking into account the latest evaluation of antineutrino spectra. The plot is taken from [30]. The mean averaged ratio is 0.943 ± 0.023.

Fig. 2.4 shows an illustration of the short baseline reactor anti-neutrino anomaly. The experimental results are compared to the prediction, taking into account the latest evaluation of anti-neutrino spectra [30]. Precise predictions of the antineutrino spectra emitted by nuclear reactors are crucial in measurements of reactor neutrino oscillations, as well as for the applications to the surveillance of power plants in the context of reactor safety. Nuclear reactors are very intense sources of neutrinos, where per fission 200 MeV of energy and about 6 neutrinos are released along the β-decay chain of the fission products. E.g., one expects $\sim 2 \times 10^{20}$ ν/s emitted in a 4π solid angle from a 1 GW reactor (thermal power). Since unstable fission products are neutron rich nuclei, all $\beta-$decays are of β^- type and the

neutrino flux contains pure electronic antineutrinos ($\bar{\nu_e}$). Reactor experiments on neutrino oscillations [30, 51–55] exploit these unique features and have played an important role in establishing a picture of neutrino mixing and masses. Experiments at reactor-detector distances < 100 m, lead to a ratio of observed event rate to predicted rate of 0.976 ± 0.024. However, with new flux evaluation from $beta-$decay data of fission fragments [30], this ratio is shifted to 0.943 ± 0.023. This deviation is referred to as "reactor anti-neutrino anomaly". There is also up to a 10% excess of high-energy $\bar{\nu_e}$ events in the 5 to 7 MeV $\bar{\nu_e}$ energy range that is referred to as the "shoulder" [51–53, 56]. These results might constitute a hint of new physics in the neutrino sector, including the possible existence of sterile neutrinos [30, 54]. Reactor antineutrinos $\bar{\nu}_e$ could then oscillate into undetectable sterile antineutrinos $\bar{\nu}_s$ [30]. Neutrino oscillation [57, 58] is a known quantum mechanical phenomenon whereby a neutrino created with a specific lepton flavor (electron, muon, or tau) can later be measured to have a different lepton flavor.

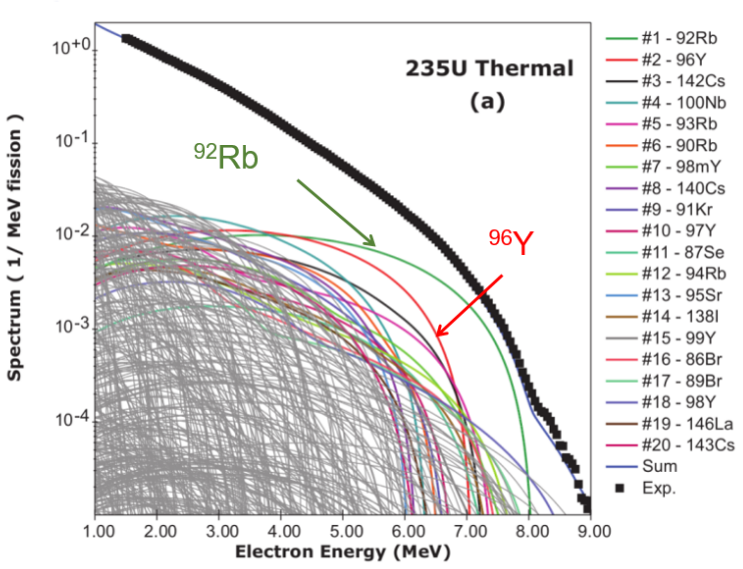

FIGURE 2.5: Calculated electron spectra (solid blue line) following thermal neutron induced fission of ^{235}U compared with high resolution data from ILL (black squares). The thin gray lines indicate the indiviual β spectrum from each fission fragment and colored lines highlight the 20 most important individual contributors at 5.5 MeV. Plot from [5].

However, it is also possible that the observed anomaly is a reflection of the shortcomings of theoretical flux predictions. Predicting antineutrino spectra is a rather

challenging task where more than 800 of individual beta decay branches contribute to the spectrum, and for many isotopes limited information is available in nuclear data tables. In order to fully analyze the unexpected features of the measured $\bar{\nu_e}$ energy spectrum, the associated $\bar{\nu_e}$ spectrum must be understood to better than a few percent. It has been assessed that for $\bar{\nu_e}$s with an energy between 5 and 7 MeV, there are a few known nuclei which are abundantly produced in the reactor and which contribute substantially to the $\bar{\nu_e}$ flux in this energy region [5, 31, 59, 60]. Antineutrino spectra calculated by A.A. Sonzogni [5] using the so called summation approach following the neutron induced fission of ^{235}U, ^{238}U, ^{239}Pu and ^{241}Pu suggest that, the energy region of the spectra most relevant to neutrino oscillations and the reactor anti-neutrino anomaly is dominated by fewer than 20 nuclei. They also provide a priority list to drive new fission yield measurements according to which the very high energy portion of the spectrum is mainly due to the decay of two nuclides, namely, ^{92}Rb and ^{96}Y. Fig. 2.5 shows the calculated electron spectra from thermal neutron induced fission of ^{235}U illustrating the contributions of the 20 most important individual beta decay branches at 5.5 MeV, highest being ^{92}Rb with 21.6% followed by ^{96}Y with 14.5% contribution.

An assumed wrong result in the yields of these nuclides could explain the anomaly. The two largest contributors near 5.5 MeV energy are ^{92}Rb and ^{96}Y due to a combination of a large cumulative fission yield, a large β^- Q value and a large ground-state to ground-state $\beta-$feeding intensity. New measurements were requested for these isotopes to obtain more precise independent values than the existing ones and also to resolve the discrepancy in the ^{92}Rb contribution between the standard data base Jeff [7] and another independent measurement by Tipnis et. al [6].

2.2 The ILL reactor and the LOHENGRIN Spectrometer

The ILL nuclear reactor

Although the underlying principle behind the design and operation of conventional nuclear reactors are quite generic, what follows in this section is the description specific to the nuclear reactor at the Institute Laue Langevin (ILL) in Grenoble (France) where the main experiment for this thesis was performed. The reactor at the ILL produces the most intense continuous neutron flux ($= 1.5 \times 10^{15}$ neutrons cm^{-2} s^{-1}) in the world in the moderator region with a thermal power of 58.3 MW.

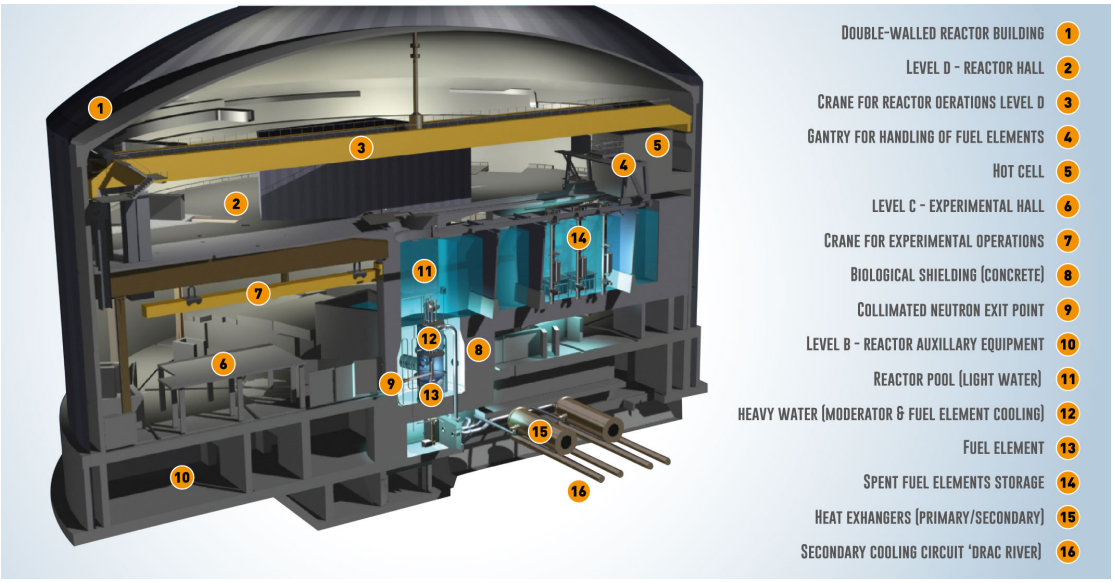

FIGURE 2.6: Schematic of the ILL nuclear reactor building taken from the ILL website (www.ill.eu). The LOHENGRIN is situated on Level C marked by number 6.

Fig. 2.6 shows the schematic of the nuclear reactor building with all the important components numbered and labelled. The reactor uses fission reactions of ^{235}U to produce an intense flux of neutrons in the reactor core (number 13 in Fig. 2.6). Several kilograms of highly enriched $^{235}U(97\%)$ is used for a 50-day cycle of reactor operation. Generally the reactor operates 4 such cycles per year. Reflector and

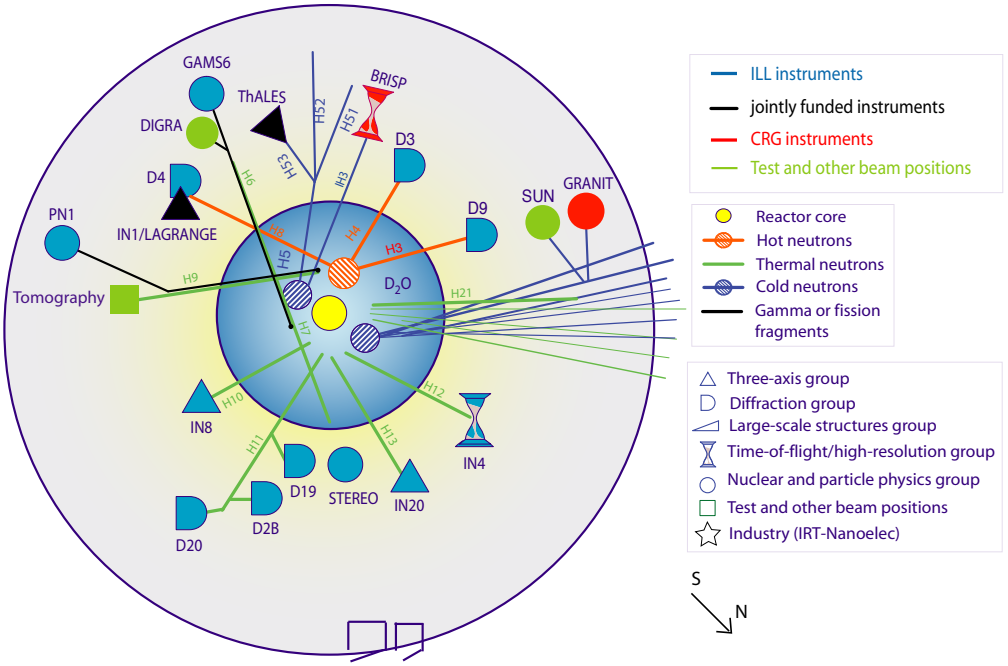

FIGURE 2.7: Top view of the reactor with schematics of the instruments layout taken from the ILL website (www.ill.eu). The present experiment was performed at PN1 where the LOHENGRIN exit is situated.

moderator are important parts of the design, as the neutrons must be slowed down and reflected back to the core to sustain the chain reaction. At the ILL, heavy water(D_2O) is used as moderator to produce neutrons with a Maxwell-Boltzmann energy distribution corresponding to the temperature of the coolant. Heavy water is also used to cool the reactor which is heat exchanged with light water cooled by the local river. This results in the production of thermal neutrons with a kinetic energy ≈ 0.025 eV. The present experiment is performed in the experimental hall numbered 6 in Fig. 2.6. A top view of the reactor with a schematics of the instruments layout is shown in Fig. 2.7 where the fission fragment beams are marked by black lines. The present experiment was performed at PN1 where the LOHENGRIN exit is situated. The beam tubes are pointing away from the fuel element to minimize the transmission of the enormous γ radiation produced by the nuclear reactions. The beam tubes are made of thin aluminum walls which are transparent to neutrons. For the present experiment, a fissile target was placed near the core of the reactor in the tube leading to LOHENGRIN spectrometer (marked as PN1 in Fig. 2.7) with a thermal neutron flux of 5.3×10^{14} n cm^{-2}

s^{-1} to induce fission using the thermal neutrons. The epithermal neutron flux is more than two orders of magnitude smaller and the fast neutron flux is more than three orders of magnitude smaller. Both contributions can be neglected for the present purposes. The fission fragments originating near the core are carried in an evacuated tube to the LOHENGRIN mass spectrometer.

The LOHENGRIN Spectrometer

LOHENGRIN [19, 20, 61] is a recoil mass spectrometer designed to study, among others like nuclear spectroscopy, the thermal neutron induced fission fragment yield distributions in terms of their mass, kinetic energy and ionic charge at high resolution since 1974. Although on its own it cannot resolve the nuclear charges, but it allows with complimentary techniques to also study the nuclear charge distribution of fission fragments.

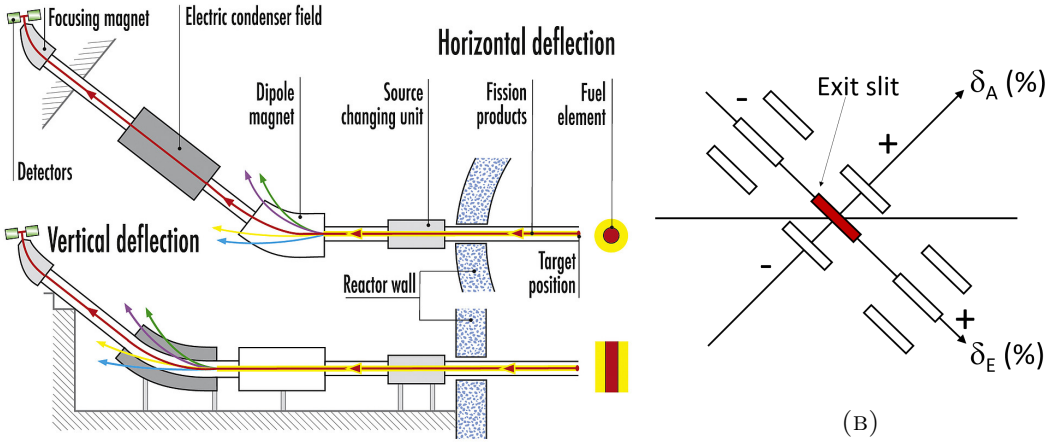

(A) (B)

FIGURE 2.8: (a) Instrument layout of the LOHENGRIN mass spectrometer taken from the ILL website (www.ill.eu), (b) Illustration of mass and energy dispersion of LOHENGRIN. The scheme of the focal plane of LOHENGRIN with the energy dispersion axes δE at an angle of 45^0 from the horizontal, viewed against beam direction is displayed. Several images of the target (the rectangles), each of which corresponds to a given change in mass and/or kinetic energy expressed in percent of the central beam parameters A_0, E_0: $\delta A = (A - A_0)/A_0$ and $\delta E = (E - E_0)/E_0$ is shown. One percent change in mass corresponds to 32 mm, and one percent change in energy to 72 mm, respectively.

The focusing parabola spectrometer LOHENGRIN is a combination of a homogeneous magnetic sector field and an electric field of a cylindrical sector. The instrument layout is displayed in the Fig. 2.8a. Fission fragments coming from the fissile target lose a small fraction of energy and a few electrons while crossing the target (see next section for properties of fissile targets). These fission fragments once ionized can be separated by the electromagnetic deflections. The deflections, x_{mag} and x_{el} in the magnetic and electric field, respectively, are perpendicular to each other. The combined action of the magnetic and the electric field separates the fission fragments (ions) with same A/q ($A-$mass, $q-$ionic charge) value but different kinetic energies E_k onto a parabola at the exit of the spectrometer in accordance with the formulae for the Thomson spectrograph:

$$x_{mag} = C_{mag}\frac{q}{Av} \tag{2.2}$$

$$x_{el} = C_{el}\frac{q}{Av^2} \tag{2.3}$$

where C_{mag} and C_{el} are instrumental constants. Eliminating the velocity v, we obtain the equation for the parabola:

$$x_{el} = \frac{C_{el}}{C_{mag}^2} \times \frac{A}{q} \times x_{mag}^2 \tag{2.4}$$

For experiments, the equations for field settings corresponding to Eqs. 2.1 to 2.3, are:

$$B\rho_{mag} = \frac{A}{q}v \tag{2.5}$$

$$F\rho_{el} = \frac{A}{q}v^2 \tag{2.6}$$

$$B^2\rho_{mag}^2 = \frac{A}{q}F\rho_{el} \tag{2.7}$$

where B - magnetic flux density; ρ_{mag} - magnetic deflection radius of the main beam; $F = U/d$ - electric field strength with U =voltage and d = distance between the electrodes of the cylindrical capacitor; ρ_{el} - electric deflection radius of the main beam.

From Eqs. 2.5 and 2.6 we get,

$$\frac{E_k}{q} = \frac{Av^2}{2q} = \frac{F\rho_{el}}{2q} \tag{2.8}$$

$$\frac{A}{q} = \frac{B^2\rho_{mag}^2}{F\rho_{el}} \tag{2.9}$$

Hence with appropriate field settings, it is possible to separate fragment beams at the exit of the spectrometer according to the ratios A/q and E_k/q.

The magnetic sector field has a mean deflection radius of 4 m and a deflection angle of 45°, and the cylindrical condenser[2] has a mean deflection radius of 5.6 m, a deflection angle of 35.35° and a separation between electrodes of 30 cm. At the exit of the spectrometer the fission fragments with the same mass number, the same kinetic energy and the same ionic charge image the rectangular fissile target in the direction of the corresponding parabola at a magnification scale of about 1:1. A 72 cm long exit slit of the spectrometer lies along the parabola which accepts ±5% of the median energy of fission fragments with an energy dispersion $D_m = 7.2$ cm for 1% difference in energy. The length of the fissile target therefore influences the energy resolution of the LOHENGRIN. The mass dispersion of the spectrometer, $D_m = 3.24$ cm for 1% mass difference is perpendicular to the parabola. The mass resolution of the spectrometer depends on the mass dispersion and the width of the image which is determined by the width of the fissile target. Fig. 2.8b illustrates the dispersion properties of the LOHENGRIN spectrometer. The scheme of the focal plane of LOHENGRIN, viewed against the beam direction, is displayed with several images of the target (the rectangles), each of which corresponds to a given change in mass and/or kinetic energy expressed in percent of the central beam parameters A_0, E_0: $\delta A = (A - A_0)/A_0$ and $\delta E = (E - E_0)/E_0$. One percent change in mass corresponds to 32 mm and one percent change in energy to 72 mm, respectively.The parabolas corresponding to the different A/q values can be approximated by straight lines for practical purposes.

[2]Capacitors were originally known as condensers.

It is thereby possible to separate fission fragments at the exit of LOHENGRIN with a specific mass, kinetic energy and ionic charge by varying the electric and magnetic field settings. Depending on the target size and the collimator settings, the standard mass resolving power can reach up to $A/\Delta A = 1500$, and the energy resolving power is between $E/\Delta E = 100$ and 1000. At the LOHENGRIN the allowed range of magnetic field settings is up to 0.24 T and the maximum high voltage of the condenser limits the E/q ratio to about 6.5 MeV, thus limiting the measurements of fragments with high kinetic energies and low charge states.

The flight path for the fission fragments is 23 m implying a flight time of the order of 2 μs from the point of fission and hence they reach the detector before undergoing β-decay (with 10^{-2}s and larger halflives, see Section 2.1). This allows the determination of the independent yields of fragments produced during fission before undergoing radioactive decay.

Fissile Targets

The LOHENGRIN spectrometer uses relatively thin actinide targets with a thickness of the order tens of μg cm^{-2} for the precise fission yield measurements, whereas up to 1 mg cm^{-2} thick targets are employed for nuclear spectroscopy applications. With relatively thin targets the correction for the energy loss in the target is minimized which enables precise determination of kinetic energy distributions of the fission fragments. Also precise fission yield measurements are based on several individual measurements with different LOHENGRIN settings for different mass, kinetic energy and ionic charge values. These individual measurements are normalized to the fission rate with an assumption of smooth evolution of the fission rate with time due to the target burnup which is typical for relatively thin targets.

Targets with a high isotopic purity are used at the LOHENGRIN spectrometer to measure the individual fission fragment yields. In order to attain the high purity, radiochemical separation is not sufficient in many cases, and the target

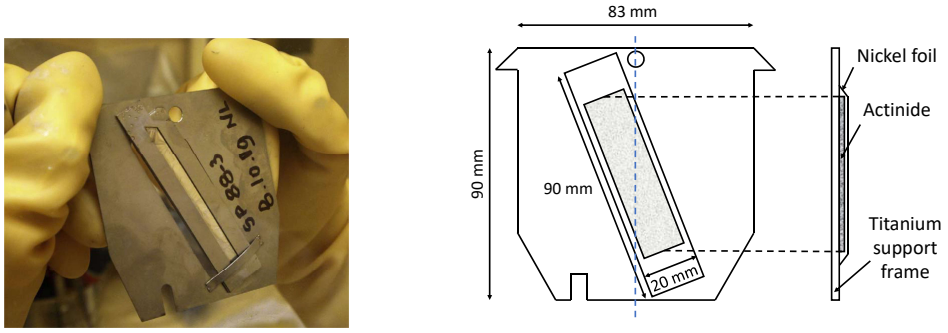

FIGURE 2.9: Design of the LOHENGRIN fissile target. Picture on the left from [62].

atoms have to pass a mass separator before use, making the target preparation an elaborate and expensive procedure. The LOHENGRIN targets [62] are produced by deposition of the actinide material as oxide on a 0.2 mm thick platinum-coated high purity titanium backing of dimension 9×2 cm^2 which is fixed on a Ti support frame by spot welding. Usually the targets are covered by a 2500 Å thick Nickel foil (except for the relatively thicker (307 μg) ^{235}U targets, which are covered with $\sim$ 100 nm tungsten foils to reduce the loss of the target material due to sputtering and to guarantee a smoother burnup. On top of the target, a diaphragm is placed to customize the size of the target corresponding to the need of the experiment. Fig. 2.9 shows picture of one such target used at LOHENGRIN as an example on the left and on the right, the schematics for such a target mount is displayed. This ensemble is installed on the beam line 0.5 m away from the reactor core with a neutron flux $\sim 5 \times 10^{14}$n cm^{-2} s^{-1}.

The mass and energy dispersion of the LOHENGRIN constrains the size of the target for a good mass and energy resolution. Since the magnification at LOHENGRIN from the object (fissile target) to the image (focal plane) is 1:1, for a 8 mm wide target a 8 mm wide mass-defining slit provides the mass resolution, $A/\Delta A \approx 400$ (since $D_m = 3.24$ cm) which is acceptable for many cases, but by reducing the target width to 3 mm with a 3 mm wide exit slit improves the resolution to $A/\Delta A \approx 1000$. Similarly a 7 cm long target measures the kinetic energy with 1% resolution which is usually acceptable. Hence the fissile targets used have surface areas ranging from few mm^2 to a maximum of $\sim 72 \times 10$ mm^2.

2.3 Methods for isotopic yield measurements

Despite several theoretical models, prediction on fission yields are presently still far from the required accuracy for nuclear applications. Due to the importance of a good knowledge on fission yields, several experimental methods have been developed and applied to study fission fragment yields in terms of their mass, kinetic energy and nuclear charge. The determination of isotopic yields in particular is rather challenging, and continuous efforts have been made to develop techniques to determine the isotopic yield, which are listed below.

2.3.1 Radiochemical techniques

The radiochemical technique is the oldest method [16] for fission yield determination. This method in principle is based on dissolving a sample of irradiated fissile material in order to be able to separate the different isobars by chemical methods. The isotopic distribution of the fission products is then established by measuring their characteristic β and γ decays [63].

This method therefore relies on the progress of knowledge on the decay data (knowledge on life time, the energies of de-excitation and the branching ratios of the β^--decay of each nucleus). Also measuring nuclei that do not emit gammas or betas is therefore not possible with this method. Both of these problems are common to all methods that rely on the measurement of radioactive decay for determining yields. The main limits of these measurements come from the time necessary for the chemical separation of the different nuclei. The yields of the primary fission products show a distribution along the (neutron rich) β^--decay chains on the nuclide chart and in general comprises nuclides one to six nuclear charges from stability with correspondingly different half-lives ranging from less than a second to several days. The determination of independent yields thus requires short irradiation time and fast chemical separation in order to measure fragments before they undergo radioactive decay. In the first attempts such procedures were hardly available and only a few exceptional nuclides (cases in which

a neutron rich stable or long-lived nuclide interrupts the decay chain producing a 'shielded nuclide') were measured e.g. ^{136}Cs, shielded by the stable ^{136}Xe. Later, fast radiochemical separation methods [64–67] were developed and applied [68] to isolate more elements from the complex mixture of fission products within a few seconds.

In spite of this, the determination of fission yields by radiochemical measurements remains a very interesting method, on the one hand because of the precision of these measurements, and on the other hand because they make it possible to measure low yield fission products.

2.3.2 Gamma spectroscopy of unseparated mixtures

In this method, the gamma ray spectroscopy is performed directly on the unseparated mixtures of fission products which makes it possible to determine the independent isotopic yields of the fission products. During these measurements a sample of fissile material is irradiated for a certain time followed by gamma spectroscopy with high resolution. In order to be able to determine the yield of all the nuclei which can have very different life times, this operation is repeated several times by varying the irradiation time of the sample [63]. This method has advantages of small sample size and short time needed for a yield survey. However the disadvantage is a complicated data analysis relying on the decay characteristics of the nuclides measured that are frequently not well known. The results in this case, due to the complexity of the gamma spectra especially for short-lived isotopes, were mostly unreliable or with limited accuracy for selected isotopes with favourable $\gamma-$decay properties.

2.3.3 Gamma spectroscopy with fast mass separation

Implementing $\gamma-$spectroscopy in combination with fast mass separation by chemical methods or by online mass separation (eg. LOHENGRIN) of fission fragments improved the results [69–71] significantly because mass separation can take place

within seconds or less and thus simplifies the $\gamma-$ray spectra by selecting the members of one $\beta-$decay chain. However, as mentioned before, it requires knowledge on the decay data of the respective nuclides, and is not well suited for measuring the yields of very short lived fission products and also this technique is unable to determine the yields of stable nuclides.

2.3.4 Z-identification with the passive absorber method

This Z-identification technique by specific energy loss is referred to as **passive absorber method** [1–3, 18]. It is based on the fact that the stopping power of matter for fast heavy ions in matter [72] depends, among other parameters, also on the atomic number, Z, of the ions. The energy loss is approximately proportional to the square of the atomic number Z of the ions. Given that all other parameters influencing energy loss are fixed, the ions will undergo energy loss proportional to the square of their atomic number (higher Z undergoes more energy loss) and thus can be separated with respect to Z. Section 2.4 discusses the energy loss process in detail for a better understanding and further discussions. The LOHENGRIN spectrometer provides the opportunity to fix other parameters like mass and velocity of the ions influencing the energy loss. Hence, this method is used (like $\gamma-$spectroscopy) in combination with an online mass separator i.e. LOHENGRIN as illustrated in the Fig. 2.10. It depicts how the dependence of the energy loss of ions in a medium on Z can be exploited to determine Z-yields. The fission fragment beam coming from LOHENGRIN consists of ions with constant mass number A and constant kinetic energy E_0 but different nuclear charges Z. This fragment beam when passing through a homogeneous absorber medium separates the different nuclear charges Z corresponding to the different peaks due to the nuclear charge dependent energy loss, $\Delta E(Z)$ as shown in Fig. 2.10.

Unlike the methods mentioned above based on chemical and nuclear properties which in general are not applicable to all fission fragments, with this method in principle it is possible to measure Z-yields for all fission fragments. From the

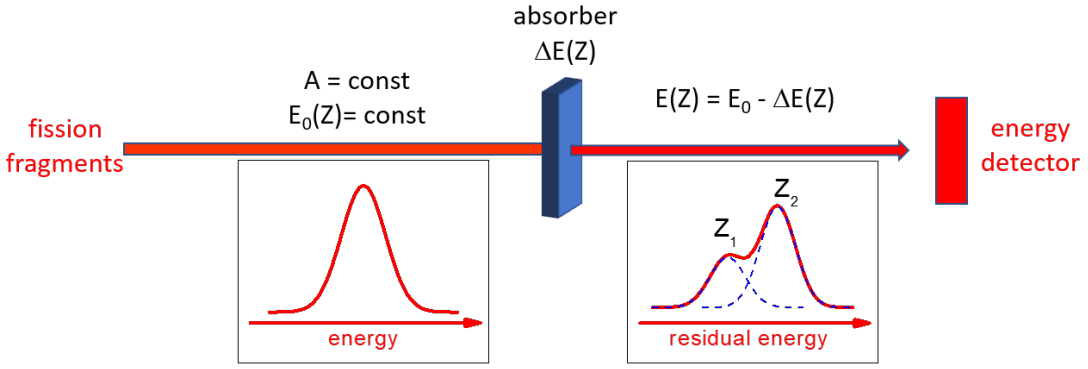

FIGURE 2.10: Illustration of the passive absorber method. The fission fragment beam coming from LOHENGRIN consists of ions with constant mass number A and constant kinetic energy E_0 but different nuclear charges Z. This fragment beam when passing through a homogeneous absorber medium separates the different nuclear charges Z corresponding to the different peaks due to the nuclear charge dependent energy loss, $\Delta E(Z)$.

previous measurements [2] with ionization chambers etc, it was evident that a detector system with better nuclear charge resolution along with more homogeneous passive absorber foils was needed to study the symmetry region and the heavy mass region of the fission fragments. However, this technique is restricted to thermal-neutron induced fission and to a limited choice of target material due to the long measurement times at LOHENGRIN with different kinetic energy and ionic charge settings required for yield determination.

The advantage of being able to determine yields for all fragments irrespective of their nuclear properties was a major breakthrough of this technique for thermal neutron induced fission yield measurements. In this work, this method is used in combination with the new detector technology of calorimetric detectors to further improve the scope of this technique.

2.3.5 Inverse kinematics experiments

This new measurement method was developed at GSI, Darmstadt [73–77]. Unlike neutron-induced fission, where neutrons are projected onto the nuclei of an actinide target, in this method the actinide is projected onto matter and fission happens

by Coulomb and nuclear interaction. This technique offers the advantage of a very good resolution in nuclear charge, since the kinetic energy of the fragments to which the projectile energy is added vectorially, becomes of the order of 1 GeV/nucleon.

2.4 Energy loss of heavy ions in matter

When ions pass through matter, they loose a part of their energy or their full energy which is described by the stopping power or the specific energy loss. The stopping power depends on the type and energy of the incident ions and on the properties of the material through which they pass. The stopping power, $S(E)$ of the material is defined as the energy loss per unit path length:

$$S(E) = -\frac{1}{\rho}\frac{dE}{dx} \tag{2.10}$$

where ρ is the density of the target material. This energy loss is essentially determined by two type of interactions between the incident ion and the material it passes through, namely - electronic and nuclear interactions. Other processes like emission of Cherenkov radiation and Bremsstrahlung and nuclear reactions [78] (in case of extremely high ion energies) also contribute to the energy loss but are not relevant for the energy range of heavy ions of interest in the present fission yield studies. Electronic stopping refers to the energy loss due to inelastic collisions between the incident ions and the bound electrons in the medium ions are passing through. The nuclear stopping refers to the elastic collisions between the incident ions and the atoms (nuclei) of the medium ions are passing through. Fig. 2.11 illustrates the energy loss of heavy ions in a material due to contributions from electronic and nuclear interactions calculated using SRIM[3] [79, 80]. As shown in Fig. 2.11, the contribution due to nuclear interactions is very small compared to electronic interactions except for low energies where energy loss due to nuclear

[3]SRIM (Stopping and Range of ions in matter) is a widely used software which calculates the interaction of ions with matter.

interaction is dominating. This is true for all ion-target combinations. The electronic stopping power for all projectile-target combinations is maximum around the Thomas-Fermi velocity $v_{TF} = Z_1^{2/3} v_0$ where $v_0 = e^2/h = e/137$ represents the Bohr-velocity. The nuclear charge of the projectile ions are represented by Z_1, and the nuclear charge of the target by Z_2 for all discussions in this section. Owing to the complexity in understanding the energy loss of ions in a medium, the theoretical development of this subject has been rather difficult. Despite the challenges, remarkable progress has been made over a century of efforts on theoretical and semi-empirical (that means prediction based on experimental data) models for the determination of stopping powers. An overview can be found in for e.g., [78, 81–83].

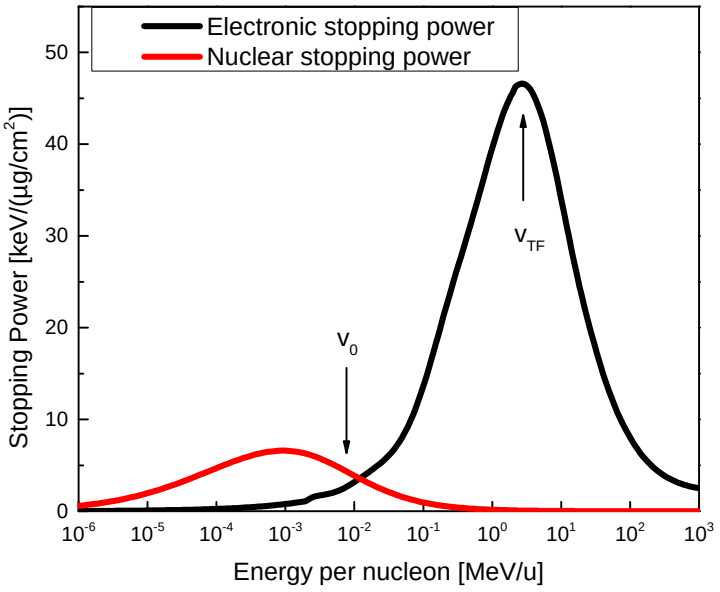

FIGURE 2.11: Stopping power for ^{92}Rb in a SiN absorber with electronic and nuclear contributions, calculated using SRIM [80].

2.4.0.1 Electronic stopping power

The quantum mechanical calculation performed by Bethe [84] and Bloch [85] are best known to describe the electronic stopping power of particles with velocities

of 10 MeV/u to 2 GeV/u and is represented by the following formula:

$$-\frac{dE}{dx} = 2\pi N_A r_e^2 m_e c^2 \rho \frac{Z_2}{A}\frac{Z_1^2}{\beta^2}\left[ln\left(\frac{2m_e\gamma^2 v^2 W_{max}}{I^2}\right) - 2\beta^2 - \delta - 2\frac{C}{Z_2}\right] \quad (2.11)$$

where:

N_A = Avagadro's number = $6.022 \times 10^{23}\text{mol}^{-1}$

r_e = classical radius of the electron = 2.817×10^{-13}cm

m_e = electron mass

c = speed of light

ρ = density of absorbing material

Z_2 = atomic number of the absorbing material

A = atomic weight of the absorbing material

Z_1 = atomic number of the incident ion

$\beta = v/c$ of the incident ion

$\gamma = 1/\sqrt{1-\beta^2}$

v = velocity of the incident ion

W_{max} = maximum energy transfer in a single collision $\approx 2m_e v^2\gamma^2$

I = mean excitation potential

δ = density correction

C = shell correction

The mean ionization potential I is basically the mean orbital frequency of the electrons of the absorber material multiplied by the Planck constant, h. Theoretically, it results from a logarithmic averaging over all orbital frequencies of the electrons, weighted with the oscillator strength of the corresponding energy levels. However, since the latter are unknown for most materials, semi-empirical formulas are used such as

$$\frac{I}{Z_2} = 12 + \frac{7}{Z_2}\text{eV} \qquad Z_2 < 13$$
$$\frac{I}{Z_2} = 9.76 + 58.8Z_2^{-1.19}\text{eV} \qquad Z_2 \geq 13$$

which were determined empirically from different dE/dx measurements [78]. However, systematic investigations show periodic deviations from the monotonic behavior of I as a function of Z_2 [86, 87]. This effect, referred to in the literature as Z_2 oscillations, is attributed to the influence of the shell structure of the target atoms. The shell and density corrections in the Bethe-Bloch equation are important at low and high energies respectively. For elementary particles (electrons,

protons, up to $\alpha-$particles), this formula provides accurate results within a few percent for velocities ranging from the relativistic region down to V_{TF} (see Fig. 2.11) which is around $\beta = 0.1$. The results for heavy ions at lower energies are unreliable with this model.

At lower energies in the range $v_0 < v < v_{TF}$, the ionic charge of projectile changes due to phenomena like electron capture and electron loss processes influencing the energy loss. In such cases, the effective charge q_{eff} is determined as the scaling parameter from the formula

$$-\frac{dE}{dx} = q_{eff}^2\left(-\frac{dE}{dx}\right)_{proton} \tag{2.12}$$

where $-dE/dx$ is the measured stopping power and $(-dE/dx)_{proton}$ is the stopping power of protons for the same velocity and the same absorber material. In order to make predictions about the electronic energy loss, the parameterization of the effective charge q_{eff} determined from measurements with different projectile-target combinations at different energies are used, and q_{eff} is usually of the form [88, 89]

$$q_{eff} = Z_1\left(1 - A(Z1)exp\left(-\frac{Bv}{Z_1^{\gamma}v_0}\right)\right) \tag{2.13}$$

with the parameters $A(Z_1), B$ and γ.

For even lower energies in the range $v < v_0$, where the ions are almost completely neutralized, three theoretical models, namely Fermi and Teller [90], Firsov [91] and Lindhard and Scharff [92], which are based on the Fermi-gas model and predict a linear dependence of the energy loss on the projectile velocity v. The approximate stopping power formula often used from Linhard and Scharff is given by

$$-\frac{dE}{dx} = Z_1^{1/6}8\pi Ne^2a_0\frac{Z_1Z_2}{Z}\frac{v}{v_0} \tag{2.14}$$

with $Z^{2/3} = Z_1^{2/3} + Z_2^{2/3}$, the Bohr-radius $a_0 = \hbar^2/m_ee^2$ and the number density of the absorber material N.

2.4.0.2 Nuclear stopping power

The nuclear energy loss resulting from the interaction between incoming projectiles and the target nuclei can be described by the Rutherford scattering, with the cross-section given by

$$\frac{d\sigma}{d\Omega} = \left(\frac{Z_1 Z_2 e^2}{4E}\right)^2 \frac{1}{\sin^4(\theta/2)} \tag{2.15}$$

where E is the incident energy of the projectile and θ is the scattering angle in the center of mass system. With $d\sigma/d\theta = 2\pi \sin(\theta) d\sigma/d\Omega$, the energy transfer

$$T = \gamma E \sin^2(\theta/2) \tag{2.16}$$

and $\gamma = 4M_1M_2/(M_1+M_2)^2$, the energy transfer cross-section can be determined by

$$\frac{d\sigma}{dT} = \frac{4\pi}{\gamma E}\frac{d\sigma}{d\theta} \tag{2.17}$$

Finally the differential nuclear energy loss is determined by the following integration

$$-\frac{dE}{dx} = N\int_0^{T_m} T\frac{d\sigma}{dT}dT \tag{2.18}$$

where N is the number density of the absorber material and $T_m = \gamma E$ is the maximum energy transfer.

In the low energy range ($v < v_{TF}$), the theoretical description becomes more complicated owing to the ionic charge fluctuations in the projectile ions due to electron loss and capture processes. Various theoretical approaches developed in this energy range include [72, 93–96].

In 1963, a first unified approach to stopping and range theory with both electronic and nuclear energy loss was developed by Lindhard, Scharff and Schiott [95] based on statistical models of atom-atom collisions, known as LSS theory. This allowed to estimate the stopping power for heavy ions in matter with good accuracy even for low energies. Several semi-empirical models were developed on the basis of this theory with improvements in calculations using numerical techniques, SRIM [80] being one of the most popular software used for stopping power and transmission

of ion in matter calculations. SRIM uses a quantum mechanical treatment of ion-atom (incident ion and target atom) collisions based on a Monte Carlo simulation method, namely the binary collision approximation [97] with a random selection of the impact parameter of the next colliding ion. Another part of the SRIM software allows calculating the electronic stopping power of any ion in any material based on an averaging parameterization of a vast range of experimental data [98]. Also a semi-empirical calculation based on the Bohr theory [99–101] was developed using the energy loss measurements performed with the present set-up and is discussed in detail in Section 4.5.3.

Energy straggling

The mean energy loss, calculated using models discussed above, is subject to statistical fluctuations in the number of collisions and the energy transferred in each collision. So, when a mono-energetic ion beam passes through a material with fixed thickness, it results in a distribution in energy rather than a delta function with a peak energy corresponding to the initial energy minus the mean energy loss. The theoretical understanding of these distributions of energy losses is rather challenging and is generally divided in two cases of thick and thin absorbers for better understanding.

For relatively thick absorbers, with a large number of collisions N, the energy loss distributions are known to be Gaussian in form which follows from the Central Limit Theorem [4] in statistics. The energy loss distribution in this case is hence given by:

$$f(x, \Delta E) \propto exp\left(\frac{-(\Delta E - \overline{\Delta E})^2}{2\sigma^2}\right) \tag{2.19}$$

where, x = thickness of the absorber; ΔE = energy loss in the absorber; $\overline{\Delta E}$ = mean energy loss; σ = standard deviation. Bohr [102] estimated the spread σ_0 of

[4]The Central limit theorem states that the sum of N random variables, all following the same statistical distribution, approaches that of a Gaussian-distributed variable in the limit N $\rightarrow \infty$.

this Gaussian for non-relativistic heavy ions to be:

$$\sigma_0^2 = 0.1569\rho\frac{Z}{A}[\mathrm{MeV}^2] \tag{2.20}$$

where, ρ, Z and A are the density, atomic number and atomic weight of the absorber, respectively.

It should be noted that in the above discussions, the energy losses are small compared to the initial energy of the ions. For very thick absorbers, where a substantial amount of energy is lost, this assumption breaks down and the formulation becomes more complex. Tschalar [103, 104] explains the energy straggling in case of very thick targets with modified Gaussian distributions.
In case of very thin absorbers or gases where the number of collisions N is too small compared to thick absorbers, the energy loss distribution is explained by theoretical calculations performed by Landau, Symon and Vavilov [105, 106]. Typical distributions in these cases are asymmetric peaks with a long high energy tail. The fission fragment Z-yield measurements with the passive absorber method uses relatively thick absorbers and also in some specific cases very thick absorbers.

2.5 Quality of Z-resolution with the passive absorber method

The quality of nuclear charge resolution with the passive absorber method depends primarily on the following criteria: *a*) proper choice of the energy loss, ΔE, of the fragment beam in the absorber *b*) energy straggling within the absorber, *c*) homogeneity of the absorber, *d*) quality of the fragment beam (energy and mass resolution) and *e*) resolution of the energy detector. The commonly used parameter $Z/\Delta Z$ to quantify the quality of nuclear charge resolution is defined as the difference of the energy loss between neighbouring Z divided by the FWHM of the

energy loss distribution (usually Gaussian) for a single Z:

$$Z/\Delta Z = Z \times \frac{\Delta E(Z) - \Delta E(Z-1)}{FWHM} \tag{2.21}$$

This makes, among others, the right choice of the absorber crucial in order to achieve good nuclear charge resolution. Special efforts were made for the choice of the absorber material and the thickness (which determines ΔE) also discussed later in this thesis. It should be noted here that the recent advancements in material sciences provide absorbers like SiN used in this work with favourable properties in terms of homogeneity, high thermal stability, extreme hardness and chemical inertness relevant for this work. Also it was found in a previous work by P. Grabitz [29] that the performance of these SiN foils was better as compared to the old favourite for the passive absorber method, Parylene C foils [2].

2.6 Calorimetric low temperature detectors

This section summarizes the basic concept, design and advantages of the calorimetric low temperature detectors used for this thesis work. From the discussion in Section 2.5, it follows that a detector system with better performance, in particular with better nuclear charge resolution, was needed to improve the Z-yield measurements and also to extend these measurements to the heavier mass region using the passive absorber method. The concept and performance of CLTDs also summarized below gave us the opportunity to implement this new technique for the passive absorber method for Z-yield measurements. For an elaborate overview on the mode of operation and applications of low temperature detectors, it is recommended to refer to [22], and the detailed description of the CLTDs used in this thesis for heavy ion detection can be found in the PhD thesis of S. Kraft-Bermuth [23], A. Echler [107] and P. Grabitz [4] and publications [21, 24–26, 28, 29, 108].

2.6.1 Detection Principle

The calorimetric Low Temperature Detectors (CLTDs) used in this work determines the kinetic energy of heavy ions by measuring the temperature rise after absorbing the ions. Due to the very low operating temperatures ($\sim$ 1 K) these are referred to as low temperature detectors. The idea is to detect the particle energy independent of ionization processes. When ions interact with matter there are two, primary and secondary interactions: *a*) primary interaction results in ionization of the matter which is the basis of the detection principle of ionization detectors, and *b*) secondary interaction in which thermalization happens where the energy of the incident ion is converted to heat resulting in the release of thermal phonons which is the detection principle of calorimetric detectors.

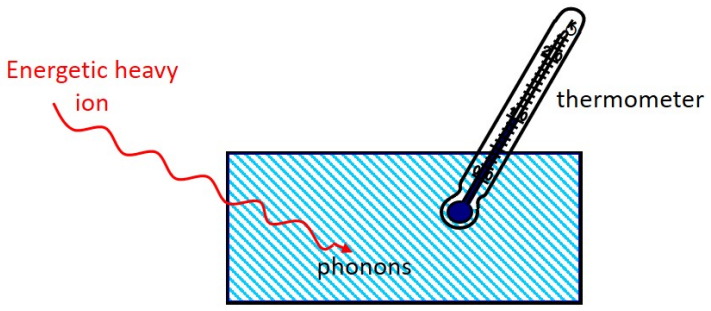

FIGURE 2.12: Detection principle of a calorimetric low temperature detector

Fig. 2.12 illustrates the detection principle of calorimetric low temperature detectors. The energy of the incident particle is transferred to the absorber by energy loss processes also discussed in Section 2.4. The interaction of ions with the detector material initially results in secondary particles like free electrons through electronic interactions and recoil nuclei due to nuclear interactions. These secondary particles on one hand emit their energy by interaction with the crystal lattice in the form of phonons, and on the other hand by impact-ionization[5] triggering a cascade of secondary particles until the kinetic energy of these secondary particles is insufficient for further ionization. The remaining energy of these particles is

[5]Impact ionization is a process in which one energetic charge carrier can lose energy by the creation of other charge carriers e.g., in semiconductors, an electron (or hole) with enough kinetic energy can promote an electron in its bound state (in the valence band) to a state in the conduction band, creating an electron-hole pair.

finally emitted via phonons to the crystal lattice [109, 110]. In semiconductors and insulators about two-third of the incident ion energy is released directly via phonons and one-third in the generation of electron-hole pairs [78, 109] which after short time recombine. In ideal crystals this recombination happens by releasing photons, but for real crystals with indirect band gap this process is non-radiative and dominated by creation and absorption of phonons at point-defects or at grain boundaries of the crystal [111, 112]. Defects in the crystal accelerate the recombination via phonons. Thus, almost the entire ion energy is finally transformed into high energy phonons which through scattering decay into thermal phonons which are spread throughout the detector material.

2.6.2 Detector design

The basic design of CLTDs comprises of an absorber, a thermometer and a heat sink [Fig. 2.13]. As shown in the figure, the incident particle with kinetic energy E is absorbed by the absorber with the specific heat capacity C, resulting in thermalization and hence in a rise in temperature (from T to $T + \Delta T$) of the absorber which is recorded by a very sensitive thermometer (superconductor resistance, R). Also the absorber is connected to the heat sink with a thermal coupling k to dissipate the absorbed energy and prepare the detector for a new measurement.

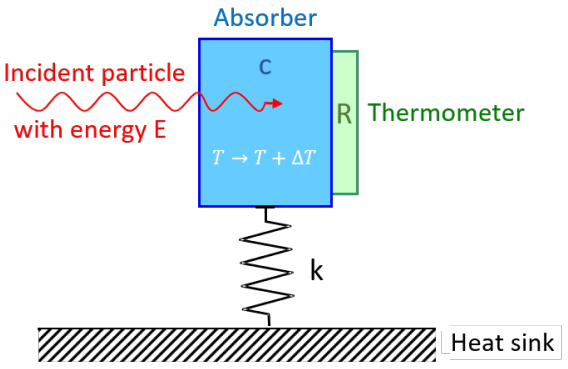

FIGURE 2.13: Design of a calorimetric low temperature detector [21, 22]

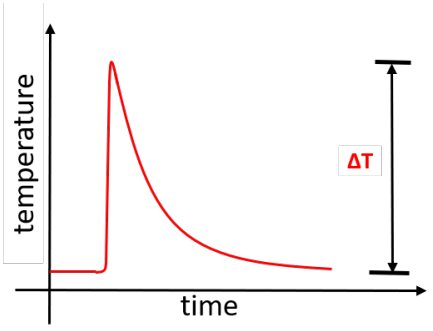

FIGURE 2.14: Thermal signal due to the impact of a particle in the CLTD.

Fig. 2.14 shows a typical thermal signal for a CLTD due to the impact of a particle in the absorber with a relatively fast rise-time corresponding to the thermalization

time and a slow decay time corresponding to the thermal coupling to the heat sink and the heat capacity of the absorber. The amplitude of the thermal signal is given by:

$$\Delta T = \frac{E}{c \times m} \tag{2.22}$$

where ΔT : is the rise in temperature of the absorber; E : is the kinetic energy of the incident particle; c : is the specific heat capacity of the absorber; and m : is the mass of the absorber. It follows from the inverse proportionality of the temperature rise to the specific heat capacity and the mass that in order to achieve high sensitivity in the energy measurement, the detectors should be designed with small values for c and m. The mass of the detector is constrained by constraining its size which comes at the cost of the detection efficiency and also the energy range of detection. For a complete energy detection of the particle, the detector should be thick enough to absorb the particle. The specific heat capacity has two contributions - electronic and lattice, given by

$$c = c_{el} + c_g = \alpha T + \beta T^3 \tag{2.23}$$

However at very low temperatures with negligible electronic contributions, we know from the Debye law (for insulators and superconductors) that the specific heat capacity is proportional to the temperature cube:

$$c \sim \frac{T^3}{\theta_D^3} \quad \text{for} \quad T << \theta_D \tag{2.24}$$

where θ_D is the Debye temperature which is a shorthand for some constants and material-dependent variables. This temperature dependence of specific heat capacity allows at low temperatures to attain very low specific heat values and hence high sensitivity for the energy measurement. This is the reason to operate CLTDs at low temperatures and the reasoning for its name.

The absorber

One of the advantages of CLTDs is the wide range of materials that can be selected as absorbers according to the need of the experiment. In contrast to conventional detectors such as semi-conductors or ionization chambers, the choice is not restricted by its electrical properties which narrows the options for the absorber material. However, insulators and superconductors below the transition temperature are attractive [113] for CLTDs due to the dominance of the contribution of conduction electrons to the heat capacity at low temperatures [113]. From Eq. 2.24, it follows that materials with high θ_D are favourable. Also, the detection principle demands quick and complete thermalization which requires high temperature conductivity at low temperatures.

All these requirements are met very well with Sapphire crystals which were used as absorber for the CLTDs in this work. Sapphire is an insulator with a high Debye temperature (θ_D = 1000 K) and is one of the materials with highest thermal conductivities at low temperatures. Sapphire also has a high resistance against radiation damage. Very importantly, the possibility of pure crystal production of Sapphire makes it practical to use these properties of Sapphire crystals for absorbers in CLTDs.

The thermometer

Transition edge sensors (TES) are used as thermometer for the CLTDs in this work. A transition-edge sensor is made from a superconducting film operated near its transition temperature T_C. In the transition region from the superconducting state to normal conducting state, a very small change in temperature causes due to the large dR/dT a relatively large change in resistance allowing high sensitivity in the temperature determination by measuring the resistance. Transition widths are typically of the order of milli-Kelvin. Fig. 2.15 shows a typical resistance versus temperature plot for superconductors. A TES is characterized by the critical temperature Tc: the temperature at which the resistance has fallen to half of its

value in the normal-conducting state R_N, and by the transition width δT: the temperature difference between which the value of the resistance R_N drops from 75% to 25%.

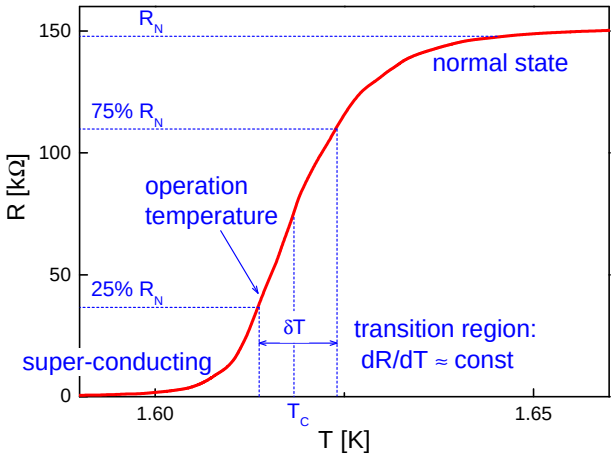

FIGURE 2.15: Typical resistance versus temperature plot for superconductors.

The TES operates in the transition region corresponding to δT as shown in Fig. 2.15 where the steep slope results in big changes in the resistance values corresponding to the small changes in temperatures with an approximately linear dependence of resistance on temperature:

$$\Delta R = \frac{dR}{dT}\Delta T \approx \frac{\delta R}{\delta T}\Delta T \tag{2.25}$$

This provides high sensitivity for temperature measurements. The sensitivity of the thermometer is given in the form

$$\alpha = \frac{1}{R}\frac{\delta R}{\delta T} \tag{2.26}$$

High sensitivity is thus achieved for small transition widths. The detectors are usually stabilized at the temperature corresponding to a resistance value $\approx 25\% R_N$ in order to exploit most of the transition region. This also determines, together with the heat capacity, the energy range that the detectors can measure. For

energies corresponding to temperatures outside the transition region, the TES is not sensitive to temperature measurements.

Thermal coupling to the heat sink

The detector is thermally coupled to a heat sink to dissipate the absorbed energy and to prepare the detector for a new measurement. For this the CLTDs are mounted on a cold plate inside a cryostat (see Section 3.2) maintained at very low temperatures ($T \sim 1$ K) which acts as a heat sink with thermal coupling k. The choice of the thermal coupling is constrained by two opposing factors: a) the thermal coupling should not be too strong to avoid heat dissipation before the incident particle energy is completely thermalized; b) also it should not be too weak to avoid signals with long decay time increasing the detector dead-time. The thermal coupling of a material is defined by:

$$k = \lambda \frac{A}{l} \tag{2.27}$$

where, λ is the thermal conductivity; A is the cross-section area; and l is the length. The infinitesimal change with time in heat Q of a cylindrical conductor with temperatures T_1 and T_2 at its end is given by

$$\frac{dQ}{dt} = \int_{T_1}^{T_2} k(T) dT \tag{2.28}$$

Assuming that $k(T)$ is constant for a small temperature difference $\Delta T = T_2 - T_1$, we have

$$\frac{dQ}{dt} = k\Delta T \tag{2.29}$$

The above equation is in analogy with the Ohm's law of electricity. Extensive discussions on thermal conductivity can be found in the references [23, 114] and books [113, 115]. In case of the impact of an ion the decay time of the thermal signal (see Fig. 2.14) is given by the time constant of thermal low pass filter $\tau = C/k$, where C is the specific heat and $1/k$ is the thermal resistance.

2.6.3 Thermal signal from CLTDs

This section contains a theoretical description of the detector signal when detecting a particle considering the specific design of the detectors used in this work. The considerations and derivations have already been discussed in various references such as [23, 107, 114, 116]. Nevertheless, the most important points are compiled again here.

The heat equation, i.e., the distribution of heat Q over time in the detector is given by

$$\frac{dQ}{dT}(t) = \frac{1}{dT}\big(C(T).T\big) = P_{in} - P_{out} \tag{2.30}$$

where P_{in} is the heat supplied to the detectors and P_{out} is the heat released. The heat released from the detectors to the cold bath through thermal coupling from Eq. 2.28 is given by

$$P_{out}(t) = \int_{T_{Bad}}^{T(t)} k(T')dT' \tag{2.31}$$

where $T(t)$ is the detector temperature and T_{bad} is the temperature of the cold bath. The heat supplied to the detectors P_{in} has three contributions. First, the heat radiation P_H or more precisely the difference in the heat radiation emitted and absorbed by the detectors. Second, the Joule heat due to the measuring current I supplied to the detectors, $P_J = R(T)I^2$. And third, the energy E of the incident particle. Assuming the energy deposition by the particle is much faster compared to the time constant of the thermal coupling, $\tau = C/k$, we have with the Dirac-delta function, $P_S = E\delta(t - t_0)$. Eq. 2.30 then becomes

$$\frac{1}{dT}\big(C(T).T\big) = E\delta(t - t_0) + R(T)I^2 + P_H(t) - \int_{T_{Bad}}^{T(t)} k(T')dT' \tag{2.32}$$

For small temperature changes, some approximations can be applied which considerably simplify the above equation allowing an analytical solution. Assuming the heat radiation P_H is constant over small time intervals for detectors in the waiting state, i.e., when no particle is incident on the detectors and an equilibrium

temperature T_0 is reached, then Eq. 2.32 becomes

$$0 = R(T_0)I^2 + P_H - \int_{T_{Bad}}^{T_0} k(T')dT' \tag{2.33}$$

Now, we redefine the detector temperature $T(t)$ in terms of the equilibrium temperature as $T(t) = T_0 + \delta T(t)$, and assume that the temperature dependent quantities $k, C, dR/dT$ are constant for sufficiently small temperature changes. With these approximations and with $R(T_0 + \Delta T) = R(T_0) + \frac{dR}{dT}\Delta T$, we have from Eqs. 2.32 and 2.33,

$$C\frac{d}{dt}\Delta T(t) + \big(k - \frac{dR}{dT}I^2\big)\Delta T(t) = E\delta(t - t_0) \tag{2.34}$$

Solving the above equation with the initial condition, $\Delta T(t = 0) = E/C$, i.e, immediately after the energy deposition of a particle in the detector, we obtain the thermal signal, $\Delta T(t)$ of the CLTDs as a function of time given by:

$$\Delta T(t) = \frac{E}{C} \times \exp\left(-t/\tau_{eff}\right) \quad \text{where} \quad \tau_{eff} = \frac{C}{k - \frac{dR}{dT}I^2} \tag{2.35}$$

where E = incident energy; C = heat capacity $(c \times m)$; k = thermal coupling; $\frac{dR}{dT}I^2$ = electrothermal feedback with R, T and I denoting the resistance, temperature and current, respectively.

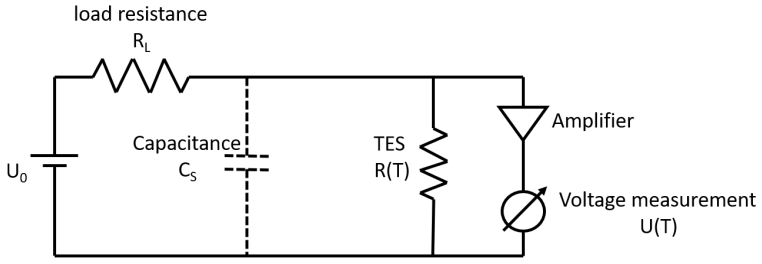

FIGURE 2.16: Electric circuit for the TES readout.

This thermal signal is recorded by the TES resistance R(T) readout. Fig. 2.16 shows the schematics of the TES readout circuit. From Eqs.2.25 and 2.35 we have:

$$\Delta R(t) = \frac{dR}{dT}.\frac{E}{C}.\exp\left(-t/\tau_{eff}\right) \tag{2.36}$$

From the electric circuit in Fig. 2.16 with a RC component we have for the voltage measurement:

$$\Delta U(t) = U_0.(1 - \exp(-t/\tau_{el}) \quad with \quad \tau_{el} = R(T).C_S \tag{2.37}$$

since $\tau_{el} << \tau_{eff}$; we get the following voltage measurement for a constant current I,

$$\Delta U(t) = U_0.(\exp(-t/\tau_{eff})) - \exp(-t/\tau_{el})) \quad \text{with} \quad U_0 = I.\frac{dR}{dT}.\frac{E}{C} \tag{2.38}$$

2.6.4 Energy Resolution

One of the most important characteristics of CLTDs is the energy resolution. Although the detection of mono-energetic particles with an ideal detector should result in a $\delta-$function at the given energy, however, in reality due to various interactions during measurement a finite structure width is observed. Usually the contributing effects are statistical in nature and thereby lead to a Gaussian distribution. The theoretical limit for the energy resolution of an ideal calorimetric detector, determined by thermodynamic fluctuations, is given by:

$$< \Delta E >= \xi \sqrt{k_B\ T^5\ c\ m} \quad \text{where} \quad 1 < \xi < 3 \tag{2.39}$$

For example, the thermal signal and the energy resolution for a 1 MeV particle in a 1 mm^3 sapphire absorber are given in the following table for different operational temperatures and the respective heat capacity of the detector:

Operation Temp. T	Heat Capacity C	Thermal Signal ΔT	Theoretical Energy Resolution ΔE_{theor}
300 K	3×10^{-3} J/K	5×10^{-11} K	1.8 GeV
10 K	4×10^{-7} J/K	4×10^{-7} K	700 keV
1 K	4×10^{-10} J/K	0.4 mK	2.2 keV
100 mK	4×10^{-13} J/K	400 mK	7 eV

TABLE 2.1: Theoretical energy resolution for an ideal calorimetric detector

The table demonstrates the significant improvement in the resolution towards lower operational temperature. However in reality, there are other sources of noise like Johnson noise, electrical noise from read out electronics, etc., which contribute to the baseline noise of the detected signal. Possible contributions to the energy resolution of CLTDs [23, 107] are listed below: Various electrical and thermal noise can contribute to the baseline noise. Thermal noise refers to the fluctuations in the detector temperature and the electrical noise contributes to the temperature readout with a TES. Different sources of these thermal and electrical noise are listed below: **a) Johnson noise/Thermal noise of the resistors:**
The thermal movement of the charge carriers in a resistor leads to random inhomogeneities in its charge distribution. Even without applying an external voltage and current to the resistor, due to the heat, the movement of the charge carriers in the resistor can generate a voltage. For frequencies less than 10^{13} Hz, this noise voltage in a frequency interval Δf is given by [117, 118]:

$$\overline{\delta U^2} = 4k_B T R \Delta f \tag{2.40}$$

where k_B is the Boltzmann constant, T is the temperature and R is the electrical resistance. Since the spectral power density of this noise is frequency-independent, it is also called "white noise". At low operational temperatures of the detectors, this noise is minimized due to the temperature dependence. b) Photonic/Radiation noise:
The detectors can exchange heat from the warm surfaces surrounding them due to blackbody radiation governed by the Stefan-Boltzmann law. This noise is minimized by installing radiation shields as far as the experiment allows. c)Phonon/ thermal fluctuation noise:
CLTDs are mounted on the cold plate of the cryostat [Fig. 3.5] with a thermal coupling resulting in continuous heat exchange with the cold plate even when no ion beam is incident. This heat exchange causes fluctuations that can be described by a simple equation [115]:

$$\overline{\delta Q^2} = k_B T^2 C \tag{2.41}$$

d) Noise from the readout electronics:
Like in any detector system, disturbances in the measured voltages and currents can be introduced through internal and external disturbances in the data acquisition or the read-out electronics. Inherent noise from the pre-amplifier is an example of the internal disturbance, while external disturbances can be introduced by nearby electronics through power cables or wireless disturbances via inductive or capacitive coupling [119]. The use of electrical shieldings and clean power lines can avoid or minimize such noises. e) Electrothermal feedback:
The electrothermal feedback discussed in Section 2.6.3, can also contribute to the baseline noise. The feedback is caused by a change in the detector resistance simultaneously causing a change in the heat input of the measuring current in the detector, which in turn influences the detector resistance due to the high temperature dependence of a superconductor within its phase transition. For detectors that are operated with constant current as in this work, this feedback is positive. This means that, an increase in the detector resistance leads to an increase in the heating power of the measuring current $P_H = RI^2$ and thus in turn to an additional increase in the resistance. With regard to the baseline noise considerations, this means that the noise of the detector resistance as well as the thermal noise contributions of the detector can be further enhanced by the positive electrothermal feedback.

2.6.5 Advantages and Applications of CLTDs

By design, CLTDs provide significant advantages in particular for low energy heavy ion detection in comparison to conventional ionization detectors (e.g. ionization chambers, semiconductor detectors, scintillators, etc.). These advantages are listed below:

- **More complete energy detection:** CLTDs detect almost the complete ion energy compared to ionization detectors. There are important benefits with CLTDs which in case of ionization detectors result in undetected energy

losses. First, there are no dead layers or entrance windows in CLTDs. Secondly, processes like charge recombination due to high ionization density (see section 2.6.1) and nuclear stopping resulting in lower secondary ionization, especially in case of low energy heavy ions contribute to significant losses at energy conversion in ionization detectors. CLTDs on the other hand convert almost the complete ion energy to heat. It follows that the statistics of loss processes contribute much less to the resolution.

- **No pulse height defect:**(which is also due to the more complete energy detection) This is one of the most crucial advantage for the work in this thesis. Unlike in ionization detectors, the energy detection in CLTDs is independent of the incident ion properties like mass and nuclear charge. Fig. 2.17 demonstrates this finding. For ions ranging from He to U, CLTDs have a very good linear energy response which is not the case in ionization detectors primarily due to recombination which is dependent on the ionization density and is therefore Z-dependent and also due to mass dependent losses at energy conversion.

- **Energy Resolution:** As also discussed in Section 2.6.4, low thermal fluctuations in energy detection results in a remarkably improved limit on energy resolution. The limit on energy resolution of ionization detectors for low energies are significantly higher. The small energy gap for the creation of phonons ($\omega_{phonon} \approx 10^{-3}$ eV) in CLTDs compared to creation of charge carriers ($\omega_{electr.} \approx 1$ eV) in semiconductor detectors, results in better statistics of the detected phonons for the same ion energy. $\left(\frac{\Delta E_{CLTDs}}{\Delta E_{semicond.det.}} = \sqrt{\frac{N_{electr.}}{N_{phonon}}} = \sqrt{\frac{\omega_{phonon}}{\omega_{electr.}}} \leq \frac{1}{30}\right)$. For the high total energies of heavy ions the statistics of the created quanta is not the dominating effect, but the statistics of loss processes is dominating.

  Fig. 2.17 shows a comparison between CLTDs and Si detectors for U ions at around 21 MeV. The resolution with CLTDs is of the order 30 times better than the Si detectors.

- **Resistance to radiation damage:** From the discussion in Section 2.6.2, it follows that CLTDs provide a large variety of choices for detector materials to optimize the detector performance for the respective experiment. Sapphire crystals as absorber material, used in this work, is less susceptible to damage of the crystal lattice due to strong radiation impact than for example Silicon.

- **Low noise contribution:** Due to the low operating temperatures (~ 1 K) of the CLTDs, several electrical and thermal noise contributions are minimized as discussed in Section 2.6.4.

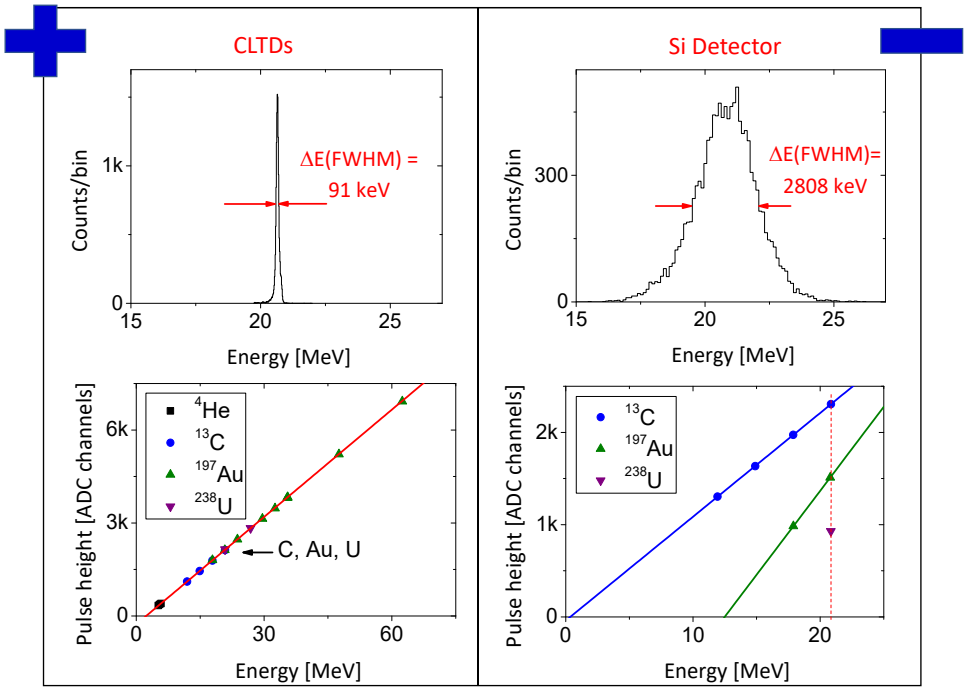

FIGURE 2.17: The top two plots compare the resolution between CLTDs and Si detectors for U ions at around 21 MeV. The bottom two plots illustrates the energy linearity because of the absence of a pulse height defects in CLTDs.(from [25])

Owing to these advantages, CLTDs have already been applied in various fields of physics, or are proposed for further applications [22, 24–29, 108, 120]. Some applications in Heavy Ion Research are: a) Nuclear Structure and astrophysics applications involved in-flight mass determination; b) In atomic physics CLTDs

were applied for the test of quantum electrodynamics; c) Specific energy loss measurements contributed to the study of interaction of heavy ions with matter; d) Accelerator mass spectroscopy. Within this thesis, CLTDs were recently also applied for nuclear fission studies.

Chapter 3

Detector Setup and tests

This chapter discusses the development of the experimental set-up used for the Z-determination of fission fragments using the passive absorber method. The details concerning design and construction of the CLTD array used for this work are discussed in Sections 3.1 and 3.2. Also a redesign of the cold plate was done to improve the efficiency of the CLTDs for the experiment at ILL which is discussed in Section 3.2. A major step to improve our experimental set-up compared to previous experiments [29] at ILL was the installation of a rotator inside the cryostat with the possibility to mount and position absorber foils with different thicknesses close to the CLTD array in order to optimize the efficiency of the Z-yield measurements. This is discussed in Section 3.3. Several lab tests at Mainz were made to test the new CLTD array and the modified set-up, results from which are discussed in Section 3.4. In addition to the CLTDs, PIN-Diodes− used as additional detectors in the ILL experiment − were prepared and tested as discussed in Section 3.5.

3.1 Design of individual CLTD pixels

An array of 24 CLTD pixels[1] was prepared for this work based on the design in the previous thesis work by A. Echler [107] and P. Grabitz [4, 29]. Modifications were implemented in order to improve the detector performance and to overcome problems like cross-talk, etc..

Fig. 3.1a shows a photo of a single CLTD pixel which is $3 \times 3 \times 0.43$ mm^3 in size, and the schematics of the design is displayed in Fig. 3.1b. The absorber used is a Sapphire crystal[2] and the inside structure with an area of 1×1 mm^2 is a 10 nm thick meander-shaped Al layer which is used as thermometer (TES). In addition there is also a heater strip which is a 25 μm thick Cr/Au layer, used to regulate the temperature of the detector at an operational temperature around 1.5 K. The TES and the heater strip were implanted on the CLTD pixel using photolithography techniques to ensure good thermal coupling to the absorber [23, 107, 116] . There are 4 bond pads for the electrical connections to the heater strip and the thermometer.

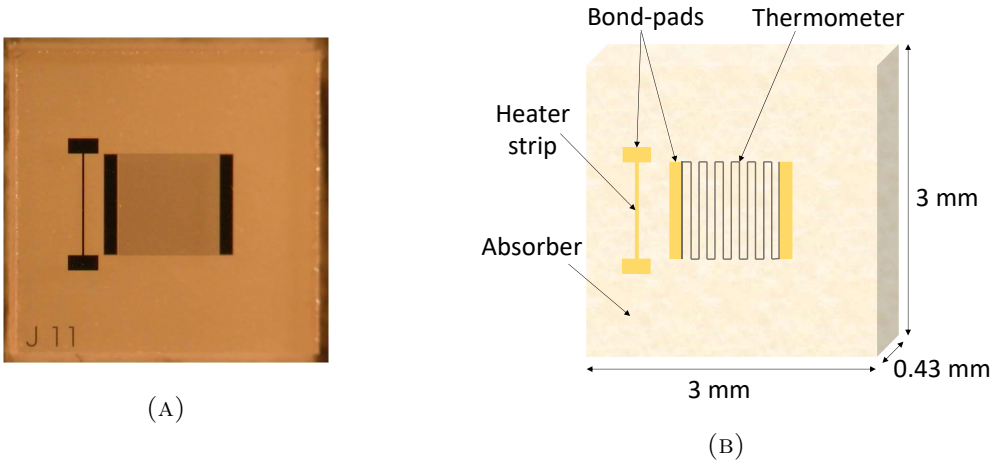

(A) (B)

FIGURE 3.1: (a) Photo of a CLTD pixel [107]; (b) schematics of the design of an individual calorimetric low temperature detector.

The detector pixels are made from a 10×10 cm^2 sapphire wafer with thermometer, heater and bond pads implanted on one side, and the other side polished (1-102

[1]Pixel is the nomenclature used in this thesis to identify a single calorimetric detector in the CLTD array of 25 individual detectors.

[2]See Section 2.6.2 for the detailed discussion on the choice of absorber.

r-plane). The thickness of 0.43 mm of the detectors is sufficient to completely stop ions with an energy upto 250 MeV according to SRIM calculations.

The thermometer (Al-layer) was implanted directly on the Sapphire wafer by photolithography. The meander-shaped thermometers were first used in the work of Meier [116], and later in others [23, 107]. The meander structure is needed for impedance matching to the amplifier input. In this work the meander structure consists of 99 interconnected 5 μm wide strips. The resistance of the thermometer at normal conduction temperature is $\sim$ 150 kΩ. The high sensitivity and linearity of the TES can only be used in a few mK wide transition region between the superconducting and the normal conducting state of the TES (Section 2.6.2).

The detectors are mounted during operation on a cold bath at a temperature $\sim$ 1.2 K which is below the transition temperatures ($\sim 1.5 - 1.6$ K) of each pixel. The TES transition temperatures vary for different pixels up to 10 mK due to manufacturing. The heater strips therefore regulate the operation temperature of each detector individually . The 1×0.02 mm^2 heater strip consists of a 120 nm thick gold and a 30 nm thick chromium layer which serves as a bonding agent between the gold layer and the sapphire absorber, and has a resistance of about 15 Ω.

3.2 Design and construction of the CLTD array

A new CLTD array consisting of 24 pixels in a 5×5 matrix with a total active area of $\sim 15 \times 15$ mm^2 was constructed for this work. The array is made up of 5 modules. Fig. 3.2a shows a picture of one module [4] along with the schematics in Fig. 3.2b. Pixels are glued on the ceramic mounting as shown in Fig. 3.2. For example, the glue points are marked for one of the pixels in the Fig. 3.2b. The GE7031 low-temperature glue is used in this work, and for better handling of the electrical connections alternate pixels are rotated by 180^0. As can be seen in the Fig. 3.1, there are three electrical connections (bond pads) on the left side and one electrical connection on the right side of the pixels, in order to distribute the

electrical wires evenly on each side of the ceramic shown in Fig. 3.2, alternate pixels are rotated by 180^0. The electrical contacts for the thermometer and heater strip are realized on the bond pads by ultrasonic bonding with 17 μm thick gold wires, also referred to as "bond wires". The bond wires in this work were soldered to the copper wires. The copper wires are glued with GE7031 - low temperature glue on the copper holder. In this way the pixels are thermally coupled to the cold bath with 4 bond wires and 2 glued points on the ceramic each. The ceramic is used to electrically decouple the detectors from the surrounding except for the 4 gold wire contacts.

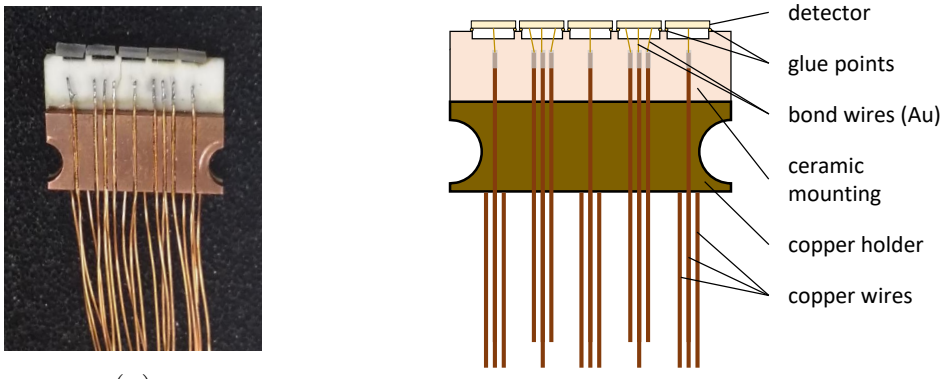

(A) (B)

FIGURE 3.2: (a) Picture of a sample module of the CLTD array with 5 pixels, (b) Schematics of a module.

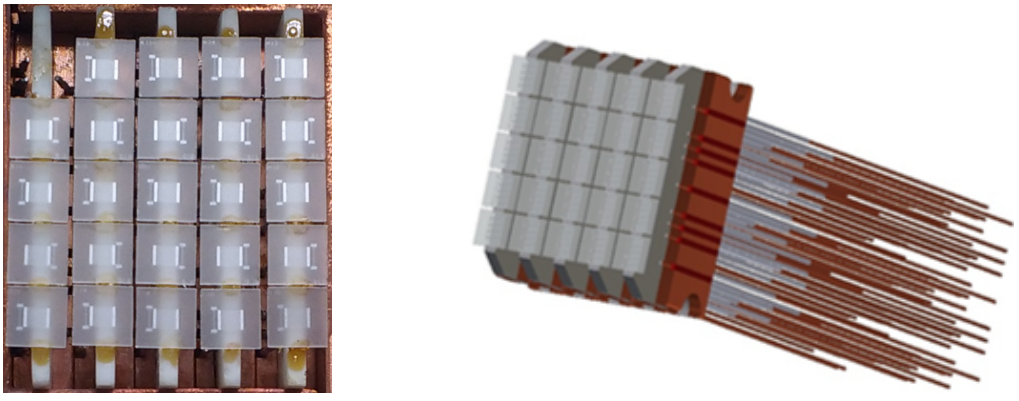

(A) (B)

FIGURE 3.3: (a) Picture of the array mounted on the cold finger, (b) Schematics of the 25 pixel array.

One of the modifications, as compared to earlier set-ups, in order to achieve better electrical contact, was to solder the bond wires to the copper wires, which in the previous work [4], [107] were glued on the copper wires.

Fig. 3.3a and 3.3b show a picture and the schematics of the new array consisting of 5 individual modules, respectively. The array is mounted on a copper holder referred to as "cold finger". Fig. 3.4 shows the CLTD array mounted on the cold bath of the cryostat. The cold finger with the CLTD array is thermally coupled to the cold plate (at $\sim$ 1.2 K) with a copper wire with a thermal conductance of ~ 0.028 W K^{-1}.

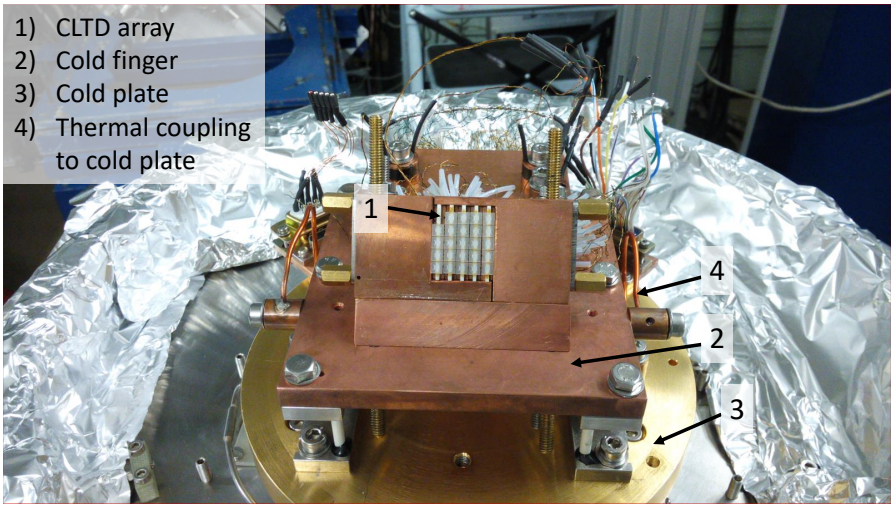

FIGURE 3.4: Picture of the CLTD array mounted in the cryostat

For the temperature measurement of the cold finger, a Platinum 100 Ω resistance sensor (Pt-100) is used as the primary thermometer, and Germanium resistance (RGe) temperature sensors were used as secondary thermometers which can measure the temperature in the range 0.05 K - 30 K. These sensors were mounted on the cold finger. Additionally, temperature sensors were mounted on the cold plate (RGe), the helium shield (carbon glass resistance temperature sensor), and Nitrogen shield (Pt-100) for monitoring the cryostat temperatures.

3.3 The cryostat

The CLTDs are mounted inside a cryostat that can reach temperatures down to 1.2K [Fig. 3.5]. The cryostat used in this work is a windowless ^{4}He - bath cryostat with a multiple radiation shielding [Fig. 3.5]. The coldplate is placed in thermal contact with the liquid helium bath. The boil-off rate of liquid helium is minimized by shielding the bath with vacuum shields with walls constructed from so-called super insulator material. The helium vapour which boils away from the bath very effectively cools the thermal shields around the outside of the bath. There is an additional liquid nitrogen bath as concentric layer of shielding around the liquid helium shields, with gradually increasing temperatures. The possibility to connect the cryostat directly to the beam tube (at vacuum) and hence to measure without any entrance window is advantageous, especially for the measurement of heavy ions at low energies to avoid energy losses in the entrance window.

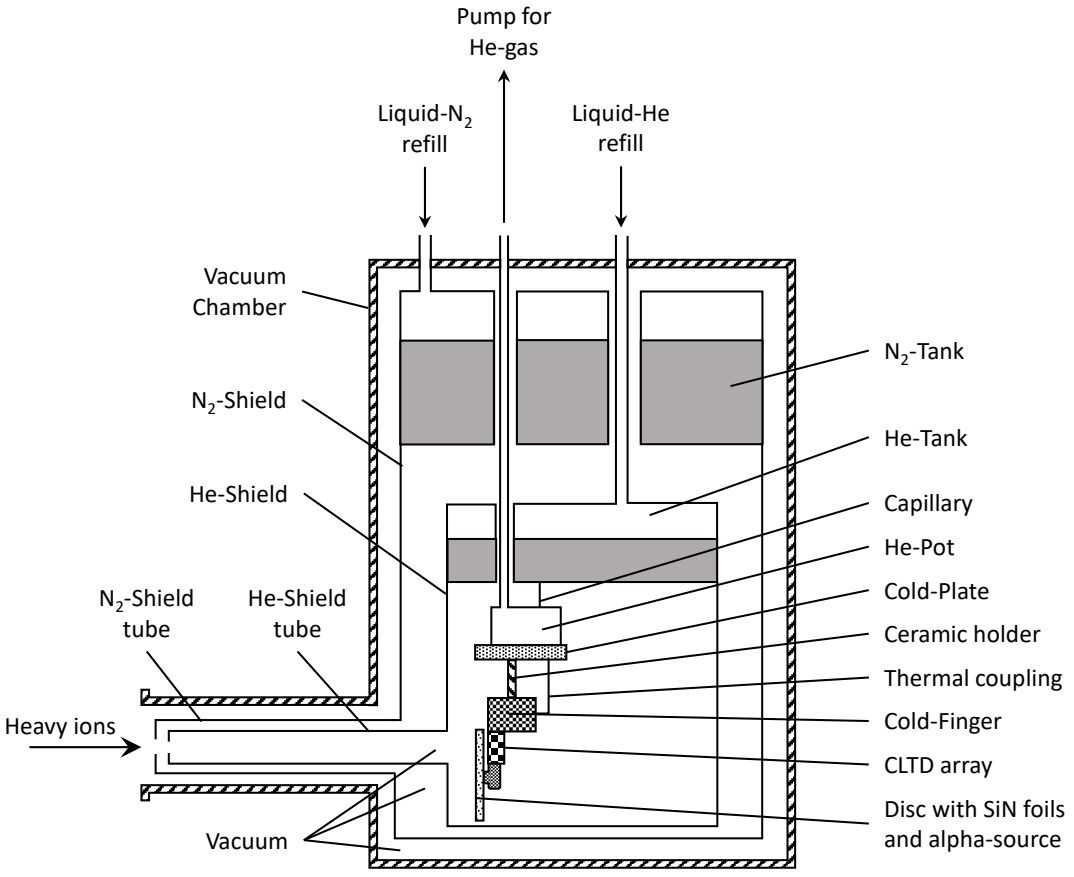

FIGURE 3.5: Windowless ^{4}He bath cryostat [107].

The shield tubes shown in Fig. 3.5 (helium, nitrogen and the vacuum) were adapted to the not horizontal beam line at the ILL (see Fig. 5.2b) whereas for the test experiment at the MLL (see Fig. 4.2), the standard horizontal shield tubes for the cryostat were used. Adaption to the ILL beam line resulted in an increased volume of the cryostat for each liquid He shields, liquid N shields and vacuum chamber with additional mountings. This reduced the performance of the cryostat due to increased heat radiation from the surfaces with several mountings. With the standard horizontal beam line, the cryostat could be comfortably cooled down to operational temperature of CLTDs with open beam line, however in the case of the cryostat adapted to the ILL beam line, initially [29] it was not possible to operate the CLTDs without a thin foil placed in front of the CLTDs providing shielding from the thermal radiation. Tests were were performed to improve the thermal shielding in this case, results of which are discussed in Section 3.7.3.

3.4 Readout electronics and data acquisition

In the previous chapter, Section 2.6.3, the conversion of the thermal signal to a voltage signal and the electrical circuit (Fig. 2.16) required for it was discussed. Fig. 3.6 shows the circuit diagram for the temperature stabilization and the signal readout of the CLTDs, as well as for recording the R(T) characteristics. The detector voltage is read out by a low-noise pre-amplifier (8 DLPVA-S from Femto and 15 VAM from Surface Concept). The CLTD signal during particle detection is read out by the analog output while the DC output is used to stabilize the detector temperature and to record the R(T) characteristics.

The analog output is digitized with integrated Flash ADCs in an FPGA card of the type NI-PXI-7852R from National Lab Instruments. Each FPGA card has 8 analog inputs with built-in 16-bit Flash ADCs to read out the amplified detector signals. Due to the slow time constants of the CLTDs (rise times$\sim$ 35 μs; decay time$\sim$ 150 μs), it is possible to get the complete signal shape with a maximum sampling rate of 750 kHz per input channel recorded. With Flash ADCs (FADCs),

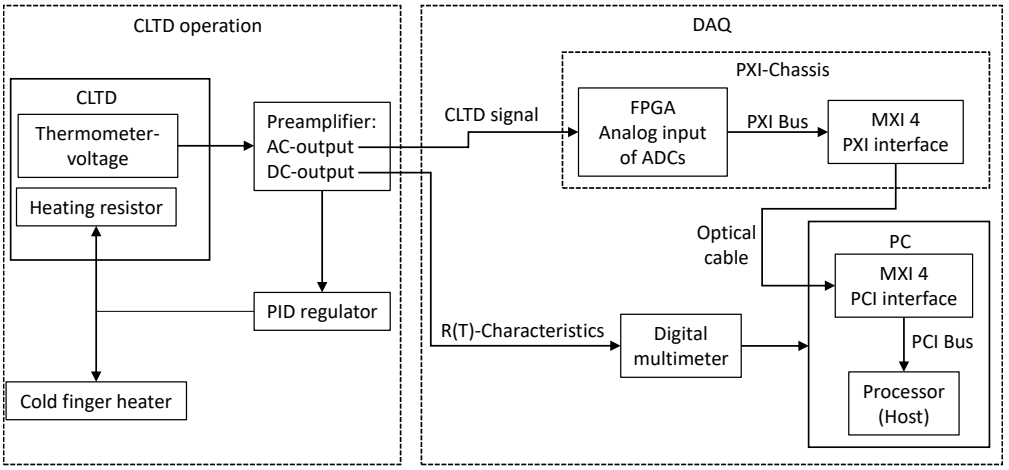

FIGURE 3.6: Circuit diagram for the CLTD temperature stabilization and the signal read out with the DAQ.

the analog input amplitude to the FPGA card are constantly sampled and written to an internal buffer. When the buffer is full, the first reading in the buffer is removed and the new reading is placed at the end of each measurement cycle. The size of the buffer is typically adapted to a signal length of about 5 ms. If the signal voltage exceeds a defined threshold, a trigger is created and the collected data in the buffer are transported using an optical cable to a PC for further processing and storage.

The data acquisition (DAQ) and an online analysis program were adapted and adjusted to a 25 pixel readout based on the thesis work by A. Echler [107] which uses National Instruments Lab-View software. The DAQ creates an ASCII file (containing the signal amplitude with 16-bit precision and a time-stamp for each event) for each pixel of the CLTD array for every measurement. In addition, a binary file is created with 4096 data points (12-bit) of the waveform for each triggered signal. These waveforms can be digitally filtered [23] offline to reduce baseline noise and to improve the energy resolution.

Another modification in the present work concerns the detector readout. The configuration of the twisted pair cables previously used [4], was changed to a read-out with individual cables for each detector pixel, in order to eliminate cross-talk between different detector pixels observed in the previous experiments [4].

3.5 Silicon Nitride foils

The silicon nitride (SiN) foils were used in this work for the implementation of the passive absorber method for determining isotopic yields at the ILL reactor. were manufactured by the company Silson (`http://www.silson.com/`) which produces and supplies ultra-thin foils with thicknesses varying from 30 nm to 1000 nm using lithographic techniques. They also produce these foils in different sizes. Regarding the nomenclature, silicon nitride is abbreviated to SiN in this work. Traditionally, silicon nitride has the stoichiometry of Si_3N_4. Due to the high stress on Si_3N_4, it is not possible to produce Si_3N_4 membranes with a thickness greater than 200 nm - 250 nm, especially for larger membranes. The membranes just break. So, silicon-rich nitride (SiRN) is used instead, which has a higher Si component, more like Si : N = 1 : 1. It has much lower stress, typically 200 MPa - 300 MPa rather than 1 GPa in case of Si_3N_4. It is also less dense so it has a higher transmission. The problem is that there are larger batch-to-batch variances in terms of density for SiRN than for Si_3N_4 [Private communications with manufacturers].

In this work several foil stacks of the required thicknesses were used from different production batches, with a nominal thickness of 1 μm per foil. Another peculiar property of these foils is that the colour of SiN foils, when light is shining through, is very sensitive to the thickness, ranging from violet to red. Varying the thickness by < 50 nm completely changes the colour of the foils in the region of interest. This provided a very good method for checking the SiN foil thickness for the same production batches. The list of the foils used with their dimensions is displayed below in the Table. 3.1. These SiN foils have several favourable properties in terms

Batch	thickness (nm)		size (mm)		amount	colour
	nominal	actual	frame	foil		
I	1000	1050 ± 0.005	15 × 20	10 × 16	15	yellow
II	1000	1050 ± 0.005	15 × 20	10 × 16	10	yellow
III	1000	996 ± 0.005	15 × 20	10 × 16	30	white

Table 3.1: Silicon Nitride foil list with dimensions.

of homogeneity, high thermal stability, extreme hardness and chemical inertness,

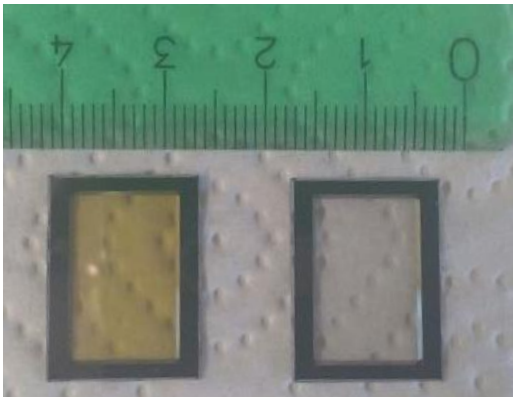

FIGURE 3.7: Picture of the SiN foils from the production batch I(left) and III(right). The difference in the colour corresponds to slight changes in the thickness. The scale is in centimeters.

relevant for this work. It was already proven in the previous runs that the SiN foils survive the cooling down and warming up procedures in the cryostat. Also it was found [29] that the performance of these SiN foils was better as compared to the old favourite Parylene C foils [3] used previously for the passive absorber method. The energy line width for ions after passing through the foil was found to be around 20% better with SiN foils compared to Parylene C absorbers [29]. However, these foils are very sensitive and special care was taken while designing the rotatable disc with the foil holders. The foils were placed loosely in the holder and were not fixed to avoid breaking during cooling down and warming up procedures. Fig. 3.7 shows a picture of the foils from the production batch I and III.

3.6 The SiN degrader foil holder

In a previous experiment at ILL [4, 29], the SiN absorbers were mounted at $\sim$ 95 cm distance from the CLTD array, and in a later experiment, part of the foils were installed at $\sim$ 95 cm, and another part fixed at $\sim$ 10 cm distance. A 4% efficiency for the transmission of the fragment beam to the CLTDs with 4.2 μm, and 2.5% efficiency with 5.3 μm of SiN foils placed 95 cm upstream the detector was reached in the first experiments at the ILL [29], limited by losses

due to small angle scattering in the degrader foils. Later the efficiency improved to 69% efficiency with 4.4 μm SiN placed 9 cm from the detectors. However, due to additional SiN foils 95 cm upstream the detector, the overall efficiency dropped again considerably to 25% for 5.5 μm and 13% for 6.5 μm SiN foils (cumulative thickness). The separation between the absorber foils and the CLTD array resulted in a considerable loss in detection efficiency, as well as limited the measurements due to contamination from neighbouring masses at LOHENGRIN, discussed in detail later in Chapter 5. For a couple of measurements, at cost of the beam time[3], all 6.5 μm foils were placed at 9 cm from the detectors and the efficiency improved to 30%. However this limited flexibility in foil thickness. As the optimum Z-resolution in different mass and energy regions is obtained for different absorber thicknesses (see Section 2.5), we have to keep flexibility in changing the foil thickness. To overcome these problems, a rotating disc with absorber foil stacks of different thicknesses was installed inside the cryostat. This allowed the placement of the absorber foils very close ($\sim 3-5$ mm) to the CLTD array, and hence significantly improved the detection efficiency to almost 100%.

A major modification in the present experimental set-up is thus the installation of a rotating disc inside the cryostat with the possibility to mount absorber foils with different thicknesses close to the CLTD array in order to optimize the Z-yield measurements. To be able to install the rotator, the cold finger had to be redesigned. This redesign was mainly due to space constraints inside the cryostat when placing the rotator with different foil stacks. In addition, for the ILL experiment CLTD detectors were tilted in order to mount them perpendicular to the beam and to increase the effective detector area by 20% as compared to the previous runs [29].

[3]it takes around 3 days to change the foil thickness inside the cryostat due to the warming up and cooling down time of the cryostat.

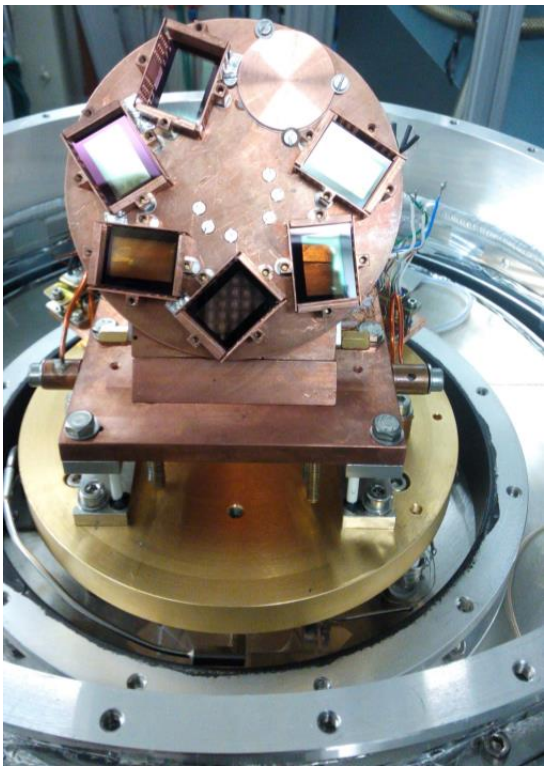

FIGURE 3.8: Picture of the rotatable disc with different thickness of SiN absorber foil stacks mounted in front of the CLTD array.

3.6.1 The rotatable SiN degrader foil holders

A rotator with SiN degrader foil holder in shape of a disc was installed on the cold finger of the cryostat as shown in the Fig. 3.8. On this disc, SiN foil stacks of different thicknesses are mounted for the application of the passive absorber method for isotopic yield determination of fission fragments at the ILL. The absorber foils were placed very close ($\sim 3-5$ mm) to the CLTD array and hence significantly improved the detection efficiency. Additionally, an alpha source was also mounted on this disc for calibration and monitoring of the CLTDs.

The rotatable disk was driven by a remote controlled piezo-driven rotary stepper positioner. In this work, we use the system ANR240/RES from Attocube, which consists of a positioner with resistive encoder and the controller ANC350. The device operates at temperatures down to below 1K, and allows a reproducible positioning with an accuracy of 0.05^0 (30 μm for the current design) based on a slip stick driving mechanism. Fig. 3.9 shows the schematics of this driving

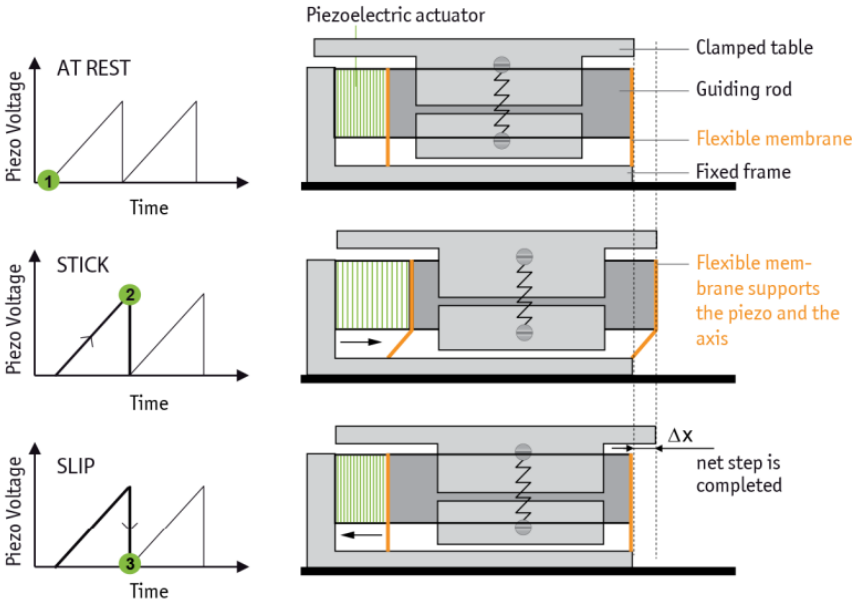

FIGURE 3.9: Illustration of the slip-stick driving mechanism of the piezo driven ANR240/RES rotator from Attocube Systems AG. 1) The sticking phase of the clamped table causes a net step (top). 2) Acceleration of the guiding rod (middle). 3) Disengagement of the clamped table (bottom).

mechanism based on applying sawtooth voltage pulses to the piezo actuator. In step one, a guiding rod is firmly connected to the piezoelectric actuator while the moving table is clamped to it. A sawtooth shaped voltage pulse is applied to the piezo (see top row of Fig. 3.9). In step two, during the phase of the slow flank, the clamped table sticks to the guiding rod and is moved over a distance Δx where Δx is bigger for higher applied maximum voltage (middle row of Fig. 3.9). Finally, in step three, by applying a steep flank of the voltage pulse to the piezo actuator, the guiding rod is accelerated rapidly over a short period of time so that the inertia of the clamped table overcomes friction. This disengages the clamped table from the accelerated guiding rod such that the table remains stationary. The net step of Δx is therefore completed. The technical specifications of the rotator can be found on the webpage: `http://www.attocube.com/Specs_Sheets/Pos/ANR240RES.pdf`. The two main advantages of this driving mechanism are - a) Grounding of the positioners: When a position is reached after a series of steps, zero voltage is applied to the piezo actuator. Therefore, there is no noise and no drift caused by any external electronics. b) Low voltages: Only low to moderate voltages are

needed to drive the positioners (maximum 60V is used).

3.6.2 Redesign of the cold-finger

As mentioned earlier, due to the installation of the rotatable disc with different foil positions, the cold-finger had to be redesigned because of the space constraints in the cryostat. Two cold finger mountings were prepared- 1) for the MLL experiment with a horizontal beam line; and 2) for the ILL set-up with a beam line at an angle of 35^0 from the horizontal. The beamline to the cryostat was adapted in the previous work [29] for connection to the ILL beam line, but the detectors were placed vertically in this case. In this work, the coldfinger was designed such that the CLTD array was tilted in order to arrange it perpendicular to the beam and to increase the effective detector area by 20% as compared to the previous runs. Fig. 3.10 shows the picture for vertical mounting of the CLTDs for the MLL experiment, and for the tilted mounting for ILL. The dimensions of the different parts of the detector mounting can be found in the Appendix A.

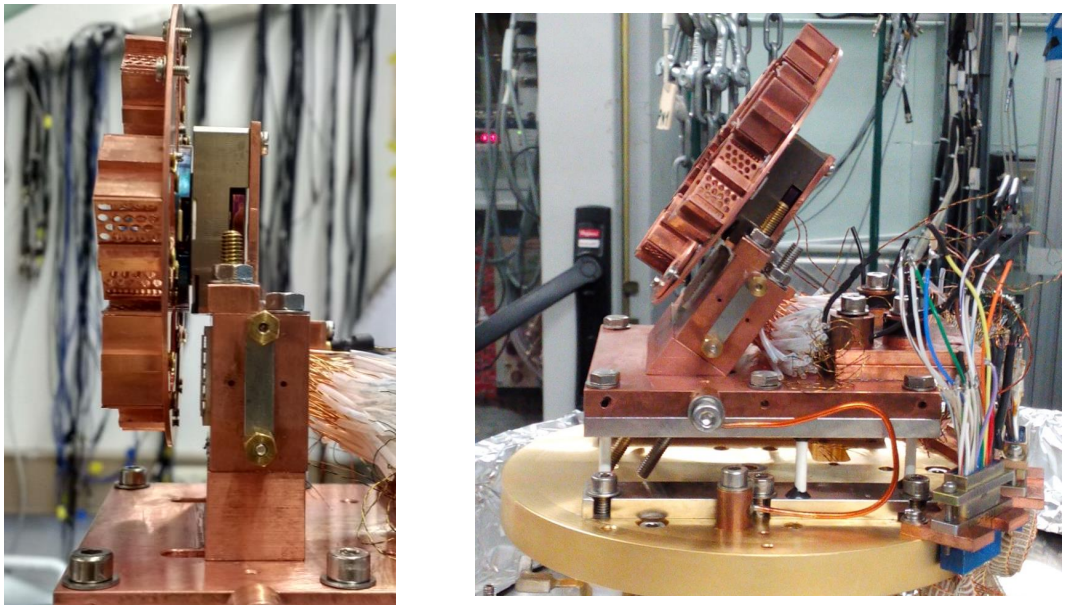

(A) (B)

FIGURE 3.10: Picture of the CLTD mounting for a) the horizontal beamline at MLL; (b) the tilted beamline at ILL.

3.7 Lab tests

This section discusses the lab tests for the performance of the new detector system and the rotator operation. An array of 24 pixels was built. With the available electronics for readout, 23 pixels can operate simultaneously for recording spectra. The energy resolution and energy - pulse height linearity of the detectors are two important properties especially for this work. These properties were tested using an alpha source along with the operation of the rotatable disc and its influence on the measurements. Efforts were made to improve the cooling down performance of the newly adapted cryostat to the beamline at the ILL.

3.7.1 Detector performance

An easy way to record energy spectra to test the detector performance and calibration without beam is to use an $\alpha-$source. Also it provides a tool to monitor the residual gas condensation [107] on the detector during operation at the beam-lines. Therefore an $\alpha-$source was placed on the rotatable disc in front of the detectors. This $\alpha-$source consisted of three radioactive isotopes ^{239}Pu, ^{241}Am and ^{244}Cm. The energies of the $\alpha-$lines emitted from these three isotopes is provided in the Table 3.2 [107].

Isotope	$\alpha-\mathrm{E}_{literature}$ [keV]	Relative Abundance [%]	$<\mathrm{E}_{lit}>$ [keV]
^{239}Pu	5105.5(8) 5144.3(8) 5156.59(14)	11.94(7) 17.11 (14) 70.77(14))	5148.4(2)
^{241}Am	5388(1) 5422.8(13) 5485.56(12)	1.7(2) 13.1(3) 84.8(5)	5478.3(1)
^{244}Cm	5762.64(3) 5804.77(5)	23.1(1) 76.9(1)	5795.0(4)

TABLE 3.2: Composition of the alpha source used for the performance test of the CLTD array with energies for the different lines. $<\mathrm{E}_{lit}>$ corresponds to the mean value of respective alpha energies.

D - Resistance of the detector thermometer H - Resistance of the heater strip				
A0 D - 252 kΩ H - 118 Ω $\frac{\Delta E}{E} = 2.1\%$	B0 D - 253 kΩ H - 115 Ω $\frac{\Delta E}{E} = 1.4\%$	C0 D - 249 kΩ H - 116 Ω $\frac{\Delta E}{E} 1.1 =\%$	D0 D - N.C. H - N.C.	E0 D - 254 kΩ H - 115 Ω $\frac{\Delta E}{E} = 1.6\%$
A1 D - 254 kΩ H - 115 Ω $\frac{\Delta E}{E} = 2.1\%$	B1 D - 254 kΩ H - 117 Ω $\frac{\Delta E}{E} = 1.7\%$	C1 D - 250 kΩ H - 116 Ω $\frac{\Delta E}{E} = 1.8\%$	D1 D - 250 kΩ H - 116 Ω $\frac{\Delta E}{E} = 1.9\%$	E1 D - 251 kΩ H - 117 Ω $\frac{\Delta E}{E} = 1.9\%$
A2 D - 256 kΩ H - 116 Ω $\frac{\Delta E}{E} = 1.4\%$	B2 D - 257 kΩ H - 115 Ω $\frac{\Delta E}{E} = 2.0\%$	C2 D - 257 kΩ H - 116 Ω $\frac{\Delta E}{E} = 1.5\%$	D2 D - 253 kΩ H - 114 Ω $\frac{\Delta E}{E} = 1.6\%$	E2 D - 252 kΩ H - 115 Ω $\frac{\Delta E}{E} = 1.7\%$
A3 D - 258 kΩ H - 116 Ω $\frac{\Delta E}{E} = 1.4\%$	B3 D - 255 kΩ H - 116 Ω $\frac{\Delta E}{E} = 1.9\%$	C3 D - 257 kΩ H - 115 Ω $\frac{\Delta E}{E} = 1.3\%$	D3 D - 251 kΩ H - 116 Ω $\frac{\Delta E}{E} = 1.4\%$	E3 D - 250 kΩ H - 115 Ω $\frac{\Delta E}{E} = 2.6\%$
A4 D - 260 kΩ H - 117 Ω $\frac{\Delta E}{E} = 1.6\%$	B4 D - 251 kΩ H - 118 Ω $\frac{\Delta E}{E} = 1.5\%$	C4 D - 254 kΩ H - 103.5 Ω $\frac{\Delta E}{E} = 1.2\%$	D4 D - 254 kΩ H - 114 Ω $\frac{\Delta E}{E} = 1.2\%$	E4 D - N.C. H - N.C.

TABLE 3.3: Table with resistance of the thermometer (D) and the heater (H) of the detector pixels at room temperature. The nomenclature of the pixels is in-beam view. Also listed is the energy resolution from the alpha measurement. (N.C. - not connected)

The pixels used to build the CLTD array in this work were from the same wafer also used in previous work [107], [4]. The R-T characteristics study of other pixels from the same wafer was already performed in the previous work and was found to be consistent. The Table. 3.3 shows the resistance of the thermometer and the heater at room temperature. Also shown is the energy resolution for each pixel from the measurements with alpha source mentioned above. We find that the resistance values of the thermometer and the heater are consistent for all the pixels and the also with the values reported in the previous works [4, 107].

An example spectrum with alpha lines recorded with the central pixel C2 is shown in Fig. 3.11. A sum of gaussians based on the relative intensities of all the contributing lines was used to fit the spectrum. Before the fitting procedure the data were filtered offline [23]. Fig. 3.11b shows a linear energy calibration plot using the three mean energies of the alpha source (see Table 3.2 for the composition of the alpha source) for the central pixel C2. The full width half maximum (FWHM) for the spectrum shown is 50(2) keV. For the other 23 pixels, the FWHM for the filtered spectrum was in the range 50 keV - 85 keV which is also comparable to the previous works [4, 107].

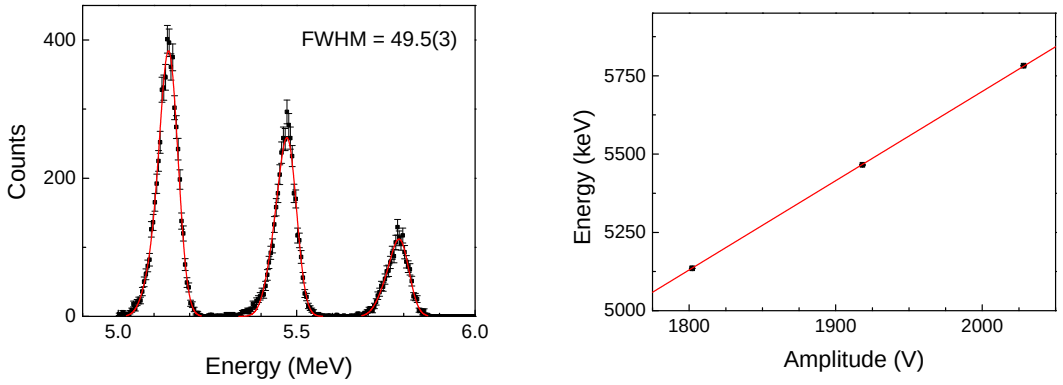

(A) (B)

FIGURE 3.11: a) An example alpha spectrum for the central pixel C2 on the array. b) energy calibration using the spectrum shown in a).

3.7.2 Operation of the rotatable SiN holders

The rotator positioner ANR240 together with the full foil holder assembly was tested both at room temperature and after cooling down to $\sim$ 1 K. The following was observed at room temperature:

- The minimum input voltage required for the rotation was $\sim$ 15 V with very slow movement in both clockwise and anticlockwise direction.
- The values of the encoder were reproducible within the test precision (by eye) of 1^0.
- The linearity of the encoder was $< 1\%$ except for the dead region of the Encoder = 16^0 (from 345^0 to 1^0).

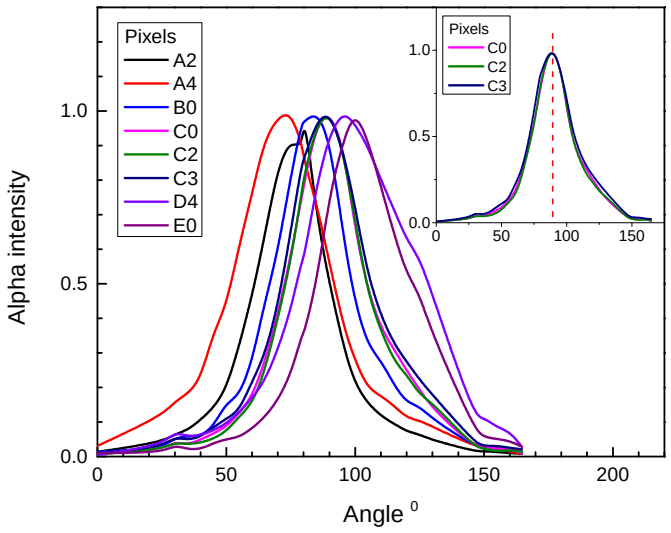

FIGURE 3.12: Alpha intensity for different positions on the disc for calibration. The angle on the x-axis corresponds to the rotation angle of the disc on which the alpha-source was mounted as shown in Fig. 3.8. The insert shows the distribution for pixels on the central column of the array (same scale).

Applied voltage (in volts)	T_{CP}	
	Before	After
15	1.0814	No change
20	1.0814	No change
25	1.0814	1.088
30	1.0814	1.093
35	1.0814	1.099
40	1.0814	1.104
45	1.0814	1.109
50	1.0814	1.114
55	1.0814	1.117
60	1.0814	1.122

TABLE 3.4: Variation in cold plate temperature with applied voltages to move the rotator

The rotator motion was also successfully tested inside the cryostat after cooling down. Calibration of the different foil positions was done using the alpha source. The alpha intensity was recorded for rotation steps of 5^0 to determine the angular position of the alpha source on the disc. The recorded alpha intensity as a function of the rotation angle (encoder readout angle) of the disc on which the alpha-source was mounted is shown in Fig. 3.12. The measurements were recorded over the

entire range of the encoder readout angle for which non-zero alpha intensity was observed on the detectors. The encoder readout for the position of the alpha source on the disc, such that the alpha source was aligned perfectly in front of the detectors, was determined based on the position at which the alpha intensity peaks for the central pixels, as shown in the insert of the Fig. 3.12. This therefore allowed the calibration for all the other SiN foil positions on the manipulator which were symmetrically distributed on the disc by construction. This was important to reproduce the exact orientation of the SiN foils for different measurements with the precision of 0.03 mm.

Owing to the low temperatures inside the cryostat, the detectors are very sensitive to any thermal noise. It was realized that the rotator movement with the applied voltages introduces heat to the system and requires thermal stabilization time. The Table 3.4 illustrates the change in the cold plate temperature with the applied voltages to move the rotator by 20 degrees.

3.7.3 Tests to improve the thermal shielding

As discussed in the Section 3.3, in the previous experiment [29] at the ILL reactor, due to the adaptation of cryostat to the angled (not horizontal) beam line at LOHENGRIN, it was not possible to cool down the cryostat to operational temperature with an open beam line. Adaption to the ILL beam line (see Fig. 5.2b) was done with new shield tubes and extra parts for each liquid He shield, liquid N shield and vacuum chamber. This resulted in an increased volume of the cryostat with several attachments and hence reduced the cooling down performance of the cryostat due to more heat radiation from the surfaces. Therefore a thin SiN foil was used to thermally shield the detectors by mounting it on the helium shield tube at roughly 10 cm from the detectors in the previous experiment [29]. Also the small aperture size on the nitrogen shield tube ($\sim$ 50 cm from the CLTDs), and the Helium shield tube (30 cm from the CLTDs) limited the detection efficiency to reduce the heat radiation from outside. This section discusses the efforts made to improve the situation concerning the thermal shielding of the CLTDs, and to

test the possibility of operating the cryostat without a SiN foil fixed on the helium shield tube of the cryostat.

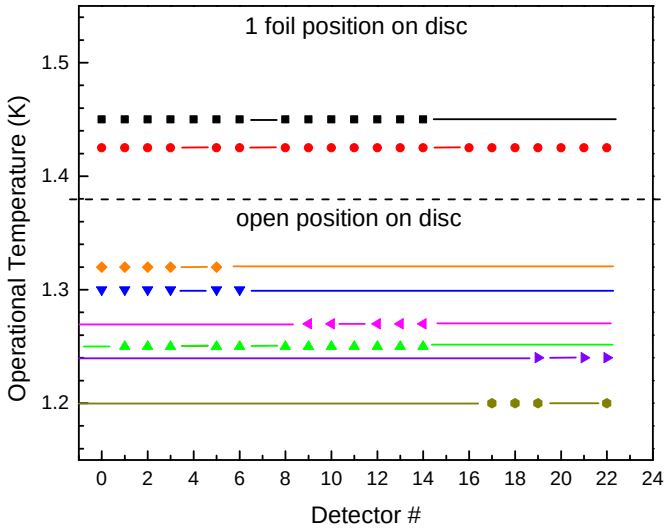

FIGURE 3.13: Set point temperature of the CLTD array for two positions of the disc in front of the array − 1 foil and open. The lines indicate respective detectors which were not operational.

In one test, more super-insulation was added on the nitrogen shield tube which improved the situation significantly and it was possible to operate the CLTDs also with the ILL beam tube set-up without any fixed SiN foils on the helium shield tube. However, it was very close to the limit of the cooling power of the cryostat and therefore on the limits of thermal stabilization of the detectors. The rotating disc in front of the detectors also partly shielded the CLTDs and improved the situation. The CLTD operation was tested with different foil settings on the disc. Fig. 3.13 shows the maximum operational temperature at which TES, the thermometers are still in the transition region and the CLTDs can be operated. For the 1 SiN foil position on the disc, almost all detectors were operating at temperature = 1.425 K with good thermal stabilization. For the open position, although it was possible to run a number of detectors at temperature = 1.25 K, it shall be noted that this temperature is very close to the temperature at which the cold-finger is stabilized ($\sim 1.18 - 1.22$ K). This means close to limit of the cooling power of the cryostat and therefore on the limits of thermal stabilization of the detectors. Based on these results, a conservative decision to use 1μm SiN foil in front of the detectors at the ILL beam line replacing the open position was made.

3.7.4 Additional tests

Additional tests of the detectors were performed with different settings to check the effect on the resolution due to the rotator movement, the relaxation time after cooling down of the cryostat and new amplifiers. With respect to the rotator movement, fluctuations were observed in the resolution ($< 2\%$) if measurements were taken just after the rotation was performed, however, no change within the error bars was observed for measurements after roughly 5 minutes post rotation. Similarly, in case of the cooling down of the cryostat, no change within error bars was observed in the resolution after 1 hour since the cryostat reached operating temperature. However, a significant improvement was observed in the resolution for measurements with new amplifiers(VAM from Surface Concept) compared to the old ones (DLPVA-S from Femto and 15). Results from these tests are shown in Fig. 3.14. It is surmised that this effect is the result of a different operating principle of the two amplifier types. The old amplifiers are operated at constant current, whereas in the case of the new amplifiers, voltage is kept constant and the small change in resistance is controlled by varying the current applied to the amplifiers to regulate the resistance providing stabilization in the thermal signals from the CLTDs. The current detector set-up was run with 8 old and 16 new amplifiers. With the improved performance with the new amplifiers, the central pixels where high intensities are expected from the beam were operated with new amplifiers, whereas the ones on the edges with either none or very few counts were operated with the old amplifiers.

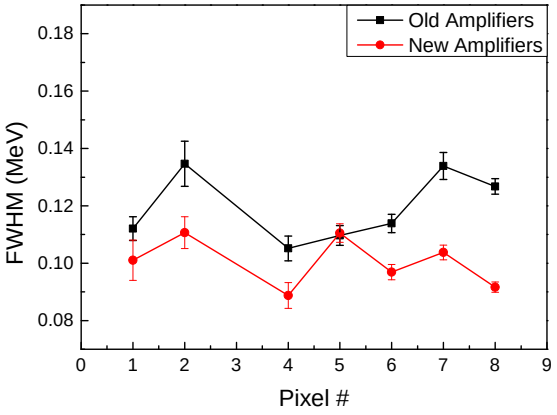

FIGURE 3.14: Comparison of alpha resolution with old and new amplifiers.

Also the resolution was tested at different disc positions where the alpha intensity could be recorded, like: open, with 1 SiN foil mounted in front and alpha source. Less than 0.5% change was observed in the measurements with alpha source when compared to the open/1 foil position which is expected to be due to the different thermal conditions of the CLTD array in the respective cases.

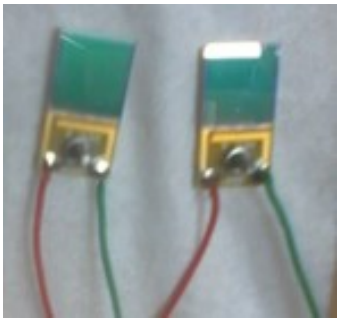

FIGURE 3.15: Picture of the PIN diodes mounted on the frames.

In addition, pin-diodes were also used in the experiments discussed in the following chapters as additional detectors which are mounted on a manipulator in front of the cryostat. The PIN diodes used are Silicon planar p on n substrate with a resistivity of 4600 ± 1400 Ωcm. Several pin-diodes ($11 \times 11 \times 0.381$ mm^3) were fabricated (see Fig. 3.15) on the frames where the backside of the pin diode was glued with epoxy adhesive and electrical connections were made from the top side with Au bonding. The sensitive area of these PIN-diodes was 10×10 mm^2 and their current response was tested for different bias voltages before application. For a change in the bias voltage from 20 V to 180 V, the measured current was in the range 0.001 μA to 0.008 μA. The PIN diodes provide high signal to noise ratio with very low current and low capacitance. Also the high breakdown voltage permits operation at full depletion.

Chapter 4

Feasibility tests with pure ion beams

4.1 Motivation

Feasibility tests with pure ion beams were performed at accelerator facility at the Maier-Leibnitz Laboratory Munich with the current detector setup discussed in the last chapter. Two crucial parameters that determine the quality of the nuclear charge determination using the absorber method are the line width in the measured residual energy spectra and the energy loss difference for adjacent Z for a given initial velocity and fixed absorber thickness. At the LOHENGRIN spectrometer only the total widths in the residual energy spectra, that are a sum of detector resolution, beam energy width mainly due to the target length (see Section 2.2), absorber-foil inhomogeneity and statistical energy straggling within the absorbers, can be measured. However, to optimize the system for different fission-fragment mass and energy regions the various shares to the energy width have to be determined separately. For this purpose, a tandem accelerator is an ideal tool, as heavy ion beams in the energy range of a few MeV to about 100 MeV can be provided with negligible energy width. Accordingly, tests at the tandem accelerator were performed with the aim to optimize the resolution of the new

CLTD pixels, to check the quality of the new SiN foils stacks, and to precisely determine the energy loss as well as energy loss straggling as a function of the initial velocity and the absorber thickness. Results from these tests provided information about the optimum absorber thickness for the best Z-resolution in case of fission fragments, which is strongly dependent on the nuclear charge Z, and mass, and the initial ion velocity.

Determining the nuclear charge yields are particularly challenging in the heavy mass region of the fission fragments. Owing to our interest in the heavy mass region of the fission fragments, measurements with the accelerator beam were designed with two different isotopes with neighboring nuclear charges in the region $Z \sim 50 - 55$, corresponding to the heavy fragments in the mass range of 125-140. In an ideal case, for these tests to determine the quality of nuclear charge determination with the new detector system, we would chose ion beams with neighboring Z value and same mass. But since it was not possible to deliver such stable beams at the accelerator facility, a good compromise was to use ^{130}Te (Tellurium, Z=52) and ^{127}I (Iodine, Z=53) beams with neighbouring Z values but different masses, which are delivered from the accelerator.

The fission kinetic energies for these masses are in the range[1] $\sim 60 - 90$ MeV [50] (see also Fig. 2.3). Assuming around 5 to 10 MeV losses in the fissile target and its cover foil, the energy range to be covered in the tests was defined to be 50 - 85 MeV. It should be noted here that LOHENGRIN is actually a velocity filter[2], and hence to match the conditions at LOHENGRIN in order to estimate the quality of nuclear charge determination, the energies of these two ion beams with different masses were chosen such that the velocities are same. Four different energies were chosen with the constraints mentioned above, details of which follow in the next section.

The thicknesses for SiN absorber foil stacks for these tests were chosen based on the SRIM calculations. The relative energy loss was determined using SRIM for ^{127}I for different thicknesses of SiN foils for different incident energies in the range

[1] the fission kinetic energy depends on the fissile target used, values shown here correspond to ^{241}Pu(n_{th}, f).

[2] since it separates both mass and velocity simultaneously, it results in an energy separation, but intrinsically it is a velocity filter.

mentioned above. These calculations suggested an energy loss of 60 to 100 % for a thickness of 4 to 9 μm of SiN, respectively. Several foil stacks, with thicknesses in this range were hence chosen for this test experiment.
In addition to information for optimizing the nuclear charge determination, this test experiment also provided other useful information regarding the detector performance. In previous experiments [[107], [4]], with focused mono-energetic beams, fluctuations were observed in the measured energy resolution beyond statistical errors. Section 4.5.4 provides insights on this observation in terms of a dependence of the energy response on the position of the pixel where the beam hits the detector (for details see also Diploma thesis of W. Lauterfeld [101])

4.2 Experimental set-up

This section describes the experimental set-up used for the series of measurements discussed in this chapter. The detector system with the newly constructed CLTD array and the rotatable disc, discussed in the previous chapter, was used for this experiment. The vertical mount for the CLTD array (Fig. 3.10a) designed for a horizontal beam line was installed in the cryostat. The experiment was performed at the accelerator facility at the Maier Leibnitz Institute (MLL) at Garching.

The accelerator [121] is based on the tandem van de Graaff-principle and is installed in a 25 m long pressure tank. The ions are accelerated to high energy with a DC voltage of up to 14 million volts. As shown in Fig. 4.1, the negatively charged ions generated in the ion source are first accelerated towards the positively charged terminal at the center of the instrument where they pass through a stripper foil which strips off the electrons. This results in positively charged ions that are further accelerated with the same voltage towards the terminal on ground potential at the other end, and hence the name tandem accelerator. After acceleration a 90^0 deflection magnet selects the ions with defined charge state and energy needed for the experiment and these ions are transported to the experimental stations in the beamlines. Different kind of ions can be accelerated here ranging from the lightest

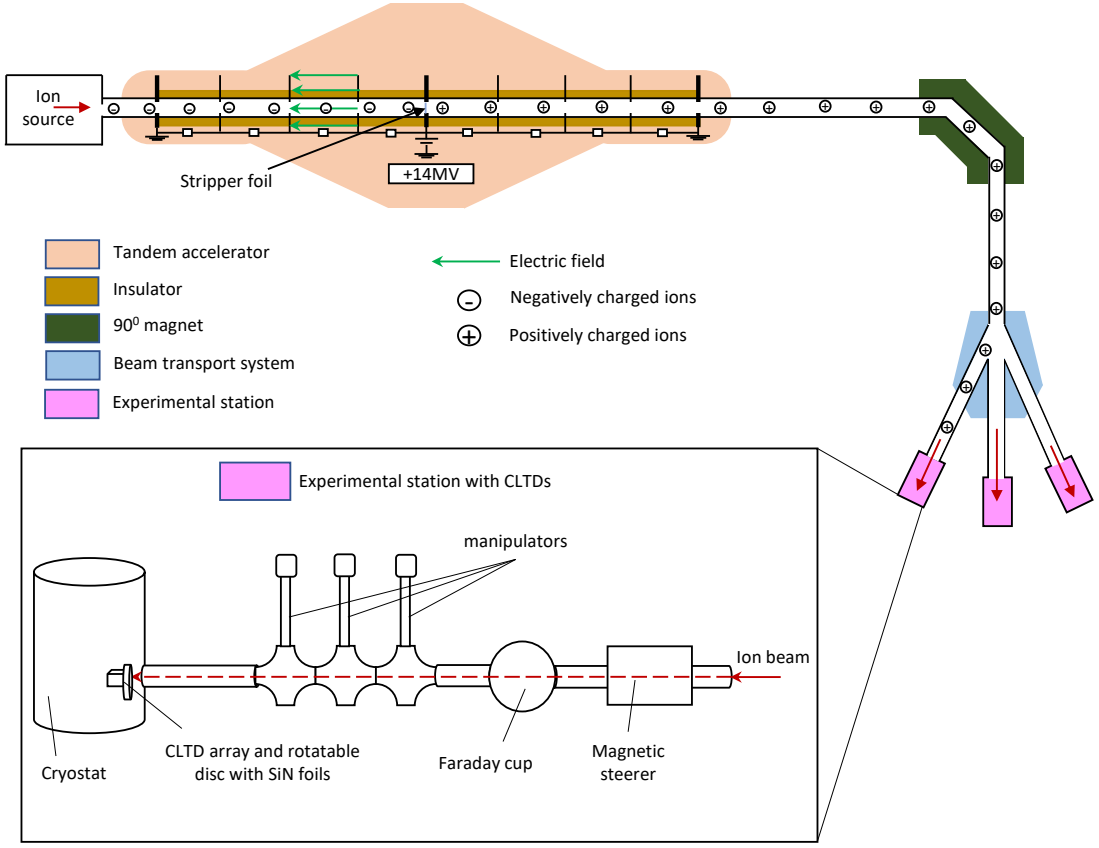

FIGURE 4.1: Schematic of the tandem accelerator at MLL and the experimental set-up with CLTDs.

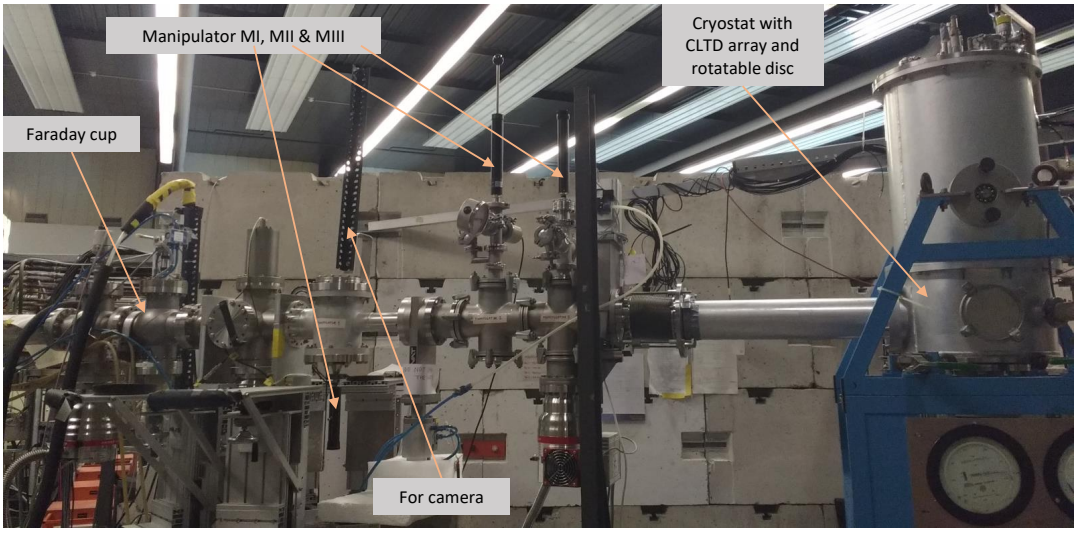

FIGURE 4.2: Picture of the experimental set-up at beam hall of the accelerator facility.

element, hydrogen, to very heavy ions, such as lead. The ion beams of interest are focussed with quarupole lenses.

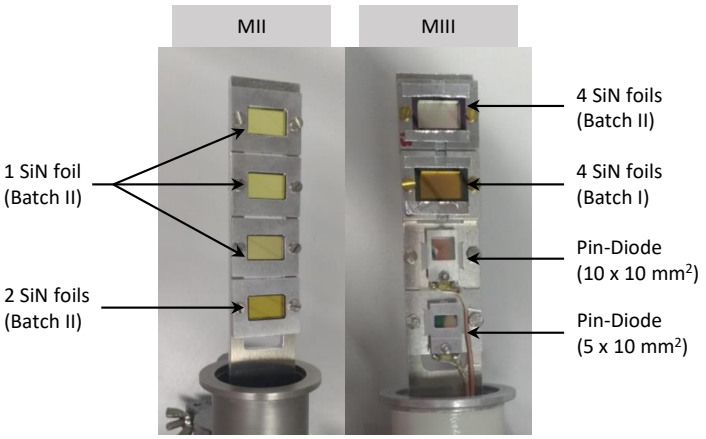

FIGURE 4.3: Picture of two manipulators MI and MII installed on the MLL beam line with different foil stacks and pin-diodes.

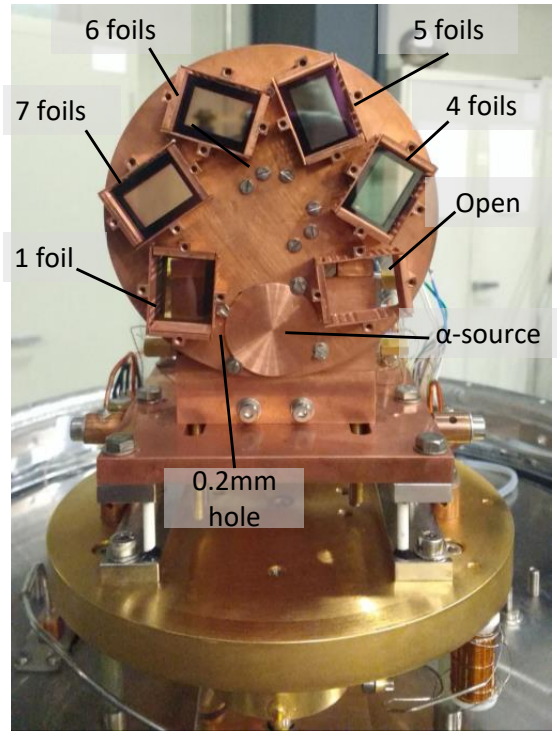

FIGURE 4.4: Picture of the rotatable disc mounted in front of the CLTD array with different SiN foil stacks, $\alpha-$source and a 0.2 mm collimator.

The accelerated ion beams are transported in the beam lines to the experiment hall. The present experiment was performed at the beam line at $+10^0$ in hall II at the MLL. Fig. 4.2 shows the installation of the detector system at the beam line. The cryostat with the detectors were carefully aligned to the beam line using a telescope. In the experiment hall, the beam passes through two steerer magnets which allow beam deflections in the x and y direction for alignment. The steerer

magnets are followed by a movable Faraday cup to determine the beam intensity. This was followed by a manipulator (MI as shown in the Fig. 4.2) with a view screen/crystal and an open position. With this crystal, it is possible to see the image of the ion beam cross-section using a camera installed on the mount as shown in Fig. 4.2, which was used for controlling the focusing procedure of the beam. This was followed by two manipulator set-ups with several stacks of SiN foils as shown in Fig. 4.3, and two pin-diodes with different apertures, used as counters after reducing the beam intensity.

Fig. 4.4 shows the picture of the rotatable disc mounted in front of the CLTD array, installed in the cryostat. The figure also shows the position of different SiN foil stacks with nominal thicknesses - 1 μm, 4 μm, 5 μm, 6 μm, 7 μm. The $\alpha-$source and a 0.2 mm hole, used for a measurement of the position dependence of the detector response (see Section 4.5.4) are also shown. The electronics available to run 23 pixels simultaneously was connected as discussed in Section 3.4. The Table. 4.1 shows the cold finger temperature settings for different positions of the disc. The small changes in the temperature setting reflect the effect of thermal radiation shielding from the beam line due to the presence of foils in front of the CLTDs. The cold finger was set to the highest temperature setting in the case of thick foil stacks providing good thermal shielding whereas the lowest temperature setting was used for the open position with no shielding.

Position on the disc	Cold finger temperature (T_{CF})
$\alpha-$source	1.59 K
1 foil	1.57 K
4 foils	1.59 K
5 foils	1.59 K
6 foils	1.59 K
7 foils	1.59 K
open	1.52 K

TABLE 4.1: Cold finger temperature(T_{CF}) settings for different positions of the disc.

4.3 Measurements

Following the discussion in Section 4.1 four different energies were chosen for both of the two ion beams - ^{130}Te (Z=52) and ^{127}I (Z=53) as presented in Table 4.2. The energies of both ions were chosen such that they correspond to the same velocity for both ions. Corresponding energies for four same velocity sets are presented in the Table 4.2. The Table also lists the different measurement settings in terms of foil thicknesses on the disc and manipulator as well as collimators on the disc. In this energy range the resolution of the ion beam from the accelerator is expected to be $\frac{\Delta E}{E} = 10^{-3}$. The spatial width of the beam however varied over the different settings, in the case of the iodine beam a relatively broad beam radius ($r \sim 3$ mm) was observed whereas the tellurium beams were better focussed ($r < 1.5$ mm). The beam intensity was adjusted using degraders in the form of grids to a rate of < 100 ions/s.

Also, in order to test the homogeneity of the SiN foils, stacks of the same thickness from the same production batch were mounted on the manipulators. Measurements were made with each stack respectively to see any difference in the energy response. These and other results are discussed in the next sections.

In addition, measurements were performed where a pixel was scanned through the 0.2 mm hole by moving the disc in small steps using the ^{130}Te beam at 68.46 MeV. Also the pixel was scanned with open position on the disc with the same beam, using the steering magnets in horizontal and vertical directions. These measurements were performed to study the dependence of the energy response on the position on the pixel where the beam hits the detector. These results are discussed separately in Section 4.5.4.

Measurement setting	^{130}Te				^{127}I			
	Energy (MeV)							
	80.36	68.46	56.55	44.64	78.50	66.88	55.25	43.61
open position on disc	✓	✓	✓	✓	✓	✓	✓	✓
1 μm SiN on disc	✓	✓	✓	✓	✓	✓	✓	✓
4 μm SiN on disc	✓	✓	✓	✓	✓	✓	✓	✓
5 μm SiN on disc	✓	✓	✓	✓	✓	✓	✓	✓
6 μm SiN on disc	✓	✓	✓	✓	✓	✓	✓	✓
7 μm SiN on disc	✓	✓	✓	✓	✓	✓	✓	✓
4 μm SiN on MIII	✓	✓	✓	✓	✓	✓	✓	✓
7 μm SiN on disc + 1 μm on MII	x	✓	x	x	x	x	✓	x
4 μm SiN on MIII + 0.2 mm hole on disc	x	✓	x	x	x	x	✓	x
0.2 mm hole on disc	x	✓	✓	✓	x	x	✓	✓
0.5 mm hole on disc	x	✓	x	x	x	x	x	x
1 mm hole on disc	x	✓	x	x	x	x	x	x
2 mm hole on disc	x	✓	x	x	x	x	x	x

TABLE 4.2: List of measurements with the two ion beams - ^{130}Te (Z=52) and ^{127}I (Z=53) at different energies and different SiN foil thicknesses on the disc and the manipulators.

4.4 Data analysis

The data acquisition provides an ASCII file for each measurement and each pixel (see Section 3.4). Using the ASCII files, a histogram can be created for the measurements for each pixel. These histograms were created and the fits of the spectra were performed with the software OriginPro 9.0. In this experiment focused ion beams with small cross-sections were used. Due to this, in almost all measurements, either one or a couple of pixels were illuminated by the beam instead of the entire array of 25 pixels. The analysis hence in this chapter was performed in most cases for the central pixel C2 (see Table 3.3) on which the beam was focused.

4.4.1 Fit function

As discussed in Section 2.4[3], the energy loss distributions of mono-energetic beams are Gaussian or modified Gaussian in form, depending on the thickness of the absorber foils. For the measurements in this experiment, fits were performed with modified Gaussian functions with an exponential tail on the left arising due to increasing contributions from nuclear energy loss for heavy masses with smaller energies (see for example Fig. 4.5). This exponential modified Gaussian is given by the formula:

$$f(x) = \frac{A}{t_0} \exp\left(\frac{x - x_c}{t_0} + \frac{\sigma^2}{2t_0^2}\right) erfc\left(\frac{1}{\sqrt{2}}\left(\frac{x - x_c}{\sigma} + \frac{\sigma}{t_0}\right)\right) \tag{4.1}$$

where A is a measure of the area, x_c and σ are the peak position, and the standard deviation of the Gaussian distribution, respectively, t_0 is the tailing parameter of the exponential component and $erfc$ is the error function. For a Gaussian distribution, the $FWHM$ is determined by the formula: $FWHM = 2.35\sigma$. In the present case however, the contribution from the exponential tail must also be considered and is determined by the co-efficient C_r which depends on both- the width of the Gaussian distribution and the tailing factor t_0. The $FWHM$ for the modified Gaussian is given by:

$$FWHM = 2.35\sigma + C_r t_0 \tag{4.2}$$

and the corresponding error in the determination of the FWHM is given by:

$$\Delta FWHM = \sqrt{(2.35\Delta\sigma)^2 + (C_r \Delta t_0)^2 + 2.235 C_r cov(\sigma, t_0)} \tag{4.3}$$

The last term in Equation 4.3 for the error of the $FWHM$ corresponds to the contribution corresponding to the correlation term between σ and t_0 in the covariance matrix determined by the origin program for the fit results and the errors. The C_r values are determined based on the ratio of $S = \frac{\sigma}{t}$ [122], and are given in

[3] in the subsection "energy straggling"

the Table 4.3.

$S = \frac{\sigma}{t_0}$	C_r
0.2	0.6793
0.4	0.6346
0.6	0.5986
0.8	0.5664
1.0	0.5361
1.2	0.5072
1.4	0.4799
1.6	0.4543
1.8	0.4303
2.0	0.4081
3.0	0.3192

TABLE 4.3: Values of C_r for different ratios S of $\frac{\sigma}{t}$.

The parameter x_c in the Eq. 4.1 corresponds to the peak position of the Gaussian contribution to the energy distribution. For the discussions following in the next sections, the peak position of the modified Gaussian fits corresponds to the most likely value of the distribution. This corresponds to the maximum amplitude of the distribution. The maximum amplitude of the distribution was determined using Mathematica from the parameters of the fit curve.

4.4.2 Energy calibration

For all four energies of both ion beams (^{130}Te and ^{127}I), measurements were made with the open position on the disc without any SiN foil in the beam line. These pure beam measurements were used to perform a one point energy calibration of the CLTDs. Eight individual calibrations were performed for the two beams at four different energies. The pure beam was measured at both, the start and the end of the measurement series, with a specified energy. The mean value of the calibration slope from both these measurements at the start and the end of a measurement series was finally used as the calibration slope. The energy of the ion beam (E_{beam}) is precisely determined (error $< 0.1\%$) by the accelerator

facility, and the peak positions of the measured energy distributions (E_{meas}) are determined by the modified Gaussian fits (Eq. 4.1) as discussed in the last section. The calibration slope m is given by:

$$m = \frac{1}{2}\left(\frac{E_{beam}}{E_{meas}(start)} + \frac{E_{beam}}{E_{meas}(end)}\right) \tag{4.4}$$

The difference in the measured energy at the start and the end of a measurement series with a particular beam energy setting was in all cases less than 0.1% indicating an insignificant effect due to condensation of residual gases on the detectors. The error in the calibration slope was determined by Gaussian error propagation.

4.5 Results

4.5.1 Test of the CLTDs and the rotator

The new detector system was successfully operational for the entire beam-time. Also the rotator mounted with the fully loaded disc was tested for the first time on a beam line and demonstrated smooth operation throughout the measurement series. All the different SiN foil stacks mounted on the disc inside the cryostat also survived the cooling down and warming up procedures on the beam line as well as the rotation.

Fig. 4.5 shows some sample spectra with the modified Gaussian fits discussed in Section 4.4.1. The plots are for an ^{127}I beam with an energy of 66.88 MeV for different SiN foil thicknesses on the disc − 1 μm , 5 μm, 6 μm and 7 μm. The quality of the fits is indicated by the reduced chi-square values presented in each spectrum. As can be seen the data is very well represented by the modified Gaussian fits due to the low energy tail.

The relative energy resolution, $\delta E/E$ (Fig. 4.6a) and the FWHM (Fig. 4.6b) were determined for the different beam energies with open position on the disc without any absorber foils for both the two - ^{130}Te and ^{127}I beams. These measurements,

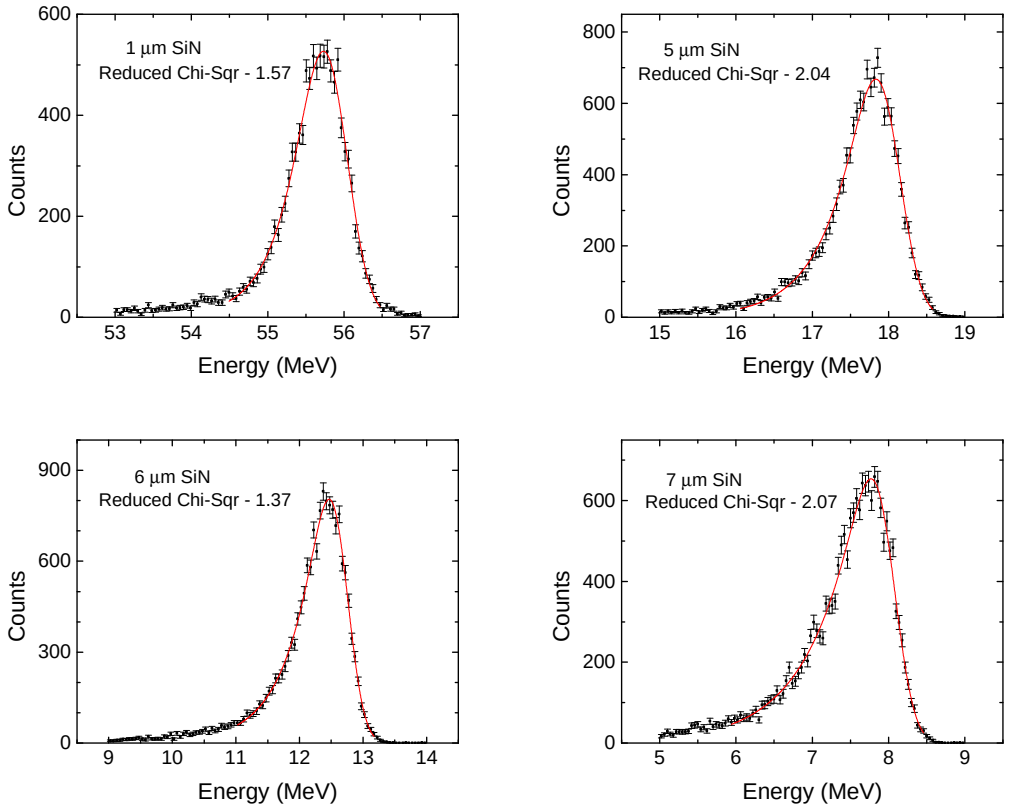

FIGURE 4.5: Sample spectra with modified Gaussian fits. The four spectra are for ^{127}I beam with an energy of 66.88 MeV for different SiN foil thicknesses on the disc − 1 μm (top left), 5 μm (top right), 6 μm (bottom left), 7 μm (bottom right).

used for energy calibration, also helped in determining the intrinsic energy resolution of the CLTDs. The relative energy resolution plotted in the Fig. 4.6a is defined as:

$$\text{Relative energy resolution}\left(\frac{\delta E}{E}\right) = \frac{FWHM}{\text{Measured Energy}} \tag{4.5}$$

The best resolutions measured in the present work are comparable to the values recorded in previous work [107] with CLTDs in the range $\delta E/E \sim 3 \times 10^{-3}$ with ^{130}Te beams at an incident energy of 80 MeV. Like in the previous work, it was observed also here that the resolution of the pure beam was sensitive to the size of the beam spot hitting the CLTDs. Focusing the beam, usually resulted in a better resolution as compared to the situation with wide beams. This difference can be seen in Fig. 4.6, in particular for the measurements at $\sim$ 80 MeV where

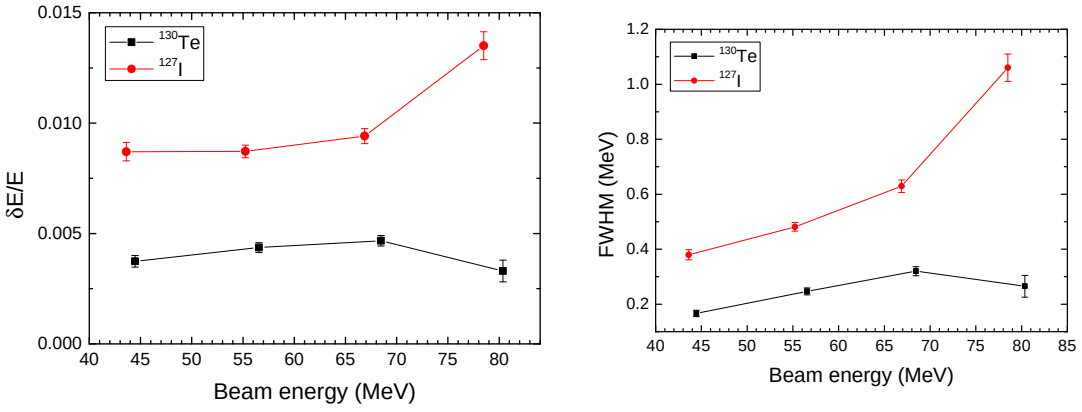

(A) (B)

FIGURE 4.6: Plots for (a) Relative energy resolution, $\delta E/E$ and (b) FWHM versus beam energy measured with open position on the disc without any absorber foils for the two - ^{130}Te and ^{127}I beams. Measurement points are connected with lines to follow the trend.

^{130}Te was measured with a focused beam and ^{127}I with a relatively wider beam. Dedicated measurements were performed to study this behaviour and the results are discussed in detail in Section 4.5.4.

4.5.2 Characterization of the SiN foils

In this section, results of the energy loss measurements with different SiN foil thicknesses are discussed. The list of measurements with different foil settings was already displayed in Table 4.2. Modified Gaussian fits discussed in Section 4.4.1 were performed on the residual energy spectra. The results of these fits determine the values for energy loss, energy resolution and the asymmetry in the residual energy spectra which are presented and discussed below.

In Fig. 4.7 the residual energy as a function of the SiN foil thickness for ^{130}Te and ^{127}I for different initial energies is plotted. Fig. 4.8 shows the tailing parameters for the same measurements which corresponds to the contribution of the exponential tail in the modified Gaussian fits. In Fig. 4.9 the relative energy resolution, $\delta E/E$, as a function of the SiN foil thickness for both ^{130}Te and ^{127}I for four different initial energy settings is plotted.

In the residual energy plots shown in Fig. 4.7, the curves which correspond to

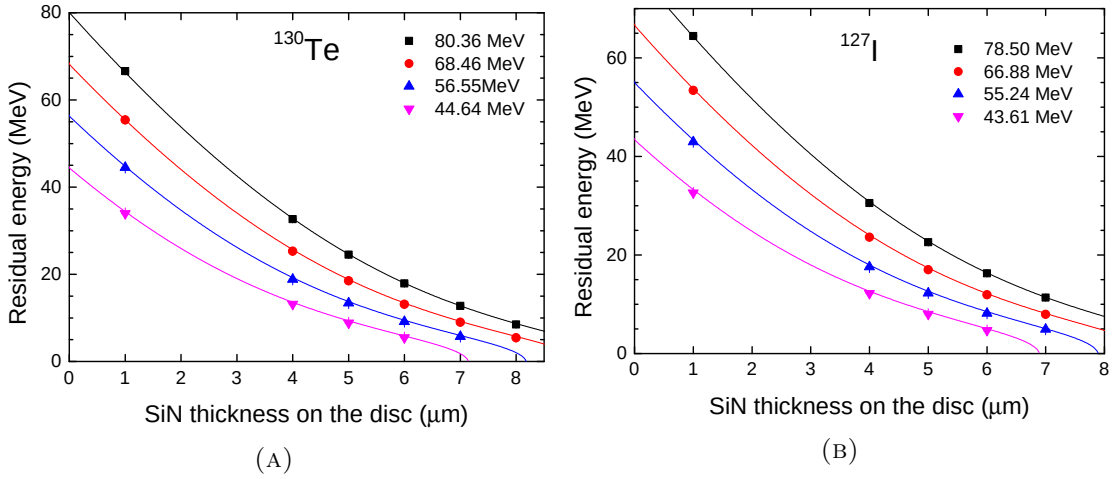

(A) (B)

FIGURE 4.7: Residual energy versus SiN foil thickness on the disc for ^{130}Te (left) and ^{127}I (right) for four different energy settings. The dots correspond to the measurements and the curves shown are semi-empirical calculations based on the Bohr theory [99, 101]. For the measurement with 8 μm thick SiN, the 7 foil position on the disc was complemented with 1 foil position on the manipulator MII.

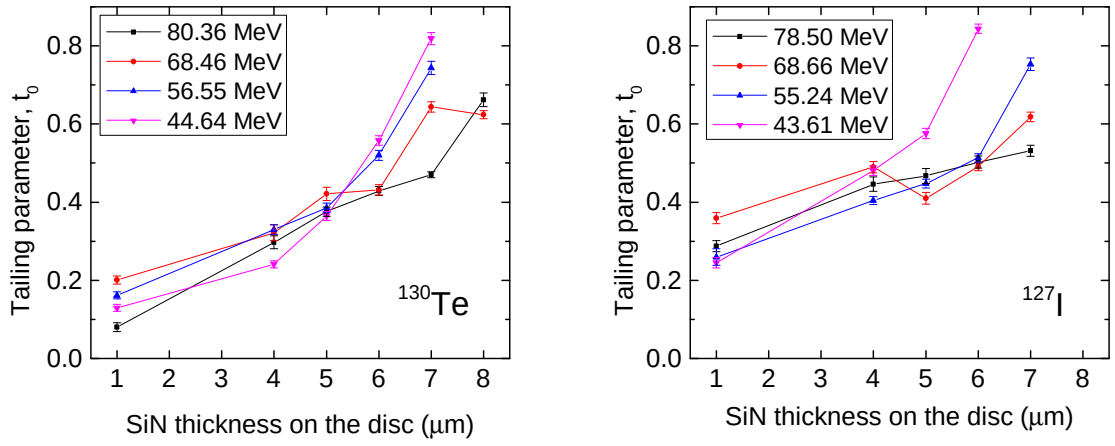

FIGURE 4.8: Tailing parameter, t_0, versus the SiN foil thickness on the disc for ^{130}Te (left) and ^{127}I (right) for four different energy settings in both cases. For the measurement with 8 μm thick SiN, the 7 foil position on the disc was complemented with 1 foil position on the manipulator MII. The data points are connected with lines to follow the trend [101].

the semi-empirical calculations based on the Bohr-theory [99] fit very well the experimental data. As expected both measured and calculated residual energies gradually decrease with increasing foil thickness. It should be noted here that the calculations are valid for energies > 0.2 MeV/u.

In Fig. 4.8, increasing tailing parameters for larger foil thicknesses are observed as expected. The contribution of the exponential tail, t_0, results in an increasing

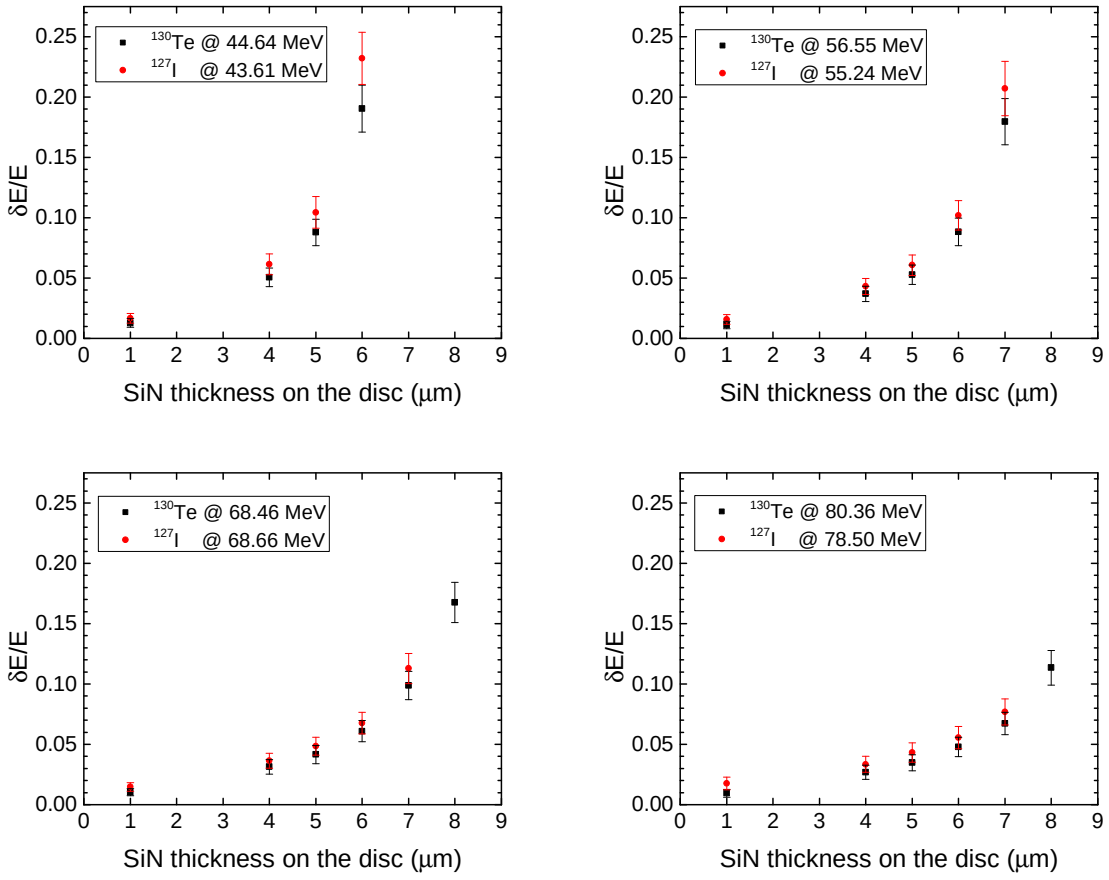

FIGURE 4.9: Relative energy resolution $\delta E/E$ versus the SiN foil thickness on the disc for both ^{130}Te (in black) and ^{127}I (in red) for four different energy settings – (top left)$\sim$ 44 MeV, (top right)$\sim$ 55 MeV, (bottom left)$\sim$ 68 MeV, (bottom right)$\sim$ 80 MeV. For the measurement with 8 foils, the 7 foil position on the disc was complemented with 1 foil position on manipulator MII [101].

asymmetry towards lower energy in the residual energy spectra. As can be seen in Fig. 4.8, this asymmetry is rather pronounced for smaller beam energy in particular towards larger foil thickness resulting in higher energy loss. This is attributed to the increasing contribution of nuclear energy loss, which contributes more in the region of higher energy loss (Fig. 2.11).

The relative energy resolution plots in Fig. 4.9 also show the expected increase in $\delta E/E$ with increasing foil thickness, due to increasing energy loss straggling. This effect is more pronounced for lower beam energy settings due to higher straggling resulting from nuclear contributions towards higher energy loss. It is observed that the relative energy resolution of ^{127}I (Z=53) for all energy settings is always slightly higher as compared to ^{130}Te (Z=52). This is attributed to the Z-dependence of the energy straggling and also to bigger beam spot of ^{127}I beams on CLTDs, see

discussion above.

An interesting observation was made from the measurements where the energy resolution for two different stacks of SiN foils with the same number of foils from the same production batch was compared. One stack was mounted on the disc at a distance of ∼5 mm from the CLTD array, and another stack was mounted on the manipulator MIII at a distance of ∼1 m from the CLTD array. Fig. 4.10 compares the FWHM for different energy settings in the two cases - 4 μm foils on the disc and manipulator MIII for both ion beams ^{130}Te and ^{127}I. It is observed that the FWHM for the SiN stack mounted on the disc closer to the CLTD array is always higher than for the stack mounted on the MIII relatively far from the detector array. The foil stack closer to the array results in bigger solid angle acceptance of the beam passing through the absorber foils, whereas, the foil stack on MIII at a distance of ∼1 m results in a significantly smaller solid angle acceptance compared to the foil stack on the disc. The fact that the nuclear energy loss has higher scattering angles and hence its contribution to the energy resolution can be reduced by the small solid angle acceptance of the detectors explains the difference we observe here.

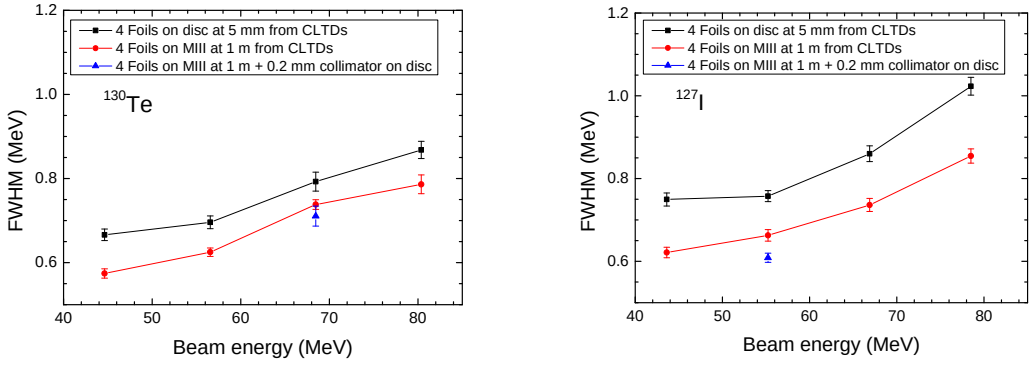

(A) (B)

FIGURE 4.10: Comparison of the FWHM for different energy settings for the three cases - 4 μm SiN foils on the disc (in black), 4 μm SiN foils on the manipulator MIII (in red), and 4 μm SiN foils on MIII + 0.2 mm collimator on the disc (in blue), for both ion beams (a) ^{130}Te and (b) ^{127}I. The data points are connected with lines to follow the trend [101].

It was hence realized with this test that the gain in detector efficiency and flexibility in the choice of the SiN thickness for the experiment with fission fragments comes

at the cost of a slight decrease in energy resolution. However the advantage from the better efficiency and the flexibility with the SiN thickness outweighs this small loss in resolution.

Fig. 4.10 also compares the measurement (in blue) with the stack of 4 μm thick SiN at the manipulator and a 0.2 mm collimator on the disc with the above mentioned measurements. It was observed that the resolution gets better by placing the collimator in front of the detector which further reduces the solid angle acceptance and also the beam spot on the CLTD (in blue). More investigations with the collimator are discussed in the Section 4.5.4.

4.5.3 Estimates on the quality of Z-resolution for fission yields

The quality of nuclear charge determination ($Z/\Delta Z$) (see Eq. 2.21) was estimated based on the measurements performed in this experiment for different foil thicknesses. This provides information on the optimum thickness of SiN foils for Z-yield measurements of fission fragments in the heavy mass region.

To determine $Z/\Delta Z$ using Eq. 2.21, the energy loss difference of ions with neighbouring Z but same mass is required. Due to the limitations of the accelerator facility on stable isotope beams which also fulfill the requirement to produce negative ions in the ion source, it was not possible to get ion beams with same mass and neighbouring Z simultaneously. Hence ion beams with neighbouring Z were chosen which had different masses. For a realistic estimate on $Z/\Delta Z$ using these beams, therefore, a correction for the contribution to the energy loss due to different masses must be performed.

The correction for this mass dependence was approached in two independent ways - 1) using SRIM calculations, and 2) using the semi-empirical calculations based on the Bohr-theory.

4.5.3.1 Using SRIM calculations

The energy loss difference measured with ^{130}Te and ^{127}I beams has contributions from both - the difference in nuclear charge (Z) and the mass (A). The velocity v dependence is already solved by choosing the same initial velocity for both the ions. In first approximation, we may separate the contributions in the measured energy loss, ΔE as follows:

$$\Delta E(Z, A) = \Delta E(Z) + E(A) \tag{4.6}$$

Hence, we could write the measured energy loss difference between ^{130}Te and ^{127}I as follows:

$$\Delta E(Z_I) - \Delta E(Z_{Te}) = \Delta E(Z_I, A_I) - \Delta E(Z_{Te}, A_{Te}) - \big(\Delta E(A_I) - \Delta E(A_{Te})\big) \tag{4.7}$$

To estimate the contribution due to the mass difference in energy loss, SRIM simulations were performed for all measured energies and the SiN foil thicknesses for ^{127}I, ^{130}I, ^{127}Te, and ^{130}Te ions. The mean of $(\Delta E(^{127}I) - \Delta E(^{130}I))$ and $E(^{127}Te) - \Delta E(^{130}Te))$ for each energy and foil thickness setting was subtracted from the measured energy loss difference $(\Delta E(Z_I, A_I) - \Delta E(Z_{Te}, A_{Te}))$. The Z-separation thus obtained was divided by the mean value of the measured FWHM for Te and I ions for the specific settings.

4.5.3.2 Using the Semi-empirical formula by Knyadzeva based on the Bohr-theory

Another approach to estimate the Z-separation was based on the semi-empirical formula developed by Knyadzeva based on the Bohr-theory [99, 100]. Readers are referred to the Diploma thesis of W. Lauterfeld [101] for the details on these calculations. The concept behind the calculations are summarized below.
The stopping power $(-dE/dx)$ of an ion with nuclear charge Z_1 with velocity v is

described as follows based on the classical Bohr-theory:

$$-\frac{dE}{dx} = \frac{4\pi Z_1^2 e^4}{m_e v^2} N Z_2 L \tag{4.8}$$

where N and Z_2 are the density and nuclear charge of the target atoms (SiN in this case). m_e and e are the mass and charge of the electron and L is the stopping number. The stopping number L_{Bohr} in classical Bohr-theory is determined as:

$$L_{Bohr} = ln\xi \quad \text{where} \quad \xi = \frac{1.1229\hbar m_e v^3}{Z_1 e^2 I} \tag{4.9}$$

where $I = I_0 Z_2$ is the mean excitation potential of the target and $I_0 \approx 10$ eV. With the variable parameter ξ, it is possible to define the difference between the experimental stopping number L and the Bohr stopping number L_{Bohr} as:

$$f(\xi) = L_{exp} - ln(\xi) \tag{4.10}$$

This can also be expressed as a power function of the form:

$$f(\xi) = \sum_{i=0}^{n} a_i ln^i(\xi) \tag{4.11}$$

The parameters a_i are determined by fitting measured values. The procedure is discussed in detail in the diploma thesis by W. Lauterfeld [101]. From this calculated stopping power, the energy loss is determined by integrating over the absorber thickness. The results for Z-separation and $Z/\Delta Z$ calculated with these methods on the basis of the measured energy loss values are plotted and discussed in the following text.

Fig. 4.11 shows predictions for the Z-separation versus the SiN foil thickness for different initial energies. Both the Z-separation estimated using SRIM and on the basis of semi-empirical calculations developed by Knyadzeva [99] based on the classical Bohr-theory are shown. The Z-separation estimated using the Knyadzeva method based on the classical Bohr-theory shows a pronounced maximum for higher beam energies which flattens for the lower beam energies. Also, for the lower beam energies, a steep increase which is unrealistic towards higher foil thickness

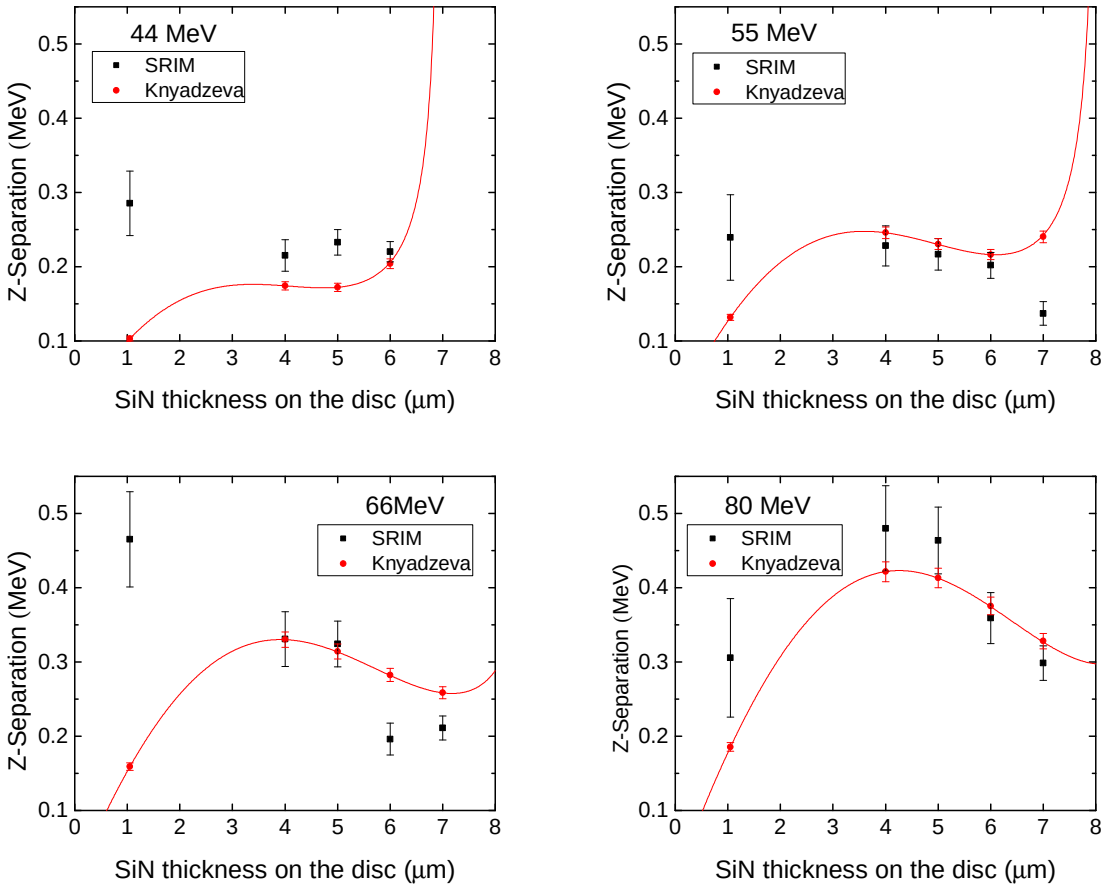

FIGURE 4.11: Predictions for the Z-separation versus the SiN foil thickness. The Z-separation estimated using SRIM is shown in black whereas the estimates on the basis of semi-empirical calculations developed by Knyadzeva [101] based on the classical Bohr-theory are shown in red. The predictions are plotted for four beam energies $\sim$ 44 MeV (top left), $\sim$ 55 MeV (top right), $\sim$ 68 MeV (bottom left), $\sim$ 80 MeV (bottom right) [101].

is observed due to the limitation of the calculations for E $<$ 0.2 MeV/u [99]. The estimates using SRIM are within error bars in most of the cases consistent with the calculations using the Knyadzeva method, except for differences in the case of a 1μm thick SiN. Such large Z-separations with 1 μm SiN are not realistic, and the possible explanation could be the systematic error accounted in energy calibration of these measurements. This is due to the fact that the thermal conditions of the CLTDs for the 1 foil position on the disc were different from those with the thicker foil stacks with a thickness $\geq$ 4 μm (see Table 4.1). This was taken care of in the calculations using Knyadzeva method by introducing a correction factor for the energy calibration [100, 101].

Fig. 4.12 shows the plots for the quality of Z-separation, $Z/\Delta Z$, versus the SiN

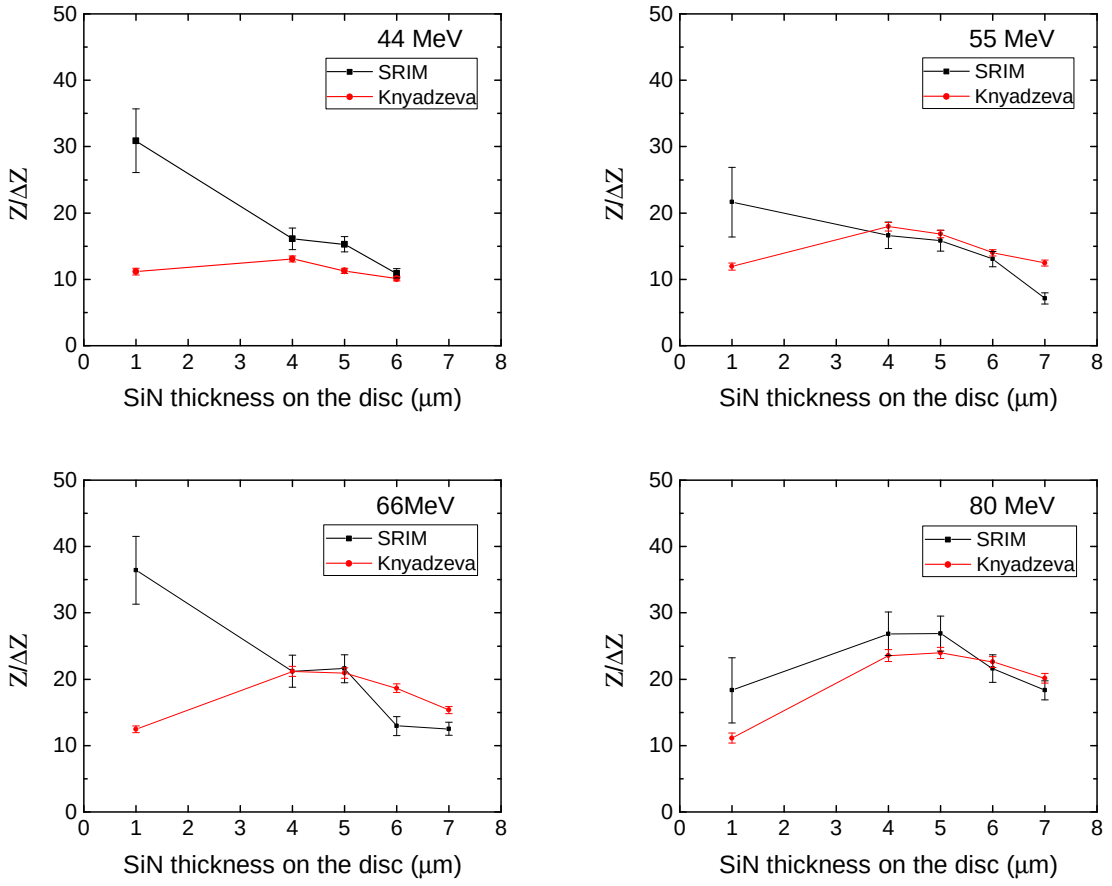

FIGURE 4.12: Quality of Z-determination, $Z/\Delta Z$, versus the SiN foil thickness. Estimates using SRIM are shown in black, whereas the estimates from semi-empirical calculations developed by Knyadzeva based on the classical Bohr-theory are shown in red. The predictions are plotted for the four beam energies $\sim$ 44 MeV (top left), $\sim$ 55 MeV (top right), $\sim$ 68 MeV (bottom left), $\sim$ 80 MeV (bottom right). The calculated data points are connected with lines to follow the trend [101].

foil thickness for different energies. The estimates from both SRIM and using the semi-empirical formula by Knyadzeva are shown. The calculations based on Knyadzeva's formula is curved with a maximum at around 5 μm which flattens towards lower beam energy. The estimates using SRIM are within error bars in most of the cases consistent with the calculations using the Knyadzeva-method, except for differences in the case of measurements with the 1μm thick SiN due to the difference in Z-separation discussed above. These estimates on the quality of nuclear charge separation $Z/\Delta Z$ indicate a possibility of fission fragment yield measurements also in the heavy mass region (more discussion in Section 6.1). As expected, $Z/\Delta Z$ increases with higher energies and we observe a reasonable

separation already with 5 μm of SiN foils.

4.5.4 Position dependence of the energy response

In previous experiments [4, 107] with pure beams, fluctuations were observed in the measured energy resolution beyond the statistical errors. It was surmised that these fluctuations occur due to inhomogeneous thermalization at different positions on the pixel. And hence the energy resolution of the recorded spectra would depend on the position on which the beam hits the detectors. The aim of the present investigations was to learn more about these effects by using focused ion beams by illuminating the pixels partly and at different positions on the pixels. This allows us to study the behaviour of the energy response of the detectors dependent on the position.

For these investigations, two approaches were used. In one attempt, a collimator (referred to a hole of different size− 0.2 mm (Fig. 4.4), 0.5 mm, 1 mm and 2 mm on the disc) was used to define the beam diameter and the energy spectra are recorded on a pixel by rotating the disc in small steps. In another attempt, a focused beam was steered through the pixel horizontally and vertically using an open position on the disc. It is important for such investigations to have as few variables as possible. The second case with the open position allows to have the same thermal conditions for the series of measurements by steering the beam, whereas. in the first case, due to the rotation of the disc, the thermal conditions of the CLTDs vary. On the other hand, the first case provides a small and well-defined beam diameter.

4.5.4.1 Investigations with the collimator

Measurements were performed with different collimators on the disc and the results for the relative energy resolution $\Delta E/E$ is shown in the Fig. 4.13. The best result was obtained for the collimator with a diameter of 0.2 mm . This collimator was hence chosen for further investigations as it was the smallest among the four

on the disc and it allowed a most detailed observation of the position dependence. In Fig. 4.13 we also observe that the results with open position (an aperture of 15 mm^2) was better compared to the results with the collimator with 2 mm diameter. This could be explained with high contributions due to slit scattering in the later case for a pixel with comparable dimensions (3×3 mm^2) like that of the collimator.

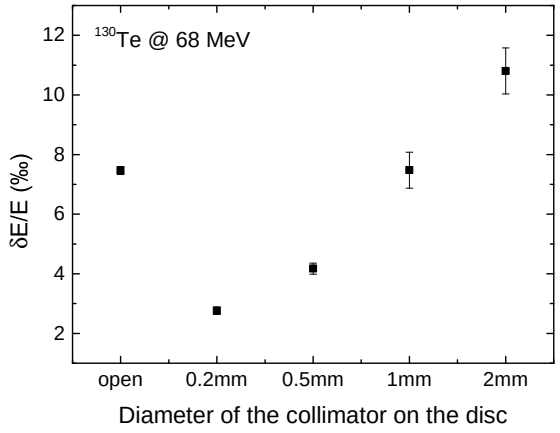

FIGURE 4.13: Relative energy resolution $\delta E/E$ versus the diameter of the collimator on the disc. These measurements were performed with a ^{130}Te beam at an energy of 68.46 MeV [101].

The 0.2 mm collimator was moved across pixel B1 in a circular arc (almost horizontal in approximation) from one end to the other. The energy spectra obtained for a ^{130}Te beam with E = 68.46 MeV were recorded after every $\sim 1^0$ rotation of the disc starting from one edge of the pixel B1. The rotation of 1^0 corresponds to ≈ 0.3 mm of horizontal displacement on the pixel.

Fig. 4.14 shows the peak position (4.14a) and the FWHM (4.14b) of the energy spectra. The first measurement at 0 on the distance scale corresponds to the left edge of the pixel. It can be seen that the measurements cover the entire width of the pixel of 3 mm. The variations in the peak position of the energy spectra and of the FWHM are observed beyond statistical errors also plotted in Fig. 4.14. This clearly indicates a position dependence of the energy response of the detector.

For a fully illuminated pixel, a FWHM of ≈ 0.5 MeV is expected (Fig. 4.6) whereas in the case with the collimator of 0.2 mm diameter, it is more than 40% smaller. It should be mentioned that also in case of Fig 4.6, the pixel might not have been

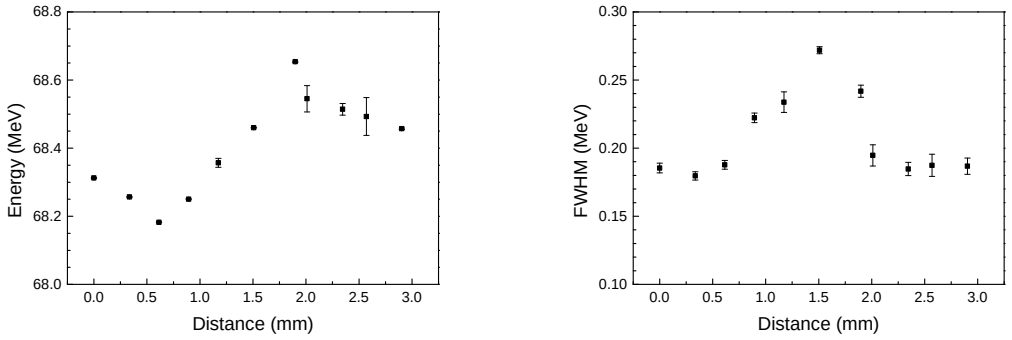

(A) (B)

FIGURE 4.14: Peak position (a) and FWHM (b) of the energy spectra obtained for a ^{130}Te beam with E = 68.46 MeV, through a collimator of 0.2mm, recorded on pixel B1, as a function of the position on which the beam hits the detector. The value zero on the distance scale corresponds to the left edge of the pixel [101].

fully illuminated but only partly. Although a clear dependence is seen, it is difficult to quantitatively decouple the effect due to the position dependence and the variation in thermal conditions due to the movement of the disc. As shown in Fig 4.4 the 0.2 mm collimator is sandwiched between the alpha source and the 1 SiN foil position on both sides. The thick copper backing of the alpha source provides a good thermal shielding as compared to the 1 foil position due to different heat absorption properties in the two cases. This is also seen in the different cold finger temperature settings (Table 4.1) for these two cases.

An attempt was made to explain the dependence in correlation with the detector design with respect to the position of the bond pads with Au bonding strongly coupled to the heat sink. As seen in Fig. 3.1a, the three bond pad connections on the left result in fast thermalization and hence a minimum in the measured energy, lower than the actual energy, is recorded, whereas towards the center of the pixel it increases and again drops towards the right end close to another bond pad. The fact that towards the right end it doesn't reach the minimum as in the left could be explained with the presence of only one bond wire connection in comparison to three on the left. However, this explanation was not confirmed with the other test performed with steering of the focused beam discussed below.

4.5.4.2 Investigations with steering of a focused beam

These investigations were carried out with a well focused ^{127}I beam with an energy of 55.24 MeV. Using magnetic steerers, the ion beam was moved across the pixel D1 horizontally and vertically. Although the beam profile is not defined quantitatively, from the intensity distribution on the array it can be conveniently assumed that in this case the beam illuminates a bigger region of the pixel as compared to the case when a 0.2 mm collimator was used.

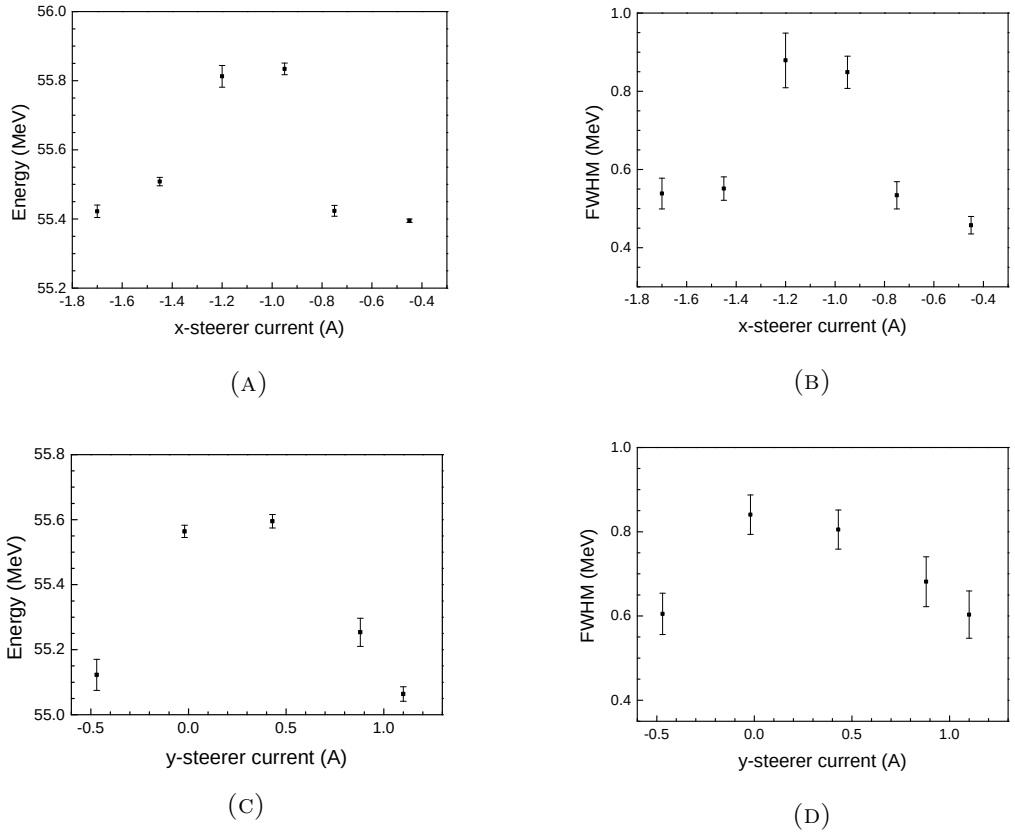

FIGURE 4.15: Peak position (a) for a horizontal scan in x-direction; (c) for a vertical scan in y-direction, and FWHM (b) for a horizontal scan; (d) for vertical scan of the energy spectra for a ^{127}I beam with an energy of 55.24 MeV, with a focused beam on pixel D1 as a function of the steerer current, indicative of the position on the detector. The first measurement on the left corresponds to the left edge of the pixel [101].

Fig. 4.15 shows the peak position and FWHM, both for the horizontal scan in x-direction and for the vertical scan in y-direction, with a focused beam on pixel D1 as a function of the steerer current, indicative of the position on the detector. The

first measurement on the left corresponds to the left edge of the pixel. Also here a clear dependence of the energy response on the position of the pixel is observed beyond statistical errors.

In Figs. 4.15a and 4.15c a comparison between the two highest peak positions at the central region of the pixel shows a slight difference of ~ 0.2 MeV. This would imply that the beam was not exactly centered for either measurement as one would expect the same value for the same illumination in the central region. Also differences are observed when the present observation is compared to the measurement with the collimator (Fig. 4.14a) in the progression from the left edge towards the right edge. The finding also disproves the explanation with the thermal coupling of the detector to the heat sink as discussed in the previous section. If that explanation was correct we would expect no change in the peak energy in the y-direction which is not the case. However, in the present case, Fig. 4.15a and 4.15c, with a similar pattern of increasing amplitude towards the central region, suggest a correlation with the location of thermometer on the pixel.

The FWHM also rises in both horizontal and vertical cases towards the central region. This tendency is comparable to the measurement with the collimator (Fig. 4.14b) where the FWHM attains highest values in the central region as well, and lower values towards the edges. However, the FWHM values in the case where the beam is steered through the open position, is substantially higher compared to the measurement with the collimator. The bigger beam profile compared to the collimated beam could be a reason for this increase in the FWHM. The Table 4.4 below shows the maximum and minimum relative energy resolution (FWHM/Energy) for the horizontal and vertical cases.

	Relative energy resolution (FWHM/Energy)	
	Minimum (%)	Maximum (%)
Horizontal	0.826 ± 0.040	1.52 ± 0.074
Vertical	1.095 ± 0.102	1.448 ± 0.084

TABLE 4.4: Maximum and minimum relative energy resolution for the beam scan through the pixel in horizontal and vertical direction.

The two investigations with collimator and focused beam demonstrate the position dependence of the energy response of the present detector pixels. This may explain the measured fluctuations in the measured energy resolution beyond the statistical errors in the previous experiments [[107], [4]]. In the cases where a pixel is partially illuminated, a fluctuation of $\approx 0.5\%$ in the relative energy resolution is observed (Table 4.4). This also may explain the differences in energy resolution for the different energies measured in this experiment with open position due to partial illumination of the pixel. This difference is reduced for measurements through SiN foils (especially for a thickness ≥ 4 μm) due to small angle scattering resulting in fully illuminated pixels. However, the explanation with relation to the detector design either in terms of thermal coupling of the thermometer location is not consistent with the two tests discussed above leaving scope for further investigations in this regard.

A couple of possibilities to implement corrections in energy resolution on the basis of these studies were investigated. A more involved process would be a redesign of the CLTDs with smaller pixel size as we observed better resolution with partially illuminated detectors, and maybe a new design for thermal coupling to avoid inhomogeneous thermalization. Another attempt could be a correction of measured data using pulse shape analysis with the assumption that the pulse shape is position dependent. Timescales required for these implications didn't allow for corrections in the present work, but nevertheless the present investigations gave us useful information on the behaviour for future modifications.

Chapter 5

Isotopic yield measurements of fission fragments at the ILL

This chapter discusses the experiment performed for determination of fission fragment isotopic yields from thermal neutron induced fission reactions using the novel technology of the calorimetric low temperature detectors with the passive absorber method. A detailed motivation for this experiment was presented in Chapter 1. The experimental set-up for this experiment is discussed in Section 5.1. The list of measurements performed for the isotopic yield determination with different fissile targets are presented in Section 5.3. Section 5.4 presents a detailed discussion on the procedure of the data analysis applied for the isotopic yield determination in this work. Finally, Section 5.5 discusses the various sources of errors contributing to the measured isotopic yield distributions.

5.1 Experimental set-up

The experiment for the determination of the nuclear charge yields of the fission fragments was performed at the LOHENGRIN separator [19, 20, 61] at the ILL reactor at Grenoble, operational details of which were discussed in Section 2.2. Fig. 5.1 shows the schematics of the experimental set-up, and Fig. 5.2 shows a

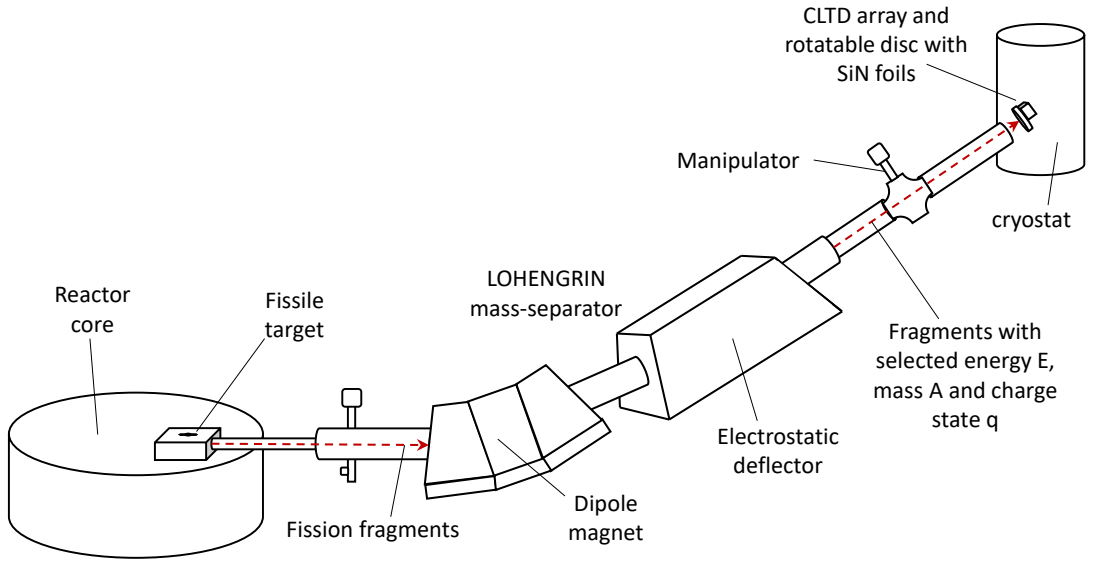

FIGURE 5.1: Schematic of the experimental set-up at the ILL reactor for Z-yield measurements (for details see text).

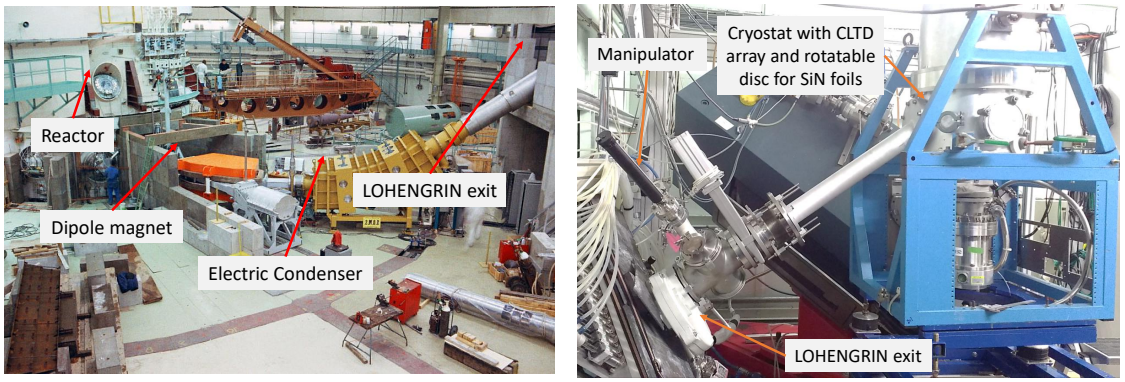

(A) (B)

FIGURE 5.2: (a) Picture of the LOHENGRIN separator at the ILL reactor, (b) Picture of the cryostat with the CLTD array connected to the exit flange of the LOHENGRIN mass separator at the ILL reactor.

picture of the LOHENGRIN and the cryostat installed at the beam line. A fissile target (Section 2.2) is placed inside the heavy water moderator of the reactor at about 50 cm from the core with high thermal neutron flux where the fissile target undergoes thermal neutron induced fission reactions. Recoiling fission fragments leave the target with a small energy loss in the target as highly charged ions (typically with ionic charge state of 16 to 30). At 8 metres from the target, the ionized fragments enter the LOHENGRIN spectrometer and pass through the LOHENGRIN magnetic and electric field where fragments with a specific A, E

and q are separated at the exit flange of the LOHENGRIN. See Section 2.2 for details on the operation of the LOHENGRIN spectrometer.

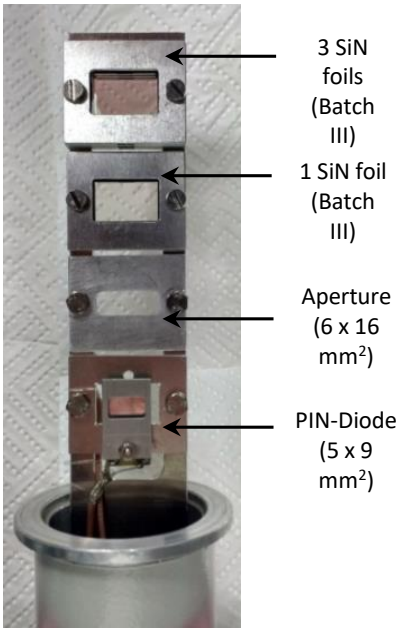

(A)

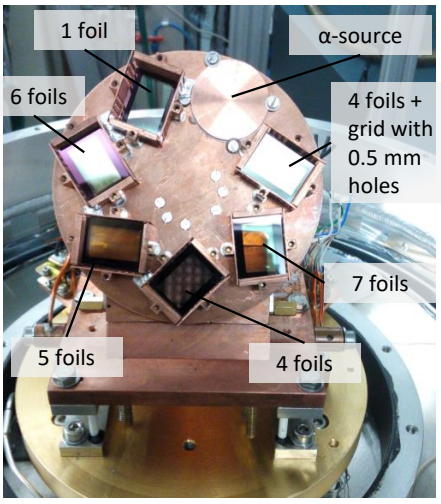

(B)

FIGURE 5.3: (a) Picture of the manipulator with different foil stacks, the aperture of size 6 × 16 mm^2 and the PIN diode, installed on the beam line at the LOHENGRIN exit (see Fig. 5.1), (b) Picture of the rotatable disc with different SiN foil stacks and the $\alpha-$source mounted in front of the CLTD array inside the cryostat.

At the LOHENGRIN exit, an aperture with lead backing of the size 10 *times* 20 mm^2 was fixed for the Z-yield measurements. A manipulator is placed in front of the LOHENGRIN exit slit (see Fig. 5.2b and 5.3a) with different SiN absorber foil stacks, an aperture and a PIN diode. The complementary detector, PIN diode, installed at the LOHENGRIN exit flange on the manipulator is used to monitor the fragment beam without any absorber foil. Along with determining the mass, kinetic energy and ionic charge distributions of the fission fragments, it also allows to align the beam. In the previous test experiments [4, 29], the PIN diode was used to determine the mass yields of the fission fragments. The cryostat housing the CLTD array is connected to the beam line after the manipulator. As discussed in Section 3.3, the helium bath cryostat used in this work comprises of LN_2 shield and the L^4He shield. The apertures installed on the LN_2 and the L^4He shield are of the size 11 × 17 mm^2, and 13 × 19 mm^2, respectively. Inside the cryostat, the

CLTD array and a rotatable disc with several SiN absorber foil stacks and the $\alpha-$source are installed.

Fig. 5.3a shows a picture of the mountings on the manipulator installed at the exit flange of the LOHENGRIN on the beam line. At the four positions of the manipulator, the 3 μm thick SiN foil stack, the 1 μm SiN foil, the aperture with a dimension of 6×16 mm^2 and the PIN diode with the 5×9 mm^2 aperture in front were mounted. Fig. 5.3b shows a picture of the rotatable disc as it was used at ILL with several SiN foil stacks and the $\alpha-$source installed in front of the CLTD array inside the cryostat. On the disc, SiN foils with five different thicknesses of 1 μm, 4 μm, 5 μm, 6 μm, 7 μm were mounted. In addition there was a 4 μm thick foil stack with a grid containing 0.5 mm holes. This was installed following the results on the position dependence of the CLTD energy response in Section 4.5.4 to further improve the energy resolution of the CLTDs for measurements with the 4 μm thick SiN foils. Also, the alpha source to monitor the performance of the CLTD array was mounted on the disc. Section 3.6 in Chapter 3 discusses the details of the redesign of the detector system in order to gain detector efficiency and flexibility in the choice of absorber foil thickness in order to optimize the Z-yield measurements.

5.2 Fissile targets

As discussed in Section 2.2, the size of the target affects the mass and energy resolution of the LOHENGRIN spectrometer. Smaller target size provides better resolution (on the cost of efficiency), where the length of the target determines the energy resolution, and the breadth determines the mass resolution. The targets usually used at LOHENGRIN range from a few mm^2 to a maximum of $\sim 7.2 \times 1$ cm^2. Since the Z-resolution when using the passive absorber method is sensitive to the energy resolution of the LOHENGRIN spectrometer, smaller targets are preferred for the Z-yield measurements. However, very small targets decay very fast and constrain the measurement time. The relatively small targets with diaphragm

sizes of the order 4×0.5 cm^2 used in this work was a good compromise with respect to the target life/intensity and the energy resolution of the LOHENGRIN spectrometer. With these thin fissile targets, the mass resolution of the LOHENGRIN was of the order $A/\Delta A \approx 1000$, and the resolution in measuring the kinetic energy is $< 1\%$. Different diaphragm sizes were used in the test experiment [4] to see the effect of the target size on the Z-resolution. A difference of around 10% was observed in the energy resolution for targets with diaphragm sizes varying from 2×0.5 cm^2 to 4×0.7 cm^2 showing a non-negligible contribution of the beam energy distribution to the total energy resolution of the system.

For the Z-yield measurements in this work, three fissile targets of highly enriched ^{235}U(99%), ^{239}Pu(99.98%) and ^{241}Pu(98.9%) were used. Targets with a high isotopic purity are used at the LOHENGRIN spectrometer to measure the individual fission fragment yields. In order to attain the high purity, radiochemical separation is not sufficient in many cases, and the target atoms have to pass a mass separator before use, thus making the target preparation an elaborate and expensive procedure. Details on the manufacturing of these fissile targets are discussed in Section 2.2. The highly enriched ^{235}U(99%) target is 128 μg cm^{-2} thick, mounted on a 4×0.6 cm^2 titanium backing with a 100 nm tungsten cover foil on the top. The titanium diaphragm in front of the target has a size of 4×0.4 cm^2. The ^{241}Pu(98.9%) target is 24 μg cm^{-2} thick, mounted on a 7×0.5 cm^2 titanium backing with a 0.25 μm Ni cover foil on the top. The ^{239}Pu(99.98%) target is 38 μg cm^{-2} thick, mounted on a 4×0.3 cm^2 titanium backing with a 0.25 μm Ni cover foil on the top. The titanium diaphragm in front of the two plutonium targets is of the dimension 4×0.5 cm^2. The ^{235}U and the ^{239}Pu target can be considered as "pure" since $\gg 99.9\%$ of the fission rate stems from the isotope of interest . For the ^{241}Pu target the remaining fraction is composed of non-fissile ^{240,242}Pu and 7.7% ^{241}Am produced by β^- decay of ^{241}Pu since the Pu/Am separation before the target preparation. Due to its small fission cross-section ^{241}Am(n,f) contributes only 0.03% to the total fission rate, but $\approx 1.1\%$ of the fission rate are due to double neutron capture reactions ^{241}Am(n,γ)^{242g}Am(n,f) and ^{241}Am(n,γ)^{242m}Am(n,f)respectively. The reaction of interest ^{241}Pu(n,f) represents

therefore 98.9% of the total fission rate. Table 5.1 describes the characteristics of the three targets.

Target	Composition	Total mass	Cover foil	Ti Diaphragm
U-235	$> 99\%$ ^{235}U	307 μg	$\sim$ 100 nm tungsten foil	4×0.4 cm^2
Pu-241	$> 98.9\%$ ^{241}Pu	117 μg	0.25 μm Ni foil	4×0.5 cm^2
Pu-239	$> 99.98\%$ ^{239}Pu	46 μg	0.25 μm Ni foil	4×0.5 cm^2

TABLE 5.1: Characteristics of the fissile targets used for the Z-yield measurements at ILL.

5.3 List of measurements

The variables for measurements in this experiment for the determination of the isotopic yields of fission fragments are the fragment mass, energy and ionic charge state, defined by setting the LOHENGRIN spectrometer, and the SiN foil thickness. For the isotopic yield determination of a particular nuclide, several measurements at different fragment masses, energies and ionic charge states, set using the LOHENGRIN spectrometer, need to be measured with a specific SiN foil thickness. The results of these measurements are normalized and integrated (See Section 5.4.10 for details) to obtain the isotopic yield of the nuclide of interest. For normalization, measurements were performed with the PIN diodes to determine the energy and ionic charge state distributions of respective fragment masses of interest without any SiN degrader foil. The process of normalization and integration of these different measurements is discussed in detail in the Section 5.4.10.
Also a point to note is that the fragment energies listed in this section are the energies set using the LOHENGRIN spectrometer which are different from the energies of the fragments released at the time of fission due to energy losses in the targets. For example, in the case of the Pu-targets, fragment energies set using LOHENGRIN are of the order of 6 MeV less than the fragment energies produced at fission due to the energy loss of the fragments while passing through the target

and the 0.25 μm thick Ni cover foil on the targets. The knowledge of the fragment energy released at the time of fission without losses in the targets is important for comparisons and correlations with the literature values as these are independent of the target characteristics. Section 5.4.3 discusses the energy loss calculation in the targets for the determination of the fragment energies released at the time of fission.

The first set of measurements was performed with the ^{235}U target in order to test and to optimize the Z-resolution for isotopic yield measurements and to cross-check the results with already existing results on parts of the masses. Masses A = 89 and A = 96 were measured with different SiN foil thicknesses to understand the dependence of the Z-resolution on the SiN foil thickness. Mass 89 was measured at a LOHENGRIN energy setting of 94 MeV, and for two different ionic charge states 19 and 25 for six different SiN foil thickness settings. The six different SiN foil settings for mass 89 are 1 μm, 4 μm, 5 μm, 6 μm and 7 μm thick SiN using foil stacks on the disc installed inside the cryostat and for a total of 8 μm SiN thickness, using the 7 μm thick SiN foil stack on the disc in addition with the 1 μm thick SiN foil on the manipulator installed at the exit of the LOHENGRIN (Fig. 5.3). Mass A = 96 was measured at a LOHENGRIN energy of E = 94 MeV and an ionic charge state Q = 18 for four different SiN foil settings - 4 μm, 5 μm, 6 μm and 7 μm thick SiN foil stacks on the disc installed inside the cryostat.

5.3.1 Measurements for ^{92}Rb and ^{96}Y yield determination

As discussed in Chapter 1, due to the big interest in anti-neutrino anomaly studies, precise yield of ^{92}Rb are determined in this work for all three targets - ^{235}U(n_{th}, f), ^{239}Pu(n_{th}, f) and ^{241}Pu(n_{th}, f) and the ^{96}Y yield is determined for ^{235}U(n_{th}, f) and ^{241}Pu(n_{th}, f). For these results a detailed set of measurements were performed for fragment masses A = 92 and A = 96 at various energy and ionic charge state settings of the LOHENGRIN spectrometer. The results for ^{235}U(n_{th}, f), being most important for the anti-neutrino anomaly studies, are measured with highest precision. All these measurements are performed with a 4 μm thick SiN foil stack

on the disc installed inside the cryostat.

In the case of the ^{235}U(n_{th}, f), measurements of mass A = 92 were performed at five different LOHENGRIN energy settings - 80 MeV, 88 MeV, 94 MeV, 100 MeV and 106 MeV. Different ionic charge states were measured at these energy settings. All the ionic charge states from 16 to 26 were measured at 94 MeV which is the mean energy of the energy distribution for mass A = 92 produced in the fission reaction ^{235}U(n_{th}, f) [1]. For all the other energies two ionic charge states 20 and 25 were measured for mass 92. For mass A = 96, measurements were performed at six different energies - 74 MeV, 80 MeV, 88 MeV, 94 MeV, 100 MeV, 102 MeV and 106 MeV. All the ionic charge states from 16 to 26 were measured at three energy settings - 84 MeV. 94 MeV and 102 MeV. For all other energies, two ionic charge states 18 and 21 were measured for mass A = 96.

In the case of ^{241}Pu(n_{th}, f), mass A = 92 was measured at four different energies - 86 MeV, 94 MeV, 100 MeV and 106 MeV. The ionic charge state 21 was measured for all these energies and at 94 MeV the ionic charge state 25 was measured as well. Measurements for mass A = 96 were performed at 86 MeV, 94 MeV and 100 MeV at an ionic charge state setting of 21. At 94 MeV the ionic charge state 18 was measured as well.

In the case of ^{239}Pu(n_{th}, f), mass A = 92 was measured at 94 MeV, 100 MeV and 106 MeV. At 100 MeV the ionic charge states 17, 20, 21, 24 and 25 were measured, and for all other energies the ionic charge state 21 was measured.

5.3.2 Measurements in the symmetry region

For the Z-yield determination of masses near the symmetry, a series of measurements were performed for masses from the light fragment region towards the symmetry region for ^{241}Pu(n_{th}, f) and ^{239}Pu(n_{th}, f). All measurements were performed with a 4 μm thick SiN foil stack on the disc installed inside the cryostat.

For ^{241}Pu(n_{th}, f), twenty-four masses from A = 89 to A = 112 were measured for different energy and ionic charge state settings. For masses A = 89, 91, 93, 94,

[1] As discussed earlier 94 MeV is the energy after losses in the target and the cover foil.

95, 97, 98, 99, 100, 101 and 102, measurements were performed at two different energy settings - 94 MeV and 100 MeV and one ionic charge state. Masses, A = 90, 92, 96, 103, 104, 105, 106, 107, 108, 109, 110, 111, 112 were measured at three different energies - 86 MeV, 94 MeV and 100 MeV. Masses A = 90, 92, 96, 104, 109, 111, 112 were measured at two different ionic charge states and Masses A =103, 105, 106, 107, 108, 110 were measured at three different ionic charge states. For ^{239}Pu(n$_{th}$, f), five masses towards the symmetry region were measured from A = 109 to A = 113 at different energies and ionic charge states. Masses A = 109 and A = 110 were measured at five different energies - 80 MeV, 84 MeV, 90 MeV, 94 MeV and 98 MeV at two different ionic charge states of 20 and 24. Mass A = 111 was measured at three energies 84 MeV, 90 MeV and 94 MeV at two different ionic charge states 20 and 24. Mass A = 112 was measured at two energies 80 MeV and 90 MeV with an ionic charge state 20. Mass A = 113 was measured at 86 MeV and with an ionic charge state 21.

5.3.3 Measurements in the heavy mass region

For ^{239}Pu(n$_{th}$, f), measurements to determine the isotopic yields in the heavy mass region of the fission fragments were performed with the 4 μm thick SiN foil stack mounted on the disc inside the cryostat. Eleven masses from A = 128 to A = 137 and A = 139 were measured at different energies. All the eleven masses from A = 128 to A = 137 and A = 139 were measured at 80 MeV and masses from A = 128 to A = 133 were measured also at 88 MeV for one ionic charge state each. In addition A = 133 and A = 139 were measured at 72 MeV.

5.4 Data analysis for the isotopic yield determination

In this Section the different steps of the data analysis for the isotopic yield determination of the fission fragments from thermal neutron induced fission reactions

are presented. The calibration and acceptance of the LOHENGRIN spectrometer are discussed in Section 5.4.1. Section 5.4.2 discusses the calculation for the target burn-up which is followed by calculations for the energy loss of fission fragments in the target (actinide material and the Nickel foil covering), in order to determine the kinetic energy of the fragments produced in fission, in Section 5.4.3. The next Sections 5.4.4 - 5.4.8 present the data analysis of the CLTD measurements which includes the energy calibration, the effect of residual gas condensation on the CLTDs, the choice of fitting functions, the Z-identification technique and the procedure for summing the results from individual pixels of the CLTD array. Section 5.4.9 discusses the systematic observations demonstrating the dependence of Z-yields on the position of the pixels on the CLTD array. Finally, Section 5.4.10 discusses the integration of Z-yields for different kinetic energies and ionic charges to determine the cumulative and the independent Z-yields.

5.4.1 Calibration and acceptance of the LOHENGRIN spectrometer

5.4.1.1 Magnetic Calibration

The values for the magnetic and electric field settings of the LOHENGRIN are calculated and set to measure a particular fragment nuclide of interest. The magnetic field settings of the LOHENGRIN spectrometer are controlled with a NMR probe. Because the NMR probe measures the field locally, whereas the fragments are deflected according to the integrated field along their flight path, hysteresis and remanence effects may change the calibration of the magnet. The optimum magnetic field settings are determined by scanning the beam horizontally over the detector placed in the focus, while keeping the electrical field fixed.
The so determined 'magnet constant', called χ, stayed constant within $< 0.05\%$ of its value for each target during the measurement period of about 2 weeks for ^{235}U(n_{th}, f), and about 1 week for both ^{239}Pu(n_{th}, f) and ^{241}Pu(n_{th}, f). The

measurements to determine the magnet constant, χ, are performed with the LOHENGRIN settings of mass A = 100, Q = 20 and E = 100 MeV with integer A/q = 5. These measurements are recorded with the PIN diodes for a fast online analysis. Measurements with the CLTDs are performed with the energy loss in the SiN foils and need summing up of all the pixels. For measurements with the CLTDs, very fine tuning of the magnet constant, χ, within $< 0.01\%$ of its value was performed to focus the fragment beam on the central pixel of the CLTD array. This was especially useful for the measurements close to the symmetry mass region with very low fission fragment intensities.

5.4.1.2 Energy Acceptance

The relation between the kinetic energy of the fragments measured by LOHENGRIN E_{LOH} and the LOHENGRIN energy acceptance ΔE_{LOH} which is, for small deviations ($\Delta E_{LOH} << E_{LOH}$), given by the linear equation: $\frac{\Delta E_{LOH}}{E_{LOH}} = \frac{\Delta x}{D_E}$ where D_E is the dispersion coefficient. For a given target the dispersion Δx does not change and so the ratio $\Delta x / D_E$ is constant. The accepted energy range is therefore proportional to the chosen energy. To correct for this effect, all count rates are divided by the energy set at the LOHENGRIN spectrometer for normalization.

5.4.2 Target burn-up

When placed in a high neutron flux, the fission rate of the target decreases with time due to the loss of target material. This loss of target material is primarily due to the nuclear burn-up since the amount of fissile nuclides in the target is reduced by neutron capture followed by fission or gamma emission. Other reasons for the loss of target material are sputtering by fission fragments, evaporation from the heated target, and diffusion and sputtering into the target backing. The slight reduction of the neutron flux (about 3 % during one reactor cycle of 50 days) can be neglected for the present investigations. Due to these effects, a target may lose more than 80% of its original material in one week of measurement. To account

for the target burn-up, the decrease in fission rate is monitored regularly(once or twice per day) by measuring a reference mass. The target burn-up curve thus obtained can in the ideal case be described with an exponential decay curve.

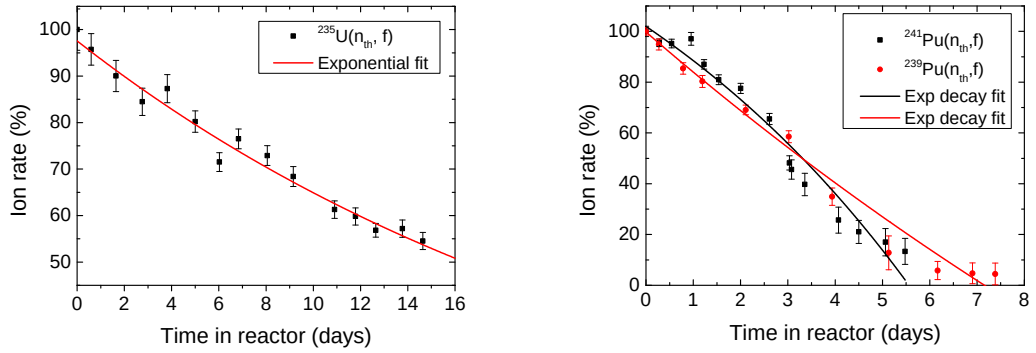

(A) (B)

FIGURE 5.4: Target burn-up curve for a) Uranium target and b) Plutonium targets.

To determine the burn-up, the reference mass A = 90 was chosen for the ^{235}U target, and mass A = 95 was chosen for the two plutonium targets. Energy scans (E-scans) at the mean ionic charge and ionic charge scans (Q scans) at the mean kinetic energy for the specified masses are performed regularly with the PIN diode (once or twice a day). The ion rate is then calculated by dividing the area under each energy scan by the percentage of fragments with the mean ionic charge in the Q-scan. This ion rate is normalized to 100 at the time of the first measurement after the target was placed inside the reactor. Fig. 5.4 shows the burn-up curves for ^{235}U(n_{th}, f), ^{239}Pu(n_{th}, f) and ^{241}Pu(n_{th}, f).

The Uranium target shows a regular smooth burn-up with a loss of less than 50 percent of the target material in 15 measurement days. It should be noted that the two plutonium targets show a less regular and very fast burn-up with a loss of more than 90 percent of the target material in less than a week of measurement time. This might be due to a rapid migration into the target backing or sideways out of the target area (see also [Fri98a]). The former explanation is supported by a broadening of the "natural" width of the energy distribution after 3 measurement days in both the plutonium targets. Also a jump of about 6 MeV in the mean of the "natural" energy distribution after 6-7 measurement days was observed in case

of the plutonium targets. This suggests that the Nickel cover foil might have been destroyed as the energy jump of 6 MeV corresponds to the loss of the fragment energy in the Nickel foil (see Section 5.4.3). These effects are difficult to quantify, but contribute to the systematic errors. Figures B.1, B.2 and B.3 in Appendix B show the plots for the mean energy distributions and the mean ionic charge distributions of mass A = 90 (for ^{235}U), and mass A = 95 (for ^{239}Pu and ^{241}Pu from all the burn up measurements. For the plutonium targets we observe that the mean energy does not evolve smoothly over time like it does for the uranium target. Hence, in case of the plutonium targets, to determine the yields, corrections were applied to the LOHENGRIN energy settings with respect to the change in the mean energy distribution. Polynomial fits to the mean energy distributions as shown in Fig. B.2 and B.3 are used to normalize the effective energy of all the other measurements.

5.4.3 Energy loss in the target

Post fission when the fragments enter the LOHENGRIN spectrometer, part of their original kinetic energy is lost in the target and the cover foil. To deduce the original kinetic energy of the fission fragments from the energy set by the LOHENGRIN spectrometer, the energy loss in the target and in the cover foil has to be taken into account. This energy loss is calculated for all measured isotopes and kinetic energies with the SRIM software (TRIM program) [79]. For the calculations, we suppose that the ions cross on average half of the target thickness and the entire thickness of the cover foil.
For example, Table 5.2 shows the calculated energy loss in the target and the cover foil for the three different targets used in this work for A = 92 (^{92}Rb at 94 MeV). $\Delta E_{CoverFoil}$ corresponds to the energy loss in the cover foil, and ΔE_{Total} corresponds to the energy loss in both - the target and the cover foil, respectively.

In general, the total energy loss for the Uranium target is of the order of 5 MeV with 55 % in the target and 45 % in the tungsten cover foil. In the case of the

Target	Thickness μg cm^{-2}	Dimension cm^2	Cover foil	Δ E$_{\text{cover foil}}$ MeV	Δ E$_{\text{total}}$ MeV
U-235	128	4 × 0.6	$\sim$ 100 nm tungsten foil	2.7 ± 0.5	4.9 ± 0.9
Pu-241	24	7 × 0.5	0.25 μm Ni foil	6.1 ± 1.2	6.3 ± 1.3
Pu-239	38	4 × 0.3	0.25 μm Ni foil	6.1 ± 1.2	6.7 ± 1.3

TABLE 5.2: Calculated energy loss of the kinetic energy of the fission fragments with mass A = 92 (^{92}Rb at 94 MeV) for the three different targets used for the Z-yield measurements. The calculations are performed with SRIM. $\Delta E_{CoverFoil}$ corresponds to the energy loss in the cover foil and ΔE_{Total} corresponds to the energy loss in both - the target and the cover foil.

plutonium targets, the total energy loss is of the order of 7 MeV for ^{239}Pu(n$_{th}$, f) and 6.5 MeV for ^{241}Pu(n$_{th}$, f). Here, the energy loss of the fission fragments in the Nickel foil cover is more than 90 percent of the total energy loss for ^{239}Pu, and more than 95 percent for ^{241}Pu. The uncertainty in the energy loss was dominated by the variation in the thickness of the cover foil to be of the order of approximately 20%.

5.4.4 Energy calibration of the CLTDs

The energy calibration of the CLTDs is performed using the measurements with the alpha source (see Section 3.7.1 and also Table. 3.2). A calibration using LOHENGRIN energy settings with fission fragments was not possible since there was no measurement without SiN foils. A linear calibration using the three line alpha source with no offset is performed (see Fig. 3.11b). The energy calibration thus achieved is precise within 0.5 %. This uncertainty in the calibration is attributed to the first order linear approximation of the calibration slope, and also to the different thermal conditions of the CLTDs during the measurement of calibration spectra with alphas and the measurement of fission fragments through the SiN foils. This is because the alpha source and the SiN foils in front of the CLTD array provide different thermal shielding. Quantifying these shielding effects is not possible due to the complexity of the set-up, and hence cannot be corrected for in the calibration.

For the Z-yield measurements itself, the absolute energy calibration is not necessary as we are interested in the precise area under the energy spectra for yield calculations rather than the precise peak energy. The analysis for precise yield determination can be achieved with the relative energy calibration. The relative energy calibration is performed with respect to the central pixel (Pixel C2) for all the other pixels. In this case, the peak of interest is identified in each pixel and the peak energy is adjusted to the peak energy of the central pixel C2. For the purpose of summing up the spectra from different pixels this proves to be a very precise method as compared to the calibration with the alpha source. Also, the Z-identification technique applied in this work (discussed later in Section 5.4.7) does not require an absolute energy calibration. However, for the discussion, an estimate on the energy is useful, and the energy calibration with the alpha source provides sufficient precision for this purpose. Fig. B.4 in Appendix B shows the calibration slope for the different CLTD pixels using the energy spectra obtained from the alpha measurements.

5.4.5 Effect of residual gas condensation on the CLTDs

Although an absolute energy calibration is not very important, but the energy stability during the measurement is very important for the Z-separation. A gradual decrease with time in the signal amplitudes of the detectors for equal energy inputs has been observed in the previous experiments with CLTDs installed in the windowless helium bath cryosat [107], [23]. This effect is attributed to the slow increase in the thermal capacity of the detectors due to condensation of vacuum residual gases from the beam line on the cold CLTDs.

Since inside the cryostat the CLTD array is almost completely surrounded by cold surfaces (N2 / He shields and the shield extensions, see Fig. 3.5), which themselves act as effective cryopumps, the residual gas condensation is caused mainly due to particles coming from warm surfaces through the opening of the cryostat directly in front of the CLTDs. An effective approach to reduce this effect is therefore the use of the shield extensions with the smallest possible apertures and the best

possible vacuum conditions in the vacuum directly in front of the cryostat. In contrast to the earlier experiments [107], [23], in the present work, the disc installed in front of the CLTD array with SiN foils (Fig. 5.3b) provided further shielding to the warm opening of the cryostat and provided therefore a major improvement.

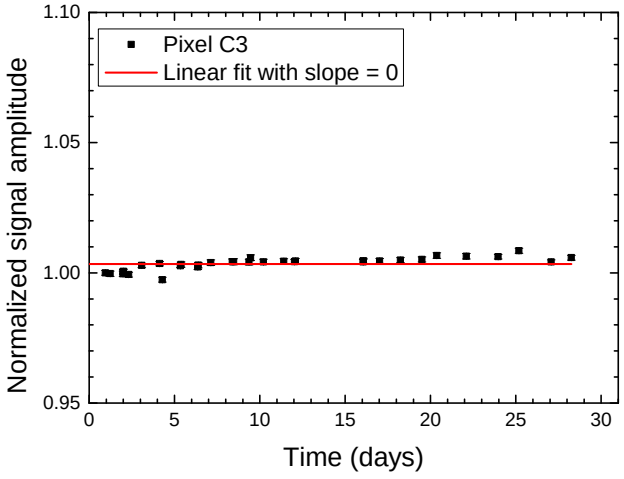

FIGURE 5.5: Signal amplitude from the alpha source for the central CLTD pixel C3, over the entire measurement period at the ILL reactor.

For long term measurements, this effect can be corrected by observing the temporal drift of monoenergetic lines in the CLTD pulse height spectra. For this purpose, the pulse height spectra generated by the alpha source mounted on the disc in front of the CLTD array are regularly investigated during the measurement. In Fig. 5.5 the signal amplitudes from the alpha source over the entire measurement period at the ILL reactor are plotted. A linear fit with zero slope performed on the data is shown by the red line in Fig. 5.5. No drop in the signal amplitude is observed due to residual gas condensation on the CLTDs in the present work unlike the previous measurements. This is due to the fact that during the measurements, the CLTD array is never exposed to the beam directly. The shielding from the disc and the SiN foils overcomes the effect due to condensation of residual gases on the detectors.

5.4.6 Fitting Function

The energy loss distributions for mono-energetic beams are expected to be in the ideal case Gaussian or modified Gaussian in form, depending on the thickness of the absorber foil (see Section 2.4[2]). The mono-energetic fragment beam delivered from the LOHENGRIN spectrometer comprises of nuclides with the same mass but several nuclear charges (see Section 2.2). Due to the Z-dependence of energy loss in the absorber foil (see Fig. 2.10), the initial mono-energetic beam with a Gaussian distribution from the LOHENGRIN spectrometer after passing through the SiN foils results in a sum of Gaussian or modified Gaussian distributions. The residual energy spectra from measurements at the ILL reactor are therefore fitted with a sum of Gaussian or a sum of modified Gaussian distributions. As already discussed in Chapter 4, for heavy masses (with $Z > 50$), a modified Gaussian distribution with an exponential tail on the low energy side (see Eq. 4.1 and also Section 4.4.1) is used to fit the residual energy spectra. The exponential tail on the left arises due to an increasing contribution from nuclear energy loss for heavy masses with smaller energies.

For the measurements in the light and symmetry mass region, $89 \leq A \geq 113$ with nuclear charges in the range $34 \leq Z \geq 45$, no significant tailing due to nuclear energy loss was observed. This was also verified by fitting both - a sum of Gaussian distributions and a sum modified Gaussian distributions to the spectra measured in the light mass region, e.g. for $A = 96$. For the fit with modified Gaussian distributions the tailing parameter was very small with values $t_0 \leq 70$, and had no measurable contribution to the proper determination of Z-yields as can be seen in Fig. 5.6b. Therefore sum of Gaussian functions are used to fit the residual energy spectra in the light and symmetry mass region. The number of Gaussian functions used to fit varies depending on the mass under investigation.

From the existing fission yield data, we know that one mass spectrum may have contributions from up to 8 different nuclear charges. However, the intensity of fragments drop very quickly as they move away from the mean nuclear charge for that specific mass. Already for two nuclear charges away from the mean, the

[2] in the subsection "energy straggling"

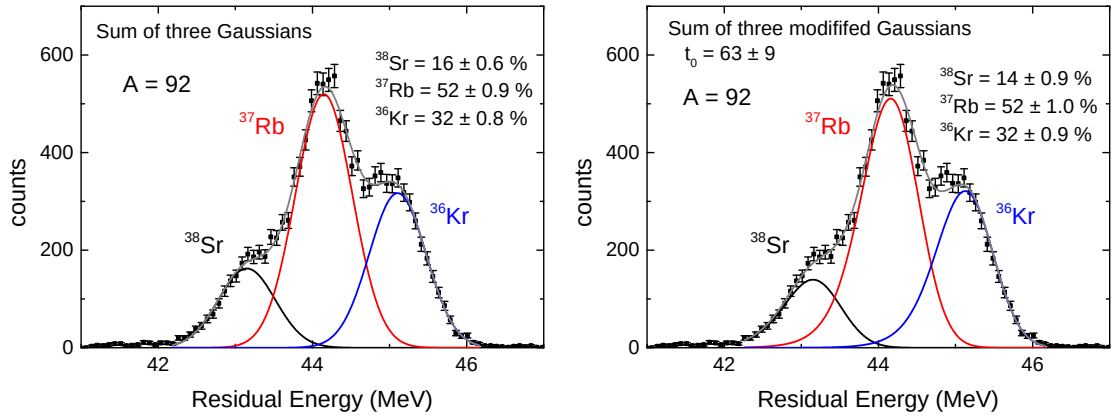

(A) (B)

FIGURE 5.6: Comparison of the fractional Z-yields determined from fits with a) sum of three Gaussians and b) sum of three modified Gaussians. The spectra correspond to mass A = 92 for ^{235}U(n$_t h$, f) measured at the LOHENGRIN energy setting of 94 MeV with 4 μm thick SiN foils on the disc. No measurable contribution on the fractional Z-yields are observed due to the relatively small tailing parameter for this case.

intensity drops typically by about a factor 100 or more (up to 10^5). Such low intensities have no significant contribution to the spectra which are in most cases dominated by either one or two nuclear charges. In general three to four Gaussian functions are sufficient for the description of one mass spectrum recorded with the CLTDs. But fitting three to four Gaussians to one spectrum with partially overlapping peaks is often challenging due to the problem of over-parameterization of the fit function. This is overcome by constraining some fit parameters. Fits are therefore performed under the assumption that in a single mass spectrum, the widths of the individual Z-peaks are same, as well as the energy separation between two neighbouring Z-peaks are equal in the same spectrum. These constraints significantly reduce the number of free parameters. A "no constraint" fit with a sum of three/four Gaussians would have nine/twelve free parameters, whereas with the above mentioned constraints on width and separation, the number of free parameters reduces to six/seven. This significantly improves the fit results in terms of error in the fit parameters and reproducibility. Equation 5.1 shows the form of the sum of Gaussian functions used to fit the residual energy spectra of

fragment masses in the light and symmetry mass region.

$$
\begin{aligned}
f(x) = & \frac{A_0}{w\sqrt{\pi/4ln(2)}} \exp -4ln(2)\left(\frac{x-(x_c-d)}{w}\right)^2 + \\
& \frac{A_1}{w\sqrt{\pi/4ln(2)}} \exp -4ln(2)\left(\frac{x-x_c}{w}\right)^2 + \\
& \frac{A_2}{w\sqrt{\pi/4ln(2)}} \exp -4ln(2)\left(\frac{x-(x_c+d)}{w}\right)^2 \\
& \frac{A_3}{w\sqrt{\pi/4ln(2)}} \exp -4ln(2)\left(\frac{x-(x_c+2d)}{w}\right)^2 + ...
\end{aligned}
\tag{5.1}
$$

where:

$A_0, A_1, A_2, .. =$ area under the peak 1, peak 2, peak 3, ..

$w =$ full width at half maximum, FWHM

$x_c =$ peak position of the second peak from the low energy side of the residual energy spectra (central peak in case of fits with a sum of three Gaussians)

$d =$ energy separation between two neighbouring Z-peaks

For the heavy masses in the range $128 \leq A \geq 139$ with nuclear charges ≥ 50, based on the results of the MLL test experiment (see Chapter 4) on the shape of residual energy spectra for heavy masses, fits were performed with a sum of modified Gaussian distributions with an exponential tail on the low energy side. Similar to the light and symmetry mass region, constrained fits are performed for the heavy masses to reduce the number of free parameters for the fit. Along with the assumption that in a single mass spectrum the widths of the individual Z-peaks are same, and the energy separations between two neighbouring Z-peaks are equal, it is also assumed that the tailing factor remains same for each peak in the same spectrum. A fit with a sum of three modified Gaussians was in general sufficient to describe the residual energy spectra of a heavy mass. The above mentioned constraints reduce the number of free parameters to seven for a sum of three modified Gaussians, which otherwise with a “no constraint version” would

have twelve in number. This significantly improves the fit results in terms of error in the fit parameters and reproducibility. Equation 5.2 shows the form of the sum of Gaussian functions used to fit the residual energy spectra of fragment masses in the heavy mass region:

$$\begin{aligned} f(x) =& \frac{A_0}{t_0} \exp\left(\frac{x-(x_c-d)}{t_0} + \frac{\sigma^2}{2t_0^2}\right) erfc\left(\frac{1}{\sqrt{2}}\left(\frac{x-(x_c-d)}{\sigma} + \frac{\sigma}{t_0}\right)\right) + \\ & \frac{A_1}{t_0} \exp\left(\frac{x-x_c}{t_0} + \frac{\sigma^2}{2t_0^2}\right) erfc\left(\frac{1}{\sqrt{2}}\left(\frac{x-x_c}{\sigma} + \frac{\sigma}{t_0}\right)\right) + \\ & \frac{A_2}{t_0} \exp\left(\frac{x-(x_c+d)}{t_0} + \frac{\sigma^2}{2t_0^2}\right) erfc\left(\frac{1}{\sqrt{2}}\left(\frac{x-(x_c+d)}{\sigma} + \frac{\sigma}{t_0}\right)\right) + ... \end{aligned} \tag{5.2}$$

where:

$A_0, A_1, A_2, ..$ =area under the peak 1, peak 2, peak 3, ..

x_c =peak position of the second peak from the low energy side of the residual energy spectra (central peak in case of fits with a sum of three Gaussians)

d =energy separation between two neighbouring Z-peaks

t_0 =tailing parameter of the exponential component

σ =standard deviation of the Gaussian distribution

For the modified Gaussian distribution, the $FWHM$ is determined by the coefficient C_r which depends on both- the width of the Gaussian distribution and the tailing factor t_0 (see Section 4.4.1 and also Table. 4.3).

Fig. 5.7a shows an example for a residual energy spectrum for mass = 108 with four nuclear charges, fitted with a sum of Gaussians, and Fig. 5.7b shows an example for a residual energy spectrum for mass = 130 with three nuclear charges fitted with a sum of modified Gaussians. The fragments with higher nuclear charge number are towards the low-energy (left) side in the residual energy spectrum, while the elements with higher nuclear charge number are on the right side. This is expected due to the Z-dependent energy loss (see Section 2.4). For the determination of the independent and cumulative Z-yields, the relative Z-yields are obtained first from the residual energy spectra of the CLTDs. Relative Z-yields are determined

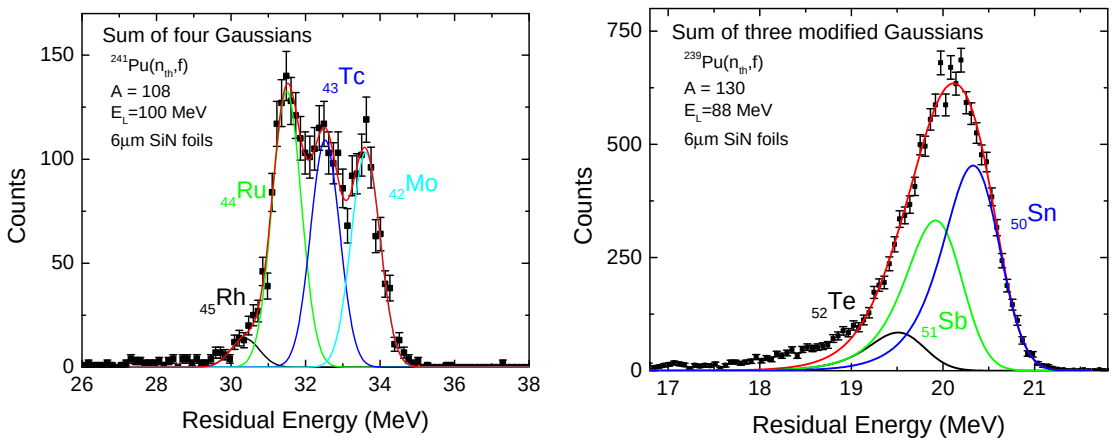

(A) (B)

FIGURE 5.7: a) An example for a residual energy spectrum for mass = 108 with four nuclear charges fitted with a sum of Gaussians and b) an example for a residual energy spectrum for mass = 130 fitted with a sum of three modified Gaussians

by the percentage of the area under an individual Z-peak to the total area of the spectra for a given mass. Therefore it is important to make very precise fits with small error bars on the parameters, especially the area parameter, in order to be able to determine the Z-yields precisely.

5.4.7 Nuclear charge identification

One of the crucial steps in the analysis for Z-yield determination is the identification of the nuclear charge in the residual energy spectrum. Therefore for the identification of the nuclear charges in this work, a systematic approach is used which is illustrated by the plot shown in the Fig. 5.8. There the peak position of the second Z-peak from the low-energy (left) side of the residual energy spectra is shown, for each mass in the range $89 \leq A \geq 112$ measured at a LOHENGRIN energy setting of 100 MeV with a 4 μm thick SiN foil stack on the disc in front of the detectors. The measurements displayed in Fig. 5.8 are performed with the ^{241}Pu(n$_{th}$, f) target. The measured residual energy spectra for each mass are fitted with four Gaussian peaks. When the peak position of the second peak from left side of the residual energy spectra is plotted against mass, due to the mass and nuclear charge dependence of the energy loss of ions in matter, a step like

structure is observed as shown in the Fig. 5.8 where each red line corresponds to a unique nuclear charge Z. The second peak was chosen as it is usually the central peak with good intensity making it a good choice for the systematic studies. From the previous measurements at the LOHENGRIN spectrometer, for selected masses like A = 89, A = 92 and A = 96, the highest nuclear charge contributions are quite well known which provides a basis for the identification of other nuclear charges on the series of masses measured at the LOHENGRIN spectrometer. For example, the Z = 39 marked red in Fig. 5.8 was identified based on the known Z-yield distributions for mass A = 96 [7]. In Fig. 5.8 nuclear charges are identified by orderly counting the red lines such that the nuclear charge Z increases by one for every red line towards the lower peak position value and higher masses while, the nuclear charge Z decreases by one for every red line towards higher peak position value and smaller masses. This method for Z-identification was then cross-checked for other well know yields for A = 89.

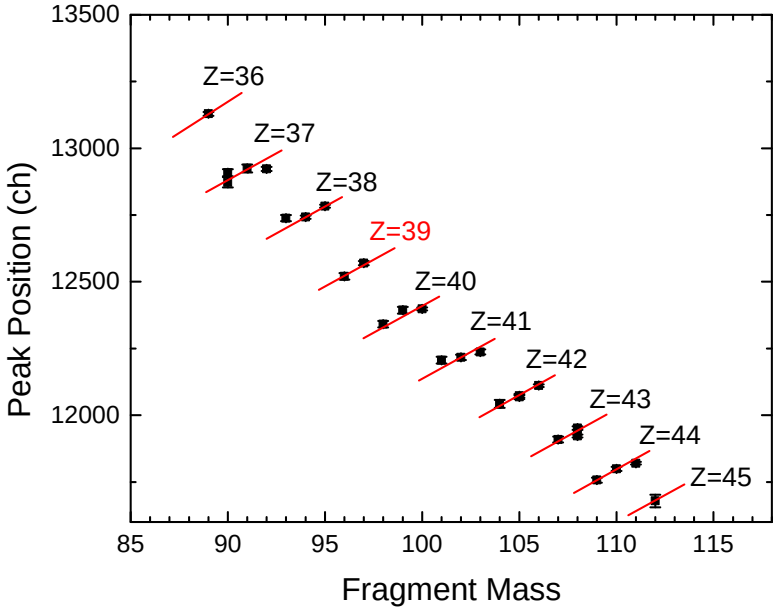

FIGURE 5.8: Z-identification plot. The peak position of the second Z-peak from the low-energy (left) side of the residual energy spectra, for each mass in the range 89 ≤ A ≥ 112 for ^{241}Pu(n$_{th}$, f) measured at a LOHENGRIN energy setting of 100 MeV with a 4 μm thick SiN foil stack on the disc in front of the detectors, is plotted versus mass. Each red line corresponds to a unique nuclear charge Z.

Fig. 5.8 is in addition a clear representation of the different scale of energy loss dependence on a) the ion mass and b) the nuclear charge. A weaker dependence

of energy loss on ion mass as compared to the dependence on the nuclear charge is observed as expected. The data points on the red line correspond to the fragments with same nuclear charge but different mass number, and on average, the energy separation between the neighbouring masses with same nuclear charge is of the order 40 channels corresponding to about 150 keV, whereas the energy separation between fragments of neighbouring nuclear charges but same mass is of the order 200 channels corresponding to about 750 keV. These values were also confirmed with the calculations for energy loss using the Knyazheva method discussed in Section 4.5.3. However, moving further towards heavier masses, these separations flatten making is rather challenging to identify the nuclear charges. The Z-identification in the special case of heavier masses is discussed later in the Section 6.4.

It should be noted here that it is due to the good energy linearity that the CLTDs offer, which makes it possible that such a Z-identification procedure works. Unlike the conventional detectors, where these structures in energy loss cannot be observed due to the pulse height defect in the detectors, CLTDs offer an energy detection independent of the ion mass, and therefore allow to exploit the nature of energy loss for the Z-identification.

5.4.8 Contamination from neighbouring masses

Each detector pixel of the CLTD array records the residual energy spectra individually for every measurement. These individual spectra are summed together in order to deduce the final results. In general, for summing up the spectra from different pixels, first an energy calibration is performed for each pixel and the calibrated spectra are summed together to analyze the residual energy peaks with good statistics. In this work the relative energy calibration with respect to the central pixel C2 (also discussed under the topic of Energy Calibration in this Section) is performed before summing up the spectra. On these summed spectra Gaussian fits are performed to deduce the fractional Z-yields. The fragment beam from LOHENGRIN is focused on a specific mass, however neighbouring masses may

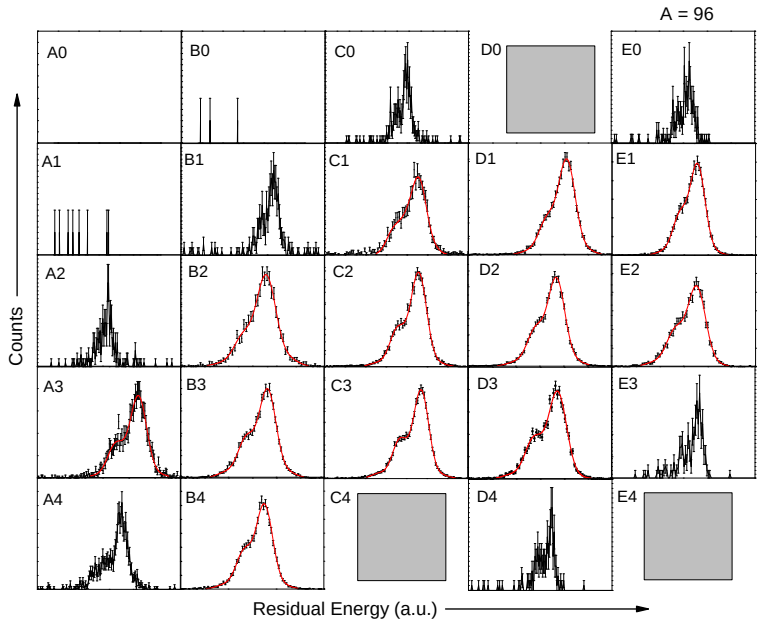

(A)

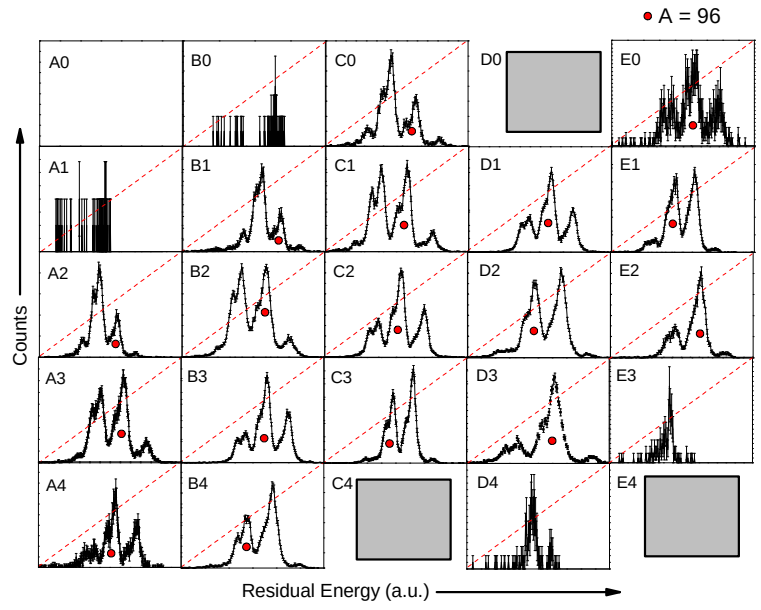

(B)

FIGURE 5.9: Examples for a clean (Fig. 5.9a) and contaminated (Fig. 5.9b) mass measurement at the LOHENGRIN for mass A = 96 at an energy of E = 94 MeV for the two ionic charge states Q = 18 (clean) and Q = 19 (contaminated), respectively, and for all pixels marked with A0,..E4. Red dots mark the contribution of mass A = 96. The red dotted lines correspond to the diagonals with similar contamination distribution.

also be present, depending on the selected charge states, as we move away from the focal point. So as we move away from the central pixel on which the beam is focused, the intensity of contaminating masses increases in some cases and the intensity of the mass of interest decreases. Although these contaminating masses are well separated in the energy spectra at the LOHENGRIN exit, after they pass through the SiN foils, they might overlap with the mass distribution which is to be measured.

Fig. 5.9 shows examples for a clean (Fig. 5.9a) and contaminated (Fig. 5.9b) mass measurement at the LOHENGRIN for mass A = 96 at an energy of E = 94 MeV for the two ionic charge states Q = 18 (clean) and Q = 19 (contaminated), respectively. In Fig. 5.9b, one can also see that the contaminating masses in the spectra along the diagonals, shown by red dotted lines, have the same distribution whereas if the spectra on different diagonals are compared, we see a change in the contributions from the different contaminating masses. This is due to the mass and energy dispersion properties of the LOHENGRIN spectrometer where fragment separation is based on their A/q and E/q ratios (see Fig. 5.10b). This allows also other masses to contribute which satisfy the set values of A/q and E/q for the measurement. To avoid adding contaminating mass distributions from all the pixels to one spectrum, instead of summing up the spectra, fits were performed on the individual spectra from each pixel, and the areas under each Z-peak determined from the fits were summed to deduce the final relative Z-yields. This procedure was applied for all the measurements where sufficient statistics (more than 500 counts/pixel) to perform good Gaussian fits were available on individual pixels.

5.4.9 Dependence of Z-yields on the pixel position

During the analysis of the measurements with mass A = 92 for each pixel, it was discovered that there is a slight dependence on the pixel position for the relative Z-yield distribution determined from the residual energy spectra of individual pixels. Fig. 5.10a shows as an example the individual spectra recorded by different pixels

on the CLTD array for the measurement of mass A = 92 at the LOHENGRIN energy setting E = 94 MeV and an ionic charge state Q =20 for ^{235}U(n$_{th}$, f). The red curves correspond to the fit with a sum of three Gaussians to the data for all pixels with reasonable statistics. Three pixels C4, D0 and E4 shown in grey boxes, were not working. Fig. 5.10b shows the schematics of the CLTD array with labels for different pixels and their orientation with respect to the SiN stacks on the disc. The directions of mass and energy dispersion from the LOHENGRIN spectrometer is also shown. Fig.5.10c shows the relative Z-yields of the three nuclear charges, Z1, Z2, Z3, corresponding to the sum of three Gaussians fits in Fig. 5.10a from different pixels. The lines passing through the data correspond to the mean value obtained by a linear fit with slope = 0. From the spectra in Fig. 5.10a one can see that the shape of the spectra varies for different pixels. Also the relative Z-yields, plotted in Fig. 5.10c for different pixels, clearly indicate that the variations in the relative Z-yields is beyond statistical fluctuations especially for the nuclear charges Z1 and Z3. This observation was made for many cases.

Several investigations were carried out for the explanation of this variation in the relative Z-yields for different pixels e.g., bias in the fit due to statistics, binning, contamination from neighbouring masses, nuclear charge dependence in the small angle scattering in the SiN absorbers, etc, but they couldn't explain such a large effect on the Z-yields observed in Fig. 5.10. Looking closely at the spectra in Fig. 5.10a indicates that the distributions vary more when compared along the diagonal from the top-left to the bottom-right of the CLTD array, whereas the distributions for pixels along the diagonals from top-right to bottom left do not change. This patterns resembles to the energy and mass dispersion direction of the LOHENGRIN transmission shown in Fig. 5.10b. The LOHENGRIN spectrometer has mass and energy dispersion perpendicular to each other and along 45^0 from the vertical axis. So, the mass dispersion is along the diagonal from top-left to the bottom-right of the CLTD array and the energy dispersion is along the top-right to bottom left (see Fig. 5.10b). The resemblance of variation in the relative Z-yields to the direction of the mass dispersion of the LOHENGRIN spectrometer further motivated the investigation of the effect due to transmission of LOHENGRIN. To

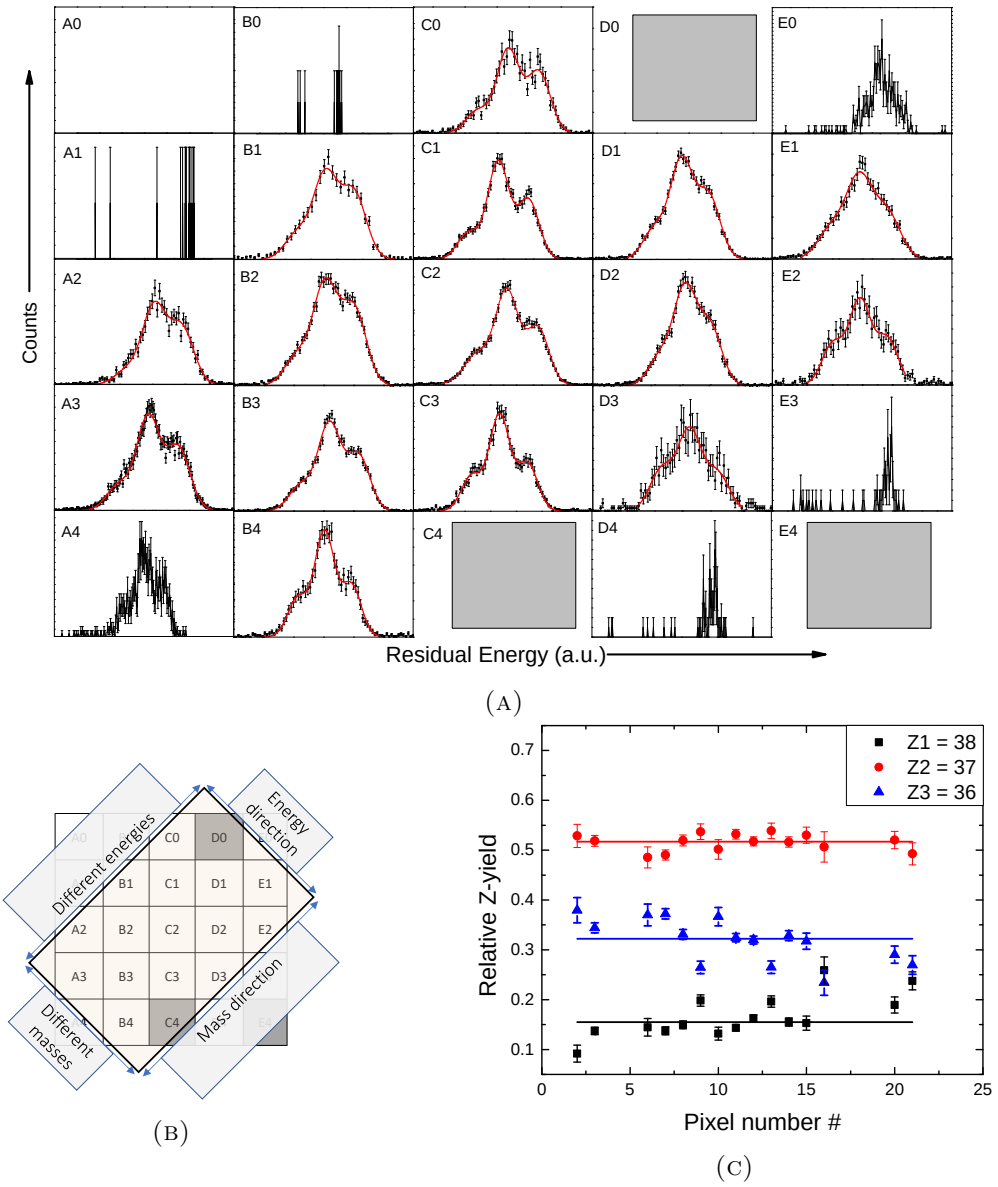

FIGURE 5.10: a) The individual spectra recorded by different pixels of the CLTD array for the measurement of mass A = 92 at the LOHENGRIN energy setting E = 94 MeV and an ionic charge state Q =20 for ^{235}U(n$_{th}$, f). The red curves correspond to the fit with a sum of three Gaussians to the data for all pixels with reasonable statistics. Three pixels C4, D0 and E4 shown in grey boxes, were not working. b) The schematics of the CLTD array with labels for different pixels and their orientation with respect to the SiN stacks on the disc. The directions of mass and energy dispersion from the LOHENGRIN spectrometer are also shown. c) Relative Z-yields of the three nuclear charges Z1, Z2, Z3 corresponding to the sum of three Gaussians fits in Fig. 5.10a from different pixels. The lines passing through the data correspond to the mean value obtained by a linear fit with slope = 0.

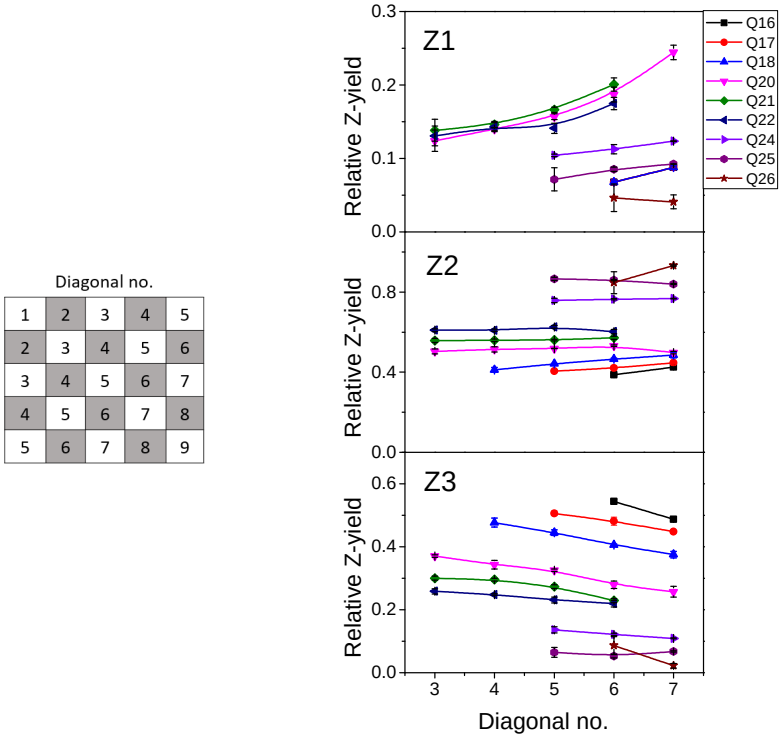

FIGURE 5.11: The figure on the left shows the pixels along diagonals represented by a number, over which the relative Z-yields are averaged, and on the right, the mean relative Z-yield over each diagonal is plotted against the diagonal number as indicated in the figure on the left. The data in different color correspond to the measurements performed with different ionic charge states, from Q = 16 to 25 for the mass A = 92 and the LOHENGRIN energy setting E = 94 MeV with a 4 μm thick SiN foil on the disc.

quantify and better visualize this pattern, the relative Z-yields were averaged over diagonals in the direction from top-right to bottom left, which is the direction of energy dispersion of LOHENGRIN, and hence a fixed mass is expected along these lines. Fig. 5.11 on the left shows the pixels along diagonals represented by a number, over which the relative Z-yields are averaged, and on the right, the mean relative Z-yield over each diagonal is plotted against the diagonal number as indicated in the figure on the left. The data in different color correspond to the measurements performed with different ionic charge states, from Q = 16 to 25 for the mass A = 92 and the LOHENGRIN energy setting E = 94 MeV with a 4 μm thick SiN foil on the disc.

In order to explain the observed effect the following investigations were made: The LOHENGRIN spectrometer has a high mass dispersion of 324 cm [20], and since isobars have slightly different mass, they will be spread accordingly. For example,

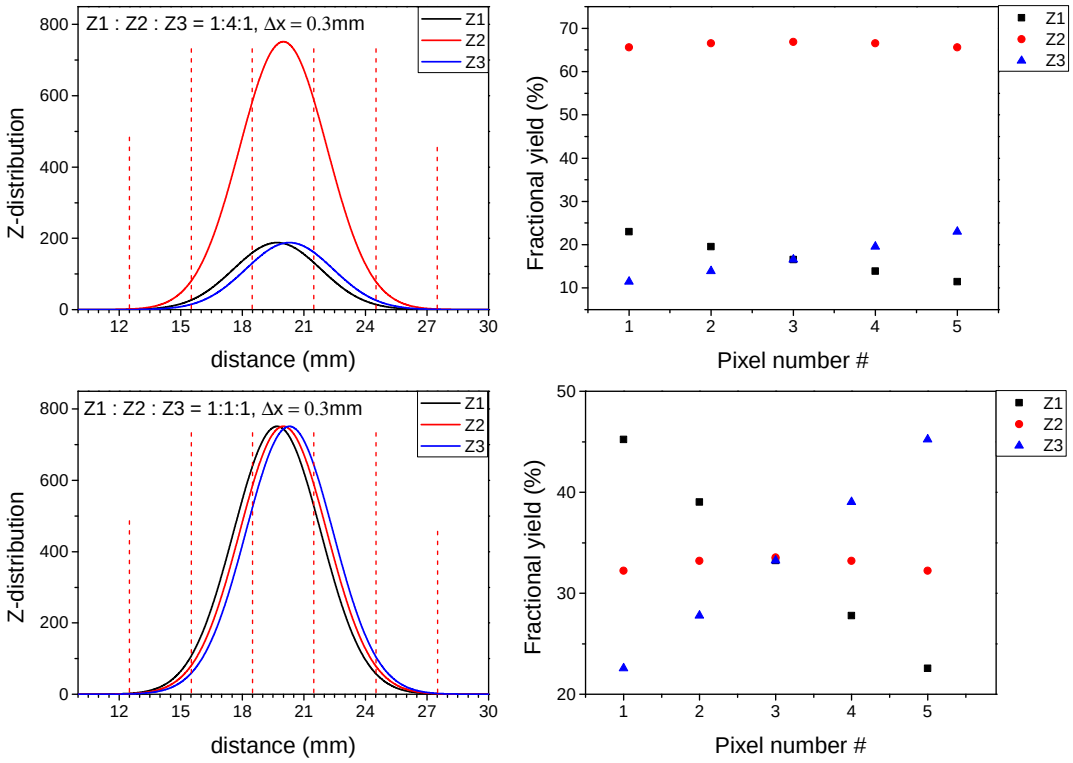

FIGURE 5.12: Simulation for Z-yields (right) with two sets of Gaussian distributions (left) to explain the position dependence. Relative Z-yields from a set of three Gaussian distributions spatially separated by 0.3 mm, corresponding to the dispersion of neighbouring Z contributions within a mass A at the LOHENGRIN spectrometer, are evaluated for equally spaced sections of 3 mm corresponding to a CLTD pixel dimension.

^{92}Rb (Z = 37) has a Q-value of 8.1 MeV/c^2 for the beta decay to ^{92}Sr, which means ^{92}Rb is $\frac{8.1}{92\times u} = \frac{8.1}{(92\times 931.5)} = 9.45 \times 10^{-5}$ times heavier than ^{92}Sr. This mass difference will result in a spatial separation of 324 cm $\times$ $(9.45\times10^{-5}) = 0.3$ mm in the focal plane. This spatial separation can cause a change of Z-yields as function of position if one looks precisely. Simulations were performed to quantify the effect of this spatial separation on the residual energy distributions. We assume that the fragment beam with a selected mass and energy at LOHENGRIN is a Gaussian distribution. Also an estimate on the spatial distribution of these Gaussians was determined by the knowledge of the area illuminated on the CLTD array with these beams. When the fragment beam is focused on the central pixel, usually a significant drop in intensity is observed towards the pixels on the sides, and sometimes already for neighbouring pixels. Therefore it is assumed for the

simulation that the Gaussian distribution of a selected mass, for example A = 92 at the LOHENGRIN has a spatial distribution of around the size of the CLTD array of about $\tilde{1}5$ mm. It is further assumed that the Gaussian distribution of the mass consists of a sum of three Gaussian distribution separated by 0.3 mm corresponding to the three isobars ^{92}Sr, ^{92}Rb, ^{92}Kr present in the mass. For the simulation two sets of such Gaussian distributions are considered as shown in the plots on the left of Fig. 5.12), one with the intensity ratios of Z1 : Z2 : Z3 = 1 : 4 : 1 and the other with the intensity rations of Z1 : Z2 : Z3 = 1 : 1 : 1. The area under the three Z-peaks are determined individually for five sections of 3 mm distance corresponding to a single pixel dimension (shown in Fig. 5.12 on the left are plots by the red dotted lines at 3 mm separation). The relative Z-yields thus determined are plotted for the five sections of 3 mm represented by the pixel number in Fig. 5.12 on the right side. It is found that there is a significant effect of a small 0.3 mm separation of isobars within the mass distribution at LOHENGRIN on the relative Z-yields determined by individual pixels. In Fig. 5.12, a large effect of up to 25% change in the relative Z-yields due to this effect can be seen which explains the differences we observe in the measurements of mass A = 92 discussed above. It should be mentioned that the very high mass dispersion of 324 cm at the LOHENGRIN is only achieved with very tiny targets produced by evaporating uranium onto a thin wire. However, for our experiment, a relatively large target (4×0.6 cm^2) is used which decreases the mass dispersion, and hence we observe a milder version of this effect for our measurements (see Fig. 5.10c). Also we observe that the relative change in the yield of the Z-peaks on the sides (Z_1 and Z_3) is, compared to the central Z-peak (Z_2), quite large, similar to the present measurements with mass A = 92. Such an effect of position dependence on the Z-yields was observed for the first time at the LOHENGRIN spectrometer with the pixelated CLTD array allowing position sensitivity in the isotopic yield measurements. This position dependence however would not influence the results with CLTD measurements as it is averaged out if the distributions over all the pixels are summed together with the knowledge of the beam distributions over the array. Careful investigations were thus made to identify the beam distributions

over the array and summing up all the pixels with reasonable intensity in the peak of interest.

5.4.10 Integration over ionic charge states and kinetic energies

The determination of isotopic yields for a nuclide is basically counting the number of all the particular nuclides produced during fission. However, the LOHENGRIN spectrometer does not allow to directly measure the complete contribution of a nuclide since it selects masses with a given ionic charge and kinetic energy. Therefore the yield determination requires an integration over ionic charge and energy. During the fission process, fragments with a mass A or a nuclear charge Z are produced with a kinetic energy distribution. These ions then leave the target with an ionic charge distribution established during the crossing of the target. The shape of these distributions are discussed below.

Ionic charge distribution

Electromagnetic spectrometers can provide precise fission yields down to very low relative abundances (at LOHENGRIN $\sim 10^{-10}$ per fission [123]), but the implicit sensitivity to the ionic charge state distribution of the fission fragments may induce artefacts in certain cases. Usually the ionic charge state distribution observed at LOHENGRIN is the result of electron stripping and electron capture when the fast ions traverse the target cover, reaching a statistical distribution around an equilibrium charge state. For fission fragments with kinetic energies of $0.5 - 1$ MeV/nucleon the ionic charge state distribution happens to be nearly Gaussian [124, 125]. An example of an ionic charge distribution for a kinetic energy E = 94 MeV obtained for ^{92}Sr from ^{235}U(n$_{th}$, f) is shown in Fig. 5.13a. However, fission populates the fragments with a certain excitation energy and spin. The high spin levels usually decay quickly via a gamma ray cascade to the ground state or a longer-lived isomer. In certain cases isomeric states exist in

the decay cascade where gamma ray emission is strongly hindered and the decay proceeds via internal conversion, i.e. emission of conversion electrons followed by a cascade of Auger electrons. When the isomeric state has a lifetime of the order of nanoseconds, the change of ionic charge state happens after leaving the target cover but before entering the magnetic deflection. Consequently a perturbed ionic charge state distribution is observed with a second component at higher charge states, corresponding to the relative isomeric yield of the nanosecond-isomer times $\alpha/(1+\alpha)$ where α is the conversion coefficient of its decay [71, 126–128]. Therefore for a number of nuclides, the ionic charge state distributions are strongly asymmetric towards higher ionic charges due to the presence of nanosecond isomers. The charge state distributions of these nuclei could often be reproduced by two Gaussian distributions: a first Gaussian centered around a lighter ionic charge (around 19/20 for light fragments, and around 22/23 for the heavy fragments) and a second Gaussian centered around higher ionic charges, up to the charge 27. Fig. 5.13b shows an example of one such ionic charge state distribution obtained for ^{92}Rb at E = 94 MeV for ^{235}U(n_{th}, f). ^{92}Rb has a series of three nanosecond isomers with partially converted $M1$ and $E2$ transitions in its yrast cascade [129] which will shift part of the ionic charge state distribution to higher Q. This ionic charge state distribution is well represented by a sum of two Gaussian distributions, shown by the red curve in Fig. 5.13b. The Gaussian on the left represents the distribution of ionic charge of the ground state of the measured nucleus and the distribution represented by a Gaussian centered on a higher ionic charge would then correspond to the charge state distribution of one or more isomeric states of the selected nucleus. For establishing such distributions, the half-life time of the isomers must be more than a few nanoseconds.

Kinetic energy distribution

The kinetic energy distributions generally resembles a Gaussian distribution with a systematically observed asymmetry on the lower energy side for all the measurements. As for determining the fission yields only the integral of this distribution

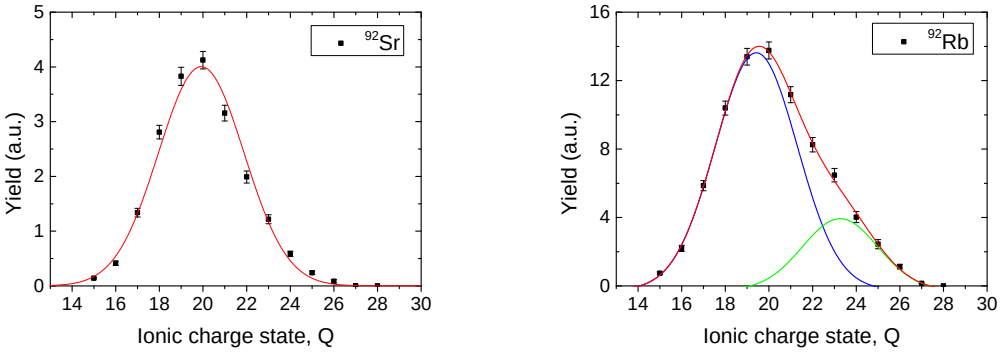

(A) (B)

FIGURE 5.13: Examples of ionic charge state distributions. a) Ionic charge state distribution resembling a Gaussian shape for the nuclide ^{92}Sr at E = 94 MeV for ^{235}U(n_{th}, f) with a Gaussian fit shown by the red curve. b) Ionic charge state distribution with a strong asymmetry towards higher ionic charges for ^{92}Rb at E = 94 MeV for ^{235}U(n_{th}, f) with a sum of two Gaussian fits shown by the red curve. The individual Gaussians used for the sum are shown by the blue and green curve.

plays a role, which is well represented by an integral over modified Gaussian distributions with a tail. This choice makes it possible to correctly reproduce the energy distributions of all the nuclides and to easily determine their integral. The asymmetry in the kinetic energy distributions has already been observed in previous work on fission yield studies and is attributed to the loss of energy of the fission products in the target and the cover foil [130]. Fig. 5.14 shows for example, the kinetic energy distribution for ^{92}Rb at the ionic charge Q = 18 for ^{235}U(n_{th}, f). It is well represented by a modified Gaussian fit with an exponential tail on the left shown by the red curve in Fig. 5.14.

Integration over kinetic energy and ionic charge state distributions

For an accurate measurement of a nuclear charge yield a summation of the yields of this nuclear charge for each combination of kinetic energy and ionic charge state is required. With a specific mass, ionic charge, and energy setting of the LOHENGRIN spectrometer, we measure Y(A, Z, q_i, E_j) which is the probability for the production of a nuclide with nuclear charge Z, ionic charge q_i and the kinetic energy E_j for a mass A from fission after the emission of the fast neutrons and before

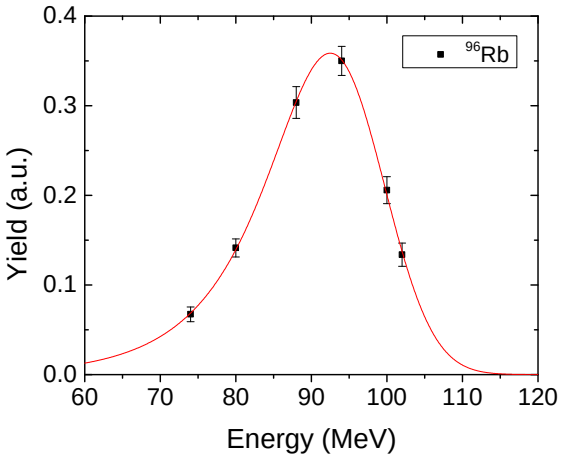

FIGURE 5.14: Example of a kinetic energy distribution. A distribution resembling a modified Gaussian distribution with a tail on the low energy side for ^{92}Rb at the ionic charge, Q = 18 for ^{235}U(n$_{th}$, f) is obtained. The red curve corresponds to the modified Gaussian fit with an exponential tail on the left.

radioactive decay. The fractional nuclear charge yield Y(A, Z), then corresponds to the integral over the ionic charges and the kinetic energy distributions of mass A and is given by the volume of the following integral:

$$Y(A,Z) = \sum_i \int_E Y(A,Z,Q_i,E)dE \tag{5.3}$$

A rigorous measurement was performed for the determination of the ^{96}Y yield for ^{235}U(n$_{th}$, f) with several ionic charge and kinetic energy settings of LOHENGRIN. Fig. 5.15, for an illustration, shows the measurements (red points) for the nuclear charge yield determination of ^{96}Y for ^{235}U(n$_{th}$, f) as a function of kinetic energy E and ionic charge Q. The yield of this nuclide is proportional to the volume of the distribution (the surface curve is obtained by fitting the data with Gaussian distributions for illustration).

However this method is much too expensive in time, and due to limitations in beam time, cannot be carried out as such for all cases. Because of the target burn up, the typical lifetime of a target is about one (in case of plutonium) or two (in case of uranium) weeks. Beyond this time, the count rate becomes insufficient to continue the measurements. An ionic charge distribution with the kinetic energy E$_j$ may require the measurement of more than ten charges, while a kinetic energy

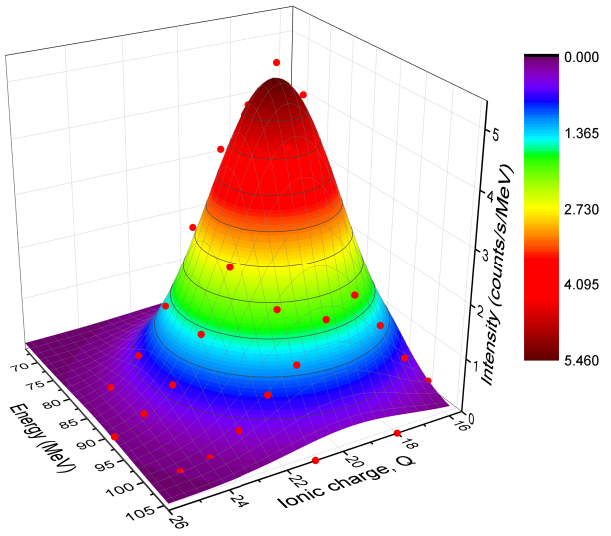

FIGURE 5.15: Measurements (red points) for the nuclear charge yield determination of ^{96}Y for ^{235}U(n$_{th}$, f) as a function of kinetic energy E and ionic charge Q. The yield of this nuclide is proportional to the volume of the distribution (the surface curve is obtained by fitting the data with Gaussian distributions for illustration).

distribution with the ionic charge Q_i covers about forty MeV, with measurement times that can range from few minutes for the nuclei at the top of the intensity distributions, to several hours for those with a lower yield. Therefore determining the nuclear charge yield for a single mass with this method requires several days of measurements. For this reason, the fission yields at the LOHENGRIN spectrometer are determined in the present work from the measurement of a single ionic charge distribution at a mean kinetic energy $\bar{E}$ and a single kinetic energy distribution at a mean ionic charge $\bar{Q}$ only. Under these conditions, the fractional yield of the nuclear charge Z and mass A is then equal to:

$$Y(A,Z) = \frac{\int_E Y(A,Z,\bar{Q},E)dE \times \sum_i (A,Z,\bar{E},Q_i)}{Y(A,Z,\bar{Q},\bar{E})} \tag{5.4}$$

Measured ionic charge states and kinetic energy distributions are adjusted with Gaussian functions as discussed above, and both the quantities $\int_E Y(A,Z,\bar{Q},E)dE$ and $\sum_i Y(A,Z,\bar{E},Q_i)$ are determined from the values of the Gaussian integral, and sum, respectively. If no correlation exists between the ionic charge state and the kinetic energy, the Eq. 5.4 is equivalent to the exact Eq. 5.3. Nevertheless, in the considered kinetic energy and ionic-charge-state ranges, a light correlation

has been observed which introduces a systematic error for the nuclear charge yield determination. This topic is discussed in Section 5.5.

5.5 Error analysis

This section discusses the potential sources of uncertainties induced by the counting statistics, the experimental set-up and by the procedure used for the data analysis. The different terms contributing to the total uncertainty associated with the nuclear charge yields of the fission products are listed below.

Statistical uncertainty: $\Delta_{statistical}$

The analysis of the measured CLTD spectra was performed using the OriginLab software. The software allows to perform Gaussian and modified Gaussian fits to the selected spectra and to deduce the area under the respective fits. The software itself provides the statistical uncertainties as well as errors owing to the fit. While summing up the yield results from each pixel the statistical error of the respective pixels were also translated by summing the errors quadratically.
Additionally, a statistical effect is caused by the thermal neutron flux stability. It is estimated that there is a slight reduction of less than 3 % in the neutron flux during one reactor cycle of 52 days. This gives a rough idea about global neutron flux variations and has a negligible effect on the yield measurements. However, previous work like [71] also determined the effect of local fluctuations exactly by measuring a given mass frequently, and based on the reproducibility of these measurements, the variations in the yields is estimated to be less than 0.6 %.
Both statistical uncertainties are combined quadratically to get the total statistical uncertainty (Δ_{stat}).

Systematic uncertainty: $\Delta_{systematic}$

One of the sources of systematic uncertainty is the target burn up. The uncertainty owing to the burn-up of the target is deduced from the weighted fit performed on the burn-up measurement (see Fig. 5.4).
Another systematic uncertainty is introduced from the procedure followed for nuclear charge yield determination. As explained in Sec.5.4.10, the isotopic yield is determined by measuring the kinetic energy distribution associated with the mean ionic charge state $\bar{Q}$, and the ionic-charge-state distribution associated with the mean kinetic energy $\bar{E}$ (Eq. 5.4). As already stated, this procedure is rigorous only when Q and E are uncorrelated, which is not strictly the case [12, 131]. The error introduced due to this assumption can be determined by comparing the results on yields with measurements for all ionic charge state and kinetic energy combinations with respect to the result from measurements for only one kinetic energy distribution at a mean ionic charge, and one ionic charge distribution at a mean energy. This leads to an uncertainty of less than 1.3% [48] owing to the use of the Eq. 5.4 for the approximation.
The total systematic uncertainty ($\Delta_{systematic}$) is calculated by summing these two contributions.

Additional errors: $\Delta_{additional}$

To determine the independent nuclear charge yields, we multiply the fractional nuclear charge yields determined from the measurements performed, with the respective mass yields from the literature and/or fission yield libraries. The uncertainty thereby introduced through these mass yields are denoted by $\Delta_{additional}$, and are taken from nuclear data libraries/ literature.
The total uncertainty is then calculated as follows:

$$\Delta_{total} = \sqrt{(\Delta_{statistical} + \Delta_{systematic})^2 + \Delta^2_{additional}} \tag{5.5}$$

Chapter 6

Results and Discussions on isotopic yields of fission fragments

In this chapter, results from the various isotopic yield measurements performed at the ILL (Section 5.3) are presented and discussed for the reactions ^{235}U(n$_{th}$, f), ^{239}Pu(n$_{th}$, f) and ^{241}Pu(n$_{th}$, f). Section 6.1 discusses the results from the systematic measurements to optimize the SiN foil thickness for the Z-yield measurements with respect to the Z-resolving power and presents the quality of Z-resolution achieved with the present set-up. The Z-resolutions presently achieved with the CLTDs are also compared to literature values where measurements were performed with the conventional ionization detectors. Section 6.2 presents and discusses the independent and cumulative yields determined for ^{92}Rb and ^{96}Y for the different targets, important for the anti-neutrino anomaly studies. Section 6.3 presents the isotopic yields measured for several masses from the light fragment region towards the symmetry for both the ^{239}Pu(n$_{th}$, f) and ^{241}Pu(n$_{th}$, f) reactions and is followed by discussions on the observed even-odd effect on the Z-yields. Finally the yields for heavy fragment masses for ^{239}Pu(n$_{th}$, f) are presented and discussed in Section 6.4.

The procedure of data analysis for determining the isotopic yields presented in this Chapter was discussed in detail in the Section 5.4. The results on isotopic yields presented in this Chapter are in terms of **a) Relative Z-yields** which are

determined individually for all the CLTD measurements for one mass with different energy and ionic charge state settings of LOHENGRIN. They are defined as the ratio of the counts under one nuclear charge peak to the sum of the counts under all the nuclear charges for that mass and ionic charge state and energy. The relative Z-yields of all the nuclear charges in a giving mass for a specific setting thus always sum up to 1. **b) Fractional Z-yields** (defined in Section 2.1) are determined from the Eq. 5.4 using the E(energy)-distribution at the mean ionic charge state and the Q(ionic charge state)-distribution at the mean energy of the yields. The E-distributions and Q-distributions of the nuclear charges for a mass A are determined by the convolution of relative Z-yields determined from the CLTD measurements with the E and Q distributions of mass yield measured with the PIN diodes. The fractional Z-yields also sum up to 1 for all the nuclear charges in a given mass. **c) Independent Z-yields** (also defined in Section 2.1) are determined by multiplying the fractional Z-yields of a particular mass with its absolute mass yield. **c) Cumulative Z-yields** (also defined in Section 2.1) are calculated by summing the independent yields of respective nuclear charge and all the other nuclear charges radioactively decaying to the same nuclear charge. All the energy distributions of isotopic yields are discussed in terms of the LOHENGRIN energies denoted by E_L unless otherwise stated.

6.1 Quality of Z-resolution

The first part of the measurement campaign at the LOHENGRIN specrtometer with CLTDs was dedicated to optimize the detector set-up for the isotopic yield determination. Measurements were performed with different SiN foil thicknesses for masses A = 89 and A = 96 for ^{235}U(n$_{th}$, f) in order to study the effect of the SiN foil thickness on the nuclear charge resolution. Fig. 6.1, for example, shows spectra for mass A = 89 for ^{235}U(n$_{th}$, f) measured with different SiN foil thicknesses at a LOHENGRIN energy of E_L = 94 MeV and an ionic charge state Q = 19. Similar spectra for mass A = 96 with different SiN foil settings are shown in the Appendix C.1. These spectra are fitted with sum of Gaussian distributions,

and the Z-resolving power Z/ΔZ (see Eq. 2.21 for the definition of Z/ΔZ) is determined for these measurements using the fit results on the FWHM and energy separation between neighbouring nuclear charges. The error in Z/ΔZ is calculated by error propagation of the statistical error using the following formula:

$$\Delta\left(\frac{Z}{\Delta Z}\right) = \sqrt{\left(Z\frac{\Delta d}{FWHM}\right)^2 + \left(Z\frac{d \times \Delta FWHM}{FWHM}\right)^2} \tag{6.1}$$

where d is the energy separation between the neighbouring nuclear charges.

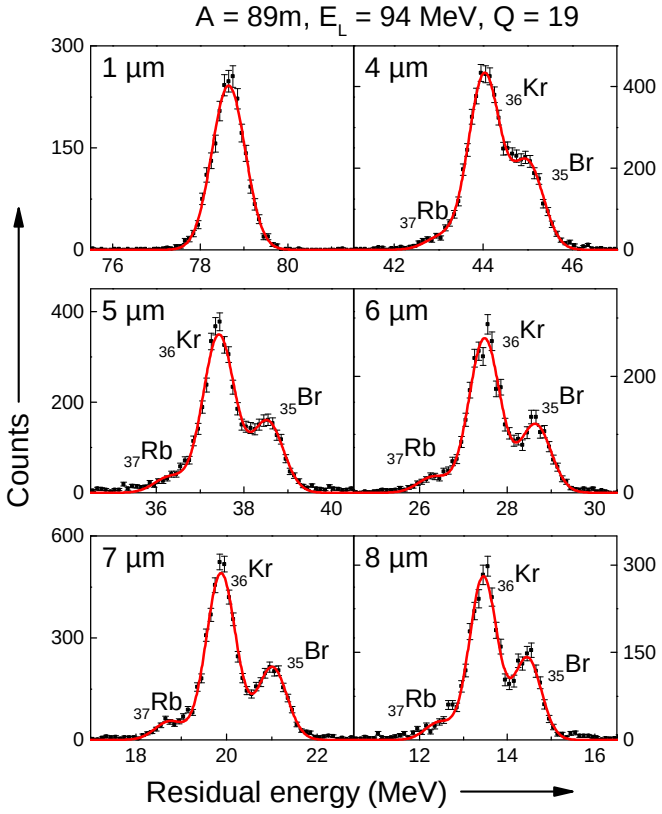

FIGURE 6.1: Residual energy spectra for the mass A = 89 for ^{235}U(n$_{th}$, f) for different SiN foil thickness- 1 μm, 4 to 8 μm, marked on each spectrum, respectively.

In Fig. 6.2, the Z-resolution as a function of the SiN foil thickness is displayed. The data points in red corresponds to the measurement with mass A =89, and the black points to mass A =96, respectively. The points plotted in Fig. 6.2 correspond to the Z/ΔZ value for the central nuclear charge Z = 36 for mass A = 89, and Z = 38 for mass A = 96, respectively. The data points are connected with lines to follow the trend. From both the Figures 6.1 and 6.2 it is clear that in

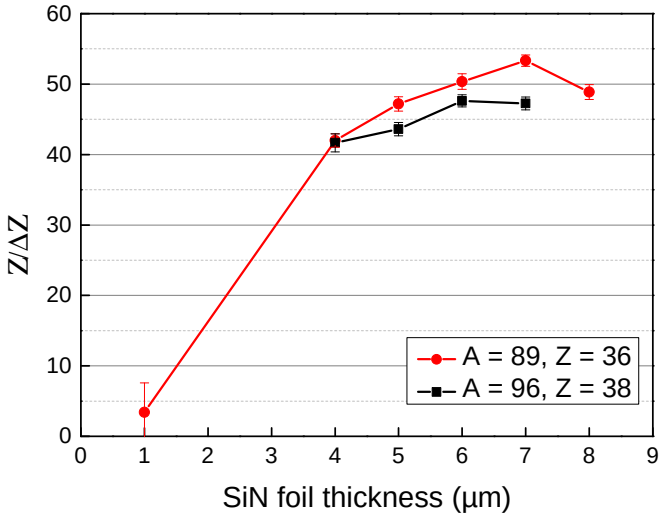

FIGURE 6.2: Z-resolving power versus SiN foil thickness for masses A = 89 and A = 96 for the ^{235}U(n$_{th}$, f) at a LOHENGRIN energy of E_L = 94 MeV and an ionic charge state Q = 18 (for A = 89), and Q = 19 (for A = 96). The data points are connected with lines to follow the trend.

the light mass region, already with a 4 μm thick SiN foil stack well resolved peaks (Z/ΔZ $\sim$ 42) for different nuclear charges are observed. In Fig. 6.2 one can see that the Z-resolving power initially increases for increasing thickness of the SiN foil stack and before it starts to decrease it reaches a maximum Z/ΔZ $\sim$ 53 at 7 μm foil thickness for mass A = 89.

The results discussed above are observed for clean spectra without any contaminating mass from the LOHENGRIN settings at the chosen ionic charge state and energy. However this is not always the case and for a proper yield determination one must consider also the other settings of ionic charge state and energy (see Section 5.4.10) where contaminating masses might as well show up in the spectra. Measurements were thus performed to investigate the influence of improved Z-resolution with higher foil thickness on the disturbance due to contamination. Therefore mass A = 92 was measured with both, 4 μm and 6 μm thick SiN foil stacks, for the LOHENGRIN setting of E_L = 94 Mev and Q = 18, where a contaminating mass appears. Fig. 6.3 compares the spectra measured with 4 μm of SiN (left) and 6 μm of SiN (right) for two different pixels C3 and D3 on the CLTD array. The contribution of the contaminating mass to the spectra is marked by the arrows in Fig. 6.3, and the red curves correspond to fits with a sum of three Gaussian distribution to the mass A = 92 spectra. The spectrum of C3 is an

illustration for a relatively small contribution of the contamination, whereas in the pixel D3 the contamination appears with high intensity. We observe that for measurements with 6 μm foil thickness, in both the pixels C3 and D3, the contaminating mass already starts overlapping with the mass A = 92 peak. In case of measurements with 4 μm of SiN, despite the contamination, it is possible to perform the Gaussian fits and to extract the necessary information to determine the isotopic yields as they are well separated in the energy spectra. It is known that the contamination on the left constitutes of heavier mass with higher energy at the LOHENGRIN due to the operational principle of the mass-energy separation (see Section 2.2). Due to the higher energy loss of more energetic and heavier ions, the contamination on the left comes even closer with 6 μm and overlaps with the mass A = 92 peak. It is possible to fit the spectra for 6 μm foil thickness for pixel C3 due to the relatively small contamination, but in the case of pixel D3 with the high contamination the situation worsens significantly and it becomes difficult or even impossible to perform good quality fits.

As already 4 μm of SiN provides a good Z-resolution, considering the above effect, this foil thickness was found to be a good choice for the systematic yield measurements. It can be seen in Fig. 6.4, that there is no significant effect on the yield determined from spectra with 4 μ of SiN or 6 μm of SiN. In Fig. 6.4 the relative Z-yield determined from the CLTD measurements of mass A = 96 at the LOHENGRIN settings of E_L = 94 MeV and Q = 18 is plotted for different SiN foil thicknesses. Different colours represent the four nuclear charges within mass A = 96. The dotted lines represent the mean value for each isotopic yield. Fig. 6.4 shows that we obtain same results within the errors for the isotopic yields from 4 to 7 μm thickness of the SiN foil stacks. Therefore, with measurements using 4 μm thick SiN foil stacks, without any loss in accuracy concerning the determination of the relative Z-yields, the problem of overlapping contamination can be overcome. As we aim to determine very precise yields specially for ^{92}Rb and ^{96}Y with several ionic charge states and energy settings where contamination would appear, it was decided to use a 4 μm thick SiN foil stack for the systematic measurements of Z-yields in the light mass region. For the heavy fragments however, for the mass

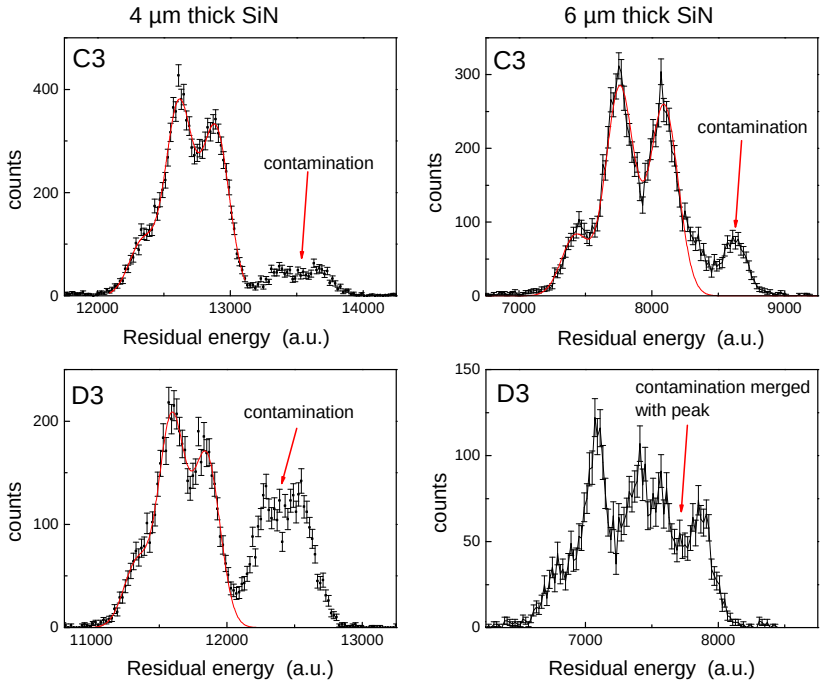

FIGURE 6.3: Comparison of the influence of contaminations for two different SiN foil thickness. On the left spectra from pixels C3 and D3 are displayed for mass A = 92, measured at E_L = 94 MeV and Q = 18 with 4 μm thick SiN foils. On the right spectra for same settings are displayed with 6 μm thick SiN foils. Contaminating mass contributions are marked by the arrows. The red curve is a sum of Gaussians fit to the mass A = 92 peak.

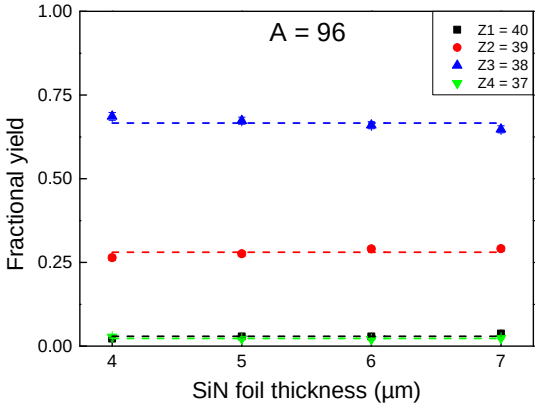

FIGURE 6.4: Comparison of relative Z-yields from measurements with different SiN foil thicknesses. The relative Z-yields determined from the CLTD measurements for mass A = 96 at the LOHENGRIN settings of E_L = 94 MeV and Q = 18 are plotted for different SiN foil thicknesses. Different colours represent the four nuclear charges within mass A = 96. The dotted lines represent the mean value for each isotopic yield.

range measured in this work, contamination from neighbouring masses is not an issue as discussed later in Section 6.4, and consequently a higher foil thickness was chosen for better separation.

The quality of nuclear charge resolution was studied in this work using the three targets of ^{235}U, ^{241}Pu and ^{239}Pu for selected masses in the region $82 \leq A \leq 139$ as a function of degrader thickness and fission fragment kinetic energy. The results on the nuclear charge resolution for mass A = 89 and A = 96 as a function of degrader thickness over the range of 1 μm to 8 μm thick SiN foil stacks was already presented in Fig. 6.2. As expected, better Z-resolving power is observed with increasing foil thickness reaching a maximum, and for further increasing the thickness the resolving power decreases due to the increased contributions from nuclear energy losses. Best Z-resolution was achieved with $\sim$ 7 μm of SiN for the mass A = 89 with an initial energy of 94 MeV (see Fig. 6.2).

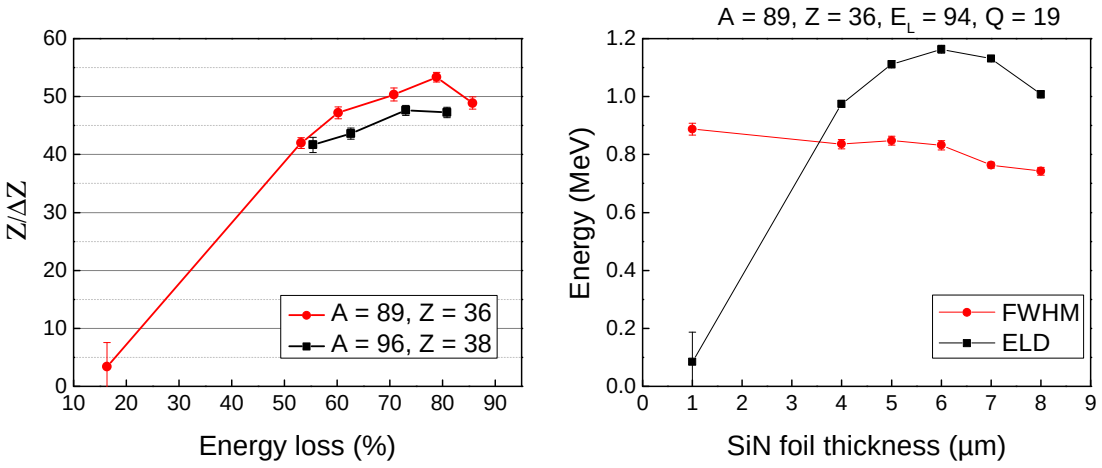

FIGURE 6.5: Left: Z resolving power (Z/ΔZ) versus energy loss (%) obtained with CLTDs and different SiN absorber foil thicknesses for masses A = 89 (Z = 36) and A = 96 (Z = 38) at a LOHENGRIN energy of E_L = 94 MeV for ^{235}U. Right: The FWHM (in red) of the Z = 36 peak and the energy loss difference, ELD (in black), between peaks from neighbouring Z in mass A = 89 for different foil thicknesses corresponding to the measurements shown on the left.

In Fig. 6.5 the Z-resolving power Z/ΔZ is plotted as a function of the energy loss (as percentage of the initial energy) for the measurements performed with mass A = 89 and A = 96. Also plotted is the FWHM of the individual Z peaks, and the energy loss difference between the neighbouring nuclear charge peaks in the residual energy spectra. The best resolution was determined for an energy loss of

$\sim$ 80% which is comparable to previous studies on Z-resolving power by Quade et. al. [2]. The typical energy resolution shown on the right plot in Fig. 6.5 is of the order of 800 keV, and the energy loss difference between the neighbouring nuclear charges is of the order $\sim$ 1.1 MeV. This was also confirmed with the calculation using the Knyazheva method (Section 4.5.3) within error bars. Such a detailed measurement with different foil thicknesses was performed only for two masses due to the limited beam-time. As discussed already above, all the Z-yield measurements in the light and symmetry mass region were not performed with the SiN foil thickness corresponding to the best resolution, rather, the optimum SiN thicknesses of 4 μm (6μm for heavy masses) was used considering the contributions from contaminating masses to the residual energy spectra. However, additionally for a couple of masses, measurements were performed with SiN foil thicknesses of 4 μm and 6 μm. From these measurements, the Z-resolving power Z/ΔZ is plotted as a function of mass and nuclear charge in Fig. 6.6 where the measurements obtained with the present set-up are shown by the red data points. The results are compared to literature values from Quade et. al [2] (shown by black symbols) and Bocquet et. al. [3] (shown by blue symbols). For the light fragment group we could already match the historically best Z-resolving power, e.g. Z/ΔZ = 53 at Z = 36, achieved conventionally with parylene-C absorbers and ionization chambers [2],[3]. The energy resolution of the CLTDs for the fission fragments with 7 μm SiN foil thickness is typically 800 keV for $\sim$ 95 MeV initial kinetic energy of the fission fragments and the energy loss difference of $\sim$ 1.1 MeV is obtained for Z = 36 (A = 89). Most of the Z-yield measurements with light masses performed with 4 μm thick SiN foils have an energy resolution of 850-900 keV and an energy loss difference between neighbouring Z peaks as $\sim$ 1 MeV for the mean fission kinetic energy of $\sim$ 95 MeV.

Near the symmetry region, we already see improvements in the Z-resolving power, e.g. Z/ΔZ = 45 at Z = 45 with the CLTD and SiN foils compared to the values given in Bocquet et. al.[3] for measurements with an ionization chamber. The FWHM and energy loss difference obtained with the present set-up in this region is typically $\sim$ 810 keV, and $\sim$ 880 keV, respectively. For the heavy mass region,

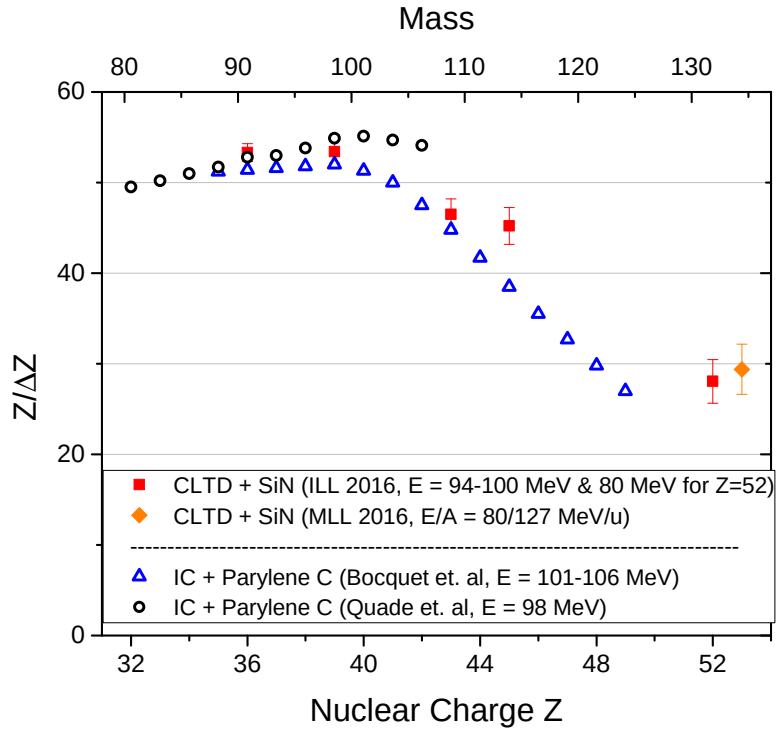

FIGURE 6.6: Z resolving power (Z/ΔZ) versus nuclear charge obtained with CLTDs and SiN absorbers for fission fragments at ILL, and for heavy ions at MLL Garching as compared to data measured by Quade et al. [2] and Bocquet et al. (partly extrapolations) [3].

constrained fits (see section 6.4) on the overlapping peaks in the residual energy spectra yield a Z-resolving power of Z/ΔZ=28 for Z=52. This value is also in very good agreement with the estimate on Z/ΔZ from the test measurements (discussed in Chapter 4) at the Munich tandem accelerator with stable ^{130}Te and ^{127}I ion beams, shown in orange in Fig. 6.6. This demonstrates a significant improvement as compared to extrapolations presented in Bocquet et. al. [3] (blue symbols in Fig. 6.6). The FWHM and energy loss difference obtained for the heavy masses with 6 μm thick SiN foils are 225 keV, and 375 keV, respectively. This allowed for the first time the investigation of the isotopic yields in the heavy mass region using the passive absorber method.

6.2 Results on the yields of ^{92}Rb and ^{96}Y

This section presents the results on isotopic yields of ^{92}Rb for the three reactions - ^{235}U(n_{th}, f), ^{239}Pu(n_{th}, f) and ^{241}Pu(n_{th}, f). And the the results on isotopic yields of ^{96}Y for ^{235}U(n_{th}, f) and ^{239}Pu(n_{th}, f). The absolute mass yields used to calculate the independent isotopic yields in these cases are taken from the JEFF nuclear data library [7]. These fission products are the dominant contributors to the high energy portion of the reactor anti-neurino spectra (See Section 2.1.2). These new measurements resolve discrepancies between previous yield measurements and fission data libraries and reduce the nuclear data uncertainties in the computation of reactor anti-neutrino spectra by the summation method [5].

6.2.1 Isotopic yields for mass A = 92 for ^{235}U, ^{241}Pu and ^{239}Pu targets

Isotopic yields for mass A = 92 were determined using the CLTDs with 4 μm thick SiN foils. Several measurements at different ionic charge states and kinetic energies were performed which were mentioned already in Section 5.3.1. Fig. 6.7 shows an example spectrum for mass A = 92 measured with CLTDs. Three nuclear charge contributions corresponding to ^{92}Sr (Z = 38), ^{92}Rb (Z = 37) and ^{92}Kr (Z = 36) were observed in the residual energy spectra measured with the CLTDs and the relative Z-yields were determined by performing the sum of three Gaussians fits on the residual energy spectra.

First, the calculation of isotopic yields for mass A = 92 for ^{235}U(n_{th}, f) are presented. For ^{235}U(n_{th}, f), a rather detailed measurements were performed at several ionic charge states and kinetic energies with the CLTDs. In principle, with Eq. 5.4, isotopic yields can be determined using one energy distribution at the mean ionic charge state of the mass distribution and one ionic charge distribution at the mean kinetic energy of the mass distribution for A = 92. However, additionally one more energy distribution was measured at a higher charge state far from the mean charge in order to further ensure the correctness of the determined values

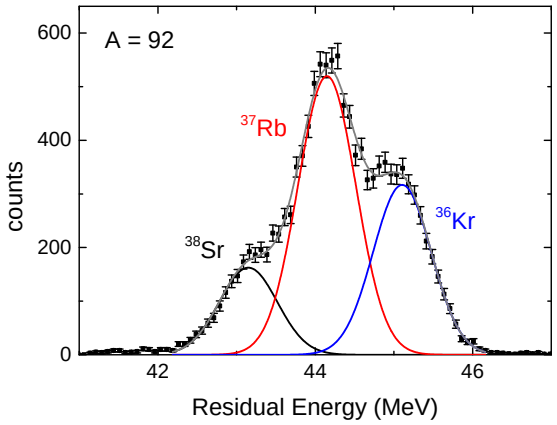

FIGURE 6.7: An example spectrum for isotopic yield calculations for mass A = 92 with the contributions from different nuclear charges.

and to evaluate the effect on isotopic yields for extreme ionic charge states of fragments produced at a very low intensity.

On the left in Fig. 6.8 the relative Z-yields from the CLTD measurements are shown. On the top the relative yields are shown for different ionic charge states at the LOHENGRIN energy E_L = 94 MeV corresponding to the fission energy $E_{Fission}$ = 99 MeV ± 1 MeV, and also the relative yields are shown for different energies at Q = 20 (center) and Q = 25 (bottom). The solid dots in Fig.6.8 correspond to the measured data points, and the open dots correspond to the interpolated and extrapolated values Values for the ionic charges states Q = 19 and Q = 23 were interpolated and for Q = 15, 27 and 28 were extrapolated to fill in the gaps for these charge states where relative Z-yields could not be determined from measurements due to contaminations and/or couldn't be measured due to very low intensity. On the right in Fig. 6.8 the energy and ionic charge state distributions of mass yields for A = 92 for ^{235}U(n_{th}, f) measured with the PIN diodes are displayed. As expected from the discussions in Section 5.4.10, we observe that these energy and charge distributions are well described by Gaussian distributions with a tail. The solid lines in Fig.6.8 are modified Gaussian fits to the data.

Using the relative Z-yields determined from the CLTD measurements with the E and Q distributions for mass 92 from the PIN diodes, the E-distributions and Q-distributions of the nuclear charges are determined as shown in Figures 6.9 (Q-distributions) and 6.10 (E-distributions). The solid lines in Fig. 6.10 are modified Gaussian fits with an exponential tail on the left to the energy distributions. One

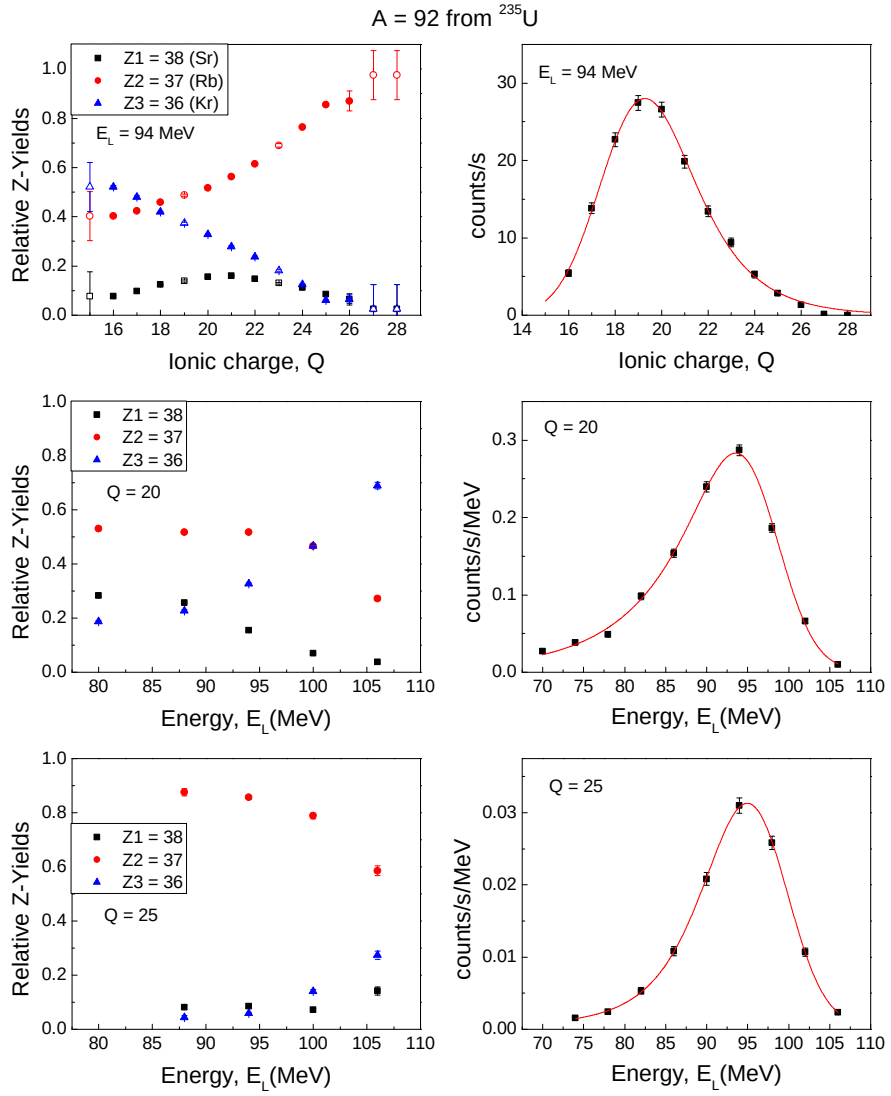

FIGURE 6.8: Relative Z-yields from the CLTD measurements for A = 92 for ^{235}U(n_{th}, f). On the left the relative yields are shown for different ionic charge states at the LOHENGRIN energy E_L = 94 MeV(top), and for different energies at Q = 20 (center) and Q = 25 (bottom). Solid points correspond to measured values and open circles correspond to interpolated/extrapolated values. The corresponding numerical data are displayed in Tables C.2 and C.1. On the right energy and ionic charge state distributions for the mass yields for A = 92 determined from the PIN diode measurements are plotted. Curves passing through the data points are modified Gaussian fits to the data. The corresponding numerical data are displayed in Table C.3.

can see in Fig. 6.9 that the Q distribution of the Rb isotope is asymmetric with more intensity towards higher ionic charge states. This suggests the presence of a nanosecond isomer in ^{92}Rb (Section 5.4.10). In principle to determine the fractional yields using Eq. 5.4, one ionic charge distribution at the mean energy and

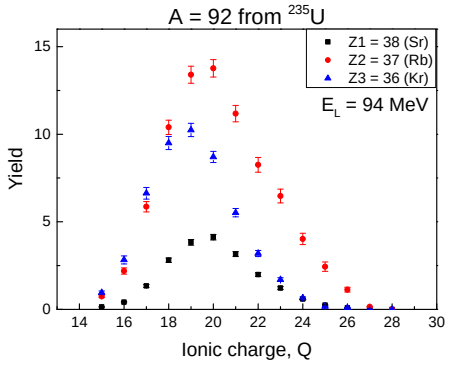

FIGURE 6.9: Q(ionic charge) distribution of nuclear charges for mass A = 92 for ^{235}U(n_{th}, f) determined from the convolution of both CLTD and PIN diode measurements. The corresponding numerical data are displayed in Table C.4.

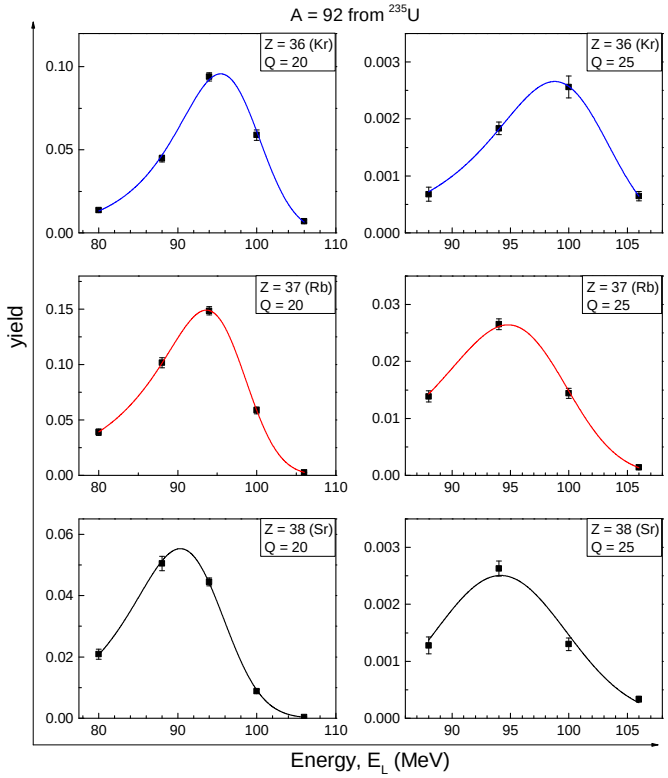

FIGURE 6.10: Energy distributions of nuclear charges for mass A = 92 for ^{235}U(n_{th}, f) determined from the convolution of both CLTD and PIN diode measurements at ionic charge states Q = 20 and Q = 25. The solid lines are modified Gaussian fits with an exponential tail on the left. The corresponding numerical data are displayed in Table C.5

one energy distribution at the mean ionic charge state for mass 92 should be sufficient. However, an additional energy distribution was measured at a higher ionic charge state Q = 25 in order to see the effect on the Z-yields due to the presence of the asymmetry in the Q distribution of nuclear charges for mass 92 towards

higher ionic charges.

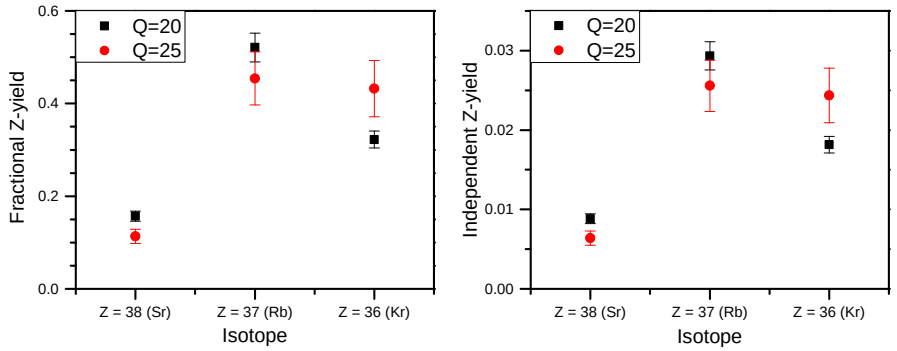

FIGURE 6.11: Fractional Z-yields (left) and Independent Z-yields (right) for A = 92 for ^{235}U(n$_{th}$, f) using the Q distribution at E_L = 94 MeV with E distributions at ionic charge states Q = 20 and Q = 25. The corresponding numerical data are displayed in Table C.6

The fractional yields were thus determined using the Q distribution at E_L = 94 MeV with both the energy distributions at the mean ionic charge state Q = 20 which actually represents the fractional yield, and also at a higher Q = 25 using Eq. 5.4 representing the case far from the mean distribution to evaluate the possible variance in the results for extreme cases. Fig. 6.11 compares the fractional Z-yields (left) and the independent Z-yields (right) using the two energy distributions at Q = 20 and Q = 25. We see that the results for ^{92}Rb (Z = 37) are in good agreement in both the cases. We also observe larger errors for the case of Q = 25 compared to Q = 20 which is due to the considerably lower count rates for fragments produced at higher ionic charge state far from the mean of the distribution. However, a small variation is observed on the yields for ^{92}Sr and ^{92}Kr for the two cases. Fig. 6.11 on the right shows the calculated independent yields of the nuclear charges for mass 92 for ^{235}U(n$_{th}$, f) using the absolute mass yield of A = 92 from the JEFF nuclear data library [7].

Similarly, yields were determined for mass A = 92 for ^{241}Pu(n$_{th}$, f) and ^{239}Pu(n$_{th}$, f). However, for these reactions measurements were not performed in as much detail as in the previous case. Fewer kinetic energies and ionic charge states were measured as mentioned in Section 5.3.1 and yields were determined from one energy distribution at the mean ionic charge state of the mass distribution and one ionic charge distribution at the mean kinetic energy of the mass distribution for

A = 92.

Fig. 6.12 shows the relative Z-yields from the CLTD measurements for A = 92 for ^{239}Pu(n_{th}, f). On the left relative Z-yields from the CLTD measurements for A = 92 for ^{239}Pu(n_{th}, f) are shown for different ionic charge states at E_L = 100 MeV (top), and for different energies at Q = 21 (bottom). In Fig. 6.12 (top left), values shown by open circles for the ionic charge states 18, 19, 22 and 23 were interpolated, and were extrapolated for Q = 26 and 27 to fill the gaps for these charge states where relative Z-yields could not be determined from measurements due to contamination and/or could not be measured due to very low intensity. Similarly, in Fig. 6.12 (bottom left), values shown in open circles are extrapolated. Fig. 6.12 on the right shows the E and Q distributions for mass 96 from PIN diode measurements. Fig. 6.13 and Fig. 6.14 show the Q(ionic charge) distribution and energy distributions of nuclear charges for mass A = 92 determined from the convolution of both CLTD and PIN diode measurements for the mass yield distribution of A =92. The red curves in Fig. 6.14 are modified Gaussian fit with an exponential tail on the left. The fractional and independent yields thus obtained are provided in Table 6.1.

Finally, the results for A = 92 for ^{241}Pu(n_{th}, f) are presented. For the ^{241}Pu(n_{th}, f) target, it was not possible to measure the distributions for mass yield with the PIN diode due to fast burn up of the target. Therefore for the mass yield distributions, recent measurements with an ionization chamber at the LOHENGRIN spectrometer [132] were used. Fig. 6.15 and Fig. 6.16 show the Q(ionic charge) distribution and energy distributions of nuclear charges for mass A = 92 determined from the convolution of both CLTD and ionization chamber measurements for the mass yield distribution of A =92. The red curves in Fig. 6.16 are modified Gaussian fits with an exponential tail on the left to the energy distributions. (The relative Z-yields and the mass yield distributions with ionization chamber can be found in the appendix - Tables C.21, C.20 and C.22). The fractional and independent yields thus obtained are provided later in Table 6.1.

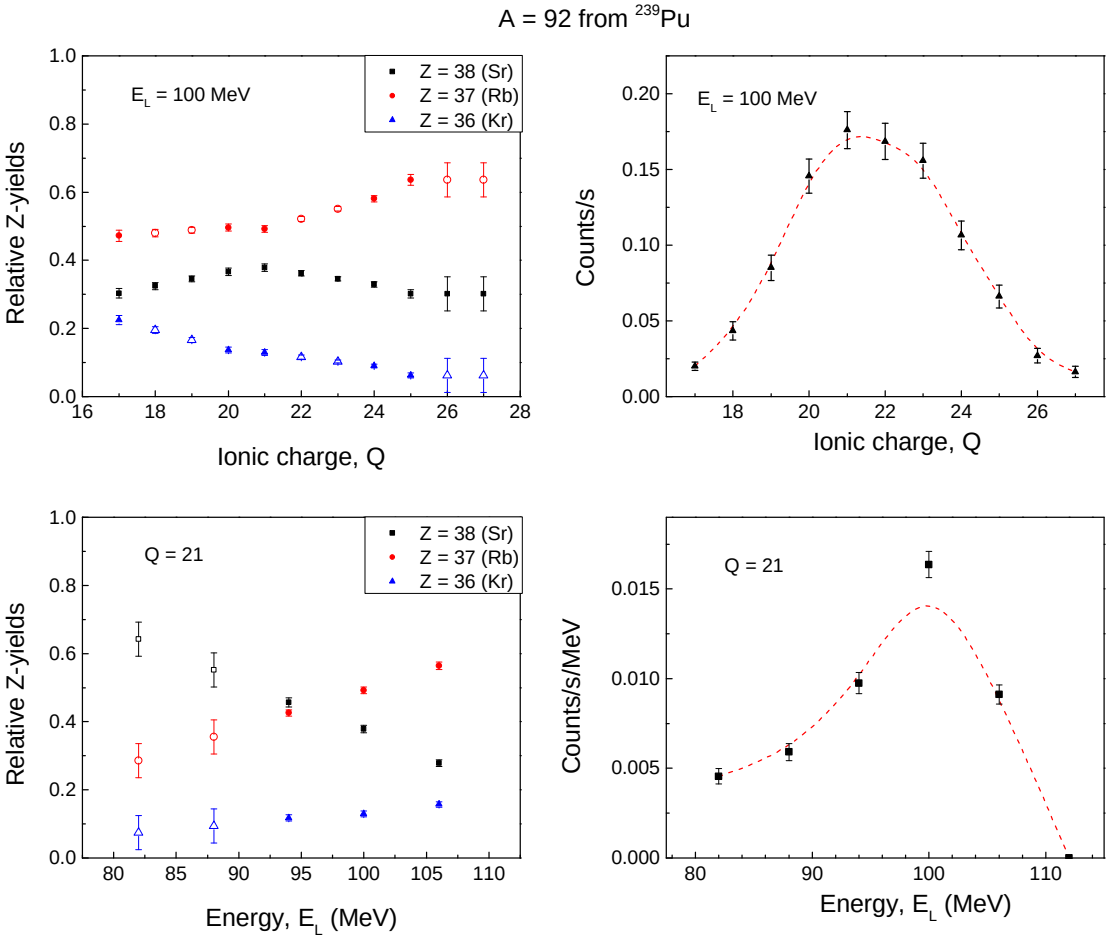

FIGURE 6.12: On the left relative Z-yields from the CLTD measurements for A = 92 for ^{239}Pu(n_{th}, f) are shown for different ionic charge states at E_L = 100 MeV (top), and for different energies at Q = 21 (bottom). Solid points correspond to measured values and open circles correspond to interpolated/extrapolated values. The corresponding numerical data are displayed in Tables C.16 and C.15. On the right, E and Q distributions for mass A = 92 for ^{239}Pu(n_{th}, f), determined from the PIN diode measurements are plotted. The corresponding numerical data are displayed in Table C.17.

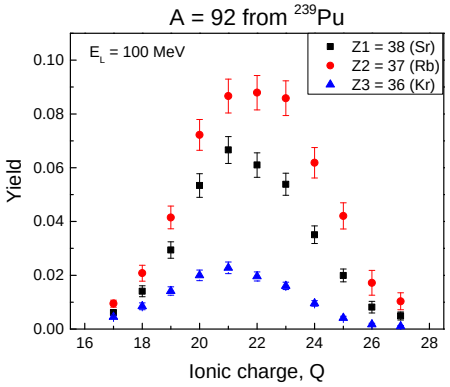

FIGURE 6.13: Q(ionic charge) distribution of nuclear charges for mass A = 92 for ^{239}Pu(n_{th}, f), determined from the convolution of both CLTD and PIN diode measurements. The data points are connected with lines to follow the trend. The corresponding numerical data are displayed in Table C.18.

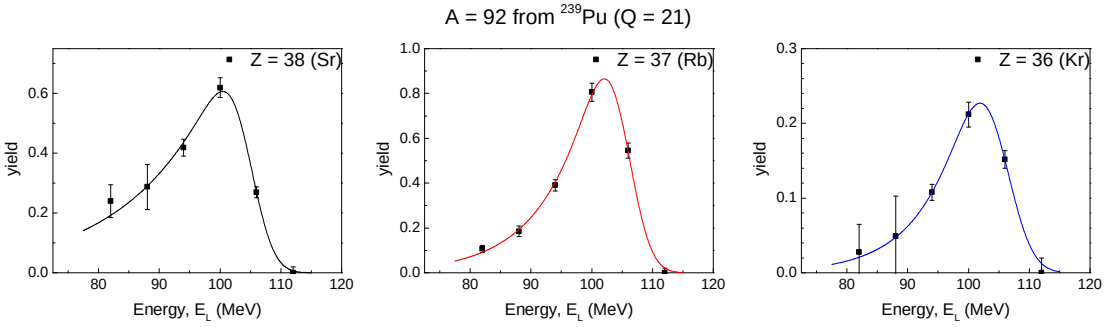

FIGURE 6.14: Energy distributions of nuclear charges for mass A = 92 for ^{239}Pu(n_{th}, f), determined from the convolution of both CLTD and PIN diode measurements. The red curves are modified Gaussian fits with an exponential tail on the left. The corresponding numerical data are displayed in Table C.19.

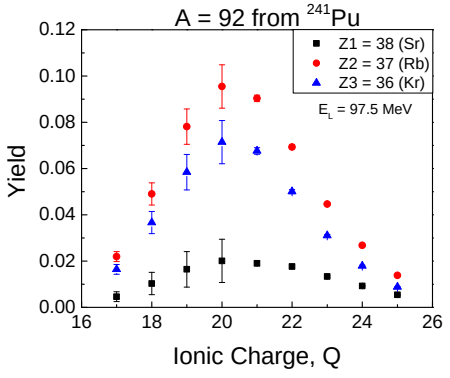

FIGURE 6.15: Q(ionic charge) distribution of nuclear charges for mass A = 92 for ^{241}Pu(n_{th}, f). The data points are connected with dotted lines to follow the trend. The corresponding numerical data are displayed in Table C.21.

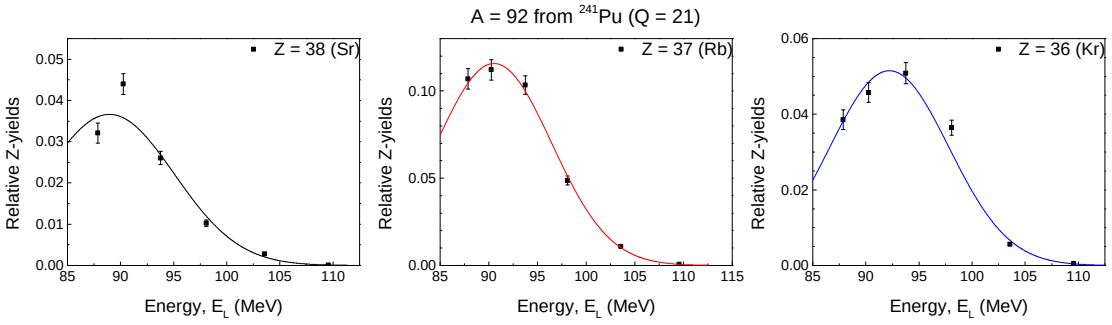

FIGURE 6.16: Energy distributions of nuclear charges for mass A = 92 for ^{241}Pu(n_{th}, f), determined from the convolution of both CLTD and ionization chamber measurements. The red curves are modified Gaussian fit with an exponential tail on the left. The corresponding numerical data are displayed in Table C.24.

6.2.2 Isotopic yields for mass A = 96 for ^{235}U and ^{241}Pu targets

In this section the isotopic yields for mass A = 96 for ^{235}U(n_{th}, f) and ^{241}Pu(n_{th}, f) are presented. Isotopic yields for mass A = 96 were also determined using the CLTDs with 4 μm thick SiN foils. Several measurements at different ionic charge states and kinetic energies were performed which were mentioned already in Section 5.3.1. Fig. 6.17 shows an example spectrum for mass A = 96 measured with CLTDs. Four nuclear charge contributions corresponding to ^{96}Zr (Z = 40), ^{96}Y (Z = 39), ^{96}Sr (Z = 38) and ^{96}Rb (Z = 37) were observed in the residual energy spectra measured with the CLTDs and the relative Z-yields were determined by performing the sum of four Gaussians fits on the residual energy spectra.

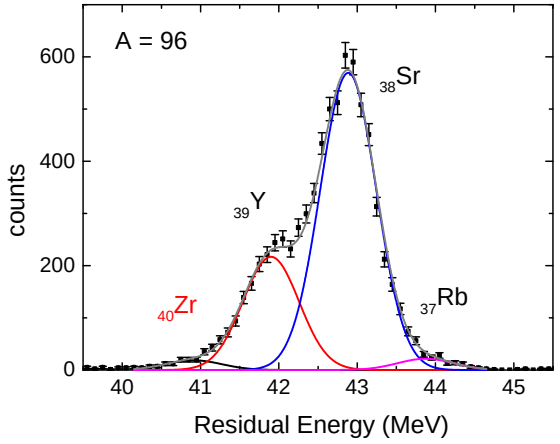

FIGURE 6.17: An example spectrum for isotopic yield calculations for mass A = 96 with the contributions from different nuclear charges.

Fig. 6.18 shows the relative Z-yields from the CLTD measurements. On the left the relative yields are shown for different ionic charge states measured at three different LOHENGRIN energies, E_L = 84, 94 and 102 MeV corresponding to the fission energies $E_{Fission}$ = 89, 99 and 107 MeV, and on the right the relative yields are shown for different energies at Q = 18 (top) and Q = 21 (bottom). Four nuclear charge contributions corresponding to ^{96}Zr (Z = 40), ^{96}Y (Z = 39), ^{96}Sr (Z = 38) and ^{96}Rb (Z = 37) were observed in the residual energy spectra measured with the CLTDs, and the relative Z-yields were determined by performing the sum of four Gaussian fits on the residual energy spectra. The dots in Fig. 6.18 corresponds to

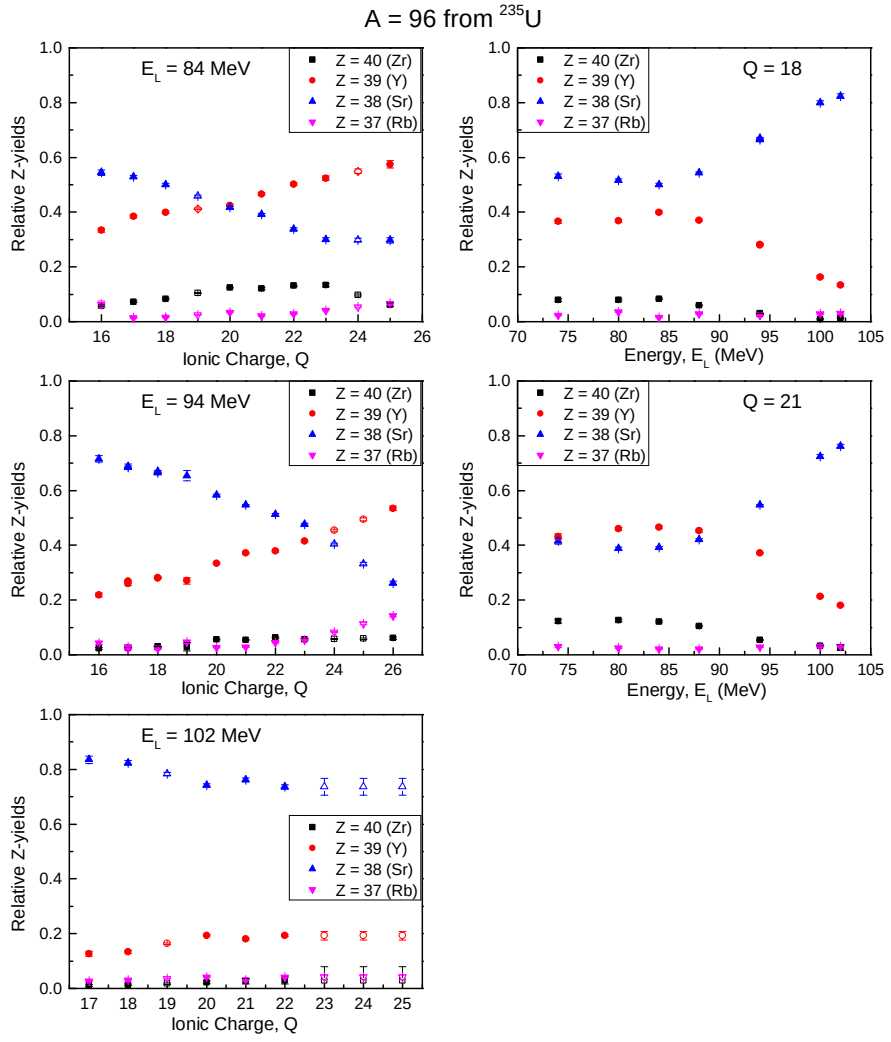

FIGURE 6.18: Relative Z-yields from the CLTD measurements for A = 96 for ^{235}U(n_{th}, f). On the left the relative yields are shown for different ionic charge states at E_L = 84, 94 and 102 MeV and on the right the relative yields for different energies at Q = 18 (top) and Q = 21 (bottom) are shown. The corresponding numerical data are displayed in Tables C.10, C.7, C.8, C.9.

the measured data points, and the lines passing through the data points are only to follow the trend. Values for the ionic charges states 19 and 23 were interpolated, for the distribution at E_L = 84 MeV. For E_L = 94 MeV the values for the ionic charges states 24 and 25 were interpolated and for E_L = 102 MeV the values for the ionic charges states 19, 23, 24 and 25 were interpolated. Fig. 6.19 shows the ionic charge distributions at three different LOHENGRIN energies, E_L = 84, 94 and 102 MeV, and the energy distributions for Q = 18 and 21 for mass A = 96 for ^{235}U(n_{th}, f), measured with the PIN diodes. As expected from the discussions in Section 5.4.10, we observe that these energy and charge distributions are well

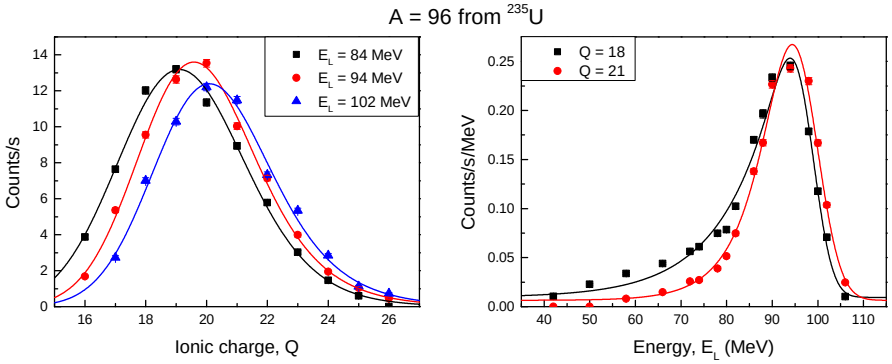

FIGURE 6.19: Plots for E and Q distributions of mass A = 96 for ^{235}U(n_{th}, f), determined from the PIN diode measurements. The corresponding numerical data are displayed in Table C.11.

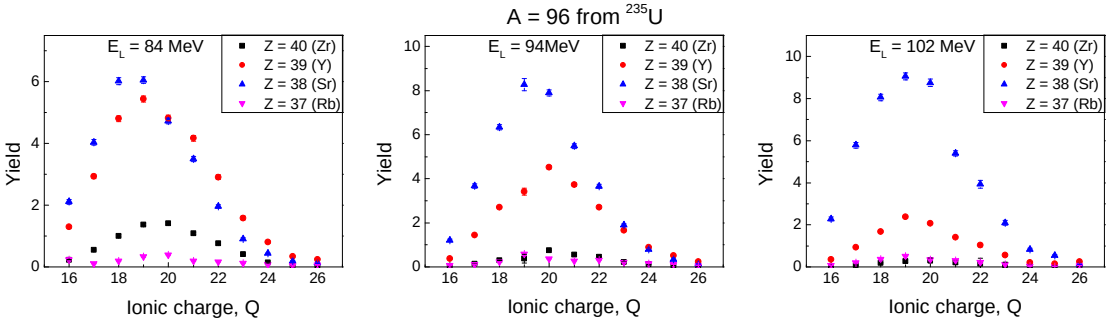

FIGURE 6.20: Q(ionic charge) distribution of nuclear charges for mass A = 96 for ^{235}U(n_{th}, f) at E_L = 84, 94 and 102 MeV, determined from the convolution of both CLTD and PIN diode measurements. The data points are connected with dotted lines to follow the trend. The corresponding numerical data are displayed in Table C.12.

explained by Gaussian distributions with a tail. The solid lines in Fig.6.19 are modified Gaussian fits to the data. Using the relative Z-yields determined from the CLTD measurements with the E and Q distributions for mass 96 from the PIN diodes, the E-distributions and Q-distributions of the nuclear charges are determined as shown in Figures 6.20 (Q-distributions) and 6.21 (E-distributions). The solid lines in Fig. 6.21 are modified Gaussian fits with an exponential tail on the left.

A detailed set of measurements with several E and Q distributions was performed to determine very precise yields. The fractional yields were thus determined for different combinations of energy distributions and charge distributions measured with the CLTDs. Three ionic charge distributions measured at E_L = 84, 94 and 102 MeV were evaluated with the two energy distributions measured at Q = 18

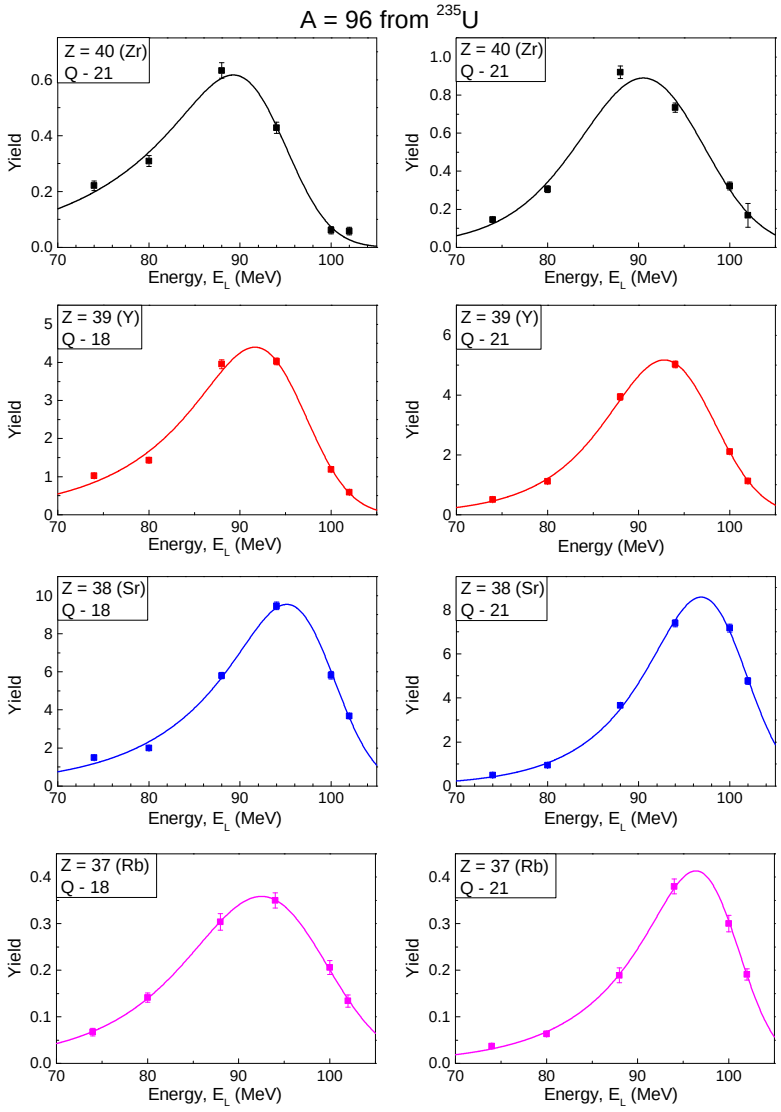

FIGURE 6.21: Energy distributions of nuclear charges for mass A = 96 for ^{235}U(n_{th}, f) for Q = 18 and Q = 21, determined from the convolution of both CLTD and PIN diode measurements. The solid lines are modified Gaussian fits with an exponential tail on the left. The corresponding numerical data are displayed in Table C.13.

and 21 using Eq. 5.4. Fig. 6.22 (upper part) compares the fractional Z-yields thus determined for all the six combinations. We see that the results for the ^{96}Y (Z = 39) are consistent for all the settings within the errors. Fig. 6.22 (lower part) shows the calculated independent yields of the nuclear charges for mass 96 for ^{235}U(n_{th}, f), using the mass yield of A = 96 from the JEFF nuclear data library [7]. We observe relatively larger errror for independent yields compared to the fractional yields which is attributed to the fact that the errors in mass yield used to determine independent yields from fractional yields dominates the total error

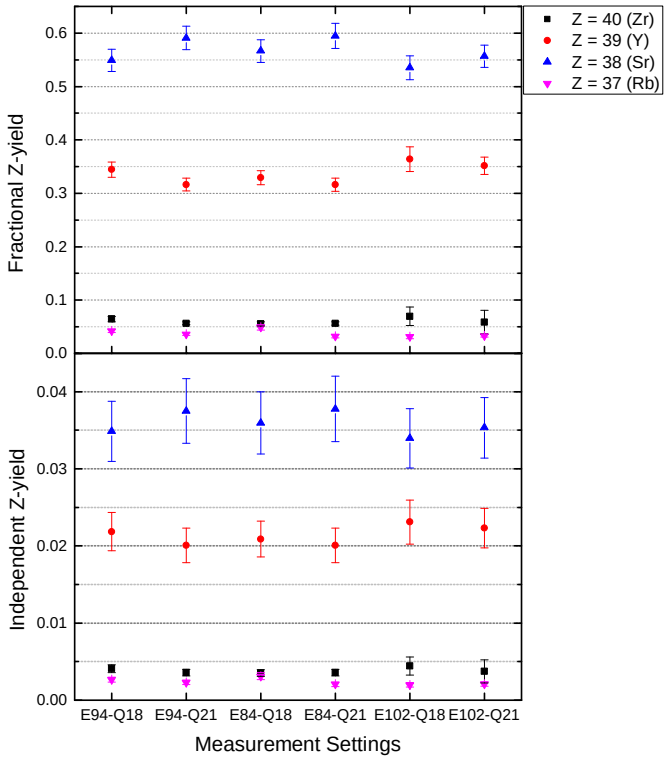

FIGURE 6.22: Fractional Z-yields (top) and Independent Z-yields (bottom) for A = 96 for ^{235}U(n$_{th}$, f) determined using Eq. 5.4 for different combinations of energy distributions and charge distributions measured with the CLTDs. Three ionic charge distributions measured at E_L = 84, 94 and 102 MeV were evaluated with the two energy distributions measured at Q = 18 and 21. Results from all the six combinations are compared. The corresponding numerical data are displayed in Table C.14.

of the independent yields.

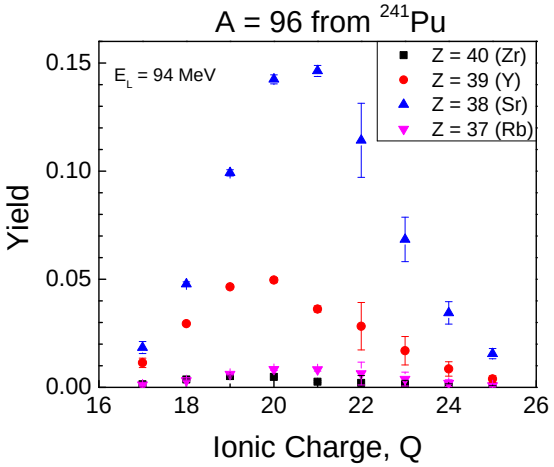

FIGURE 6.23: Q(ionic charge) distribution of nuclear charges for mass A = 96 for ^{241}Pu(n$_{\rm th}$, f) determined from the convolution of both CLTD and ionization chamber measurements. The corresponding numerical data are displayed in Table C.28.

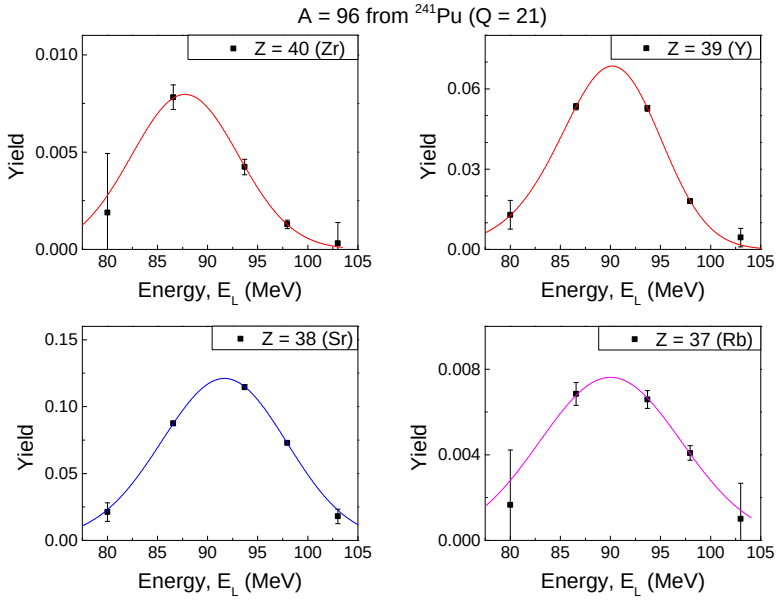

FIGURE 6.24: Energy distributions of nuclear charges for mass A = 96 for ^{241}Pu(n_{th}, f) determined from the convolution of both CLTD and ionization chamber measurements. The red curves are modified Gaussian fits, with an exponential tail on the left. The corresponding numerical data are displayed in Table C.29.

Similarly the isotopic yields for mass A = 96 for ^{241}Pu(n_{th}, f) were determined. However, for this reaction measurements were not performed in as much detail as in the previous case. Fewer kinetic energies and ionic charge states were measured as mentioned in Section 5.3.1 and yields were determined from one energy distribution at the mean ionic charge state of the mass distribution and one ionic charge distribution at the mean kinetic energy of the mass distribution for A = 96. As mentioned before, for the ^{241}Pu(n_{th}, f) target, it was not possible to measure the distributions for mass yield with the PIN diode due to fast burn up of the target. Therefore for the mass yield distributions, recent measurements with an ionization chamber at the LOHENGRIN spectrometer [132] were used. Fig. 6.23 and Fig. 6.24 show the Q(ionic charge) distribution and energy distributions of nuclear charges for mass A = 96, determined from the convolution of both CLTD and ionization chamber measurements for the mass yield distribution of A =96. The red curves in Fig. 6.24 are modified Gaussian fit with an exponential tail on the left. (The relative Z-yields and the mass yield distributions with ionization chamber can be found in the appendix - Tables C.26, C.25 and C.27). The fractional and independent yields obtained are provided in Table 6.3.

6.2.3 Summary and discussion on the ^{92}Rb and ^{96}Y yields

Finally the fractional and independent isotopic yields of ^{92}Sr (Z = 38), ^{92}Rb (Z = 37) and ^{92}Kr (Z = 36), deduced for mass A = 92 for all the three reactions ^{235}U (n_{th}, f), ^{239}Pu (n_{th}, f) and ^{241}Pu (n_{th}, f), are listed in Table 6.1. The cumulative yields for ^{92}Rb which corresponds to the yield produced directly from fission as well as via radioactive decay of precursors was determined by summing the independent yields determined for ^{92}Rb and ^{92}Kr. The results are presented in Table 6.2. The fractional and independent isotopic yields of ^{96}Zr (Z = 40), ^{96}Y (Z = 39), ^{96}Sr (Z = 38) and ^{96}Rb (Z = 37) for mass A = 96 for all the three targets ^{235}U (n_{th}, f), ^{239}Pu (n_{th}, f) and ^{241}Pu (n_{th}, f) are listed in Table 6.3.

Fractional and Independent nuclear charge yields for A = 92				
^{235}U (n_{th}, f)				
Isotope	fractional yield	Δ	independent yield	Δ
Z = 38 (Sr)	0.157	0.011	0.0088	0.0006
Z = 37 (Rb)	0.521	0.031	0.0293	0.0018
Z = 36 (Kr)	0.322	0.018	0.0181	0.0010
^{239}Pu (n_{th}, f)				
Isotope	fractional yield	Δ	independent yield	Δ
Z = 38 (Sr)	0.382	0.053	0.0120	0.0017
Z = 37 (Rb)	0.501	0.047	0.0157	0.0015
Z = 36 (Kr)	0.117	0.016	0.0037	0.0005
^{241}Pu (n_{th}, f)				
Isotope	fractional yield	Δ	independent yield	Δ
Z = 38 (Sr)	0.185	0.020	0.0047	0.0005
Z = 37 (Rb)	0.561	0.043	0.0143	0.0012
Z = 36 (Kr)	0.253	0.019	0.0065	0.0005

TABLE 6.1: Fractional and Independent nuclear charge yields for Sr, Rb and Kr for mass A = 92 for the three targets ^{235}U (n_{th}, f), ^{239}Pu (n_{th}, f) and ^{241}Pu (n_{th}, f).

As discussed earlier, new measurements were requested [5] for ^{92}Rb and ^{96}Y in regard to the reactor antineutrino anomaly studies to obtain more precise independent values than the existing ones and also to resolve the discrepancy in the ^{92}Rb contribution between the standard data base Jeff and another independent

Cumulative yield of ^{92}Rb		
Target	Cumulative yield	Δ
^{235}U (n_{th}, f)	0.0475	0.0023
^{239}Pu (n_{th}, f)	0.0193	0.0016
^{241}Pu (n_{th}, f)	0.0209	0.0014

TABLE 6.2: Cumulative yield for ^{92}Rb for the three targets ^{235}U (n_{th}, f), ^{239}Pu (n_{th}, f) and ^{241}Pu (n_{th}, f).

Fractional and Independent nuclear charge yields for A = 96				
^{235}U (n_{th}, f)				
Isotope	fractional yield	Δ	independent yield	Δ
Z = 40 (Zr)	0.064	0.005	0.0041	0.0005
Z = 39 (Y)	0.344	0.014	0.0219	0.0025
Z = 38 (Sr)	0.549	0.021	0.0349	0.0039
Z = 37 (Rb)	0.042	0.003	0.0027	0.0003
^{241}Pu (n_{th}, f)				
Isotope	fractional yield	Δ	independent yield	Δ
Z = 40 (Zr)	0.055	0.012	0.0026	0.0006
Z = 39 (Y)	0.351	0.031	0.0166	0.0015
Z = 38 (Sr)	0.555	0.028	0.0263	0.0016
Z = 37 (Rb)	0.039	0.006	0.0019	0.0003

TABLE 6.3: Fractional and Independent nuclear charge yields for Zr, Y, Sr and Rb with mass A = 96 for the two targets ^{235}U (n_{th}, f) and ^{241}Pu (n_{th}, f).

measurement by Tipnis et. al [6]. The measurements in the present work provide ^{92}Rb yields for ^{235}U(n_{th}, f), ^{239}Pu(n_{th}, f) and ^{241}Pu(n_{th}, f) and ^{96}Y yield for ^{235}U(n_{th}, f) and ^{241}Pu(n_{th}, f). Fig. 6.25 presents the cumulative yields of ^{92}Rb for the three targets ^{235}U(n_{th}, f), ^{239}Pu(n_{th}, f) and ^{241}Pu(n_{th}, f) shown in red. The present data are compared to the nuclear data libraries JEFF, ENDF and JAEA (also with results of Tipnis et. al. [6] for ^{235}U) and the results of a previous experiment. The results on the ^{92}Rb yields for ^{235}U(n_{th}, f) are also comparable to the results from the previous experiment [4] - 0.0471 $\pm$ 0.0037 and provides more accurate values with consistent and detailed measurements performed in this work. In case of ^{235}U(n_{th}, f), we see a good agreement with the nuclear data libraries.

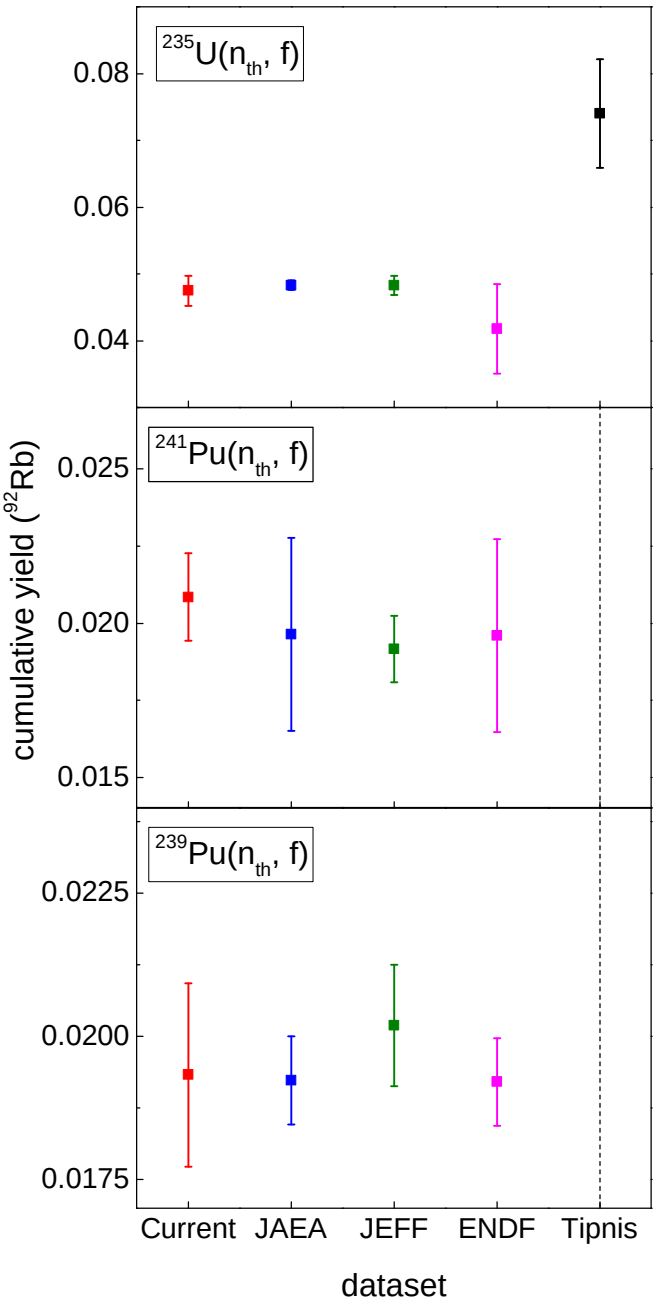

FIGURE 6.25: Cumulative yields of ^{92}Rb determined for the three targets ^{235}U(n$_{th}$, f), ^{239}Pu(n$_{th}$, f) and ^{241}Pu(n$_{th}$, f) are shown in red. The current results are compared to the nuclear data libraries JEFF and JAEA, and also with the results of Tipnis et. al. [6] for ^{235}U. For numerical data see Table 6.2.

However, on comparing the yields determined in this work for ^{92}Rb with the independent measurement reported by Tipnis et. al [6] for ^{235}U(n$_{\rm th}$, f), we find a clear disagreement for the cumulative yield. The values reported by Tipnis et. al are almost twice the value determined in the present work.

Fig. 6.26 presents the independent yields of ^{96}Y for the targets ^{235}U(n$_{th}$, f) and

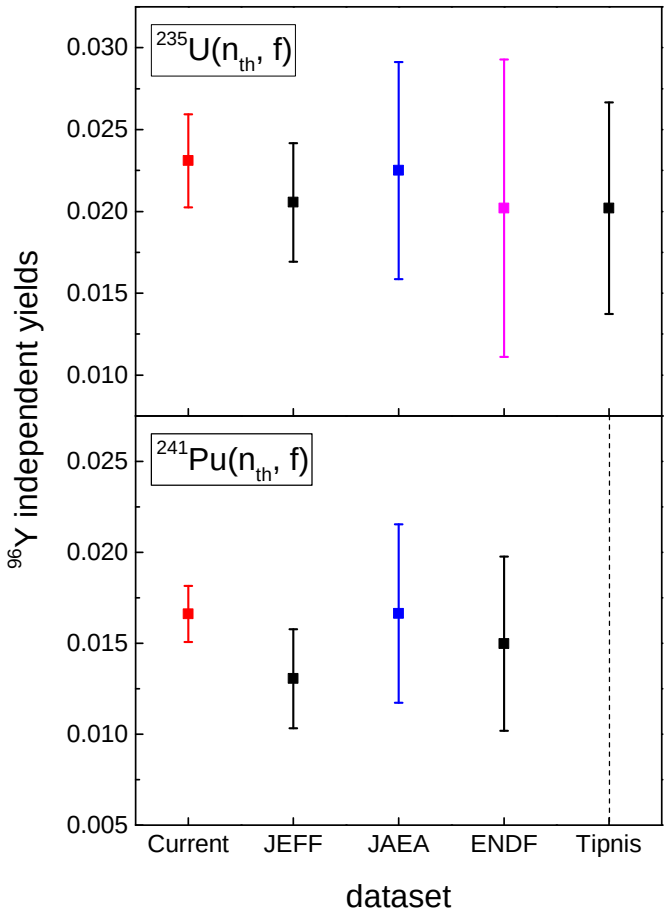

FIGURE 6.26: Independent yields of ^{96}Y measured for the targets ^{235}U(n$_{th}$, f) and ^{241}Pu(n$_{th}$, f) are shown in red. The present results are compared to the nuclear data libraries JEFF, JAEA and ENDF, and also with the results of Tipnis et. al. [6] for ^{235}U. For numerical data see Table 6.3.

^{241}Pu(n$_{th}$, f) shown in red. The present results are compared to the nuclear data libraries JEFF, JAEA and ENDF for ^{235}U and ^{241}Pu(n$_{th}$, f). The ^{92}Rb and ^{96}Y yields are in good agreement with the nuclear data libraries like JAEA, JEFF and ENDF, with improved accuracy with respect to ENDF and JAEA data in several cases, in particular for the plutonium targets.

It shall be noted that ^{96}Y has two beta-decaying states, the 0^- ground state ^{96g}Y ($T_{1/2} = 5.34$ s) and the 8^+ isomeric state ^{96m}Y ($T_{1/2} = 9.6$ s). Both are populated in nuclear fission, but only the beta decay of ^{96g}Y contributes significantly to antineutrino spectra above 4 MeV while the beta decay of ^{96m}Y feeds higher-lying high-spin levels in ^{96}Zr, which increases the fraction of the Q value released as gamma rays at the expense of energy released by betas and antineutrinos. The method used in our experiment is only sensitive to isotopes but not to isomers.

Thus in this work, the isotopic yield ^{96}Y which represents the sum of the yields of both beta-decaying isomers ^{96g}Y and ^{96m}Y are presented. An additional measurement with an independent method (gamma ray spectrometry at LOHENGRIN) is required to obtain the isomeric ratio ^{96g}Y/^{96m}Y and thus transform the ^{96}Y sum yield reported here into the individual yield of ^{96g}Y relevant for the antineutrino spectra. Since ^{96g}Y decays dominantly to the ground state of ^{96}Zr or to the first excited 0^+ state, only few gamma rays accompany this decay and their intensities carry large uncertainties. Thus, a more precise value for the individual ^{96g}Y yield can be obtained by comparing the ^{96m}Y and ^{96}Sr yields which emit both intense gamma rays with well-known intensities, then subtract the so determined ^{96m}Y yield from the total $^{96g+m}$Y yield. For this purpose the newly measured independent isotopic yields for mass A = 96 (in particular ^{96g}Y and ^{96g}Sr) could be used to cancel experimental uncertainties.

In light of the reactor anti-neutrino anomaly, with the yields reported by Tipnis et. al for ^{92}Rb, the ^{92}Rb contribution to the high energy end of the anti-neutrino spectra, which represents a significant contribution for the anomaly, would further increase by 8% resulting in an even larger anti-neutrino anomaly. With the independent measurement in the present work, we could confirm that the yields reported by the data libraries are indeed better estimates.

6.3 Isotopic yields towards and in the symmetry region

Isotopic yields were determined for 24 masses in the range $89 \geq A \leq 112$ for ^{241}Pu(n_{th}, f) for the first time with LOHENGRIN. Towards the mass symmetry known Z-yield data were supplemented for masses A = 110 to 112 for ^{241}Pu(n_{th}, f), and for masses A = 110 to 113 for ^{239}Pu(n_{th}, f). Results from these measurements are presented in this section. Rather than precision in the yield measurements like in the previous section for ^{92}Rb and ^{96}Y yields, the challenge here was to measure the yields for heavier masses with worsening resolution (see Fig. 6.6) and very low

intensity towards the symmetry region. Thus, fewer LOHENGRIN energy and ionic charge settings for one mass were measured, but, with good statistics. A detailed list of measurements performed was already presented in Section 5.3.2.

6.3.1 Isotopic yields for ^{241}Pu(n_{th}, f)

A systematic approach was performed for the measurements with the ^{241}Pu(n_{th}, f) target. All 24 masses were measured with the same energy settings of LOHENGRIN with the same number of SiN foils (4 mum thick). This provided a very consistent Z-identification technique as discussed in Section 5.4.7, which is also demonstrated in Fig. 6.27. Fig. 6.27 shows the fit parameters from several mass measurements for ^{241}Pu(n_{th}, f), like the FWHM (top), separation (center) and peak position (bottom). The three columns represent the three different energies at which the measurements were performed, $E_L = 84$ MeV, 94 MeV and 102 MeV. The parameters are obtained from sum of Gaussians fits on the residual energy spectra from all these measurements. From the data analysis as discussed in Section 5.4, the relative, fractional and independent yields of the different nuclear charges for all these masses are obtained. The fractional and independent Z-yields are presented in Fig. 6.28.

The Tables C.30, C.31, C.32 and C.33 present the relative Z-yields from the CLTD measurements for all masses investigated at different LOHENGRIN energies and ionic charge settings. The nomenclature E_L is for LOHENGRIN energy and E_F is for the fission energy. The fission energy, E_F is obtained by first correcting E_L with respect to the mean energy distribution of the burn up measurements as discussed in Section 5.4.2, and then adding the estimated energy loss in the target and the cover foil as given in Section 5.4.3. Q(ionic charge) distributions and energy distributions of nuclear charges as discussed in the previous section are determined from the convolution of both CLTD and ionization chamber measurements for the mass yield distribution. For the ^{241}Pu(n_{th}, f) target it was again not possible to measure the distributions of the mass yield with the PIN diode due to limited

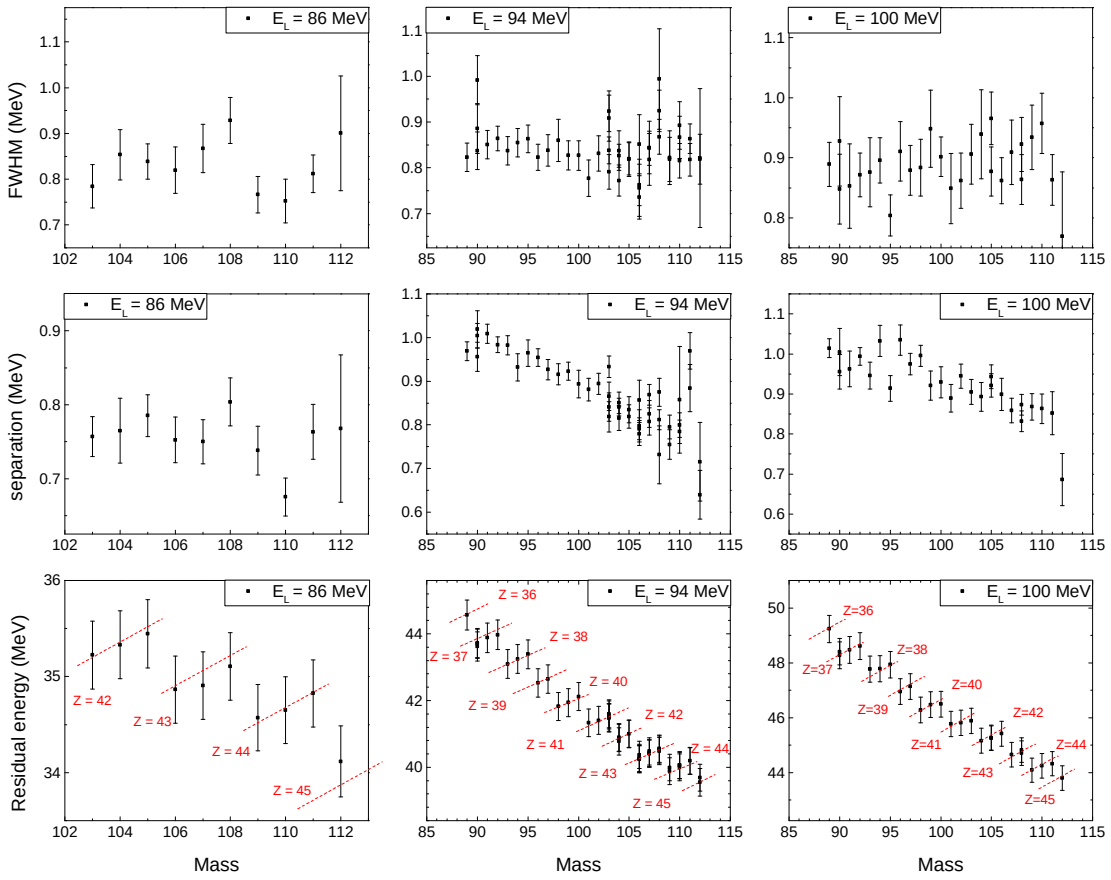

FIGURE 6.27: Fit parameters from several mass measurements for ^{241}Pu(n$_{th}$, f) like width (top), separation (center) and peak position (bottom) in the residual energy spectra. The three columns represent the three different energies at which the measurements are performed E_L = 84 MeV, 94 MeV and 102 MeV.

beam time with the thin target. Therefore for the mass yields distributions already existing measurements with an ionization chamber [132] were used for all isotopic yield measurements with the ^{241}Pu target. Tables 6.4 and 6.5 presents the fractional yields and Tables 6.6 and 6.7 present the independent yields of the nuclear charges for the masses A = 89 to A = 112. In the Fig. 6.28 the fractional Z-yields and independent Z-yields versus mass are plotted where data points in the same colour correspond to a particular nuclear charge as marked on the plot. The lines passing through the data points in the Fig. 6.28 are to follow the trend. The discussion on the behaviour of these isotopic yields follows in Section 6.3.3.

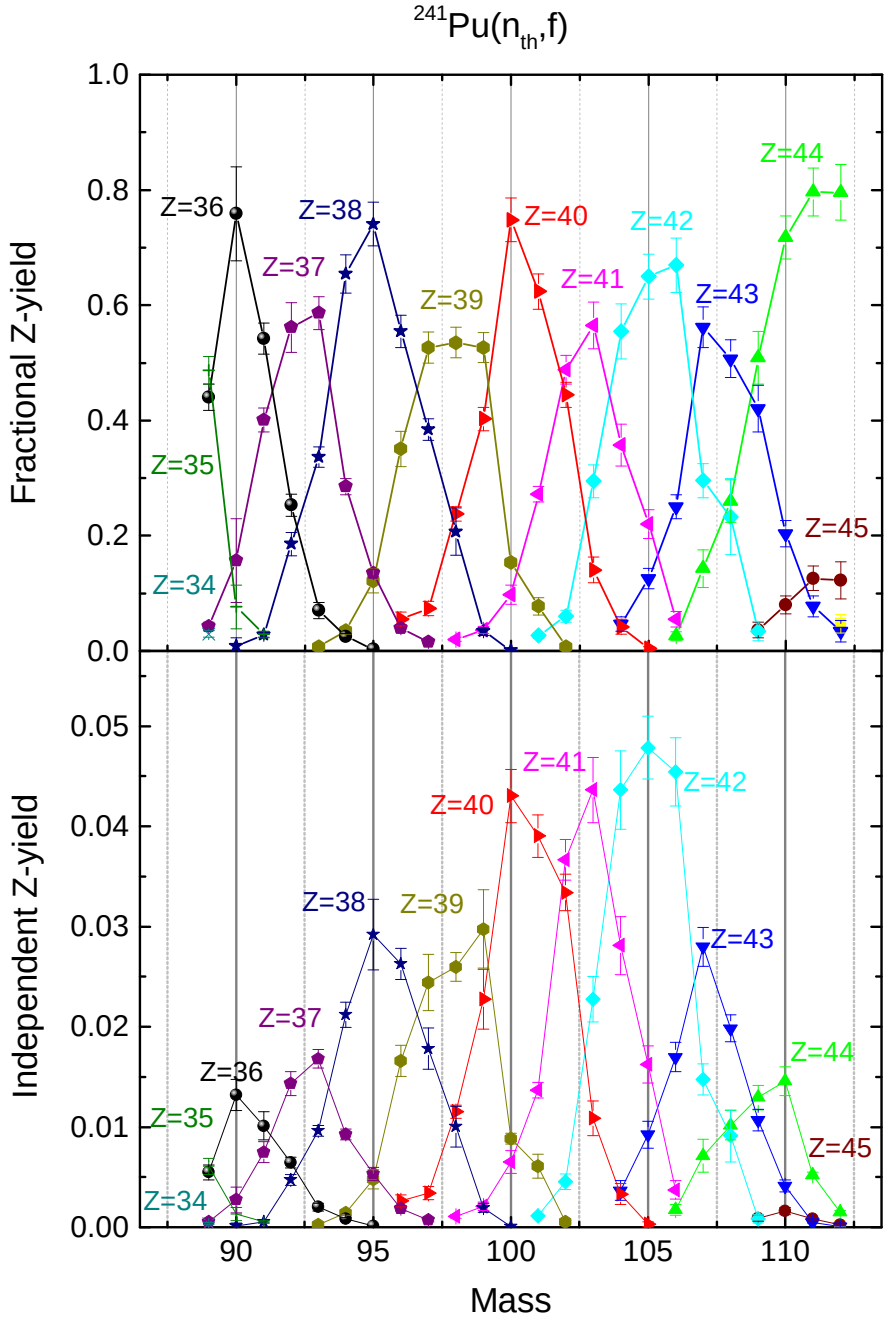

FIGURE 6.28: Fractional (top) and independent (bottom) Z-yields for ^{241}Pu (n_{th}, f). The data points are connected with lines to follow the trend.

Mass	Fractional Z-yield for ^{241}Pu (n_{th}, f)															
A	Z=46	Δ	Z=45	Δ	Z=44	Δ	Z=43	Δ	Z=42	Δ	Z=41	Δ	Z=40	Δ	Z=39	Δ
112	0.047	0.016	0.123	0.032	0.796	0.048	0.034	0.018								
111			0.126	0.022	0.797	0.041	0.078	0.018								
110			0.080	0.016	0.717	0.037	0.203	0.023								
109			0.036	0.013	0.509	0.046	0.421	0.041	0.034	0.017						
108					0.260	0.037	0.507	0.033	0.233	0.066						
107					0.143	0.033	0.561	0.035	0.296	0.030						
106					0.026	0.008	0.250	0.021	0.669	0.048	0.055	0.013				
105							0.126	0.018	0.650	0.039	0.221	0.025	0.004	0.003		
104							0.046	0.012	0.555	0.048	0.357	0.036	0.042	0.013		
103									0.294	0.029	0.565	0.040	0.141	0.022		
102									0.060	0.010	0.488	0.025	0.445	0.022	0.007	0.001
101									0.027	0.005	0.272	0.014	0.624	0.031	0.077	0.015

TABLE 6.4: Fractional Z-yields for ^{241}Pu (n_{th}, f).

Mass	Fractional Z-yield for ^{241}Pu (n_{th}, f)															
A	Z=41	Δ	Z=40	Δ	Z=39	Δ	Z=38	Δ	Z=37	Δ	Z=36	Δ	Z=35	Δ	Z=34	Δ
100	0.097	0.016	0.748	0.038	0.154	0.008	0.001	0.000								
99	0.037	0.006	0.402	0.021	0.527	0.026	0.034	0.007								
98	0.020	0.003	0.238	0.012	0.535	0.026	0.207	0.041								
97			0.073	0.012	0.527	0.027	0.384	0.019	0.015	0.003						
96			0.055	0.012	0.351	0.031	0.555	0.028	0.039	0.006						
95					0.121	0.021	0.741	0.038	0.135	0.007	0.003	0.001				
94					0.035	0.006	0.654	0.033	0.285	0.014	0.025	0.005				
93					0.007	0.001	0.336	0.017	0.586	0.029	0.070	0.014				
92							0.185	0.020	0.561	0.043	0.253	0.019				
91							0.028	0.005	0.401	0.020	0.542	0.027	0.029	0.006		
90							0.008	0.015	0.157	0.073	0.759	0.082	0.076	0.038		
89									0.043	0.007	0.440	0.022	0.487	0.024	0.029	0.006

TABLE 6.5: Fractional Z-yields for ^{241}Pu (n_{th}, f).

Mass	Independent Z-yield for ^{241}Pu (n_{th}, f)													
A	Z=46	Δ	Z=45	Δ	Z=44	Δ	Z=43	Δ	Z=42	Δ	Z=41	Δ	Z=40	Δ
112	0.0001	0.0000	0.0002	0.0001	0.0015	0.0002	0.0001	0.0000						
111			0.0006	0.0001	0.0041	0.0004	0.0004	0.0001						
110			0.0016	0.0003	0.0146	0.0014	0.0041	0.0006						
109			0.0011	0.0004	0.0151	0.0025	0.0125	0.0021	0.0010	0.0005				
108					0.0113	0.0021	0.0221	0.0031	0.0102	0.0031				
107					0.0079	0.0021	0.0311	0.0043	0.0164	0.0026				
106					0.0015	0.0005	0.0149	0.0022	0.0399	0.0057	0.0033	0.0009		
105							0.0083	0.0015	0.0432	0.0054	0.0147	0.0023	0.0003	0.0002
104							0.0031	0.0009	0.0370	0.0051	0.0238	0.0035	0.0028	0.0009
103									0.0193	0.0030	0.0369	0.0053	0.0092	0.0018
	Z=42	Δ	Z=41	Δ	Z=40	Δ	Z=39	Δ	Z=38	Δ	Z=37	Δ	Z=36	Δ
102	0.0038	0.0008	0.0304	0.0038	0.0277	0.0034	0.0004	0.0001						
101	0.0016	0.0003	0.0163	0.0022	0.0373	0.0051	0.0046	0.0011						
100			0.0056	0.0011	0.0430	0.0045	0.0088	0.0009	0.0001	0.0000				
99			0.0021	0.0004	0.0227	0.0030	0.0298	0.0039	0.0019	0.0005				
98			0.0010	0.0002	0.0115	0.0015	0.0260	0.0034	0.0101	0.0024				
97					0.0034	0.0007	0.0244	0.0028	0.0178	0.0021	0.0007	0.0002		
96					0.0024	0.0006	0.0149	0.0021	0.0235	0.0029	0.0017	0.0003		
95							0.0048	0.0010	0.0292	0.0035	0.0053	0.0006	0.0001	0.0000
94							0.0012	0.0002	0.0212	0.0027	0.0093	0.0012	0.0008	0.0002
93							0.0002	0.0000	0.0096	0.0013	0.0168	0.0023	0.0020	0.0005

TABLE 6.6: Independent Z-yields for ^{241}Pu (n_{th}, f). Continued on next table..

Mass	Independent Z-Yields for ^{241}Pu (n_{th}, f)									
A	Z=38	Δ	Z=37	Δ	Z=36	Δ	Z=35	Δ	Z=34	Δ
92	0.0042	0.0007	0.0127	0.0019	0.0057	0.0008				
91	0.0005	0.0001	0.0075	0.0011	0.0101	0.0014	0.0005	0.0001		
90	0.0001	0.0002	0.0024	0.0012	0.0117	0.0017	0.0012	0.0006		
89			0.0005	0.0001	0.0055	0.0008	0.0061	0.0008	0.0004	0.0001

TABLE 6.7: Independent Z-yields for ^{241}Pu (n_{th}, f).

6.3.2 Isotopic yields for ^{239}Pu(n_{th}, f)

Similarly isotopic yields were determined for ^{239}Pu(n_{th}, f) for the masses A = 109 to A = 113. Tables 6.8 and 6.9 present the fractional and independent nuclear charge yields, respectively for the masses A = 109 to 113. In Fig. 6.29 the fractional and independent charge yields for the above mentioned masses are plotted. Fig. 6.30 shows the fractional Z-yields of the measured masses (solid data points) for ^{239}Pu(n_{th}, f) along with the previous measurements from Schmitt et. al. [133] (open data points).

Mass	Fractional Z-Yields: ^{239}Pu (n_{th}, f)							
A	Z = 46	Δ	Z = 45	Δ	Z = 44	Δ	Z = 43	Δ
109			0.067	0.019	0.686	0.052	0.247	0.027
110			0.078	0.018	0.905	0.040	0.017	0.009
111			0.264	0.033	0.722	0.044	0.014	0.011
112	0.125	0.050	0.477	0.057	0.398	0.066		
113	0.254	0.129	0.746	0.243	0.000			

TABLE 6.8: Fractional Z-yields for ^{239}Pu (n_{th}, f).

Mass	Independent Z-yield: ^{239}Pu (n_{th}, f)							
A	Z=46	Δ	Z=45	Δ	Z=44	Δ	Z=43	Δ
109			0.112	0.035	1.148	0.165	0.414	0.068
110			0.049	0.012	0.565	0.070	0.011	0.006
111			0.081	0.014	0.222	0.029	0.004	0.004
112	0.016	0.007	0.061	0.011	0.051	0.011		
113	0.021	0.011	0.060	0.021				

TABLE 6.9: Independent Z-yields for ^{239}Pu (n_{th}, f).

Fig. 6.31 (left) shows the fractional Z-yields of the measured masses from ^{241}Pu(n_{th}, f) in comparison with previous measurements from P. Schillebeeckx et. al. [134] for Z = 39, 41 and 43 in the right plot of Fig. 6.31. A good agreement is observed between the results of this work obtained with CLTDs and the results of P.Schillebeeckx et. al [134] determined from an experiment with the Cosi-Fan-Tutte spectrometer. Having a good agreement of the present results obtained with

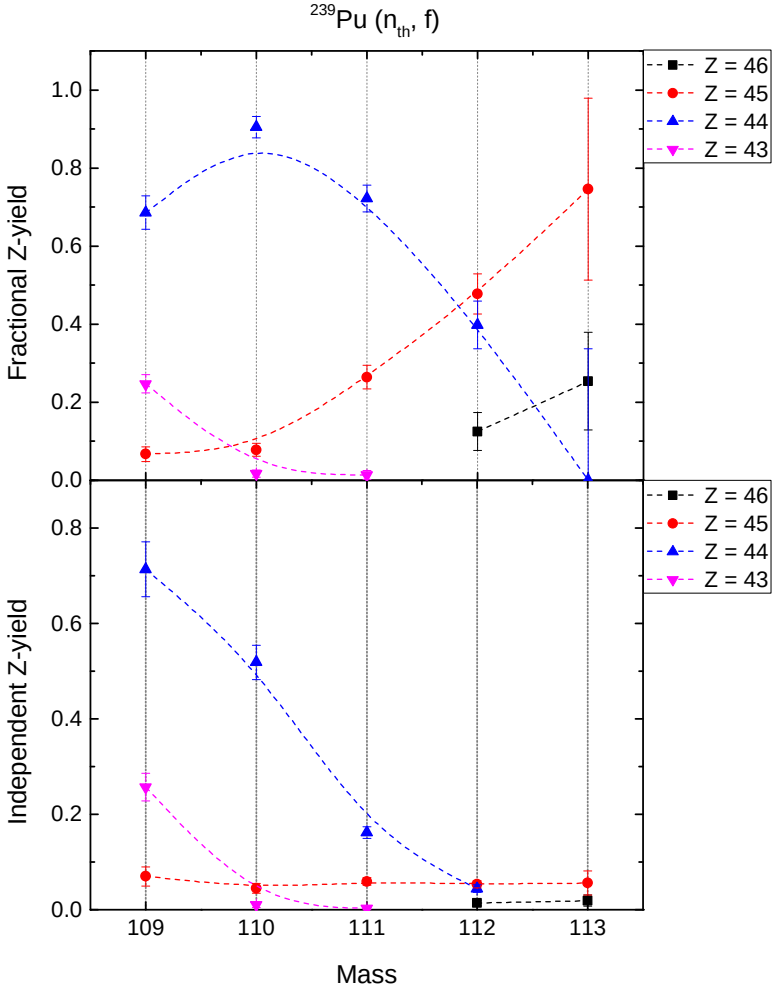

FIGURE 6.29: Fractional and Independent Z-yields for ^{239}Pu (n_{th}, f). The data points are connected with dotted lines to follow the trend.

CLTDs with a completely different experimental set-up, namely a time-of-flight apparatus [134], gives confidence in the results obtained with the CLTDs.

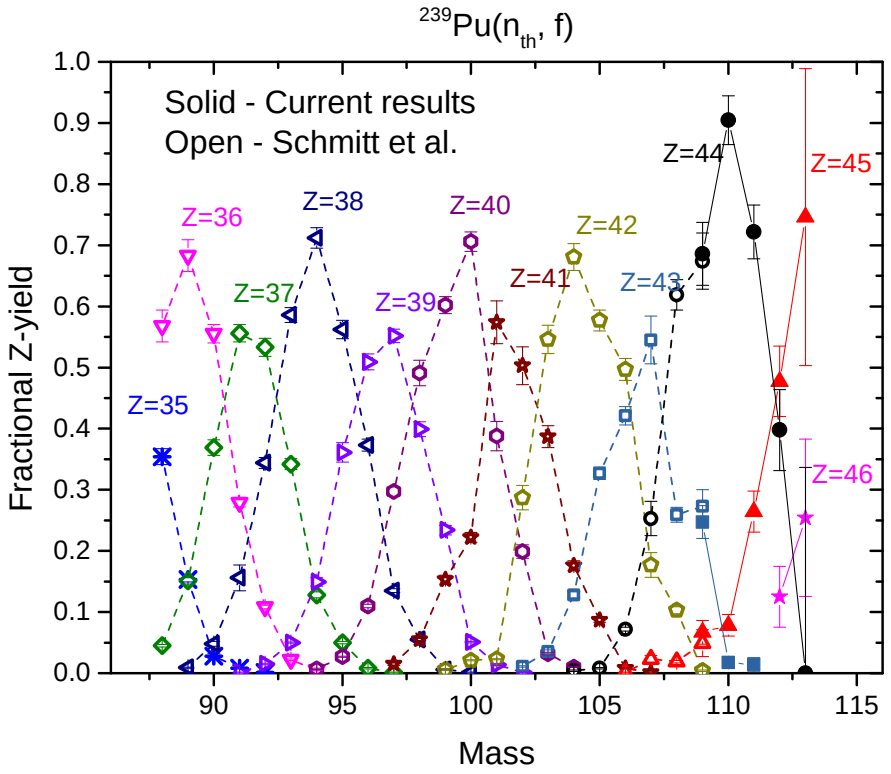

FIGURE 6.30: Fractional isotopic yields of the measured masses (solid data points) from ^{239}Pu(n_{th}, f) along with previous measurements from Schmitt et. al. [133] (open data points).

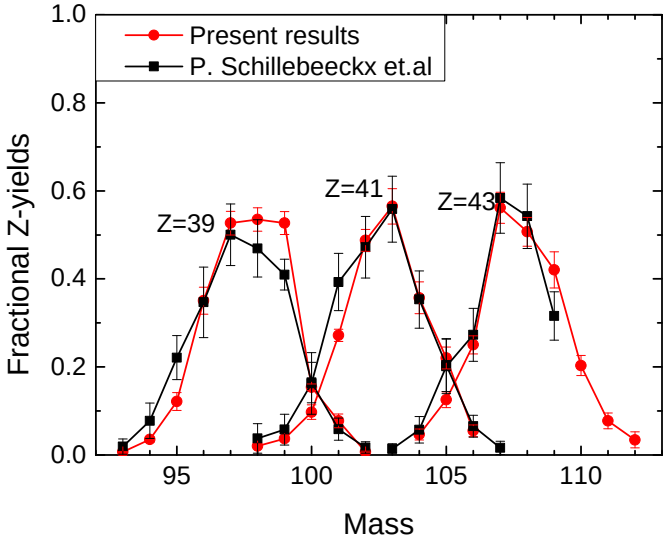

FIGURE 6.31: Comparison of measured isotopic yields to previous measurements from P. Schillebeeckx et. al. with the Cosi-Fan-Tutte spectrometer [134] for Z = 39, 41 and 43

6.3.3 Discussions on even-odd effect in isotopic yields

Towards the mass symmetry known Z-yield data were supplemented for masses A = 110 to 112 for ^{241}Pu(n_{th}, f), and for masses A = 110 to 113 for ^{239}Pu(n_{th}, f). In both the Figures 6.28 and 6.30, we observe the even-odd staggering in the Z-yields. The even Z-peaks are consistently higher compared to the odd Z-peaks. The evident reason for this staggering which favours even charge splits is proton pairing in fragments from fissioning even-Z compounds (Plutonium with an even Z = 94 for example in this case). In the case of thermal neutron induced fission where the excitation energy is below the proton-pairing energy at the saddle point, a dominant even-odd effect is observed reflecting that the nuclear shell and pairing effects play a major role but at present, this is not very well understood theoretically. The even-odd staggering in fragment yields is therefore a critical test of theoretical calculations of pair-breaking in fission.

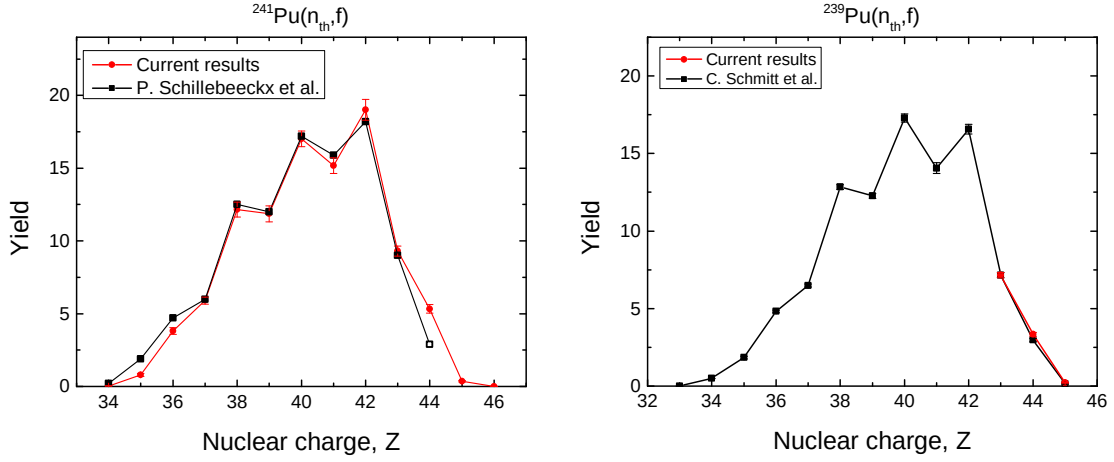

FIGURE 6.32: The isotopic yields summed over all the masses for ^{241}Pu(n_{th}, f) (left) and ^{239}Pu(n_{th}, f) (right). Measured yields (red data points) are compared to literature values (black data points) from P. Schillebeeckx et. al. [134] for ^{241}Pu, and from Schmitt et. al [133] for ^{239}Pu, respectively.

Fig. 6.32 which shows the isotopic yields summed over all masses for ^{241}Pu(n_{th}, f) (left) and ^{239}Pu(n_{th}, f) (right) is a good demonstration for the even-odd effect observed in the measured isotopic yields. Measured yields (red data points) are also compared to the literature values (black data points) from P. Schillebeeckx et al. [134] for ^{241}Pu, and from Schmitt et al. [133] for ^{239}Pu. The data at Z = 44 from P. Schillebeeckx et al. for ^{241}Pu(n_{th}, f) (left) was partially measured

and hence is shown by an open dot. The heavier masses which also contribute for Z = 44 were not measured by P. Schillebeeckx et al.. In this work, with the new measurements for heavier masses towards symmetry we could determine the Z - yields upto Z = 46. Since we also include the contributions to Z = 44 from heavier masses, our results estimate a larger value for the isotopic yield for Z = 44 compared to the value from P. Schillebeeckx et al.. We observe the even-odd staggering with a peak for the even charges and a fall for odd charges for both for ^{241}Pu(n_{th}, f) (left) and for ^{239}Pu(n_{th}, f) (left).

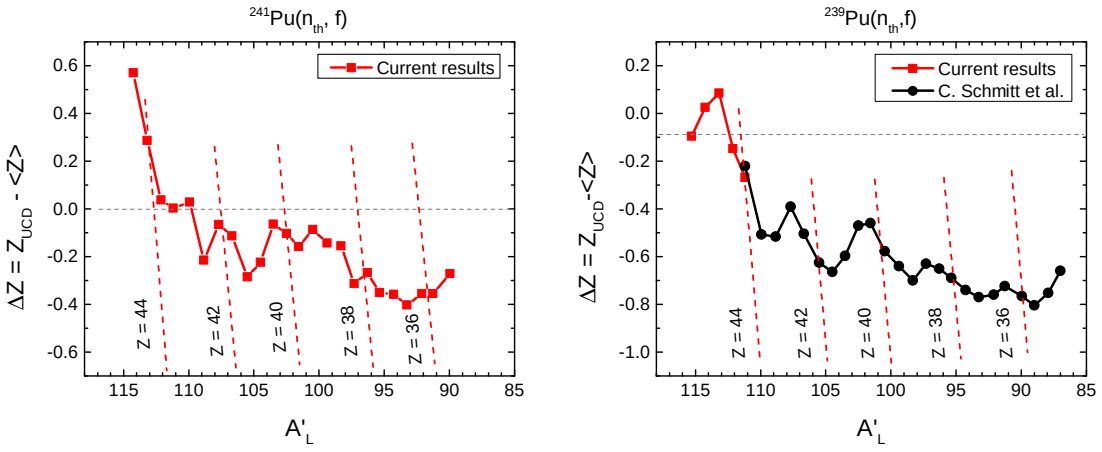

FIGURE 6.33: $\Delta Z = Z_{UCD} - < Z >$ as a function of the pre-neutron emission mass of the light fragments A'_L where ΔZ is the deviation from the average isobaric charge $< Z >$ from an unchanged charge distribution (Z_{UCD}) for both ^{241}Pu(n_{th}, f) (left) and ^{239}Pu(n_{th}, f) (right).

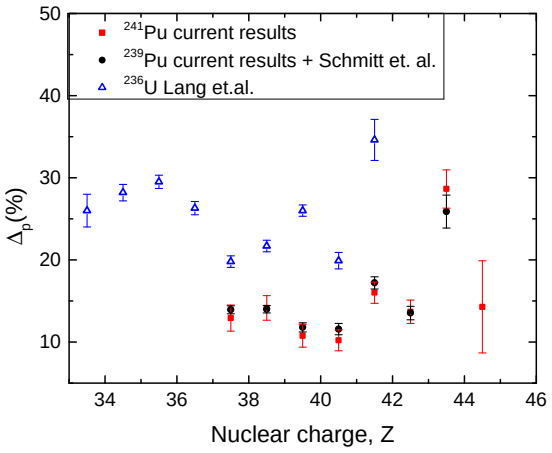

FIGURE 6.34: Local proton odd even effect Δ_p versus the nuclear charge.

In order to study the behaviour of the average nuclear charge, the quantity usually used in the literature [2], ΔZ, is plotted as a function of the mass of the light

fragments in Fig, 6.33. ΔZ is the deviation of the mean nuclear charge $< Z >$ from an unchanged charge density (Z_{UCD}) which is given by:

$$\Delta Z = Z_{UCD} - < Z > \tag{6.2}$$

$$Z_{UCD} = A'_L \times Z_F / A_F \tag{6.3}$$

where $< Z >$ is the average value of the isobaric nuclear charge distributions summed over the kinetic energy. The quantity A'_L is defined as $A'_L = A_L + \nu(A'_L)$ where A_L is mass number of the light fission product after neutron evaporation and $\nu(A_L)$ is the average number of neutrons emitted from the fission fragment as a function of the pre-neutron emission mass number. Also, the modulation of the deviation ΔZ of the average nuclear charge from the unchanged charge density value Z_{UCD} which represents the "democratic" distribution of neutron excess, is a consequence of the proton even-odd effect. A significant rise is observed in the ΔZ values towards the symmetry region. with highest values for Z = 44 corresponding to the closed shell Z = 50 of the heavy fragment. In case of ^{239}Pu(n_{th}, f), the measurements were performed at the heavier masses to see the dip in the ΔZ values beyond Z = 44. These measurements were performed to push the measurements to study even-odd effects in the isotopic yields of fission fragments towards symmetry as it is evident from mass-energy correlations of fragments that asymmetric and symmetric fission are two distinct modes [9]. It is so far conjectured from structures in the mass yield curves that only a small even-odd effect should be present. On the way from asymmetry to symmetry, LOHENGRIN experiments in the past point however to the onset of a sizable even-odd effect [9]. Extending the isotopic yield measurements to more masses towards the symmetry shows that the even-odd effect is not continually rising from asymmetry to symmetry but indeed drops beyond Z = 44 corresponding to the closed shell Z = 50 of the heavy fragment. This proves to be a sensitive test of models claiming that the even-odd effects always decrease from asymmetry to symmetry [9, 38]. In addition the proton odd-even effect is determined using the definition of Δ_p from Tracy et. al. [135] based

on a method of differences, given by:

$$\Delta_p = \frac{1}{8}(-1)^{Z+1}[(L_3 - L_0) - 3(L_2 - L_1)] \tag{6.4}$$

where L_0, L_1, L_2 and L_3 are natural logarithms of the energy-summed element yields for Z, Z+1, Z+2, Z+3, respectively. Fig. 6.34 shows the proton odd even effect Δ_p versus the nuclear charge. The present results are displayed in red for ^{241}Pu, and in black for ^{239}Pu (along with data from Schmitt et al. [133] for smaller nuclear charges supplementing measurements with the CLTDs). These results are also compared to the results for ^{235}U from Lang et. al. [136]. Here again we see that the proton even-odd effect decreases beyond Z = 44 for ^{239}Pu and the same is expected for ^{241}Pu.

6.4 Isotopic yields in the heavy mass region

Finally, isotopic yields were determined in the heavy fragment region for masses A = 128 to 137 for the first time with the passive absorber method for ^{239}Pu(n_{th}, f). These measurements as mentioned already in Section 5.3.3 were performed with 6 μm thick SiN foils. Due to fast target burn-up for ^{239}Pu(n_{th}, f), measurements could be performed at only two energies, E_L = 80 MeV and 88 MeV. Fig. 6.35 shows an example spectrum for mass A = 133 measured with CLTDs. Three nuclear charge contributions corresponding to ^{133}Zr (Z = 51), ^{96}Y (Z = 52) and ^{96}Sr (Z = 53) were determined by performing the sum of three exponentially modified Gaussians fits on the residual energy spectra.

6.4.1 Z-yields for masses A = 128 to 137 for ^{239}Pu (n_{th}, f)

This section presents the results from the measurements in the heavy mass region for masses A = 128 to A = 137 for ^{239}Pu (n_{th}, f). These measurements were performed for two energies E_L = 80 MeV and E_L = 88 MeV. The analysis for these measurements was rather challenging because the residual energy

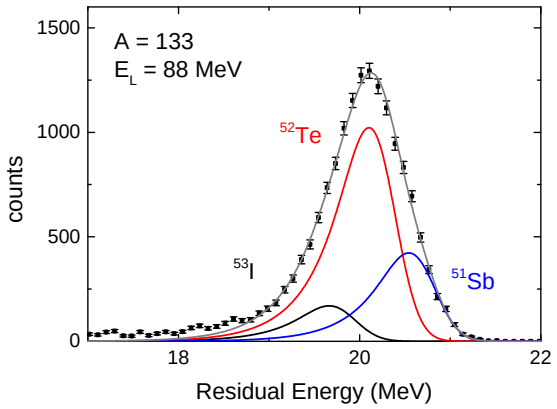

FIGURE 6.35: An example spectrum for isotopic yield calculations for mass A = 133 with the contributions from different nuclear charges.

spectra compromised of overlapping nuclear charge peaks. The technique implemented here to retrieve the Z-yields was to perform constrained fits with iterations. The problem of identification and separate quantification of overlapping peaks is present in many fields of research and various computational approaches for this deconvolution problem have been reported in literature (see [137]). Basically, the quality of the results depend on the knowledge on spectroscopic parameters, such as peak width and separation, the response function and, last but not least, on the available counting statistics. All these measurements had over 10000 counts in the peak and were fitted with a sum of three modified Gaussians given in Eq. 5.2 (see also Fig. 5.7b for example, a spectrum for mass A = 130 with the fits). Already from the measurements at the MLL tandem accelerator, estimates on the width and asymmetry parameter of the modified Gaussians were know for mass A = 130. With this knowledge, the first iteration of fits were initialized with all free parameters of Eq. 5.2, results of which are presented in the Fig.6.36 for an energy of E_L = 80 MeV. From these first iteration fits, the mean width parameter and the asymmetry parameter were determined. For the second iteration of fits, the width and asymmetry parameters were fixed to the mean value obtained from the first iteration, results of which are presented in Fig. 6.37. From the second iteration of fits, the mean separation between the neighbouring nuclear charges is determined and the final iteration of fits is performed with fixed width, asymmetry and separation determined from the first two iterations. A similar analysis is performed for the measurements at E_L = 88 MeV where a first iteration of fits is

performed to determine the mean width and asymmetry parameter which is then fixed for the next iteration to determine the relative Z-yields. Due to the higher energy settings at $E_L = 88$ MeV, better Z-resolution is achieved and already with two iterations consistent fits with reasonable error bars are possible. Figures 6.39 and 6.40 show the results from the first and second iterations, respectively, for the measured masses at an energy of $E_L = 88$ MeV. Also the relative Z-yields thus obtained are listed in the Table 6.10.

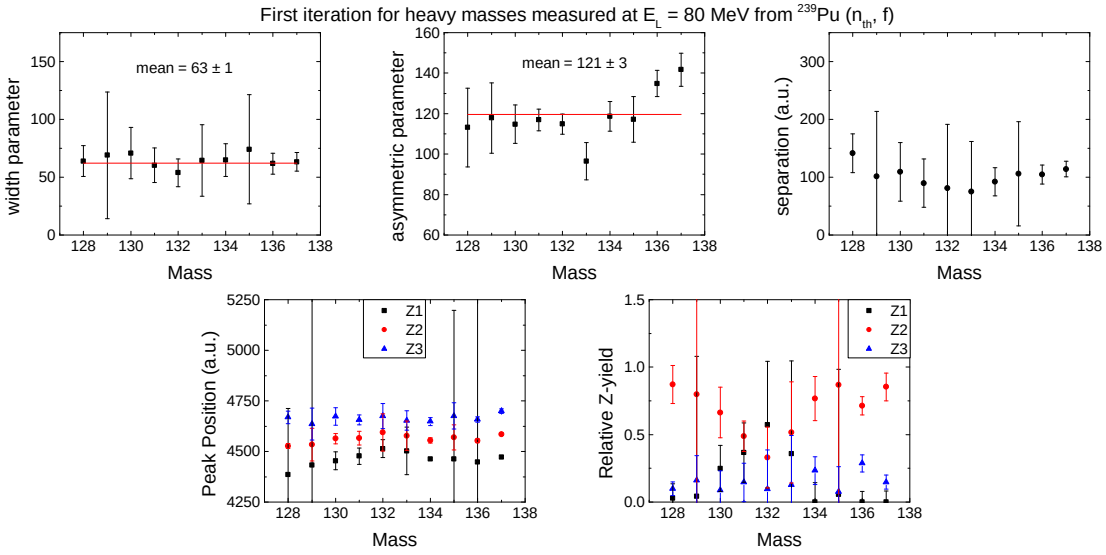

FIGURE 6.36: Fit results on the width parameter, the asymmetry parameter, the separation, the peak position and the relative Z-yields from the first iteration of fits to estimate the width parameter and the asymmetry parameter for heavy masses in the range A = 128 to A = 137 at E_L = 80 MeV for ^{239}Pu (n_{th}, f).

For the heavy mass region, a significant improvement in the Z resolving power is demonstrated (Fig. 6.6) in comparison to the extrapolations from values given in Bocquet et. al. [3]. Test measurements at the tandem accelerator at the MLL Garching (discussed in Chapter 4) with stable ^{130}Te and ^{127}I ion beams, aiming at determining the energy loss difference for adjacent Z values with the CLTD and SiN foils set-up, provided valuable data on the peak shapes in the heavy mass region. Here, residual energy peaks reveal asymmetric shapes at larger degrader thicknesses, attributed to the influence of energy loss processes. With the knowledge on the response function, constrained fits on the measured residual energy spectra could be reliably performed as discussed in Section 6.4, with a resolving power of Z/ΔZ=28 for Z=52. This demonstrates a significant improvement as

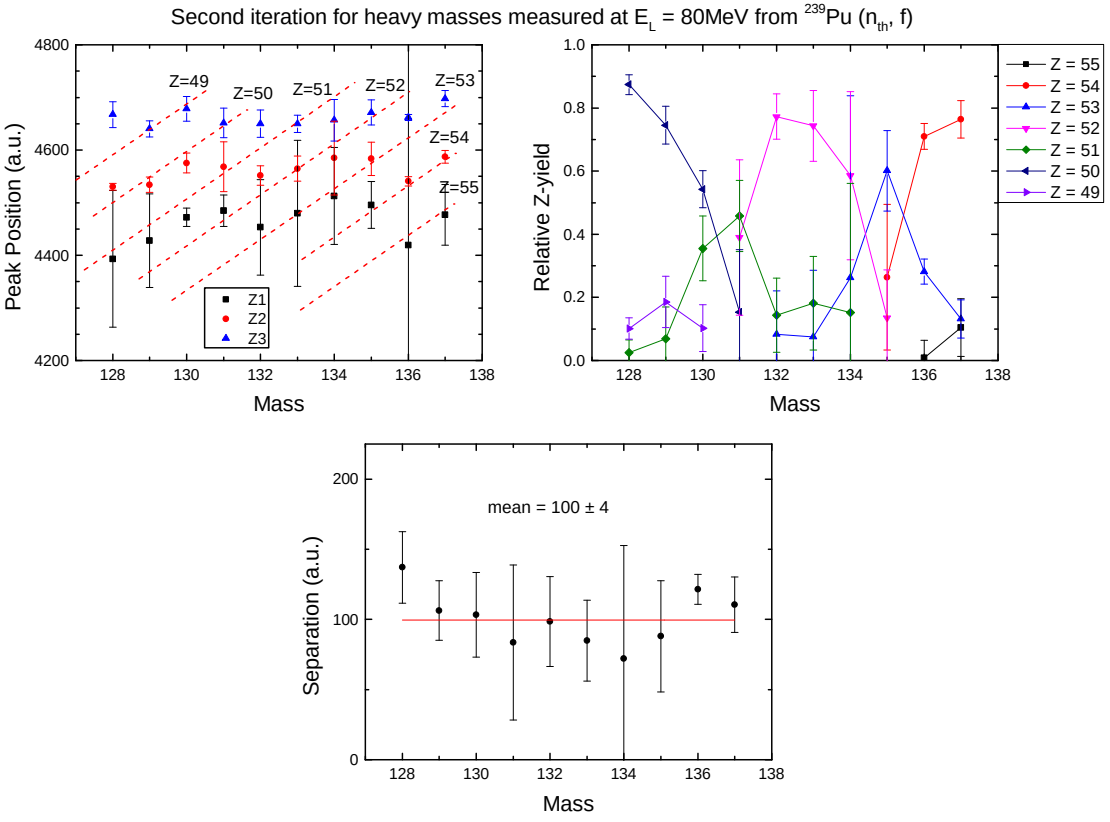

FIGURE 6.37: Fit results on the separation, the peak position and the relative Z-yields from the second iteration of fits with fixed width and asymmetry parameter determined from the first iterations to estimate the separation for heavy masses in the range A = 128 to A = 137 at E_L = 80 MeV for ^{239}Pu (n_{th}, f).

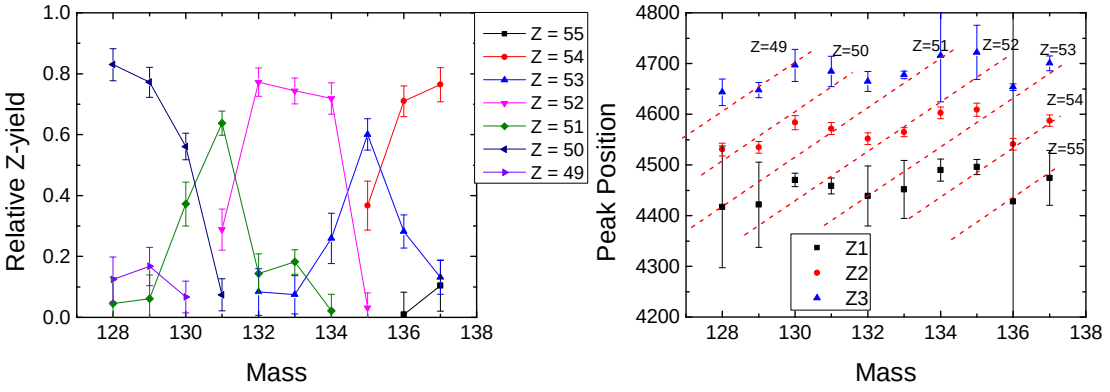

FIGURE 6.38: Results on relative Z-yields (left) with a consistent Z-identification (right) for heavy masses in the range A = 128 to A = 137 at E_L = 80 MeV for ^{239}Pu (n_{th}, f). The results were obtained from constrained fits with fixed width, asymmetry parameter and separation determined from the previous iterations shown in Fig.6.36 and 6.37.

compared to the extrapolations from previous measurements [3] as shown in Fig. 6.6.

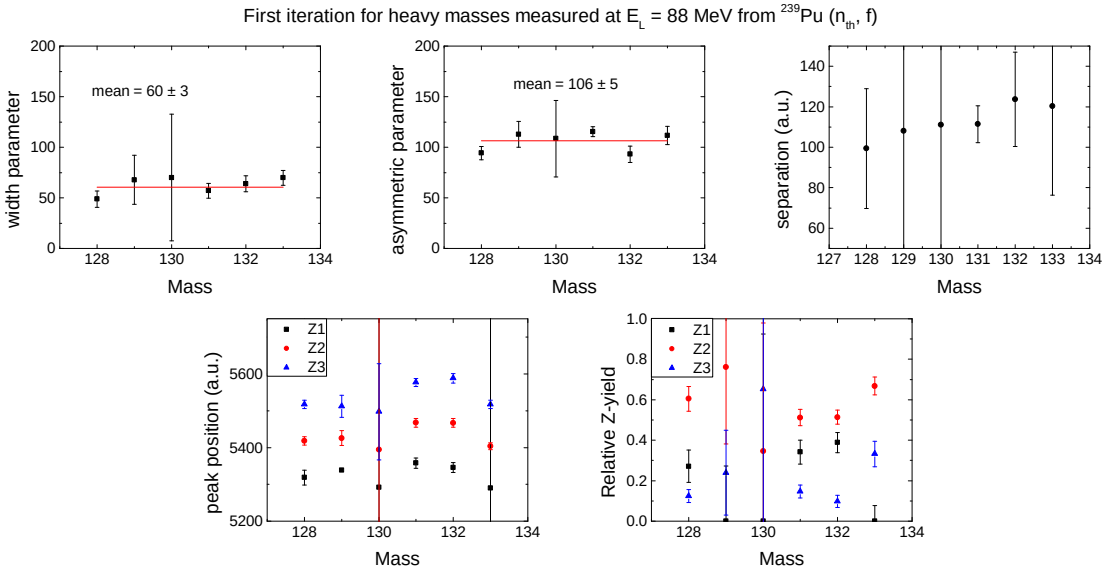

FIGURE 6.39: Fit results on the width parameter, the asymmetry parameter, the separation, the peak position and the relative Z-yields from the first iteration of fits to estimate the width parameter and the asymmetry parameter for heavy masses in the range A = 128 to A = 133 at E_L = 88 MeV for ^{239}Pu (n_{th}, f).

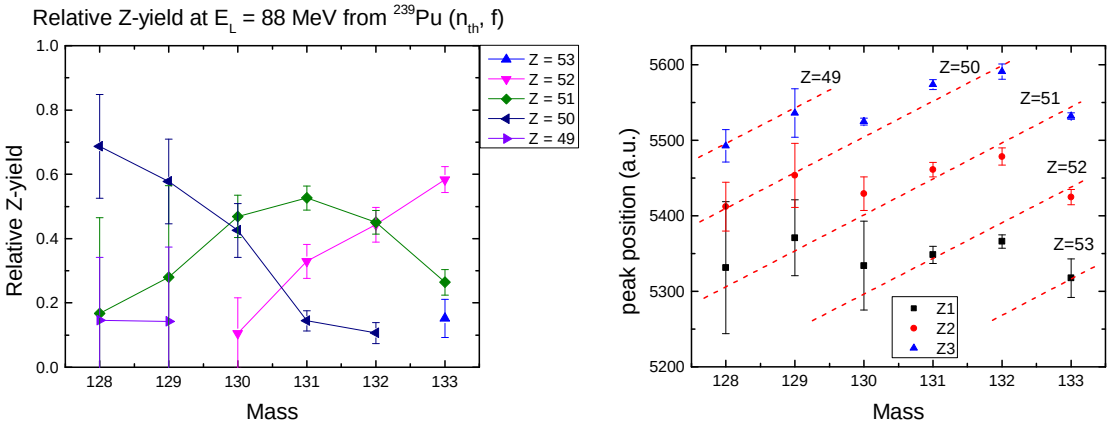

FIGURE 6.40: Results on relative Z-yields (left) with a consistent Z-identification (right) for heavy masses in the range A = 128 to A = 133 at E_L = 88 MeV for ^{239}Pu (n_{th}, f). The results were obtained from constrained fits with fixed width and asymmetry parameter determined from the first iteration shown in Fig.6.39.

In Fig. 6.41a the fractional Z-yields in the heavy mass region determined from the measurements with the present experimental set-up (solid data points) are plotted, and the results are compared to recent measurements by $\gamma-$ray spectrometry [71] (open data points) for available masses for ^{239}Pu(n_{th}, f). Also the calculated fractional Z-yields from nuclear data library JEFF 3.1.1 are plotted in Fig. 6.41b for comparison with the present results. In Fig. 6.41, a reasonable agreement

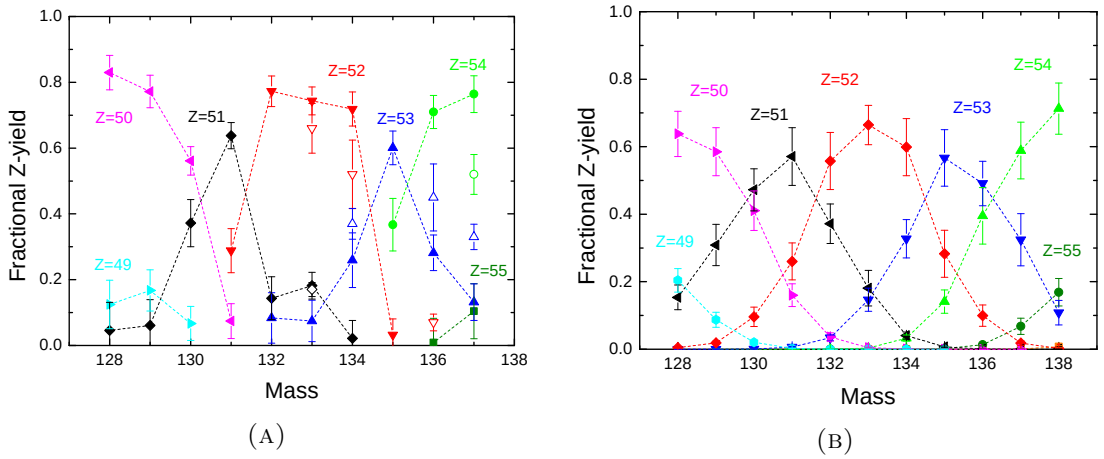

FIGURE 6.41: (a) Fractional Z-yields in the heavy mass region for ^{239}Pu(n_{th}, f) determined from the measurements with CLTD and SiN foils (solid data points). The present results are compared to recent measurements by $\gamma-$ray spectrometry [71] (open data points) for available masses. (b) calculated fractional Z-yields from the nuclear data library JEFF 3.1.1 for comparison.

is observed for the results on overall Z-yield distributions. This finding confirms the nuclear charge identification from the present CLTD measurements and the calculations from the nuclear data library JEFF 3.1.1. Also in the present results we see an odd-even effect in the Z-yields with all the even Z peaks higher than the odd Z. It should be noted here that the calculations of the JEFF data-base are averaged over the kinetic energy distributions whereas the results obtained from the present measurements, due to limited beam time, are based on measurements at two energies only, and hence the differences in the Z-yield values. Also the energies at which the CLTD measurements were performed are towards the higher energy side of the kinetic energy distribution (E_L = 80 MeV and E_L = 88 MeV), and therefore a stronger odd-even effect is observed as compared to the JEFF calculations, which supports that the odd-even effect on Z- yields increases with increasing kinetic energies of the fission fragments [138]. In the measurement of heavy masses which was performed at the very end of the target's lifetime, fragment energies $E_{fission}$ are difficult to deduce due to the irregular target burn-off. For the series of measurements at E_L 88 MeV we can assume that the target cover was obviously no longer existing at the time of the measurement. We estimate $E_{fission}$ to be about 90 MeV. For the series at E_L = 80 MeV , a partly covered target is assumed to had caused a wider energy distribution from $E_{fission}$ = 82 to

90 MeV. A more detailed set of measurements with several energies for each mass would yield more accurate results on the Z-yields. However, with the present accuracy, we have a close agreement with the JEFF data. The comparison is indeed a valuable proof that this innovative techniques and analysis are well suited for the purpose. On the other hand, an analysis of charge polarisation in the measured range of heavy fragments prove that the present charge identification is correct and the experimental method and analysis serves the purpose.

Besides the possibility of cross-checking available experimental Z-yield data with an alternative technique, the measurements performed with CLTDs and SiN foils in this work allow to complete the experimental data sets with masses 130 - 132 and 135, which are either not easily or not at all accessible with γ-ray spectrometry. We finally believe that our approach of deducing isotopic fission-fragment yields with applying the novel technologies of CLTDs and SiN degraders provides a wide scope for further improvements both from a methodical and technological point of view.

Mass	Relative Z-yield for ^{239}Pu (n_{th}, f) at E_L = 80 MeV													
A	Z=55	Δ	Z=54	Δ	Z=53	Δ	Z=52	Δ	Z=51	Δ	Z=50	Δ	Z=49	Δ
128									0.046	0.085	0.830	0.052	0.125	0.074
129									0.061	0.078	0.772	0.049	0.167	0.063
130									0.372	0.072	0.561	0.044	0.067	0.052
131							0.288	0.067	0.638	0.040	0.074	0.053		
132					0.084	0.077	0.773	0.047	0.144	0.065				
133					0.075	0.063	0.744	0.042	0.182	0.041				
134					0.259	0.083	0.719	0.052	0.022	0.054				
135			0.367	0.080	0.601	0.051	0.032	0.048						
136	0.009	0.074	0.710	0.050	0.282	0.054								
137	0.104	0.084	0.764	0.056	0.132	0.055								
Mass	Relative Z-yield for ^{239}Pu (n_{th}, f) at E_L = 88 MeV													
A	Z=55	Δ	Z=54	Δ	Z=53	Δ	Z=52	Δ	Z=51	Δ	Z=50	Δ	Z=49	Δ
128									0.168	0.297	0.686	0.161	0.146	0.195
129									0.280	0.285	0.577	0.131	0.143	0.231
130							0.106	0.110	0.469	0.066	0.425	0.083		
131							0.329	0.053	0.526	0.037	0.144	0.031		
132							0.443	0.054	0.450	0.037	0.106	0.033		
133					0.152	0.059	0.583	0.040	0.264	0.040				

TABLE 6.10: Relative Z-yield for ^{239}Pu (n_{th}, f) for masses A = 128 to A =137 at E_L = 80 MeV and for masses A = 128 to A = 133 at E_L = 80 MeV.

Chapter 7

Conclusions and Future Perspectives

In this work isotopic yield investigations were performed for thermal neutron induced fission reactions using CLTDs with the passive absorber method in a series of experiments at the LOHENGRIN spectrometer at the ILL Grenoble. The present work expands the isotopic yield determination with the passive absorber method [1–3] from the light fragment mass region to the symmetry and heavy fragment mass region where the isotopic yield determinations were rather challenging or hardly accessible until now [2]. A new CLTD array of 25 detector pixels was constructed based on the previous work by A. Echler [107] and P. Grabitz [4]. One of the modifications compared to the previous versions was to solder instead of gluing the Au bond wires from individual pixels to the read-out cables (Fig. 3.2b) in order to achieve better electrical contact. Secondly, the configuration of the twisted pair cables previously used for the read out [4] was changed to a read-out with individual cables for each detector pixel in order to eliminate cross-talk between different pixels observed in the previous experiments [4]. These detectors can be used to measure heavy ions with energies up to 300 MeV with an energy resolution of less than 1%. A major development in the detector setup for the fission yield studies was the installation of a manipulator with several positions for SiN absorber foil stacks (used for the passive absorber method) in front of the detectors

at only 5 mm distance. It was technically challenging to operate the manipulator at temperatures down to 1 K close to sensitive detectors (at $\sim$ 5 mm distance) with limited space inside the cryostat. But it provided flexibility in the absorber foil thickness and improved the detection efficiency as compared to the previously used set-up in the first tests of CLTDs with fission fragments [4] which was in the range of 10 - 70 % depending on the SiN absorber foil thickness to almost 100% for all absorber thicknesses in the present case. These improvements allowed to perform first systematic isotopic yield studies from thermal neutron induced fission reactions with CLTDs for fission fragments particularly in the symmetry region with extremely low intensities and in the heavy mass region by adapting optimum absorber thicknesses in the respective cases.

The operation of the new detector set-up was successfully tested at the Munich tandem accelerator (MLL) with the heavy ion beams ^{130}Te and ^{127}I in the energy range of 45 MeV to 80 MeV, comparable to the kinetic energy distribution of the fission fragments in the heavy mass region (Fig. 2.3). The energy resolutions of ^{130}Te and ^{127}I ion beams measured with CLTDs at the MLL was less than 1 %. Energy loss measurements with the heavy ion beams ^{130}Te and ^{127}I were performed at different SiN absorber thicknesses to estimate the expected quality of the nuclear charge separation in the heavy mass region of fission fragments and to gain insights on the shape of energy loss distributions. Residual energy spectra revealed increasing asymmetry in the peaks at larger degrader thicknesses, which could be well represented by an exponentially modified Gaussian with a tail on the lower energy side of the peak attributed to increasing nuclear energy straggling with increasing degrader thicknesses. This was in particular helpful for the analysis of overlapping peaks in order to determine the isotopic yields in the heavy fragment mass region. Additionally tests were performed to investigate the fluctuations beyond the statistical errors in the detector response (i.e., energy resolution), observed in the measured energy resolution with pure beams in the previous experiments [4, 107]. These tests revealed a dependence of the energy response on the position of the CLTD pixel where the ion beam hits the detector, as well as a dependence on the dimension of the beam spot which could explain the previously

observed fluctuations in energy resolution (δE/E) of the order 0.5%. Nevertheless already the present performance of CLTDs with SiN absorber foils provide substantial improvement in nuclear charge resolution in particular for medium heavy and heavy masses as compared to the previously used conventional techniques for the passive absorber method.

In the experiments performed at the ILL reactor, isotopic yields were determined with the new detector set-up in the light, symmetry and heavy fragment mass regions for the thermal neutron induced fission of ^{235}U, ^{239}Pu and ^{241}Pu targets. Results from these measurements are summarized below:

A first set of measurements was performed for the precise yield determination of ^{92}Rb for the three targets and ^{96}Y for ^{235}U and ^{241}Pu targets due to its importance for the understanding of the reactor anti-neutrino anomaly studies [5]. The ^{92}Rb and ^{96}Y yields thus determined (Fig. 6.25 and Fig.6.26) allowed to resolve the discrepancy between the recent independent measurement presented in [6] and the nuclear data libraries like [7] for the ^{92}Rb, yield as well as confirms the ^{96}Y yields from an independent measurement. It is concluded that the value by Tipnis et al. [6] has to be considered as clear outlier for the ^{92}Rb yield in comparison to values reported in this work and values from the data libraries (Fig. 6.25). Computing the reactor anti-neutrino anomaly based on the yields reported by Tipnis et al. [6] for ^{92}Rb, the high energy part of the anti-neutrino spectra would further increase the anomaly by 8%. With the new measurement in the present work, we could confirm that the yields reported by the data libraries are indeed better estimates.

Secondly, first LOHENGRIN data on the isotopic yields for ^{241}Pu(n_{th}, f) in the light mass group towards symmetry were determined for the masses A = 89 to 112. Fragments from ^{241}Pu(n_{th}, f) were previously studied for masses A = 91 to 110 at the ILL by time-of-flight mass spectrometry using the Cosi-Fan-Tutte spectrometer [134], but no experimental values on isotopic yields were communicated, except for data at Z = 93, 41 and 43 given as graphs. The nuclear charge yield distributions deduced from the two experiments are in good agreement in view of the different experimental approaches applied (Fig. 6.31 and 6.32).

Another topic was the study of isotopic yields towards the symmetry region. The

known Z-yield data were extended for the masses A = 110 to 112 for ^{241}Pu(n_{th}, f) and for the masses A = 110 to 113 for ^{239}Pu(n_{th}, f). It is so far conjectured from structures in the mass yield curves that only a small even-odd effect should be present. On the way from asymmetry to symmetry, LOHENGRIN experiments up to mass chain A = 109 point however to the onset of a sizable even-odd effect. The investigation of isotopic yields for A $\geq$ 109 in this work permits to elucidate how the local proton even-odd effect develops towards mass symmetry, which is of high interest for nuclear model description near scission [9, 38]. We observe a sharp rise in the so-called charge polarization $\Delta Z = Z_{UCD} - < Z >$ for Z = 44 at A > 110 attributed to stabilization by the closed shell Z = 50 in the correlated heavy fragments (Fig. 6.33). The present data on ^{239}Pu(n_{th}, f) make the situation even clearer, where Z = 44 dominates ΔZ for A up to 111 but decreases thereafter. Finally, Isotopic yields were determined in the heavy fragment region for masses in the range $128 \geq A \leq 137$ for the first time with the passive absorber method for ^{239}Pu(n_{th}, f) with the novel technology of CLTDs using SiN absorber foils. Due to their principle of operation, CLTDs provide good energy linearity and resolution (Fig. 2.17) for the spectroscopy of heavy ions at low energies [21, 24–26, 28] and are therefore predestined for measuring heavy fission fragments after degradation of a large proportion of kinetic energy. Furthermore, for the first time, stacks of commercially available silicon nitride (SiN) membranes were used as degrader material, favourably replacing the previously used Parylene-C plastic foils with respect to the energy-loss straggling and, thus, Z resolving power. For the heavy fragments, the obtained Z-resolution did not permit to fully resolve individual peaks in the residual energy spectra, but to reliably retrieve fractional isotopic yields by constrained fitting of the overlapping peaks. This method is well established in high-precision mass spectroscopy [137]. It should be noted that unfortunately due to fast target burn-up, measurements in the heavy mass region could not be performed at several kinetic energies and ionic charge states but only at two kinetic energies E_L = 80 MeV (for A = 128 to 137) and 88 MeV (for A = 128 to 133). Isotopic yields for heavy masses A $\leq$ 132 were only sparsely measured in the past, mainly by radiochemical methods [139]. The comparison of the

current results on isotopic yields of heavy masses with JEFF 3.1.1 and gamma spectroscopy measurements (Fig. 6.41) proves the Z assignment to be correct and the yields in reasonable agreement with the compared values. Also, for the ^{239}Pu(n_{th}, f), isotopic yields were determined for masses A = 128 to 132 and 135 where data were not available in the recent measurements at LOHENGRIN with gamma-ray spectrometry [71] and thus completing the series for missing values.

Future Perspectives

The approach of deducing isotopic fission fragment yields with applying CLTDs and SiN degraders still presented in this work provides a wide scope for further improvements both, from a methodical and technological point of view and is briefly discussed in this section. The successful application of CLTDs for Z-yield measurements as presented in this work provides motivation for extending the Z-yield measurements particularly in the heavy fragment region for ^{239}Pu in more detail as well as for other targets. It will provide a possibility of cross-checking available data with gamma spectrometry and complete the data sets where no data are available until now.

One of the limitations we did not overcome in the present work with the current detector setup was the measurement of fission fragment beams with CLTDs without SiN absorber foils which is rather useful for a precise absolute energy calibration of CLTDs and the determination of the energy resolution of the fission fragment beams without energy loss in the absorber foils with CLTDs at the LOHENGRIN spectrometer. A discussion on tests to improve the thermal shielding in order to directly measure fission fragments with CLTDs without any absorber foils with the ILL setup was presented in Section 3.7.3. Although it was already possible to operate a few CLTD pixels under lab conditions, it was just at the limit of the thermal stability of the detectors and hence a conservative decision to use a 1μm SiN foil in front of the detectors at the ILL beam line was made given that it was not a necessity for the present measurement campaign. However, it would be very useful to estimate the different contributions- e.g., contribution of the beam energy distribution, energy straggling in the absorber foil, etc., in the total energy

resolution observed with CLTDs at the ILL.

Unfortunately due to the limited beam time, we could not perform a few foreseen tests at the ILL in order to further improve the CLTD performance that could possibly be investigated in future. As discussed in Section 4.5.4, a position dependence of the energy response of the CLTDs was observed. Better resolutions were observed when the individual CLTD pixels were illuminated partially with ion beams instead of being completely illuminated. Based on these findings, a grid with 0.2 mm holes was mounted on the disc with SiN absorber foil stacks as shown in Fig. 5.3b in order to estimate the contribution due to this effect in the total energy resolution at the LOHENGRIN spectrometer. A more sophisticated approach to improve the situation could be construction of CLTD array with smaller individual CLTD pixel size or with new designs to overcome the position dependence based on the findings presented in Section 4.5.4.

A well established approach for deducing isotopic yields at the LOHENGRIN spectrometer with ionization chambers is by running the detectors in a ΔE-E mode [3]. Due to the pulse height defect in ionization detectors, nuclear charge determination and separation becomes rather challenging towards heavier masses. Although it is just an idea for the moment, the development of calorimetric ΔE (transmission) detectors allowing ΔE-E measurements (for example using the ΔE detector as an active absorber) could bring a remarkable improvement in the quality of nuclear charge separation. This would be a rather interesting advancement from the technological point of view.

Appendix A

Appendix for Chapter 3

The dimensions of the new design are listed in the table below:

Dimensions of the new detector mount design			
Parts	Length mm	Breadth mm	Height mm
Cold finger base	90	90	7
Cold finger extension MLL	56	17	15
Cold finger extension ILL	56	17.5	35^0 slope
Detector holder	56	17	27
Rotator	35	13.5	35
Disc	ϕ 88 mm, 1 mm thick		
Foil holder_inside	18	15	10.5
SiN foils	10	16	0.001
SiN foil frames	15	20	0.5
Alpha Source	ϕ 1 inch, 0.5 mm thick		
Alpha Source backing	ϕ 1 inch, 1.1 mm thick		
height to the center of the pixel from cold finger base (mm)			
old	49.75		
new-MLL	37		

TABLE A.1: Dimensions of the cold finger parts in the new design.

Appendix B

Appendix for Chapter 5

B.1 Appendix for Section 5.4.2: Target burn-up

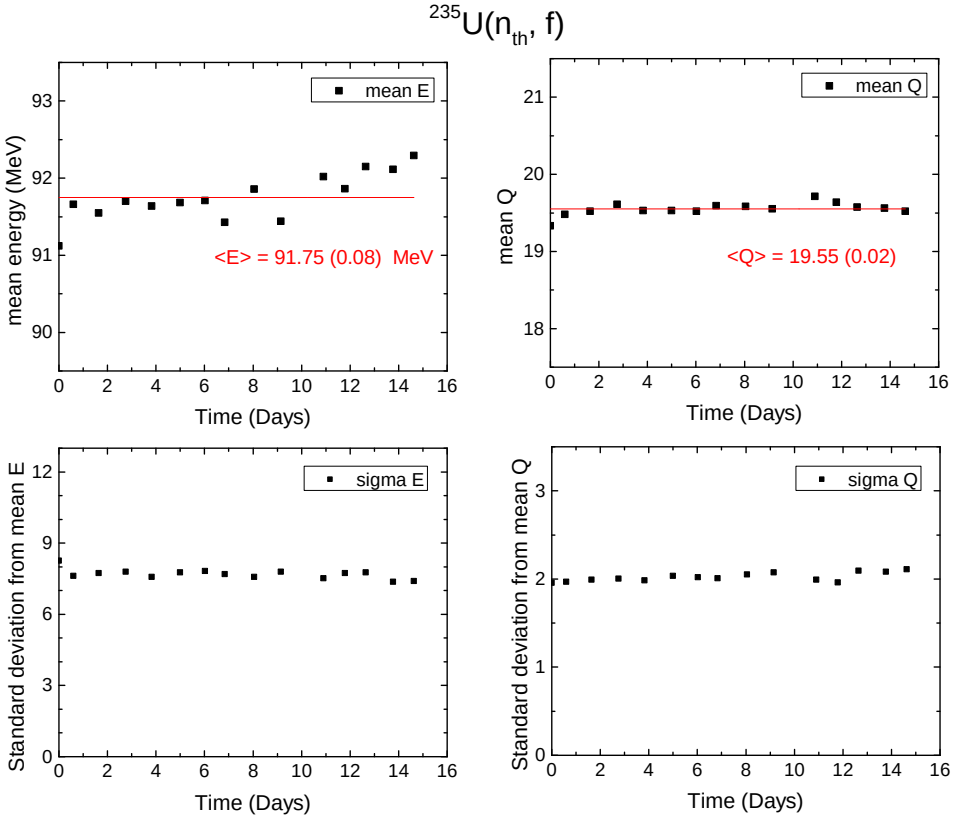

FIGURE B.1: Plots for mean energy (top-left) and mean ionic charge state (top-right) for the ^{235}U(n_{th}, f) burn-up measurements for mass A = 90 using the PIN diode over a period of 15 days. Also the standard deviation of the energy (bottom-left) and the standard deviation of the ionic charge state (bottom-right) are shown.

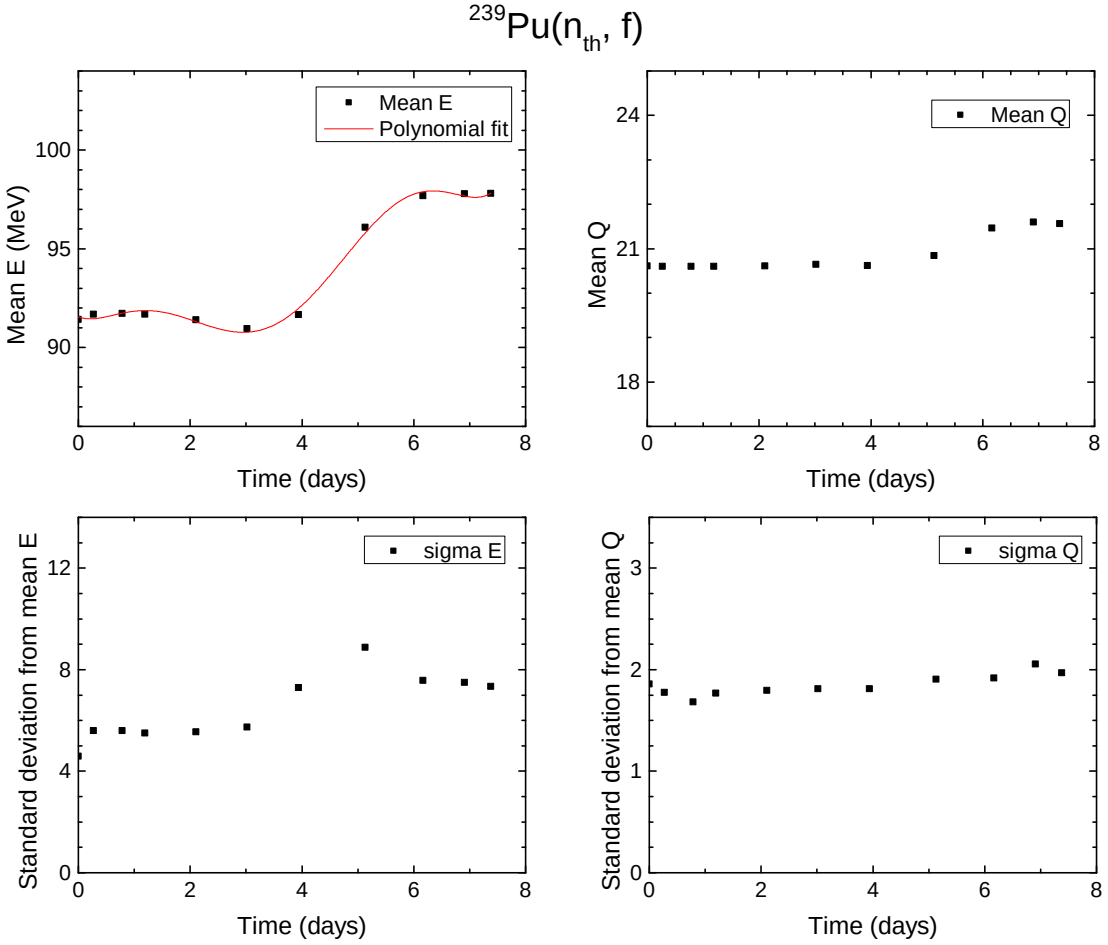

FIGURE B.2: Plots for the mean energy (top-left) and the mean ionic charge state (top-right) for the ^{239}Pu(n$_{th}$, f) burn-up measurements for mass A = 95 using the PIN diode over a period of 15 days. Also the standard deviation in energy (bottom-left) and the standard deviation in ionic charge state (bottom-right) are shown. Energy scans were performed at ionic charge setting Q = 21, and of the ionic charge scans (Q-scans) were performed at an energy of E_L = 92 MeV.

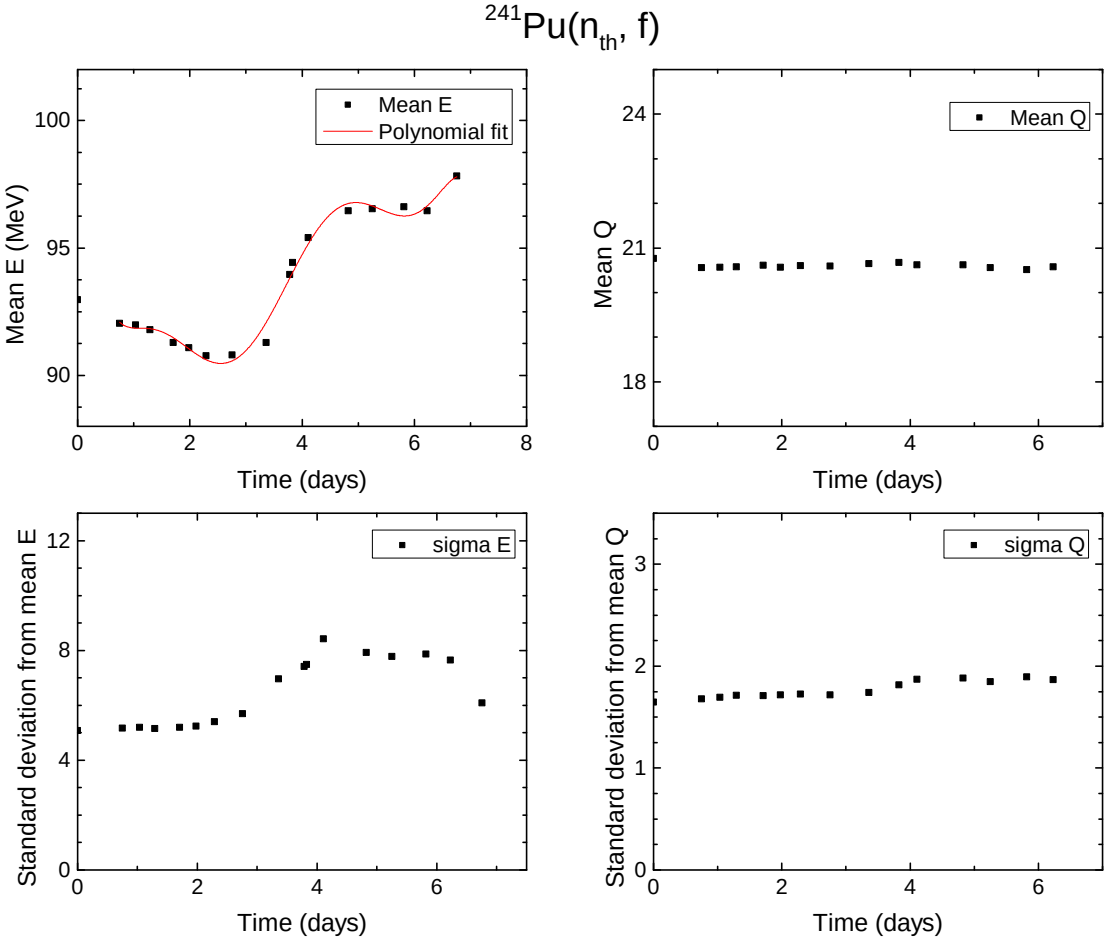

FIGURE B.3: Plots for the mean energy (top-left) and the mean ionic charge state (top-right) for the ^{241}Pu(n$_{th}$, f) burn-up measurements for mass A = 95 using the PIN diode over a period of 15 days. Also the standard deviation in energy (bottom-left) and the standard deviation of the ionic charge state (bottom-right) are shown. Energy scans were performed at an ionic charge setting Q = 21, and ionic charge scans (Q-scans) were performed at an energy of E_L =94 MeV.

B.2 Appendix for Section 5.4.4: Energy calibration of the CLTDs

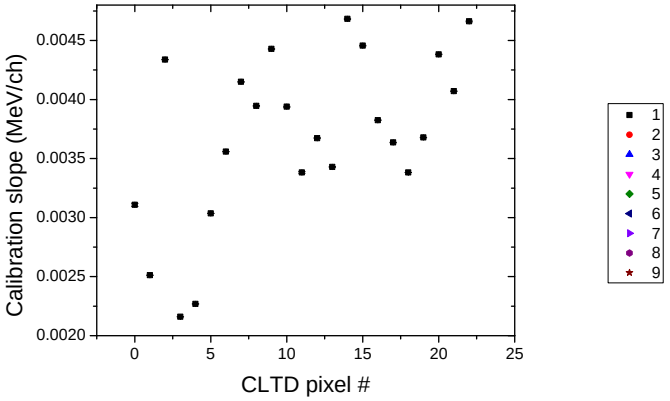

FIGURE B.4: Calibration slope for the different CLTD pixels using the alpha source.

Appendix C

Appendix for Chapter 6

C.1 Appendix for Section 6.1: Quality of Z-resolutions

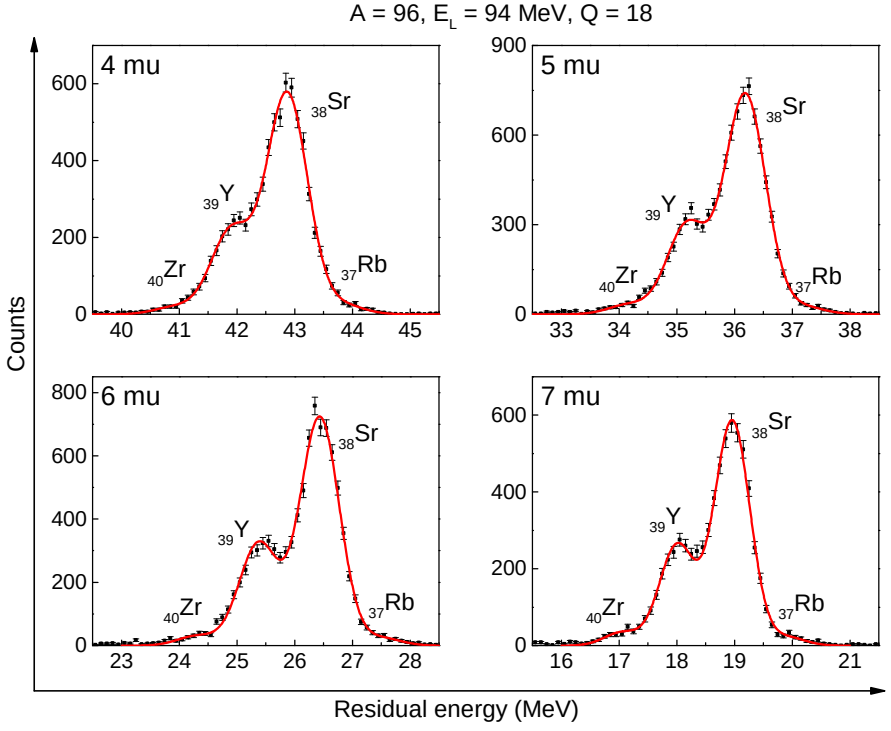

FIGURE C.1: Measurements with different SiN foil thicknesses for mass A = 96 from ^{235}U(n_{th}, f) at a LOHENGRIN energy of $E_L = 94$ MeV and an ionic charge state Q = 18. Different spectra correspond to measurements with a specific SiN foil thickness marked on the top left of each spectrum. Measurements were performed with four, five, six and seven micrometer thick SiN foil stacks.

C.2 Appendix for Section 6.2: ^{92}Rb and ^{96}Y yields

Appendix for Section 6.2.1

Relative Z-yields for A = 92 from ^{235}U(n_{th}, f) at E_L = 94 MeV						
Ionic charge, Q	Z = 38 (Sr)	Δ	Z = 37 (Rb)	Δ	Z = 36 (Kr)	Δ
16	0.076	0.004	0.403	0.006	0.521	0.007
17	0.097	0.003	0.424	0.005	0.479	0.005
18	0.124	0.003	0.458	0.003	0.418	0.004
20	0.155	0.002	0.518	0.003	0.327	0.003
21	0.159	0.003	0.563	0.004	0.278	0.003
22	0.148	0.003	0.614	0.005	0.238	0.004
24	0.111	0.003	0.764	0.006	0.125	0.003
25	0.085	0.003	0.856	0.007	0.059	0.003
26	0.065	0.023	0.870	0.041	0.065	0.018
linearly interpolated values						
19	0.139	0.004	0.488	0.005	0.373	0.005
23	0.130	0.004	0.689	0.007	0.181	0.005
extrapolated values						
15	0.076	0.004	0.403	0.006	0.521	0.007
27	0.025	0.025	0.975	0.025	0.025	0.025
28	0.025	0.025	0.975	0.025	0.025	0.025

TABLE C.1: Relative Z-yields from the CLTD measurements at E_L = 94 MeV for A = 92 from ^{235}U(n_{th}, f). Values for the ionic charges states 19 and 23 were interpolated and were extrapolated for Q = 15, 27 and 28 to fill in the gaps for these charge states where relative Z-yields could not be determined from measurements due to contamination and/or couldn't be measured due to very low intensity.

C.3 Appendix for Section 6.3: Z-yields for ^{241}Pu(n_{th}, f)

Relative Z-yields for A = 92 from ^{235}U(n_{th}, f)						
Q = 20						
E (MeV)	Z = 38 (Sr)	Δ	Z = 37 (Rb)	Δ	Z = 36 (Kr)	Δ
106	0.038	0.004	0.273	0.009	0.689	0.012
100	0.069	0.003	0.465	0.005	0.465	0.006
94	0.155	0.002	0.518	0.003	0.327	0.003
88	0.256	0.004	0.516	0.005	0.227	0.004
80	0.284	0.006	0.531	0.007	0.186	0.006
Q = 25						
E (MeV)	Z = 38 (Sr)	Δ	Z = 37 (Rb)	Δ	Z = 36 (Kr)	Δ
106	0.142	0.014	0.585	0.018	0.273	0.015
100	0.071	0.004	0.789	0.010	0.140	0.006
94	0.085	0.003	0.856	0.007	0.059	0.003
88	0.081	0.008	0.876	0.013	0.043	0.007

TABLE C.2: Relative Z-yields for A = 92 from ^{235}U(n_{th}, f) from the CLTD measurements at Q = 20 and Q = 25.

E and Q distribution of mass A = 92 from ^{235}U(n_{th}, f) from PIN Diode							
Q	E_L = 94 MeV		E (MeV)	Q = 20		Q = 25	
	Cnts/s	Δ		Cnts/s	Δ	Cnts/s	Δ
16	5.4	0.43	106	0.010	0.001	0.002	0.0003
17	13.8	0.68	102	0.066	0.003	0.011	0.0006
18	22.7	0.88	98	0.186	0.006	0.026	0.0009
19	27.5	0.96	94	0.287	0.007	0.031	0.0010
20	26.6	0.94	90	0.240	0.007	0.021	0.0009
21	19.9	0.83	86	0.154	0.005	0.011	0.0006
22	13.4	0.69	82	0.098	0.004	0.005	0.0005
23	9.4	0.57	78	0.049	0.003	0.002	0.0003
24	5.3	0.42	74	0.039	0.003	0.002	0.0003
25	2.8	0.31	70	0.027	0.003	-	-
26	1.3	0.15					
27	0.2	0.03					
28	0.0	0.00					

TABLE C.3: Table for E and Q distributions of mass A = 92 from ^{235}U(n_{th}, f) determined from the PIN diode measurements.

Q distribution of nuclear charges in A = 92 from ^{235}U(n_{th}, f) at E_L = 94 MeV						
Q	Z = 38 (Sr)	Δ	Z = 37 (Rb)	Δ	Z = 36 (Kr)	Δ
15	0.141	0.015	0.743	0.071	0.960	0.092
16	0.414	0.039	2.189	0.176	2.827	0.228
17	1.338	0.079	5.860	0.295	6.628	0.334
18	2.808	0.124	10.397	0.408	9.496	0.375
19	3.828	0.166	13.398	0.485	10.240	0.380
20	4.123	0.159	13.762	0.496	8.704	0.319
21	3.156	0.142	11.175	0.472	5.522	0.239
22	1.990	0.109	8.253	0.426	3.191	0.170
23	1.218	0.083	6.473	0.396	1.700	0.111
24	0.586	0.049	4.022	0.325	0.656	0.055
25	0.241	0.028	2.437	0.266	0.168	0.020
26	0.084	0.031	1.127	0.138	0.084	0.025
27	0.004	0.004	0.146	0.025	0.004	0.004
28	0.000	0.000	0.000	0.000	0.000	0.000

TABLE C.4: Q(ionic charge) distribution of nuclear charges in mass A = 92 from ^{235}U(n_{th}, f) at E_L = 94 MeV, determined from the convolution of both CLTD and PIN diode measurements.

E distribution of nuclear charges in A = 92 from ^{235}U(n_{th}, f)						
Q = 20						
E (MeV)	Z = 38 (Sr)	Δ	Z = 37 (Rb)	Δ	Z = 36 (Kr)	Δ
106	0.0004	0.0001	0.0027	0.0004	0.0068	0.0009
100	0.0088	0.0006	0.0588	0.0031	0.0588	0.0031
94	0.0445	0.0013	0.1486	0.0038	0.0940	0.0025
88	0.0504	0.0023	0.1017	0.0045	0.0448	0.0021
80	0.0209	0.0016	0.0390	0.0030	0.0137	0.0011
Q = 25						
E (MeV)	Z = 38 (Sr)	Δ	Z = 37 (Rb)	Δ	Z = 36 (Kr)	Δ
106	0.0003	0.0001	0.0014	0.0002	0.0006	0.0001
100	0.0013	0.0001	0.0144	0.0009	0.0026	0.0002
94	0.0026	0.0001	0.0265	0.0009	0.0018	0.0001
88	0.0013	0.0002	0.0139	0.0010	0.0007	0.0001

TABLE C.5: Energy distribution of nuclear charges in mass A = 92 from ^{235}U(n_{th}, f) at Q = 20 and Q = 25, determined from the convolution of both CLTD and PIN diode measurements.

Fractional Z-yields and independent Z-yields for A = 92				
Q = 20				
Isotope	fractional yield	Δ	independent yield	Δ
Z = 38 (Sr)	0.157	0.011	0.0088	0.0006
Z = 37 (Rb)	0.521	0.031	0.0293	0.0018
Z = 36 (Kr)	0.322	0.018	0.0181	0.0010
Q = 25				
Isotope	fractional yield	Δ	independent yield	Δ
Z = 38 (Sr)	0.113	0.016	0.0064	0.0009
Z = 37 (Rb)	0.454	0.057	0.0256	0.0032
Z = 36 (Kr)	0.432	0.061	0.0244	0.0034

TABLE C.6: Fractional Z-yields and independent Z-yields for A = 92 from ^{235}U(n_{th}, f) using the two E distributions at Q = 20 and Q = 25.

Relative Z-yield for A = 96 from ^{235}U(n_{th}, f) at E_L =84 MeV								
Q	Z = 40 (Zr)	Δ	Z = 39 (Y)	Δ	Z = 38 (Sr)	Δ	Z = 37 (Rb)	Δ
16	0.058	0.004	0.334	0.007	0.545	0.010	0.063	0.013
17	0.073	0.003	0.385	0.005	0.529	0.006	0.014	0.002
18	0.084	0.003	0.400	0.004	0.501	0.005	0.016	0.001
20	0.125	0.003	0.425	0.004	0.416	0.004	0.034	0.002
21	0.121	0.003	0.466	0.005	0.391	0.005	0.022	0.002
22	0.131	0.003	0.503	0.005	0.338	0.004	0.028	0.002
23	0.134	0.005	0.524	0.008	0.300	0.006	0.042	0.003
25	0.062	0.006	0.574	0.014	0.297	0.010	0.067	0.006
linearly interpolated values								
19	0.104	0.002	0.412	0.003	0.458	0.003	0.025	0.001
24	0.098	0.004	0.549	0.008	0.299	0.006	0.055	0.003

TABLE C.7: Relative Z-yields from the CLTD measurements at E_L = 84 MeV for A = 96 from ^{235}U(n_{th}, f). Values for the ionic charges states 19 and 23 were interpolated to fill in the gaps for these charge states where relative Z-yields could not be determined from measurements due to contamination.

Relative Z-yield for A = 96 from ^{235}U(n_{th}, f) at E_L =94 MeV								
Q	Z = 40 (Zr)	Δ	Z = 39 (Y)	Δ	Z = 38 (Sr)	Δ	Z = 37 (Rb)	Δ
16	0.023	0.004	0.218	0.007	0.716	0.012	0.043	0.005
17	0.024	0.003	0.259	0.006	0.688	0.010	0.029	0.003
17	0.025	0.002	0.268	0.004	0.684	0.006	0.022	0.001
18	0.028	0.002	0.281	0.003	0.669	0.005	0.023	0.001
18	0.030	0.001	0.282	0.003	0.663	0.004	0.025	0.001
19	0.029	0.016	0.270	0.012	0.654	0.019	0.046	0.005
20	0.056	0.001	0.334	0.002	0.583	0.003	0.027	0.001
21	0.054	0.001	0.371	0.003	0.546	0.003	0.028	0.001
22	0.064	0.002	0.380	0.004	0.512	0.004	0.045	0.002
23	0.056	0.002	0.414	0.003	0.476	0.004	0.054	0.002
26	0.061	0.004	0.535	0.008	0.261	0.007	0.143	0.005
linearly interpolated values								
24	0.058	0.002	0.454	0.003	0.404	0.003	0.083	0.002
25	0.059	0.003	0.495	0.005	0.333	0.005	0.113	0.003

TABLE C.8: Relative Z-yields from the CLTD measurements at E_L = 94 MeV for A = 96 from ^{235}U(n_{th}, f). Values for the ionic charges states 24 and 25 were interpolated to fill in the gaps for these charge states where relative Z-yields could not be determined from measurements due to contamination.

Relative Z-yield for A = 96 from ^{235}U(n_{th}, f) at E_L =102 MeV								
Q	Z = 40 (Zr)	Δ	Z = 39 (Y)	Δ	Z = 38 (Sr)	Δ	Z = 37 (Rb)	Δ
17	0.011	0.003	0.126	0.009	0.835	0.013	0.028	0.003
18	0.013	0.003	0.133	0.006	0.824	0.009	0.030	0.003
20	0.022	0.004	0.194	0.003	0.742	0.005	0.042	0.002
21	0.027	0.010	0.181	0.004	0.762	0.007	0.031	0.002
22	0.029	0.012	0.193	0.004	0.736	0.008	0.042	0.002
linearly interpolated values								
19	0.018	0.003	0.163	0.003	0.783	0.005	0.036	0.002
23	0.029	0.050	0.193	0.016	0.736	0.031	0.042	0.009
24	0.029	0.050	0.193	0.016	0.736	0.031	0.042	0.009
25	0.029	0.050	0.193	0.016	0.736	0.031	0.042	0.009

TABLE C.9: Relative Z-yields from the CLTD measurements at E_L = 102 MeV for A = 96 from ^{235}U(n_{th}, f). Values for the ionic charges states 19, 23, 24 and 25 were interpolated to fill in the gaps for these charge states where relative Z-yields could not be determined from measurements due to contamination.

Relative Z-yield for A = 96 from ^{235}U(n_{th}, f)								
Q = 18								
E (MeV)	Z = 40 (Zr)	Δ	Z = 39 (Y)	Δ	Z = 38 (Sr)	Δ	Z = 37 (Rb)	Δ
74	0.079	0.005	0.366	0.006	0.531	0.008	0.024	0.003
80	0.080	0.003	0.368	0.005	0.516	0.006	0.036	0.002
84	0.084	0.003	0.400	0.004	0.501	0.005	0.016	0.001
88	0.059	0.002	0.370	0.003	0.543	0.004	0.028	0.001
94	0.028	0.002	0.281	0.003	0.669	0.005	0.023	0.001
94	0.030	0.001	0.282	0.003	0.663	0.004	0.025	0.001
100	0.009	0.002	0.163	0.005	0.800	0.007	0.028	0.002
102	0.013	0.003	0.133	0.006	0.824	0.009	0.030	0.003
Q = 21								
E (MeV)	Z = 40 (Zr)	Δ	Z = 39 (Y)	Δ	Z = 38 (Sr)	Δ	Z = 37 (Rb)	Δ
74	0.123	0.007	0.432	0.010	0.415	0.011	0.031	0.004
80	0.126	0.004	0.460	0.006	0.389	0.005	0.026	0.002
84	0.121	0.003	0.466	0.005	0.391	0.005	0.022	0.002
88	0.106	0.003	0.452	0.004	0.420	0.004	0.022	0.002
94	0.054	0.001	0.371	0.003	0.546	0.003	0.028	0.001
100	0.033	0.002	0.213	0.004	0.724	0.006	0.030	0.002
102	0.027	0.010	0.181	0.004	0.762	0.007	0.031	0.002

TABLE C.10: Relative Z-yields for A = 96 from ^{235}U(n_{th}, f) from the CLTD measurements at Q = 18 and Q = 21.

E and Q distribution of A = 96 from ^{235}U(n_{th}, f) from PIN Diode											
Q	E_L = 84 MeV		E_L = 94 MeV		E_L = 102 MeV		E (MeV)	Q = 18		Q = 21	
	Cnts/s	Δ	Cnts/s	Δ	Cnts/s	Δ		Cnts/s	Δ	Cnts/s	Δ
16	4	0.11	2	0.07	3	0.10	42	0.011	0.001	0.000	0.000
17	8	0.16	5	0.13	7	0.15	50	0.023	0.001	0.000	0.000
18	12	0.20	10	0.18	10	0.19	58	0.034	0.001	0.008	0.000
19	13	0.21	13	0.21	12	0.20	66	0.044	0.001	0.015	0.001
20	11	0.19	14	0.21	11	0.20	72	0.056	0.001	0.026	0.001
21	9	0.17	10	0.18	7	0.16	74	0.061	0.003	0.027	0.001
22	6	0.14	7	0.15	5	0.13	78	0.075	0.002	0.039	0.002
23	3	0.10	4	0.12	3	0.10	80	0.079	0.003	0.051	0.002
24	1	0.07	2	0.08	1	0.06	82	0.102	0.003	0.075	0.002
25	1	0.04	1	0.06	1	0.05	86	0.170	0.003	0.138	0.003
26	0	0.00	0	0.04	-	-	88	0.196	0.004	0.167	0.003
							90	0.233	0.004	0.226	0.004
							94	0.245	0.004	0.243	0.004
							98	0.179	0.003	0.230	0.004
							100	0.118	0.003	0.167	0.003
							102	0.071	0.002	0.104	0.002
							106	0.010	0.000	0.025	0.001

TABLE C.11: Table for E and Q distribution of mass A = 96 from ^{235}U(n_{th}, f) determined from the PIN diode measurements.

Q distribution of nuclear charges in A = 96 from ^{235}U(n_{th}, f) at E_L = 94 MeV								
Q	Z = 40 (Zr)	Δ	Z = 39 (Y)	Δ	Z = 38 (Sr)	Δ	Z = 37 (Rb)	Δ
16	0.04	0.01	0.37	0.02	1.20	0.06	0.07	0.01
17	0.14	0.01	1.44	0.04	3.67	0.10	0.12	0.01
18	0.29	0.01	2.69	0.06	6.34	0.12	0.23	0.01
19	0.37	0.20	3.42	0.16	8.27	0.28	0.58	0.07
20	0.76	0.02	4.51	0.08	7.90	0.13	0.37	0.01
21	0.54	0.02	3.73	0.07	5.48	0.11	0.28	0.01
22	0.46	0.02	2.71	0.06	3.66	0.08	0.32	0.02
23	0.22	0.01	1.65	0.05	1.90	0.06	0.21	0.01
24	0.11	0.01	0.88	0.04	0.79	0.03	0.16	0.01
25	0.06	0.00	0.51	0.03	0.34	0.02	0.12	0.01
26	0.03	0.00	0.25	0.02	0.12	0.01	0.07	0.01

TABLE C.12: Q(ionic charge) distribution of nuclear charges in mass A = 96 from ^{235}U(n_{th}, f) at E_L = 94 MeV, determined from the convolution of both CLTD and PIN diode measurements.

E distribution of nuclear charges in A = 96 from ^{235}U(n_{th}, f)								
Q = 18								
E (MeV)	Z = 40 (Zr)	Δ	Z = 39 (Y)	Δ	Z = 38 (Sr)	Δ	Z = 37 (Rb)	Δ
66	0.003	0.001	0.016	0.001	0.023	0.001	0.001	0.001
72	0.004	0.001	0.021	0.001	0.030	0.001	0.001	0.001
74	0.221	0.018	1.025	0.058	1.487	0.084	0.067	0.008
80	0.309	0.019	1.430	0.069	2.003	0.096	0.141	0.010
88	0.633	0.028	3.953	0.116	5.802	0.168	0.304	0.018
94	0.428	0.020	4.024	0.089	9.464	0.195	0.350	0.016
100	0.062	0.013	1.187	0.053	5.821	0.204	0.206	0.015
102	0.059	0.014	0.593	0.033	3.675	0.135	0.134	0.013
106	0.000	0.000	0.001	0.000	0.008	0.000	0.000	0.000
Q = 21								
E (MeV)	Z = 40 (Zr)	Δ	Z = 39 (Y)	Δ	Z = 38 (Sr)	Δ	Z = 37 (Rb)	Δ
66	0.002	0.000	0.006	0.000	0.006	0.000	0.000	0.000
72	0.003	0.001	0.011	0.001	0.011	0.001	0.001	0.001
74	0.145	0.013	0.511	0.037	0.491	0.036	0.037	0.005
80	0.306	0.017	1.119	0.055	0.946	0.047	0.063	0.006
88	0.919	0.033	3.940	0.106	3.663	0.099	0.189	0.016
94	0.734	0.025	5.023	0.108	7.385	0.156	0.380	0.016
100	0.323	0.020	2.104	0.063	7.162	0.181	0.300	0.018
102	0.168	0.062	1.131	0.043	4.766	0.149	0.191	0.012
106	0.001	0.000	0.004	0.001	0.019	0.001	0.001	0.000

TABLE C.13: Energy distribution of nuclear charges in mass A = 96 from ^{235}U(n_{th}, f) at Q = 18 and Q = 21, determined from the convolution of both CLTD and PIN diode measurements.

Fractional yield and independent Z-yields for A = 96				
Q = 18				
Isotope	fractional yield	Δ	independent yield	Δ
Z = 40 (Zr)	0.064	0.005	0.0041	0.0005
Z = 39 (Y)	0.344	0.014	0.0219	0.0025
Z = 38 (Sr)	0.549	0.021	0.0349	0.0039
Z = 37 (Rb)	0.042	0.003	0.0027	0.0003
Q = 21				
Isotope	fractional yield	Δ	independent yield	Δ
Z = 40 (Zr)	0.057	0.003	0.0036	0.0004
Z = 39 (Y)	0.316	0.012	0.0201	0.0022
Z = 38 (Sr)	0.591	0.022	0.0375	0.0042
Z = 37 (Rb)	0.036	0.002	0.0023	0.0003

TABLE C.14: Fractional yield and independent Z-yields for A = 96 from ^{235}U(n$_{th}$, f) using the two E distributions at Q = 18 and Q = 21.

Relative Z-yield for A = 92 from ^{239}Pu(n$_{\text{th}}$, f) at E_L = 100 MeV						
Q	Z = 38 (Sr)	Δ	Z = 37 (Rb)	Δ	Z = 36 (Kr)	Δ
17	0.303	0.015	0.472	0.016	0.225	0.013
20	0.367	0.011	0.496	0.010	0.137	0.009
21	0.378	0.011	0.492	0.010	0.129	0.008
24	0.330	0.008	0.581	0.009	0.090	0.005
25	0.301	0.012	0.636	0.015	0.062	0.007
linearly interpolated values						
18	0.324	0.010	0.480	0.011	0.195	0.009
19	0.346	0.009	0.488	0.009	0.166	0.007
22	0.362	0.008	0.522	0.007	0.116	0.006
23	0.346	0.006	0.551	0.007	0.103	0.004
extrapolated values						
26	0.301	0.060	0.636	0.127	0.062	0.012
27	0.301	0.060	0.636	0.127	0.062	0.012

TABLE C.15: Relative Z-yields from the CLTD measurements at E_L = 100 MeV for A = 92 from ^{239}Pu(n$_{\text{th}}$, f). Values for the ionic charges states 18, 19, 22 and 23 were interpolated and were extrapolated for Q = 26 and 27 to fill in the gaps for these charge states where relative Z-yields could not be determined from measurements due to contamination and/or couldn't be measured due to very low intensity.

Relative Z-yield for A = 92 from ^{239}Pu(n_{th}, f) at Q = 21						
E (MeV)	Z = 38 (Sr)	Δ	Z = 37 (Rb)	Δ	Z = 36 (Kr)	Δ
94	0.457	0.013	0.426	0.009	0.117	0.009
100	0.378	0.011	0.492	0.010	0.129	0.008
106	0.279	0.010	0.564	0.011	0.157	0.008
extrapolated values with linear fit						
82	0.642	0.135	0.286	0.033	0.074	0.099
88	0.552	0.139	0.355	0.034	0.094	0.102

TABLE C.16: Relative Z-yields for A = 92 from ^{239}Pu(n_{th}, f) from the CLTD measurements at Q = 21.

E and Q distribution of A = 92 from ^{239}Pu(n_{th}, f) from PIN Diode					
Ionic charge, Q	E_L = 100 MeV		E (MeV)	Q = 21	
	Cnts/s	Δ		Cnts/s	Δ
17	0.020	0.003	82	0.0045	0.0004
18	0.043	0.006	88	0.0059	0.0005
19	0.085	0.009	94	0.0097	0.0006
20	0.146	0.011	100	0.0163	0.0007
21	0.176	0.012	106	0.0091	0.0005
22	0.168	0.012	112	0.0000	0.0000
23	0.156	0.012			
24	0.106	0.010			
25	0.066	0.007			
26	0.027	0.005			
27	0.016	0.004			

TABLE C.17: Table for E and Q distribution of mass A = 92 from ^{239}Pu(n_{th}, f) determined from the PIN diode measurements.

Q distribution of nuclear charges in A = 92 from ^{239}Pu(n_{th}, f) at E_L = 100 MeV						
Ionic charge, Q	Z = 38 (Sr)	Δ	Z = 37 (Rb)	Δ	Z = 36 (Kr)	Δ
17	0.006	0.001	0.009	0.001	0.005	0.001
18	0.014	0.002	0.021	0.003	0.008	0.001
19	0.029	0.003	0.041	0.004	0.014	0.002
20	0.053	0.004	0.072	0.006	0.020	0.002
21	0.067	0.005	0.087	0.006	0.023	0.002
22	0.061	0.005	0.088	0.006	0.020	0.002
23	0.054	0.004	0.086	0.006	0.016	0.001
24	0.035	0.003	0.062	0.006	0.010	0.001
25	0.020	0.002	0.042	0.005	0.004	0.001
26	0.008	0.002	0.017	0.005	0.002	0.000
27	0.005	0.001	0.010	0.003	0.001	0.000

TABLE C.18: Q(ionic charge) distribution of nuclear charges in mass A = 92 from ^{239}Pu(n_{th}, f) at E_L = 100 MeV, determined from the convolution of both CLTD and PIN diode measurements.

E distribution of nuclear charges in A = 92 from ^{239}Pu(n_{th}, f) at Q = 21						
E (MeV)	Z = 38 (Sr)	Δ	Z = 37 (Rb)	Δ	Z = 36 (Kr)	Δ
82	0.0029	0.0007	0.0013	0.0002	0.0003	0.0005
88	0.0033	0.0009	0.0021	0.0003	0.0006	0.0006
94	0.0045	0.0003	0.0042	0.0003	0.0011	0.0001
100	0.0062	0.0003	0.0081	0.0004	0.0021	0.0002
106	0.0025	0.0002	0.0051	0.0003	0.0014	0.0001

TABLE C.19: Energy distribution of nuclear charges in mass A = 92 from ^{239}Pu(n_{th}, f) at Q = 21, determined from the convolution of both CLTD and PIN diode measurements.

Relative Z-yield for A = 92 from ^{241}Pu(n_{th}, f) at E_L = 97.5 MeV						
Q	Z = 38 (Sr)	Δ	Z = 37 (Rb)	Δ	Z = 36 (Kr)	Δ
21	0.107	0.006	0.511	0.008	0.382	0.008
25	0.193	0.007	0.492	0.009	0.315	0.008
linearly interpolated values						
22	0.129	0.005	0.506	0.006	0.365	0.006
23	0.150	0.005	0.501	0.006	0.349	0.006
24	0.171	0.005	0.497	0.007	0.332	0.006
extrapolated values						
17	0.107	0.050	0.511	0.050	0.382	0.050
18	0.107	0.050	0.511	0.050	0.382	0.050
19	0.107	0.050	0.511	0.050	0.382	0.050
20	0.107	0.050	0.511	0.050	0.382	0.050

TABLE C.20: Relative Z-yields from the CLTD measurements at E_L = 97.5 MeV for A = 92 from ^{239}Pu(n_{th}, f). Values for the ionic charges states 22, 23 and 24 were interpolated and were extrapolated for Q = 17, 18, 19 and 20 to fill in the gaps for these charge states where relative Z-yields could not be determined from measurements due to contamination and/or couldn't be measured due to very low intensity.

Relative Z-yield for A = 92 from ^{241}Pu(n_{th}, f) at Q = 21						
E (MeV)	Z = 38 (Sr)	Δ	Z = 37 (Rb)	Δ	Z = 36 (Kr)	Δ
87.86299	0.181	0.010	0.602	0.013	0.217	0.010
90.27098	0.218	0.006	0.556	0.008	0.227	0.006
93.75738	0.145	0.005	0.573	0.007	0.282	0.006
98.07784	0.107	0.006	0.511	0.008	0.382	0.008
103.55903	0.145	0.009	0.565	0.012	0.290	0.010
109.56727	0.091	0.008	0.525	0.012	0.383	0.012

TABLE C.21: Relative Z-yields for A = 92 from ^{241}Pu(n_{th}, f) from the CLTD measurements at Q = 21.

E and Q distribution of A = 92 from ^{241}Pu(n_{th}, f)					
Ionic charge, Q	E_L = MeV		E (MeV)	Q = 21	
	Cnts/s	Δ		Cnts/s	Δ
16	0.013	7E-05	111	0.0006	4E-06
17	0.043	2E-04	108	0.0024	2E-06
18	0.096	4E-04	105	0.0105	1E-06
19	0.153	5E-04	102	0.0245	7E-07
20	0.187	7E-04	99	0.0768	4E-07
21	0.177	1E-03	96	0.1401	3E-07
22	0.137	1E-03	93	0.1959	3E-07
23	0.089	2E-03	90	0.1997	3E-07
24	0.054	2E-03	87	0.1548	3E-07
25	0.028	2E-03	84	0.1014	4E-07
26	0.014	2E-03	81	0.0522	6E-07
27	0.007	1E-03	78	0.0234	8E-07
28	0.002	9E-04	75	0.0098	1E-06
29	0	5E-04	72	0.0042	2E-06
			69	0.0016	3E-06
			66	0.0012	4E-06
			63	0.001	5E-06

TABLE C.22: Table for E and Q distribution of mass A = 92 from ^{241}Pu(n_{th}, f) determined from the ionization chamber measurements [132].

Q distribution of nuclear charges in A = 92 from ^{241}Pu(n_{th}, f) at E_L = MeV						
Ionic charge, Q	Z = 38 (Sr)	Δ	Z = 37 (Rb)	Δ	Z = 36 (Kr)	Δ
17	0.005	0.002	0.022	0.002	0.016	0.002
18	0.010	0.005	0.049	0.005	0.037	0.005
19	0.016	0.008	0.078	0.009	0.058	0.008
20	0.020	0.009	0.095	0.010	0.071	0.010
21	0.019	0.001	0.090	0.005	0.068	0.004
22	0.018	0.001	0.069	0.004	0.050	0.003
23	0.013	0.001	0.045	0.002	0.031	0.002
24	0.009	0.001	0.027	0.001	0.018	0.001
25	0.005	0.0003	0.014	0.001	0.009	0.0005

TABLE C.23: Q(ionic charge) distribution of nuclear charges in mass A = 92 from ^{241}Pu(n_{th}, f) at E_L = 97.5 MeV, determined from the convolution of both CLTD and PIN diode measurements.

E distribution of nuclear charges in A = 92 from ^{241}Pu(n_{th}, f) at Q =						
E (MeV)	Z = 38 (Sr)	Δ	Z = 37 (Rb)	Δ	Z = 36 (Kr)	Δ
87.9	0.032	0.002	0.107	0.006	0.039	0.003
90.3	0.044	0.003	0.112	0.006	0.046	0.003
93.8	0.026	0.002	0.103	0.005	0.051	0.003
98.1	0.010	0.001	0.049	0.003	0.036	0.002
103.6	0.003	0.0002	0.011	0.001	0.006	0.0003
109.6	0.0001	0.00001	0.001	0.00004	0.0005	0.00003

TABLE C.24: Energy distribution of nuclear charges in mass A = 92 from ^{241}Pu(n_{th}, f) at Q = 21, determined from the convolution of both CLTD and PIN diode measurements.

Relative Z-yield for A = 96 from ^{241}Pu(n_{th}, f) at E_L = 94 MeV								
Q	Z = 40 (Zr)	Δ	Z = 39 (Y)	Δ	Z = 38 (Sr)	Δ	Z = 37 (Rb)	Δ
18	0.043	0.003	0.351	0.007	0.569	0.008	0.037	0.00288
21	0.013	0.002	0.187	0.007	0.757	0.011	0.042	0.00349
linearly interpolated values								
19	0.033	0.002	0.296	0.005	0.632	0.007	0.039	0.002
20	0.023	0.002	0.242	0.005	0.694	0.008	0.041	0.003
extrapolated values								
17	0.043	0.033	0.351	0.066	0.569	0.084	0.037	0.029
22	0.013	0.023	0.187	0.073	0.757	0.113	0.042	0.035
23	0.013	0.023	0.187	0.073	0.757	0.113	0.042	0.035
24	0.013	0.023	0.187	0.073	0.757	0.113	0.042	0.035
25	0.013	0.023	0.187	0.073	0.757	0.113	0.042	0.035

TABLE C.25: Relative Z-yields from the CLTD measurements at E_L = 94 MeV for A = 96 from ^{239}Pu(n_{th}, f). Values for the ionic charges states 19 and 20 were interpolated and were extrapolated for Q = 17, 22, 23, 24 and 25 to fill in the gaps for these charge states where relative Z-yields could not be determined from measurements due to contamination and/or couldn't be measured due to very low intensity.

Relative Z-yield for A = 96 from ^{241}Pu(n_{th}, f) at Q = 21								
E	Z = 40 (Zr)	Δ	Z = 39 (Y)	Δ	Z = 38 (Sr)	Δ	Z = 37 (Rb)	Δ
86.6	0.050	0.004	0.343	0.007	0.562	0.009	0.044	0.003
93.7	0.024	0.002	0.296	0.005	0.643	0.008	0.037	0.002
98.0	0.013	0.002	0.187	0.007	0.757	0.011	0.042	0.003
extrapolated values								
80	0.050	0.081	0.343	0.142	0.562	0.185	0.044	0.068
103	0.013	0.045	0.187	0.146	0.757	0.227	0.042	0.070

TABLE C.26: Relative Z-yields for A = 96 from ^{241}Pu(n_{th}, f) from the CLTD measurements at Q = 21.

E and Q distribution of A = 96 from ^{241}Pu(n_{th}, f)					
Ionic charge, Q	E_L = 94 MeV		E (MeV)	Q = 21	
	Cnts/s	Δ		Cnts/s	Δ
16	0.0090	4E-04	111	0.0005	8E-05
17	0.0324	7E-04	108	0.0028	2E-04
18	0.0840	1E-03	105	0.0090	3E-04
19	0.1571	2E-03	102	0.0309	6E-04
20	0.2052	2E-03	99	0.0787	1E-03
21	0.1934	2E-03	96	0.1453	1E-03
22	0.1510	2E-03	93	0.2000	2E-03
23	0.0904	1E-03	90	0.1882	2E-03
24	0.0455	8E-04	87	0.1603	2E-03
25	0.0206	6E-04	84	0.0963	1E-03
26	0.0074	3E-04	81	0.0497	9E-04
27	0.0028	2E-04	78	0.0231	6E-04
28	0.0010	1E-04	75	0.0079	4E-04
29	0.0003	7E-05	72	0.0037	3E-04
			69	0.0017	2E-04
			66	0.0010	1E-04
			63	0.0008	1E-04

TABLE C.27: Table for E and Q distribution of mass A = 96 from ^{241}Pu(n_{th}, f) determined from the ionization chamber measurements [].

Q distribution of nuclear charges in A = 96 from ^{241}Pu(n_{th}, f) at E_L = 94 MeV								
Q	Z = 40 (Zr)	Δ	Z = 39 (Y)	Δ	Z = 38 (Sr)	Δ	Z = 37 (Rb)	Δ
17	0.0014	0.0011	0.0113	0.0021	0.0184	0.0028	0.0012	0.0009
18	0.0036	0.0003	0.0295	0.0007	0.0478	0.0010	0.0031	0.0002
19	0.0052	0.0004	0.0465	0.0009	0.0992	0.0014	0.0061	0.0004
20	0.0048	0.0004	0.0496	0.0012	0.1425	0.0021	0.0083	0.0005
21	0.0026	0.0004	0.0362	0.0014	0.1464	0.0025	0.0082	0.0007
22	0.0020	0.0034	0.0283	0.0110	0.1143	0.0171	0.0064	0.0053
23	0.0012	0.0020	0.0169	0.0066	0.0685	0.0103	0.0038	0.0032
24	0.0006	0.0010	0.0085	0.0033	0.0345	0.0052	0.0019	0.0016
25	0.0003	0.0005	0.0039	0.0015	0.0156	0.0024	0.0009	0.0007

TABLE C.28: Q (ionic charge) distribution of nuclear charges in mass A = 96 from ^{241}Pu(n_{th}, f) at E_L = 94 MeV, determined from the convolution of both CLTD and PIN diode measurements.

E distribution of nuclear charges in A = 96 from ^{241}Pu(n_{th}, f) at Q = 21								
E	Z = 40 (Zr)	Δ	Z = 39 (Y)	Δ	Z = 38 (Sr)	Δ	Z = 37 (Rb)	Δ
80	0.0019	0.0030	0.0129	0.0054	0.0212	0.0070	0.0017	0.0026
86.6	0.0078	0.0006	0.0534	0.0012	0.0874	0.0017	0.0068	0.0005
93.7	0.0042	0.0004	0.0527	0.0011	0.1146	0.0017	0.0066	0.0004
98	0.0013	0.0002	0.0180	0.0007	0.0728	0.0013	0.0041	0.0003
103	0.0003	0.0011	0.0044	0.0035	0.0180	0.0054	0.0010	0.0017

TABLE C.29: Energy distribution of nuclear charges in mass A = 96 from ^{241}Pu(n_{th}, f) at Q = 21, determined from the convolution of both CLTD and PIN diode measurements.

A	Q	E_L	E_F	Relative Z-Yields from ^{241}Pu (n_{th}, f)												Mean Z
		(MeV)	(MeV)	Z=39	Δ	Z=38	Δ	Z=37	Δ	Z=36	Δ	Z=35	Δ	Z=34	Δ	
89	20	94	99					0.043	0.007	0.440	0.017	0.487	0.018	0.029	0.006	35.50
89	20	100	105					0.061	0.008	0.411	0.016	0.497	0.018	0.032	0.006	35.50
90	20	94	99			0.007	0.003	0.137	0.011	0.803	0.018	0.053	0.006			36.10
90	20	94	100			0.011	0.005	0.135	0.014	0.779	0.025	0.075	0.010			36.08
90	20	100	100			0.006	0.006	0.161	0.020	0.785	0.030	0.049	0.015			36.12
90	24	94	103			0.268	0.019	0.469	0.023	0.243	0.019	0.021	0.008			35.98
90	20	106	103			0.008	0.009	0.088	0.038	0.868	0.052	0.036	0.014			36.07
90	20	100	105			0.012	0.011	0.132	0.013	0.790	0.023	0.066	0.008			36.09
91	20	94	99			0.028	0.005	0.401	0.016	0.542	0.018	0.029	0.005			36.43
91	20	100	105			0.030	0.011	0.288	0.025	0.643	0.035	0.039	0.012			36.31
93	21	94	99	0.007	0.004	0.336	0.016	0.586	0.020	0.070	0.009					37.28
93	21	100	104	0.029	0.009	0.327	0.023	0.577	0.028	0.067	0.013					37.32
94	21	94	100	0.035	0.008	0.654	0.024	0.285	0.017	0.025	0.007					37.70
94	21	100	104	0.028	0.008	0.660	0.028	0.276	0.019	0.036	0.008					37.68
95	21	94	99	0.121	0.012	0.741	0.023	0.135	0.013	0.003	0.003					37.98
95	21	100	104	0.112	0.014	0.711	0.027	0.172	0.017	0.005	0.006					37.93

TABLE C.30: Relative Z yields from ^{241}Pu (n_{th}, f). Continued on next page..

A	Q	E_L	E_F	Relative Z-Yields from ^{241}Pu (n_{th}, f)												Mean Z
		(MeV)	(MeV)	Z=42	Δ	Z=41	Δ	Z=40	Δ	Z=39	Δ	Z=38	Δ	Z=37	Δ	
97	22	94	99					0.073	0.010	0.527	0.020	0.384	0.018	0.015	0.005	38.66
97	22	100	104					0.053	0.010	0.482	0.021	0.446	0.021	0.019	0.009	38.57
98	22	94	100			0.020	0.006	0.238	0.017	0.535	0.021	0.207	0.016			39.07
98	22	100	105			0.011	0.005	0.112	0.013	0.556	0.020	0.320	0.018			38.81
99	22	94	99			0.037	0.006	0.402	0.015	0.527	0.018	0.034	0.006			39.44
99	22	100	104			0.020	0.009	0.339	0.024	0.600	0.031	0.041	0.011			39.34
100	22	94	100			0.097	0.012	0.748	0.025	0.154	0.015	0.001	0.003			39.94
100	22	100	105			0.024	0.007	0.731	0.027	0.231	0.019	0.013	0.006			39.77
101	22	94	99	0.027	0.006	0.272	0.016	0.624	0.022	0.077	0.010					40.25
101	22	100	104	0.017	0.007	0.229	0.020	0.653	0.028	0.102	0.014					40.16
102	23	94	100	0.060	0.010	0.488	0.021	0.445	0.021	0.007	0.005					40.60
102	23	100	105	0.027	0.008	0.319	0.017	0.627	0.023	0.027	0.007					40.35
103	19	94	98	0.104	0.016	0.728	0.031	0.160	0.018	0.008	0.007					40.93
103	22	94	100	0.203	0.024	0.619	0.031	0.178	0.025	0.000	0.006					41.02
103	23	94	102	0.379	0.030	0.527	0.025	0.091	0.021	0.003	0.007					41.28
103	23	100	104	0.126	0.017	0.587	0.029	0.287	0.022	0.00	0.012					40.84

TABLE C.31: Relative Z-yields from ^{241}Pu (n_{th}, f). Continued on next page..

A	Q	E_L	E_F	Relative Z-Yields from ^{241}Pu (n_{th}, f)										Mean Z
		(MeV)	(MeV)	Z=44	Δ	Z=43	Δ	Z=42	Δ	Z=41	Δ	Z=40	Δ	
104	23	86	90			0.064	0.017	0.661	0.043	0.262	0.029	0.013	0.011	41.78
104	19	94	98			0.032	0.009	0.472	0.025	0.425	0.022	0.071	0.014	41.46
104	23	94	100			0.043	0.009	0.519	0.022	0.393	0.019	0.045	0.009	41.56
104	23	100	105			0.023	0.014	0.318	0.026	0.558	0.032	0.101	0.019	41.26
105	23	86	90			0.256	0.024	0.660	0.028	0.084	0.018	0.000	0.006	42.17
105	20	94	98			0.071	0.012	0.654	0.028	0.267	0.020	0.009	0.007	41.79
105	23	94	99			0.118	0.014	0.653	0.025	0.220	0.018	0.009	0.005	41.88
105	23	100	104			0.018	0.010	0.620	0.028	0.363	0.023	0.000	0.009	41.65
105	24	100	104			0.046	0.010	0.594	0.025	0.351	0.020	0.008	0.012	41.68
106	24	86	92	0.082	0.017	0.570	0.031	0.332	0.026	0.017	0.009			42.72
106	20	94	98	0.006	0.006	0.171	0.022	0.772	0.033	0.052	0.011			42.13
106	23	94	100	0.036	0.011	0.259	0.022	0.623	0.033	0.082	0.015			42.25
106	24	94	100	0.043	0.011	0.385	0.021	0.515	0.024	0.057	0.011			42.41
106	24	100	106			0.139	0.017	0.774	0.029	0.087	0.013	0.001	0.005	42.05
107	24	86	90	0.154	0.027	0.622	0.030	0.224	0.028					42.93
107	20	94	98	0.080	0.017	0.455	0.027	0.412	0.026	0.053	0.014			42.56
107	23	94	100	0.153	0.025	0.573	0.032	0.273	0.028					42.88
107	24	94	100	0.074	0.013	0.567	0.022	0.359	0.021					42.72
107	24	100	104	0.028	0.011	0.405	0.023	0.567	0.030					42.46

TABLE C.32: Relative Z-yields from ^{241}Pu (n_{th}, f). Continued on next page..

A	Q	E_L	E_F	Relative Z-yields from ^{241}Pu (n_{th}, f)										Mean Z
		(MeV)	(MeV)	Z=46	Δ	Z=45	Δ	Z=44	Δ	Z=43	Δ	Z=42	Δ	
108	24	86	90					0.279	0.029	0.695	0.033	0.025	0.012	43.25
108	20	94	98					0.294	0.019	0.346	0.025	0.359	0.020	42.93
108	25	94	100					0.256	0.063	0.675	0.062	0.069	0.044	43.19
108	24	94	100					0.211	0.022	0.708	0.029	0.080	0.016	43.13
108	24	100	104					0.135	0.018	0.652	0.026	0.213	0.020	42.92
108	20	100	110					0.383	0.021	0.310	0.027	0.308	0.020	43.08
109	24	86	90			0.050	0.012	0.658	0.034	0.277	0.024	0.015	0.008	43.74
109	20	94	98			0.025	0.009	0.398	0.024	0.536	0.027	0.040	0.011	43.41
109	24	94	99			0.058	0.017	0.502	0.033	0.392	0.028	0.049	0.016	43.57
109	24	100	104			0.009	0.011	0.496	0.032	0.445	0.026	0.051	0.016	43.46
110	24	86	91			0.123	0.024	0.613	0.028	0.265	0.027			43.86
110	25	94	99			0.000	0.015	0.529	0.029	0.471	0.033			43.53
110	20	94	99			0.047	0.018	0.897	0.043	0.056	0.021			43.99
110	24	94	100			0.080	0.015	0.717	0.028	0.203	0.020			43.88
110	24	100	105			0.069	0.017	0.722	0.033	0.209	0.026			43.86
111	24	86	91			0.167	0.023	0.781	0.033	0.052	0.013			44.12
111	20	94	98			0.108	0.013	0.831	0.026	0.060	0.010			44.05
111	24	94	99			0.087	0.015	0.844	0.031	0.069	0.013			44.02
111	24	100	105			0.066	0.020	0.807	0.034	0.127	0.021			43.94
112	21	86	92	0.031	0.025	0.236	0.044	0.733	0.069	0.000	0.012			44.30
112	24	94	98	0.000	0.029	0.205	0.056	0.722	0.085	0.073	0.030			44.13
112	21	94	100	0.047	0.016	0.123	0.030	0.796	0.037	0.034	0.018			44.18
112	21	100	106	0.000	0.000	0.148	0.052	0.811	0.063	0.041	0.021			44.11

TABLE C.33: Relative Z-yields from ^{241}Pu (n_{th}, f).

Bibliography

[1] Uwe Quade, Klaus Rudolph, and Günter Siegert. A high resolution ionisation chamber tested with fission products of 235u. *Nuclear Instruments and Methods*, 164(3):435–436, 1979. doi: 10.1016/0029-554x(79)90075-2.

[2] U. Quade et al. Nuclide yields of light fission products from thermal-neutron induced fission of 233u at different kinetic energies. *Nuclear Physics A*, 487(1):1–36, oct 1988. doi: 10.1016/0375-9474(88)90127-3. URL `https://doi.org/10.1016/0375-9474(88)90127-3`.

[3] J.P. Bocquet, R. Brissot, and H.R. Faust. A large ionization chamber for fission fragment nuclear charge identification at the LOHENGRIN spectrometer. *Nuclear Instruments and Methods in Physics Research Section A: Accelerators, Spectrometers, Detectors and Associated Equipment*, 267(2-3):466–472, may 1988. doi: 10.1016/0168-9002(88)90487-1. URL `https://doi.org/10.1016/0168-9002(88)90487-1`.

[4] P. Grabitz. *Construction and first use of a calorimetric low-temperature detector for determining the nuclear charge yields of fission fragments*. PhD thesis, Johannes Gutenberg University Mainz (submitted), 2019.

[5] A. A. Sonzogni, T. D. Johnson, and E. A. McCutchan. Nuclear structure insights into reactor antineutrino spectra. *Physical Review C*, 91(1), jan 2015. doi: 10.1103/physrevc.91.011301. URL `https://doi.org/10.1103/physrevc.91.011301`.

[6] S. V. Tipnis et al. Yields of short-lived fission products produced following 235-u fission. *Physical Review C*, 58(2):905–915, aug 1998. doi: 10.1103/physrevc.58.905. URL https://doi.org/10.1103/physrevc.58.905.

[7] JEFF-3.1.1. *The JEFF-3.1.1 Nuclear Data Library*. OECD/NEA Data Bank, May 2009. JEFF Report 22.

[8] Otto Hahn and Fritz Strassmann. Nachweis der entstehung aktiver bariumisotope aus uran und thorium durch neutronenbestrahlung; nachweis weiterer aktiver bruchstücke bei der uranspaltung. *Die Naturwissenschaften*, 27 (6):89–95, feb 1939. doi: 10.1007/bf01488988. URL https://doi.org/10.1007/bf01488988.

[9] Hans G Börner and Friedrich Gönnenwein. *The Neutron*. WORLD SCIENTIFIC, nov 2011. doi: 10.1142/7283. URL https://doi.org/10.1142/7283.

[10] B. D. Wilkins, E. P. Steinberg, and R. R. Chasman. Scission-point model of nuclear fission based on deformed-shell effects. *Physical Review C*, 14(5): 1832–1863, nov 1976. doi: 10.1103/physrevc.14.1832. URL https://doi.org/10.1103/physrevc.14.1832.

[11] P. Möller et al. Nuclear fission modes and fragment mass asymmetries in a five-dimensional deformation space. *Nature*, 409(6822):785–790, feb 2001. doi: 10.1038/35057204. URL https://doi.org/10.1038/35057204.

[12] H. Goutte et al. Microscopic approach of fission dynamics applied to fragment kinetic energy and mass distributions inU238. *Physical Review C*, 71 (2), feb 2005. doi: 10.1103/physrevc.71.024316. URL https://doi.org/10.1103/physrevc.71.024316.

[13] K. Heyde J. Moreau. *The Nuclear Fission Process*. CRC Press, Boca Raton, FL, 1991. edited by C. Wageman.

[14] M.B. Chadwick et al. ENDF/b-VII.0: Next generation evaluated nuclear data library for nuclear science and technology. *Nuclear Data Sheets*, 107

(12):2931–3060, dec 2006. doi: 10.1016/j.nds.2006.11.001. URL https://doi.org/10.1016/j.nds.2006.11.001.

[15] Keiichi SHIBATA et al. JENDL-4.0: A new library for nuclear science and engineering. *Journal of Nuclear Science and Technology*, 48(1):1–30, jan 2011. doi: 10.1080/18811248.2011.9711675. URL https://doi.org/10.1080/18811248.2011.9711675.

[16] H. L. Anderson, E. Fermi, and A. V. Grosse. Branching ratios in the fission of uranium (235). *Physical Review*, 59(1):52–56, jan 1941. doi: 10.1103/physrev.59.52. URL https://doi.org/10.1103/physrev.59.52.

[17] J. K. Dickens. Fission yields for thermal-neutron fission of plutonium-241. *Nuclear Science and Engineering*, 70(2):177–183, may 1979. doi: 10.13182/nse79-a19650. URL https://doi.org/10.13182/nse79-a19650.

[18] J.P. Bocquet and R. Brissot. Mass, energy and nuclear charge distribution of fission fragments. *Nuclear Physics A*, 502:213–232, oct 1989. doi: 10.1016/0375-9474(89)90663-5. URL https://doi.org/10.1016/0375-9474(89)90663-5.

[19] E. Moll et al. Analysis of 236u-fission products by the recoil separator "lohengrin". *Nuclear Instruments and Methods*, 123(3):615–617, feb 1975. doi: 10.1016/0029-554x(75)90219-0. URL https://doi.org/10.1016/0029-554x(75)90219-0.

[20] P. Armbruster et al. The recoil separator lohengrin: Performance and special features for experiments. *Nuclear Instruments and Methods*, 139:213–222, dec 1976. doi: 10.1016/0029-554x(76)90677-7. URL https://doi.org/10.1016/0029-554x(76)90677-7.

[21] P. Egelhof. High resolution calorimetric low temperature detectors for applications in atomic and nuclear physics. In *Advances in Solid State Physics*, pages 61–76. Springer Berlin Heidelberg, 1999. doi: 10.1007/bfb0107465. URL https://doi.org/10.1007/bfb0107465.

[22] C. Enss. *Topics in Applied Physics, Volume 99: Cryogenic Particle Detection*. Springer, 2005. doi: 10.1007/b12169.

[23] S. Kraft-Bermuth. *Kalorimetrische Tieftemperaturdetektoren für niederenergetische ($E \leq$ 1 MeV/amu) Schwerionen und ihr erster Einsatz in der Beschleuniger Massenspektrometrie zur Spurenanalyse von ^{236}U*. PhD thesis, Johannes Gutenberg University Mainz, 2004.

[24] Peter Egelhof and Saskia Kraft-Bermuth. Topics in Applied Physics. In *Cryogenic Particle Detection*, volume 99, page 469. Springer, 2005. doi: 10.1007/b12169.

[25] S. Kraft-Bermuth et al. Calorimetric low temperature detectors for low-energetic heavy ions and their application in accelerator mass spectrometry. *Review of Scientific Instruments*, 80(10):103304, oct 2009. doi: 10.1063/1.3213622. URL https://doi.org/10.1063/1.3213622.

[26] A. Echler et al. Application of calorimetric low temperature detectors (CLTD's) for precise stopping power measurements of heavy ions in matter. *Journal of Low Temperature Physics*, 176(5-6):1033–1039, jan 2014. doi: 10.1007/s10909-013-1043-y. URL https://doi.org/10.1007/s10909-013-1043-y.

[27] S Kraft-Bermuth et al. Precise determination of the 1s lamb shift in hydrogen-like lead and gold using microcalorimeters. *Journal of Physics B: Atomic, Molecular and Optical Physics*, 50(5):055603, feb 2017. doi: 10.1088/1361-6455/50/5/055603. URL https://doi.org/10.1088/1361-6455/50/5/055603.

[28] A. Echler et al. Determination of electronic stopping powers of 0.05–1mev/u 131xe ions in c-, ni- and au-absorbers with calorimetric low temperature detectors. *Nuclear Instruments and Methods in Physics Research Section B: Beam Interactions with Materials and Atoms*, 391:38–51, jan 2017. doi: 10.1016/j.nimb.2016.10.011. URL https://doi.org/10.1016/j.nimb.2016.10.011.

[29] P. Grabitz et al. Determination of nuclear charge distributions of fission fragments from ^{235}U(n_{th}, f) with calorimetric low temperature detectors. *Journal of Low Temperature Physics*, 184(3-4):944–951, March 2016. doi: 10.1007/s10909-016-1566-0. URL https://doi.org/10.1007/s10909-016-1566-0.

[30] G. Mention et al. Reactor antineutrino anomaly. *Physical Review D*, 83(7), apr 2011. doi: 10.1103/physrevd.83.073006. URL https://doi.org/10.1103/physrevd.83.073006.

[31] D. A. Dwyer and T. J. Langford. Spectral structure of electron antineutrinos from nuclear reactors. *Physical Review Letters*, 114(1), jan 2015. doi: 10.1103/physrevlett.114.012502. URL https://doi.org/10.1103/physrevlett.114.012502.

[32] H. Kwon, F. Boehm, A. A. Hahn, H. E. Henrikson, J. L. Vuilleumier, J. F. Cavaignac, D. H. Koang, B. Vignon, F. v. Feilitzsch, and R. L. Mössbauer. Search for neutrino oscillations at a fission reactor. *Phys. Rev. D*, 24:1097–1111, Sep 1981. doi: 10.1103/PhysRevD.24.1097. URL https://link.aps.org/doi/10.1103/PhysRevD.24.1097.

[33] Y. Declais et al. Study of reactor antineutrino interaction with proton at bugey nuclear power plant. *Physics Letters B*, 338(2):383 – 389, 1994. ISSN 0370-2693. doi: https://doi.org/10.1016/0370-2693(94)91394-3. URL http://www.sciencedirect.com/science/article/pii/0370269394913943.

[34] B. Achkar et al. Search for neutrino oscillations at 15, 40 and 95 meters from a nuclear power reactor at bugey. *Nuclear Physics B*, 434(3):503 – 532, 1995. ISSN 0550-3213. doi: https://doi.org/10.1016/0550-3213(94)00513-E. URL http://www.sciencedirect.com/science/article/pii/055032139400513E.

[35] G. Zacek et al. Neutrino-oscillation experiments at the gösgen nuclear power reactor. *Phys. Rev. D*, 34:2621–2636, Nov 1986. doi: 10.1103/PhysRevD.34.2621. URL https://link.aps.org/doi/10.1103/PhysRevD.34.2621.

[36] Greenwood et al. Results of a two-position reactor neutrino-oscillation experiment. *Phys. Rev. D*, 53:6054–6064, Jun 1996. doi: 10.1103/PhysRevD.53.6054. URL https://link.aps.org/doi/10.1103/PhysRevD.53.6054.

[37] U. Brosa et al. Systematics of fission-channel probabilities. *Physical Review C*, 59(2):767–775, feb 1999. doi: 10.1103/physrevc.59.767. URL https://doi.org/10.1103/physrevc.59.767.

[38] F. REJMUND and M. CAAMANO. Systematics on even-odd effects in fission fragment yields: Comparison between symmetric and asymmetric splits. In *Seminar on Fission*. WORLD SCIENTIFIC, apr 2008. doi: 10.1142/9789812791061_0006. URL https://doi.org/10.1142/9789812791061_0006.

[39] Lise Meitner and O. R. Frisch. Disintegration of uranium by neutrons: a new type of nuclear reaction. *Nature*, 143(3615):239–240, feb 1939. doi: 10.1038/143239a0. URL https://doi.org/10.1038/143239a0.

[40] Niels Bohr and John Archibald Wheeler. The mechanism of nuclear fission. *Physical Review*, 56(5):426–450, sep 1939. doi: 10.1103/physrev.56.426. URL https://doi.org/10.1103/physrev.56.426.

[41] Maria G. Mayer. On closed shells in nuclei. *Physical Review*, 74(3):235–239, aug 1948. doi: 10.1103/physrev.74.235. URL https://doi.org/10.1103/physrev.74.235.

[42] K A Petrzhak and G N Flerov. SPONTANEOUS FISSION OF NUCLEI. *Soviet Physics Uspekhi*, 4(2):305–322, feb 1961. doi: 10.1070/pu1961v004n02abeh003339. URL https://doi.org/10.1070/pu1961v004n02abeh003339.

[43] Tsien San-Tsiang et al. Ternary and quaternary fission of uranium nuclei. *Nature*, 159(4049):773–774, jun 1947. doi: 10.1038/159773a0. URL https://doi.org/10.1038/159773a0.

[44] James Chadwick. Atomic energy and its applications. *Nature*, 159(4039): 421–425, mar 1947. doi: 10.1038/159421a0. URL https://doi.org/10.1038/159421a0.

[45] A.H. Wapstra and N.B. Gove. Part i. atomic mass table. *Atomic Data and Nuclear Data Tables*, 9(4-5):267–301, jul 1971. doi: 10.1016/s0092-640x(09)80001-6. URL https://doi.org/10.1016/s0092-640x(09)80001-6.

[46] R K Bhaduri M.A. Preston. *STRUCTURE OF THE NUCLEUS*. Westview Press, 2013. ISBN 8190806432.

[47] Leo Yaffe. *Nuclear chemistry, Vol 2*. New York : Academic Press, 1968. ISBN 9781483232317. see Fig. 1 in the article "Nuclear Fission" by Gindler and Huizenga.

[48] A. Bail. *Mesures de rendements isobariques et isotopiques des produits de fission lourds sur le spectrométre de masse LOHENGRIN*. PhD thesis, University of Bordeaux, 2009.

[49] A N Andreyev, K Nishio, and K-H Schmidt. Nuclear fission: a review of experimental advances and phenomenology. *Reports on Progress in Physics*, 81(1):016301, nov 2017. doi: 10.1088/1361-6633/aa82eb. URL https://doi.org/10.1088/1361-6633/aa82eb.

[50] Karl-Heinz Schmidt, Beatriz Jurado, and Charlotte Amouroux. General description of fission observables - jeff report 24. gef model. *JEFF Report 24*, 45(39):421–425, jun 2014.

[51] J. K. Ahn et al. Observation of reactor electron antineutrinos disappearance in the RENO experiment. *Physical Review Letters*, 108(19), may 2012. doi: 10.1103/physrevlett.108.191802. URL https://doi.org/10.1103/physrevlett.108.191802.

[52] Y. Abe, , et al. Improved measurements of the neutrino mixing angle theta13 with the double chooz detector. *Journal of High Energy Physics*, 2014(10),

oct 2014. doi: 10.1007/jhep10(2014)086. URL https://doi.org/10.1007/jhep10(2014)086.

[53] F. P. An et al. Measurement of the reactor antineutrino flux and spectrum at daya bay. *Physical Review Letters*, 116(6), feb 2016. doi: 10.1103/physrevlett.116.061801. URL https://doi.org/10.1103/physrevlett.116.061801.

[54] Patrick Huber. Determination of antineutrino spectra from nuclear reactors. *Physical Review C*, 84(2), aug 2011. doi: 10.1103/physrevc.84.024617. URL https://doi.org/10.1103/physrevc.84.024617.

[55] Sung Chang. The new case of missing antineutrinos. *Physics Today*, 69 (5):16–17, may 2016. doi: 10.1063/pt.3.3156. URL https://doi.org/10.1063/pt.3.3156.

[56] A. C. Hayes et al. Possible origins and implications of the shoulder in reactor neutrino spectra. *Physical Review D*, 92(3), aug 2015. doi: 10.1103/physrevd.92.033015. URL https://doi.org/10.1103/physrevd.92.033015.

[57] Y. Fukuda et al. Evidence for oscillation of atmospheric neutrinos. *Physical Review Letters*, 81(8):1562–1567, aug 1998. doi: 10.1103/physrevlett.81.1562. URL https://doi.org/10.1103/physrevlett.81.1562.

[58] P.F. de Salas et al. Status of neutrino oscillations 2018: 3 σ hint for normal mass ordering and improved CP sensitivity. *Physics Letters B*, 782:633–640, jul 2018. doi: 10.1016/j.physletb.2018.06.019. URL https://doi.org/10.1016/j.physletb.2018.06.019.

[59] A. C. Hayes et al. Systematic uncertainties in the analysis of the reactor neutrino anomaly. *Physical Review Letters*, 112(20), may 2014. doi: 10.1103/physrevlett.112.202501. URL https://doi.org/10.1103/physrevlett.112.202501.

[60] M. Fallot et al. New antineutrino energy spectra predictions from the summation of beta decay branches of the fission products. *Physical Review Letters*, 109(20), nov 2012. doi: 10.1103/physrevlett.109.202504. URL https://doi.org/10.1103/physrevlett.109.202504.

[61] Eberhard Moll, Heinrich Schrader, and G Siegert. Design and working principles of the lohengrin mass separator for fission products at the high flux reactor in grenoble. *Kerntechnik und Atompraxis*, 19:374–380, 08 1977.

[62] U. Köster et al. Experience with in-pile fission targets at LOHENGRIN. *Nuclear Instruments and Methods in Physics Research Section A: Accelerators, Spectrometers, Detectors and Associated Equipment*, 613(3):363–370, feb 2010. doi: 10.1016/j.nima.2009.09.078. URL https://doi.org/10.1016/j.nima.2009.09.078.

[63] Dorin N. Poenaru and Walter Greiner, editors. *Experimental Techniques in Nuclear Physics*. DE GRUYTER, jan 1997. doi: 10.1515/9783110809824. URL https://doi.org/10.1515/9783110809824.

[64] G Herrmann. Rapid radiochemical separations. *Arkiv för Fysik*, 36:111, 1967.

[65] G Herrmann and H O Denschlag. Rapid chemical separations. *Annual Review of Nuclear Science*, 19(1):1–32, dec 1969. doi: 10.1146/annurev.ns.19.120169.000245. URL https://doi.org/10.1146/annurev.ns.19.120169.000245.

[66] Gunter Herrmann and Norbert Trautmann. Rapid chemical methods for identification and study of short-lived nuclides. *Annual Review of Nuclear and Particle Science*, 32(1):117–147, 1982.

[67] K. Rengan, R.A. Meyer, and R.L. Hahn. *Ultrafast Chemical Separations*. Nuclear science series. National Academy Of Sciences, 1993. URL https://books.google.de/books?id=rT4rAAAAYAAJ.

[68] Hans Otto Denschlag. Independent fission yield measurements. *Nuclear Science and Engineering*, 94(4):337–352, 1986.

[69] G. Rudstam et al. Yields of products from thermal neutron-induced fission of 235u. *Radiochimica Acta*, 49(4), jan 1990. doi: 10.1524/ract.1990.49.4.155. URL https://doi.org/10.1524/ract.1990.49.4.155.

[70] J. Galy et al. Yields of products from fast neutron-induced fission of 233u measured by means of an isotope separator on-line (ISOL) system. *The European Physical Journal A*, 8(3):331–354, sep 2000. doi: 10.1007/s100500070086. URL https://doi.org/10.1007/s100500070086.

[71] A. Bail et al. Isotopic yield measurement in the heavy mass region for239pu thermal neutron induced fission. *Physical Review C*, 84(3), sep 2011. doi: 10.1103/physrevc.84.034605. URL https://doi.org/10.1103/physrevc.84.034605.

[72] N. Bohr. The penetration of atomic particles through matter. *Mat. Fys. Medd. Dan. Vid. Selsk*, 18(8), 1948.

[73] P. Armbruster et al. Low-energy fission investigated in reactions of 750 AMeV 238U ions with Pb and Be targets. *Zeitschrift für Physik A: Hadrons and Nuclei*, 355(1):191–201, dec 1996. doi: 10.1007/bf02769684. URL https://doi.org/10.1007/bf02769684.

[74] P. Armbruster et al. Measurement of a complete set of nuclides, cross sections, and kinetic energies in spallation of 238U at 1AGeV with protons. *Physical Review Letters*, 93(21), nov 2004. doi: 10.1103/physrevlett.93.212701. URL https://doi.org/10.1103/physrevlett.93.212701.

[75] M. Bernas et al. Fission-residues produced in the spallation reaction $238U_{+p}$ at 1AGeV. *Nuclear Physics A*, 725:213–253, sep 2003. doi: 10.1016/s0375-9474(03)01576-8. URL https://doi.org/10.1016/s0375-9474(03)01576-8.

[76] M. Bernas et al. Very heavy fission fragments produced in the spallation reaction 238U$_{+p}$ at 1AGeV. *Nuclear Physics A*, 765(1-2):197–210, jan 2006. doi: 10.1016/j.nuclphysa.2005.10.009. URL https://doi.org/10.1016/j.nuclphysa.2005.10.009.

[77] K.-H. Schmidt et al. Relativistic radioactive beams: A new access to nuclear-fission studies. *Nuclear Physics A*, 665(3-4):221–267, feb 2000. doi: 10.1016/s0375-9474(99)00384-x. URL https://doi.org/10.1016/s0375-9474(99)00384-x.

[78] William R. Leo. *Techniques for Nuclear and Particle Physics Experiments*. Springer Berlin Heidelberg, 1994. doi: 10.1007/978-3-642-57920-2. URL https://doi.org/10.1007/978-3-642-57920-2.

[79] James F. Ziegler, M.D. Ziegler, and J.P. Biersack. SRIM – the stopping and range of ions in matter (2010). *Nuclear Instruments and Methods in Physics Research Section B: Beam Interactions with Materials and Atoms*, 268(11-12):1818–1823, jun 2010. doi: 10.1016/j.nimb.2010.02.091. URL https://doi.org/10.1016/j.nimb.2010.02.091.

[80] James F. Ziegler. The stopping and range of ions in matter. http://www.srim.org. Version - SRIM-2013.

[81] Peter Sigmund. Stopping power in perspective. *Nuclear Instruments & Methods in Physics Research Section B: Beam Interactions with Materials and Atoms*, 135(1-4):1–15, feb 1998. doi: 10.1016/s0168-583x(97)00638-1. URL https://doi.org/10.1016/s0168-583x(97)00638-1.

[82] H Geissel, H Weick, C Scheidenberger, R Bimbot, and D Gardès. Experimental studies of heavy-ion slowing down in matter. *Nuclear Instruments & Methods in Physics Research Section B-beam Interactions With Materials and Atoms - NUCL INSTRUM METH PHYS RES B*, 195:3–54, 10 2002. doi: 10.1016/S0168-583X(02)01311-3.

[83] Stopping of ions heavier than helium. *Journal of the International Commission on Radiation Units and Measurements*, 5(1), jun 2005. doi: 10.1093/jicru/ndi001. URL https://doi.org/10.1093/jicru/ndi001.

[84] H. Bethe. Zur theorie des durchgangs schneller korpuskularstrahlen durch materie. *Annalen der Physik*, 397(3):325–400, 1930. doi: 10.1002/andp.19303970303. URL https://doi.org/10.1002/andp.19303970303.

[85] F. Bloch. Zur bremsung rasch bewegter teilchen beim durchgang durch materie. *Annalen der Physik*, 408(3):285–320, 1933. doi: 10.1002/andp.19334080303. URL https://doi.org/10.1002/andp.19334080303.

[86] Wei-Kan Chu and D Powers. Alpha-particle stopping cross section in solids from 400 kev to 2 mev. *Physical Review - PHYS REV X*, 187:478–490, 11 1969. doi: 10.1103/PhysRev.187.478.

[87] H. Geissel et al. Energy loss and energy loss straggling of fast heavy ions in matter. *Nuclear Instruments and Methods in Physics Research*, 194(1-3): 21–29, mar 1982. doi: 10.1016/0029-554x(82)90483-9. URL https://doi.org/10.1016/0029-554x(82)90483-9.

[88] J.S. Forster et al. Stopping power measurement for 19f, 24mg, 27al, 32s and 35cl at energies ∼0.2 to ∼3.5 MeV/nucleon in ti, fe, ni, cu, ag and au. *Nuclear Instruments and Methods*, 136(2):349–359, jul 1976. doi: 10.1016/0029-554x(76)90218-4. URL https://doi.org/10.1016/0029-554x(76)90218-4.

[89] L.C. Northcliffe and R.F. Schilling. Range and stopping-power tables for heavy ions. *Atomic Data and Nuclear Data Tables*, 7(3-4):233–463, jan 1970. doi: 10.1016/s0092-640x(70)80016-x. URL https://doi.org/10.1016/s0092-640x(70)80016-x.

[90] E. Fermi and E. Teller. The capture of negative mesotrons in matter. *Physical Review*, 72(5):399–408, sep 1947. doi: 10.1103/physrev.72.399. URL https://doi.org/10.1103/physrev.72.399.

[91] O.B. Firsov. A qualitative interpretation of the mean electron excitation energy in atomic collisions. *Sov. Phys. JETP*, 9(5):1076, 1959.

[92] J. Lindhard and M. Scharff. Energy dissipation by ions in the kev region. *Physical Review*, 124(1):128–130, oct 1961. doi: 10.1103/physrev.124.128. URL https://doi.org/10.1103/physrev.124.128.

[93] A. Sommerfeld. Asymptotische integration der differentialgleichung des thomas-fermischen atoms. *Zeitschrift für Physik*, 78(5-6):283–308, may 1932. doi: 10.1007/bf01342197. URL https://doi.org/10.1007/bf01342197.

[94] Gert Moliere. Theorie der streuung schneller geladener teilchen i. einzelstreuung am abgeschirmten coulomb-feld. *Zeitschrift für Naturforschung A*, 2(3):133–145, mar 1947. doi: 10.1515/zna-1947-0302. URL https://doi.org/10.1515/zna-1947-0302.

[95] J. Lindhard, M. Scharff, and H. E. Schiott. Range concepts and heavy ion ranges. *Mat. Fys. Medd. Dan. Vid. Selsk*, 33(14), 1963.

[96] J. Lindhard, V. Neilson, and M. Scharff. Approximation method in classical scattering by screened coulomb fields. *Mat. Fys. Medd. Dan. Vid. Selsk*, 36 (10), 1968.

[97] Mark Robinson and Ian Torrens. Computer simulation of atomic-displacement cascades in solids in the binary-collision approximation. *Physical Review B*, 9(12):5008–5024, jun 1974. doi: 10.1103/physrevb.9.5008. URL https://doi.org/10.1103/physrevb.9.5008.

[98] James F. Ziegler. *Handbook of Stopping Cross-Sections for Energetic Ions in All Elements (The Stopping and ranges of ions in matter ; v. 5)*. Pergamon Pr, apr 1980. ISBN 0080216072. URL https://www.xarg.org/ref/a/0080216072/.

[99] G.N. Knyazheva et al. Energy losses of 252cf fission fragments in thin foils. *Nuclear Instruments and Methods in Physics Research Section B: Beam Interactions with Materials and Atoms*, 248(1):7–15, jul 2006. doi: 10.1016/j.nimb.2006.04.071. URL https://doi.org/10.1016/j.nimb.2006.04.071.

[100] Saskia Kraft-Bermuth. private communication.

[101] Werner Lauterfeld. Systematische untersuchungen zur optimierung der z-auflösung bei der bestimmung von element-verteilungen von spaltfragmenten mit kalorimetrischen tieftemperatur-detektoren. Master's thesis, Johannes Gutenberg University Mainz, 2017.

[102] N. Bohr. LX. on the decrease of velocity of swiftly moving electrified particles in passing through matter. *The London, Edinburgh, and Dublin Philosophical Magazine and Journal of Science*, 30(178):581–612, oct 1915. doi: 10.1080/14786441008635432. URL https://doi.org/10.1080/14786441008635432.

[103] C. Tschalär. Straggling distributions of large energy losses. *Nuclear Instruments and Methods*, 61(2):141–156, may 1968. doi: 10.1016/0029-554x(68)90535-1. URL https://doi.org/10.1016/0029-554x(68)90535-1.

[104] C. Tschalär. Straggling distributions of extremely large energy losses. *Nuclear Instruments and Methods*, 64(3):237–243, oct 1968. doi: 10.1016/0029-554x(68)90159-6. URL https://doi.org/10.1016/0029-554x(68)90159-6.

[105] B Rossi. *High-Energy Particles*. Prentice Hall, 1952. ISBN 0133873242. URL https://www.amazon.com/High-Energy-Particles-B-Rossi/dp/0133873242?SubscriptionId=0JYN1NVW651KCA56C102&tag=techkie-20&linkCode=xm2&camp=2025&creative=165953&creativeASIN=0133873242.

[106] P. V. Vavilov. *Sov. Phys. JETP*, 5:749, 1957.

[107] A. Echler. *E-ToF Messungen mit kalorimetrischen Tieftemperatur-Detektoren zur Bestimmung spezifischer Energieverluste und zur*

Massenidentifikation niederenergetischer Schwerionen. PhD thesis, Johannes Gutenberg University Mainz, 2013.

[108] Santwana Dubey et al. Application of calorimetric low-temperature detectors for the investigation of z-yield distributions of fission fragments. *Journal of Low Temperature Physics*, jun 2018. doi: 10.1007/s10909-018-1988-y. URL https://doi.org/10.1007/s10909-018-1988-y.

[109] Harald Büker. Arten und eigenschaften der kernstrahlung. In *Theorie und Praxis der Halbleiterdetektoren für Kernstrahlung*, pages 1–21. Springer Berlin Heidelberg, 1971. doi: 10.1007/978-3-642-80613-1_1. URL https://doi.org/10.1007/978-3-642-80613-1_1.

[110] William Shockley and Hans J. Queisser. Detailed balance limit of efficiency of p-n junction solar cells. *Journal of Applied Physics*, 32(3):510–519, mar 1961. doi: 10.1063/1.1736034. URL https://doi.org/10.1063/1.1736034.

[111] W. Shockley and W. T. Read. Statistics of the recombinations of holes and electrons. *Physical Review*, 87(5):835–842, sep 1952. doi: 10.1103/physrev.87.835. URL https://doi.org/10.1103/physrev.87.835.

[112] R. N. Hall. Electron-hole recombination in germanium. *Physical Review*, 87(2):387–387, jul 1952. doi: 10.1103/physrev.87.387. URL https://doi.org/10.1103/physrev.87.387.

[113] C. Kittel. *Introduction to Solid State Physics*. Wiley, 2004. ISBN 9780471415268. URL https://books.google.de/books?id=kym4QgAACAAJ.

[114] A. Echler. Aufbau und test eines arrays kalorimetrischer tieftemperatur-detektoren für schwerionen, 2007. Diploma Thesis.

[115] Frederick Reif. *Statistische Physik und Theorie der Wärme (German Edition)*. De Gruyter, oct 1987. ISBN 311011383X. URL https://www.xarg.org/ref/a/311011383X/.

[116] H.J. Meier. *Kalorimetrische Tieftemperaturdetektoren mit supraleitendem Phasenübergangsthermometer zum Schwerionennachweis*. PhD thesis, Johannes Gutenberg University Mainz, 1994.

[117] T.H Wilmshurst. *Signal Recovery from Noise in Electronic Instrumentation*. CRC Press, jan 1990. ISBN 0750300582. URL https://www.xarg.org/ref/a/0750300582/.

[118] Stephen H. Lewis Rober G. Meyer Paul R. Gray, Paul J. Hurst. *Analysis and Design of Analog Integrated Circuits, 5th Edition*. Wiley, jan 2009. ISBN 0470245999. URL https://www.xarg.org/ref/a/0470245999/.

[119] Kohlrausch – praktische physik, band 3, tabellen und diagramme. herausgegeben von d. hahn und s. wagner, b. g. teubner stuttgart, 23. auflage 1986, 344 s., DM 165, –. *Physik in unserer Zeit*, 18(1):32–32, 1987. doi: 10.1002/piuz.19870180109. URL https://doi.org/10.1002/piuz.19870180109.

[120] Santwana Dubey et al. Application of calorimetric low-temperature detectors for the investigation of z-yield distributions of fission fragments. *EPJ Web of Conferences*, 193:04002, 2018. doi: 10.1051/epjconf/201819304002. URL https://doi.org/10.1051/epjconf/201819304002.

[121] Maier-leibnitz-laboratorium, besucherinfo. http://www.bl.physik.uni-muenchen.de/tandem/besucherinfo/besucherinfo.pdf. Accessed: 21-02-2017.

[122] N. S. Wu and M. Hu. Criterion for an EMG peak. *Chromatographia*, 28 (7-8):415–416, oct 1989. doi: 10.1007/bf02261025. URL https://doi.org/10.1007/bf02261025.

[123] U. Köster et al. Ternary fission yields of 241pu(nth, f). *Nuclear Physics A*, 652(4):371–387, jun 1999. doi: 10.1016/s0375-9474(99)00115-3. URL https://doi.org/10.1016/s0375-9474(99)00115-3.

[124] HANS-DIETER BETZ. Charge states and charge-changing cross sections of fast heavy ions penetrating through gaseous and solid media. *Reviews of*

Modern Physics, 44(3):465–539, jul 1972. doi: 10.1103/revmodphys.44.465. URL https://doi.org/10.1103/revmodphys.44.465.

[125] Hans D. Betz. Charge equilibration of high-velocity ions in matter. In *Methods in Experimental Physics*, pages 73–148. Elsevier, 1980. doi: 10.1016/s0076-695x(08)60298-7. URL https://doi.org/10.1016/s0076-695x(08)60298-7.

[126] H. Wohlfarth et al. The ionic charge distribution of fission products and the influence of internal conversion on highly preionized heavy ions. *Zeitschrift fr Physik A: Atoms and Nuclei*, 287(2):153–163, jun 1978. doi: 10.1007/bf01408085. URL https://doi.org/10.1007/bf01408085.

[127] A.D. Belyaev et al. Some peculiarities in ionic charge distributions of 241pu(nth, f)-fission products. *Nuclear Instruments and Methods in Physics Research Section B: Beam Interactions with Materials and Atoms*, 43(1):5–8, aug 1989. doi: 10.1016/0168-583x(89)90070-0. URL https://doi.org/10.1016/0168-583x(89)90070-0.

[128] Boon Quan Lee. *A Numerical Model of Atomic Relaxation and its Applications*. PhD thesis, Department of Nuclear Physics, Research School of Physics and Engineering, The Australian National University, 2017.

[129] Coral M. Baglin. Nuclear data sheets for a = 92. *Nuclear Data Sheets*, 113(10):2187–2389, oct 2012. doi: 10.1016/j.nds.2012.10.001. URL https://doi.org/10.1016/j.nds.2012.10.001.

[130] G. Martinez et al. Mass and nuclear charge yields for 237np(2nth, f) at different fission fragment kinetic energies. *Nuclear Physics A*, 515(3):433–465, sep 1990. doi: 10.1016/0375-9474(90)90593-b. URL https://doi.org/10.1016/0375-9474(90)90593-b.

[131] J.F. Berger, M. Girod, and D. Gogny. Time-dependent quantum collective dynamics applied to nuclear fission. *Computer Physics Communications*, 63 (1-3):365–374, feb 1991. doi: 10.1016/0010-4655(91)90263-k. URL https://doi.org/10.1016/0010-4655(91)90263-k.

[132] Sylvain Julien-Laferrière. private communication.

[133] C. Schmitt et al. Fission yields at different fission-product kinetic energies for thermal-neutron-induced fission of 239pu. *Nuclear Physics A*, 430(1): 21–60, nov 1984. doi: 10.1016/0375-9474(84)90191-x. URL https://doi.org/10.1016/0375-9474(84)90191-x.

[134] P. Schillebeeckx et al. Investigation of mass, charge and energy of 241pu(nth, f) fragments with the cosi-fan-tutte spectrometer. *Nuclear Physics A*, 580 (1):15–32, nov 1994. doi: 10.1016/0375-9474(94)90812-5. URL https://doi.org/10.1016/0375-9474(94)90812-5.

[135] B. L. Tracy et al. Rb and cs isotopic cross sections from 40-60-MeV-proton fission ofU238, th232, andU235. *Physical Review C*, 5(1):222–234, jan 1972. doi: 10.1103/physrevc.5.222. URL https://doi.org/10.1103/physrevc.5.222.

[136] W. Lang et al. Nuclear charge and mass yields for 235u(nth, f) as a function of the kinetic energy of the fission products. *Nuclear Physics A*, 345(1): 34–71, aug 1980. doi: 10.1016/0375-9474(80)90411-x. URL https://doi.org/10.1016/0375-9474(80)90411-x.

[137] M. J. Cubison and J. L. Jimenez. Statistical precision of the intensities retrieved from constrained fitting of overlapping peaks in high-resolution mass spectra. *Atmospheric Measurement Techniques*, 8(6):2333–2345, jun 2015. doi: 10.5194/amt-8-2333-2015. URL https://doi.org/10.5194/amt-8-2333-2015.

[138] G. Simon et al. Pulse height defect in an ionization chamber investigated by cold fission measurements. *Nuclear Instruments and Methods in Physics Research Section A: Accelerators, Spectrometers, Detectors and Associated Equipment*, 286(1-2):220–229, jan 1990. doi: 10.1016/0168-9002(90)90224-t. URL https://doi.org/10.1016/0168-9002(90)90224-t.

[139] Arthur C. Wahl. Nuclear-charge distribution and delayed-neutron yields for thermal-neutron-induced fission of 235u, 233u, and 239pu and for spontaneous fission of 252cf. *Atomic Data and Nuclear Data Tables*, 39(1):1–156, may 1988. doi: 10.1016/0092-640x(88)90016-2. URL `https://doi.org/10.1016/0092-640x(88)90016-2`.

Acknowledgements